Silicon photonic crystals
and
spontaneous emission

Silicon photonic crystals and spontaneous emission
Michiel Jacob Andries de Dood
Ph. D. Thesis Utrecht University, April 2002
ISBN: 90-9015654-2

A digital version of this thesis can be downloaded from http://www.amolf.nl
Printed copies can by obtained by request via e-mail to library@amolf.nl or by addressing the library at the FOM-Institute for Atomic and Molecular Physics, Kruislaan 407, 1098 SJ Amsterdam, The Netherlands.

Silicon photonic crystals
and
spontaneous emission

Silicium fotonische kristallen
en
spontane emissie

(met een samenvatting in het Nederlands)

Proefschrift

Ter verkrijging van de graad van doctor aan de Universiteit Utrecht op gezag van de Rector Magnificus, Prof. Dr. W. H. Gispen, in gevolge het besluit van het College voor Promoties in het openbaar te verdedigen op donderdag 11 april 2002 des middags te 12:45 uur

door

Michiel Jacob Andries de Dood

geboren op 18 januari 1975 te Landsmeer

Promotor: Prof. Dr. A. Polman
Faculteit der Natuur- en Sterrenkunde Universiteit Utrecht
FOM-Instituut voor Atoom- en Molecuulfysica Amsterdam

The work described in this thesis was performed at the FOM-Institute for Atomic and Molecular Physics, Kruislaan 407, 1098 SJ Amsterdam, The Netherlands. It is part of the research program of the Foundation for Fundamental Research on Matter (FOM), and was made possible by financial support from the Dutch Organization for the Advancement of Research (NWO).

Contents

1

Introduction

1.1 General introduction

The revolution in the electronics industry that took place over the last decades has changed our daily life in a way never envisaged at the time when the transistor was invented [1, 2]. At the basis of this revolution stood the discovery and basic understanding of semiconductors which enabled mankind to invent and develop the electronics that we have become so used to over the years. Compared to electronics, optical technology is only at a very modest level nowadays. Just as semiconductors have revolutionized the electronics technology, photonic crystals, being the optical analogue of electronic semiconductor crystals, might lead to a major breakthrough in opto-electronics and integrated optics.

Originally photonic crystals were proposed as materials that could localize light [3] and completely inhibit spontaneous emission if a light source is embedded in such a crystal [4], an extreme example of the Purcell effect [5]. Analogous to the electronic bandgap in semiconductors such photonic crystals exhibit a certain frequency range where light cannot propagate in any direction in the structure. This frequency range is known as the photonic bandgap. While semiconductors exist by the virtue of the periodicity of the underlying crystalline lattice of atoms, photonic crystals are formed by a periodic variation in dielectric constant on a length scale comparable to the wavelength of interest. If an atom is placed inside such a structure, the atom cannot radiate away energy if its transition frequency falls within the photonic bandgap, and thus spontaneous emission can be completely inhibited.

As described above, photonic crystals are materials that have a periodic arrangement of the dielectric constant on a length scale comparable to the wavelength of interest. Due to this periodicity one can find a frequency band for which the propagation of light in a certain direction is forbidden; this band is called the stop gap in that particular direction. This frequency band is centered around the frequency that fulfills the Bragg condition ($2d\sin(\theta) = n\lambda$) in that direction. Here, d denotes the distance between the set of lattice planes responsible for Bragg reflection, θ is the angle of incidence, n is the order of the Bragg reflection and λ denotes the wavelength. The Bragg peak of an infinite photonic crystal designed for optical wavelengths displays a certain spectral width, in contrast to the Bragg peaks observed in ordinary x-ray diffraction. This is due to the fact that only a limited number of lattice planes are involved in the Bragg reflection taking place in a photonic crystal, which is caused by the high index contrast between the materials used. If the width of this stop gap is large enough to overlap with stop gaps in other directions one can achieve a complete photonic bandgap where no waves can propagate in any direction in the crystal. Strictly speaking such a complete photonic bandgap can only exist in three dimensions since in one and two-dimensional systems one cannot define sets of lattice planes leading to Bragg reflection in directions where the structure is not periodic.

The possibility of complete inhibition of spontaneous emission is thus limited to three-dimensional (3-D) photonic crystals. However, most of the other physical concepts of 3-D crystals do apply to their lower dimensional counterparts. Since the lower dimensional crystals are generally easier to fabricate, they can be used to study some of the aspects of 3-D crystals and may lead to applications and devices that do not require the complete inhibition of spontaneous emission. For instance, to understand the emission of light sources in photonic crystals even one-dimensional (1-D) structures, such as a single interface, are of importance, since the influence of the dielectric structure on spontaneous emission is relatively easy to calculate. Experiments on 1-D structures, e. g. involving atoms placed near a metallic mirror [6, 7] or dielectric interface [8], can be compared to theory. In this way the decay of the atom can be split into a radiative contribution and contributions from other decay mechanisms that do not involve photons, generally referred to as non-radiative decay.

Photonic crystals may also find use in applications where one needs to manipulate and steer light on a wavelength scale. A classical example is formed by 1-D crystals that have been known for decades and are commonly referred to as Bragg-mirrors. These crystals show efficient reflection for a certain frequency band and as such find application as dielectric laser mirrors or band-filters. The extension to two-dimensional (2-D) systems is of great practical importance since 2-D structures can be integrated relatively easily with existing planar waveguide and fiber technology for optical communication purposes. The confinement of the light in the third (out of plane) direction is in this case provided by the planar waveguide, while the in plane propagation is dictated by the properties of the 2-D photonic crystal involved. The use of such 2-D photonic crystals was demonstrated in e. g. add-drop filters [9] and highly efficient light emitting diodes [10] that make use of a 2-D photonic crystal to couple light out of an integrated waveguide structure.

Most of these applications do not use a perfect 2-D crystal, but rely on the use of well defined and controlled defects in the otherwise perfect structure, analogous to the doping of a semiconductor crystal with impurity atoms. In a photonic crystal, such a defect is formed by adding or removing dielectric material at one or more well defined positions in the lattice. A single point defect, made by changing a single scatterer in the perfect lattice, can be used to define a high-Q cavity with a very small mode volume. A line defect can be made by removing a row of rods from a square lattice of dielectric rods [11]. Such a line defect can be used to guide light using the reflective properties of the photonic crystal. Because the refractive index of this guide is lower than that of the surrounding medium the guiding mechanism fundamentally differs from the principle of total internal reflection in a "classical" waveguide or optical fiber. This opens the possibility to guide and steer light in air on a wavelength scale [11]; a concept that was demonstrated in the microwave regime [12]. The same principle for optical wavelengths is used in a photonic crystal fiber that is composed of a hollow core surrounded by a photonic crystal [13]. These guides are considered superior to ordinary fibers and waveguides in high power applications, since air (vacuum) has less absorption, and thus such fibers have a higher damage threshold and lower optical nonlinearities than classical fibers.

1.2 Photonic crystals

1.2.1 Fabrication of photonic crystals

To fabricate photonic crystals, materials with a periodic refractive index on a wavelength length scale are needed. The most common way to accomplish this is to use two materials of different refractive index and use these as building blocks for a periodic lattice. If microwaves are used, the typical length scale is in the mm to cm range and crystals can be fabricated by hand. Because of the scaling properties of photonic crystals [14], experiments on such crystals were used to verify the early photonic bandstructure calculations [15–17]. To scale down these ideas to visible and near-infrared wavelengths calls for fabrication techniques that assemble structures on a submicron length scale. Over the

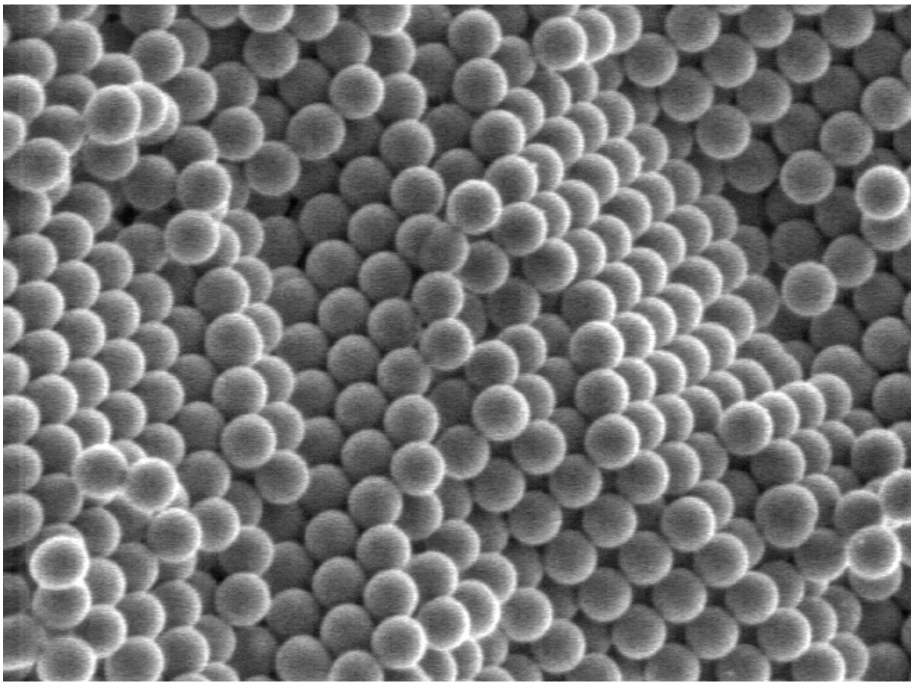

Figure 1.1: *Scanning electron micrograph of a 3-D photonic crystal made by self-assembly of colloidal* SiO_2 *spheres, taken from Ref. [23]. The crystal is grown from a dispersion of silica spheres with a mean diameter of 300 nm and a size polydispersity of 0.7%.*

years the nanofabrication problem has proven to be a main research direction for many research groups and up to now the fabrication of large, high quality crystals still is a major challenge. Two fundamentally different approaches have been tried, based on either self-assembly of colloidal particles, or lithography combined with etching techniques.

The self-assembly approach utilizes colloidal spheres that can self-organize in several different colloidal crystal symmetries if their size polydispersity (i. e. the relative width of the size distribution) is low enough [18, 19]. Particles can be made from different materials (e. g. latex, SiO_2, ZnS) by a corresponding wet chemical synthesis route and are available in a size range from well below 100 nm up to several microns in diameter, providing the length scales required for visible and near-infrared wavelengths. An example of such a colloidal crystal is shown by the scanning electron microscope (SEM) image in Fig. 1.1. The crystal is grown from a colloidal dispersion of silica spheres with a mean diameter of 300 nm and a size polydispersity as low as 0.7%. Figure 1.1 clearly demonstrates the regular structure formed by self-assembly of the spherical SiO_2 particles.

Although large 3-D colloidal crystals can be grown, the difficulty of this technique is to control the crystallization process in such a way as to make structures with different lattice symmetries. This technique inevitably leads to the incorporation of random defects in the crystal. Drying of the crystals results in cracking of the crystal, caused by shrinkage of the individual colloidal particles in the crystal. In practice most colloidal crystals thus consist of a number of relatively small single crystalline domains. In addition, the colloids used typically do not have a high enough index contrast to obtain a complete photonic bandgap. The latter issue can be solved by infiltrating the crystal with a high index material (e. g. TiO_2 [20] or Si [21, 22]) followed by removal of the original particles, thus creating an inverse structure of high index contrast.

The other main route to fabricate photonic crystals is to use etching techniques in

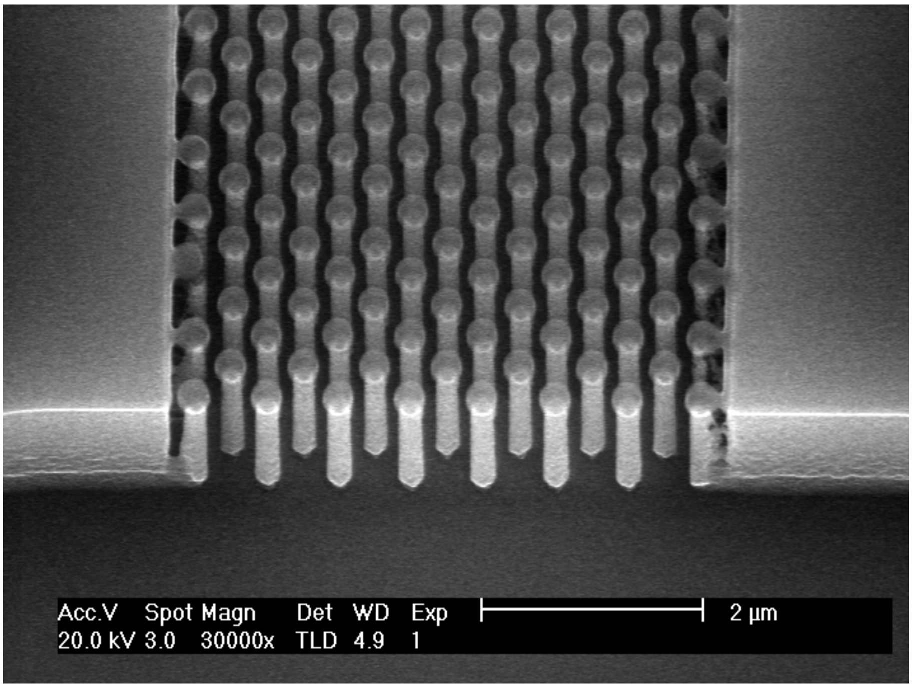

Figure 1.2: *Example of a 2-D photonic crystal of Si rods placed on a square lattice made by deep anisotropic etching, using the method described in detail in Chapter 3, in a silicon-on-insulator substrate (1.5 μm Si on 3.0 μm SiO_2). The crystal is designed to have a photonic bandgap around 1.5 μm and has a lattice constant a of 420 nm. The pillars are cylindrical and are 210 nm in diameter.*

a planar substrate. This approach requires the fabrication of lithographic masks with feature sizes down to 100 nm. The mask is then used in an anisotropic etching process in high index materials, such as Si [24], GaAs [25, 26] and other semiconductors [27, 28]. Although deep-UV optical lithography can be used for this purpose, most masks are fabricated by electron-beam lithography which provides a high level of control over the structure. This technique is most suited for 2-D structures since the mask technology is essentially a 2-D technology. As an example, Fig. 1.2 shows a 2-D photonic crystal made of cylindrical Si rods of 210 nm diameter placed on a square lattice with a lattice constant of 420 nm. The rods are etched in a silicon-on-insulator (SOI) wafer with a 1.5 μm thick Si layer on top of a 3.0 μm thick SiO_2 layer, to provide the necessary index contrast to guide the light in the vertical direction. The design and fabrication method of such SOI devices are described in Chapters 2 and 3 respectively. The Si waveguides to the left and right side of the crystal serve to couple light into the device and collect the light being transmitted.

Although a silicon photonic crystal of dielectric rods is used here as an example, other structures and other materials can be used to fabricate photonic crystals. The etching of other materials calls for a different reactive ion etching process, using different reactive species to etch the material. To etch different structures one needs to change the lithographically defined mask and tune the etching process to fabricate the structure. Two important limitations of the technique exist, being the minimum feature size that can be defined in the lithography process and the anisotropy of the reactive ion etching process which limits the maximum attainable aspect ratio of the elements constituting the photonic crystal. Feature sizes down to 100 nm and aspect ratios of 1–2 are readily available given modern semiconductor processing technology. By tuning the electron-beam lithography process, a smaller minimum feature size can be attained which enables fabrication of structures for visible and near-infrared wavelengths. For the aspect ratio, the requirements to fabricate most photonic crystals are just beyond these standards. A major challenge therefore is the optimization of the processing conditions to fulfill the requirements on aspect ratio.

The fabrication of 3-D structures for near-infrared wavelengths using lithographic tools is more difficult and is limited to a finite number of layers given the present technology. Different approaches have been tried, including the layer-by-layer fabrication of woodpile structures in Si [29, 30] and GaAs [31], direct etching of the "Yablonovite" structure in GaAs [32], and a deposition technique in which a 2-D pattern defined in the first layer is propagated in the growth of a SiO_2/Si stack. Although in all these processes the number of layers is limited, these photonic crystals display many of the properties of their infinite counterparts because of the high index contrast that is typically used. Furthermore, since ion etching techniques are used, it becomes possible to define, control and tailor defects that add functionality to the structure; this is much more difficult to achieve in structures defined by self assembly.

1.2.2 Photonic bandstructure

The theoretical description of the propagation of light in photonic crystals is provided by calculating the photonic bandstructure from Maxwell's equations. Such calculations are done numerically and make use of the periodicity of the lattice by imposing periodic boundary conditions. Based on concepts well known from solid state physics, the solutions to Maxwell's equations are represented in terms of a photonic bandstructure or dispersion relation $\omega(\mathbf{k})$ (analogous to the electronic bandstructure $E(\mathbf{k})$ in semiconductor crystals). The optical modes in this structure are Bloch waves, i. e. functions that have the periodicity of the lattice with an additional phase factor $\exp(i\mathbf{k}\cdot\mathbf{r})$. The periodic structure can diffract a wave, thereby shifting the dispersion relation by a reciprocal lattice vector. This implies that for any $\mathbf{k}$-vector in reciprocal space the dispersion relation can always be shifted back to the first Brillouin zone by adding or subtracting an integer number of reciprocal lattice vectors. By making use of all symmetries of the lattice it suffices to specify the bandstructure in the irreducible part of the Brillouin zone [33] only. In general the bandstructure is only plotted along the characteristic path of the irreducible part of the Brillouin zone, i. e. a line following all edges of the irreducible part. In practice [33], all maxima and minima of the bandstructure lie on this characteristic path. Hence the existence and frequency range of a photonic bandgap can be deduced from a plot of the bandstructure along the characteristic path.

1.2.3 Transfer matrix method

Throughout this thesis the transfer matrix method (TMM) [34, 35] is used to calculate photonic bandstructures in two-dimensional structures. The results of the calculations were compared with results obtained from the plane wave method [36] and the photonic analogue of the Korringa-Kohn-Rostocker (KKR) method [37]. The TMM relies on the construction of a transfer matrix $\chi(\omega)$ that relates the electro-magnetic fields at one side

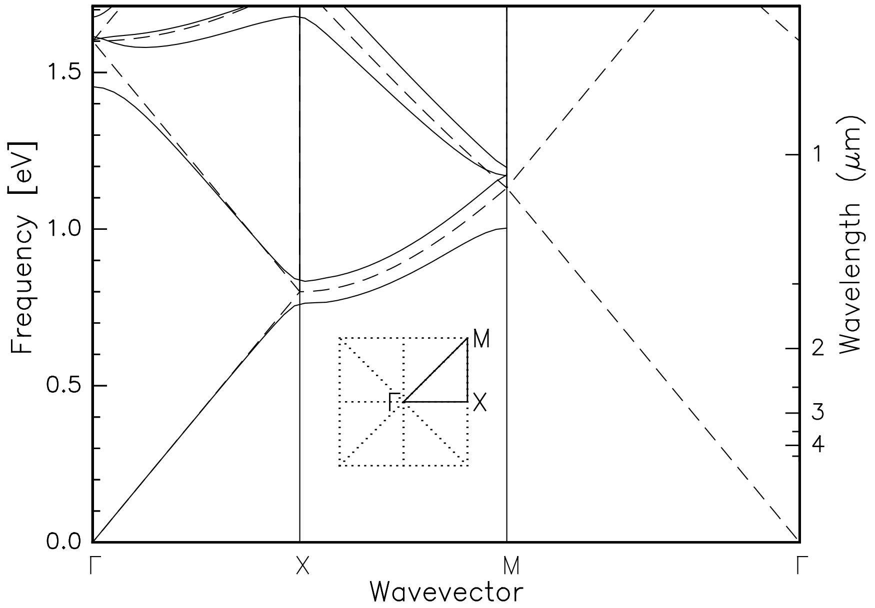

Figure 1.3: *2-D photonic bandstructure of a square lattice of infinitely long cylindrical rods in air (drawn lines). The rods are 295 nm in diameter and placed on a lattice with a lattice constant of 735 nm. The dielectric constant of the rods $\varepsilon = 2$. The dashed lines represents the "light line" of a homogeneous dielectric folded back to the irreducible part of the Brillouin zone. The inset shows the irreducible part of the Brillouin zone of the square lattice within the first Brillouin zone.*

of the unit cell ($z = 0$) to the fields at the other side of the cell ($z = a$)*. By imposing the Bloch condition one can write:

$$\begin{pmatrix} \mathbf{E}(z=a) \\ \mathbf{H}(z=a) \end{pmatrix} = \chi(\omega) \begin{pmatrix} \mathbf{E}(z=0) \\ \mathbf{H}(z=0) \end{pmatrix} = \mathrm{e}^{iK_z(\omega)a} \begin{pmatrix} \mathbf{E}(z=0) \\ \mathbf{H}(z=0) \end{pmatrix} \tag{1.1}$$

where $K_z(\omega)$ denotes the inverse of the bandstructure $\omega(\mathbf{k})$ in a specific direction K_z. The bandstructure can thus be obtained as the eigenvalues of the transfer matrix, $\chi(\omega)$. The essential step in the calculation is thus to obtain the real space transfer matrix. In the calculation scheme a real space mesh is used on which the Maxwell equations are solved numerically. This is done by deriving a number of finite difference equations at a fixed frequency ω that relate the $\mathbf{E}$ and $\mathbf{H}$ fields at a certain point to the fields at neighboring mesh points. By specifying boundary conditions at one side of the unit cell, the solution can be found by numerical integration.

As an example, the calculated dispersion relation for a relatively low index contrast 2-D photonic crystal is shown in Fig. 1.3. The crystal consists of dielectric cylinders with a diameter of 295 nm and a dielectric constant $\varepsilon = 2$ (a typical value for glass and polymer materials) placed on a square lattice with a lattice constant of 735 nm. Results are shown for transverse magnetic polarization only, i. e. the $\mathbf{E}$-field is parallel to the long axis of the cylinders. The wavevector on the horizontal axis is limited to the edge of

---

*The propagation of waves in other directions than the z direction can be treated in a similar manner.

the irreducible part of the Brillouin zone ($\mathbf{\Gamma} \rightarrow \mathrm{X} \rightarrow \mathrm{M} \rightarrow \mathbf{\Gamma}$, see the inset in Fig. 1.3). The vertical axis displays the photon energy $\hbar\omega$. Making use of the scaling properties of photonic crystals, the lattice constant and diameter of the rods are chosen such that the first order Bragg reflections occur near 0.8 eV, corresponding to the important telecommunication wavelength of 1.5 μm. The index contrast in this case is not sufficient to open up a photonic bandgap. The bandstructure however, clearly demonstrates the concept of Bragg reflection at the edges of the Brillouin zone, and it demonstrates the folding of the dispersion relation to the first Brillouin zone. For comparison the dispersion relation of a homogeneous dielectric ($\omega = c\mathbf{k}$), or "light line", is added to the figure (dashed lines). Here c is the speed of light in the medium, of which the dielectric constant was chosen such that it matches the effective dielectric constant of the photonic crystal, i. e. the slope of the "light line" is the same as that of the bandstructure in the long wavelength limit (close to 0 eV). Chapter 2 discusses the bandstructure and effective dielectric constant (for both polarizations) in more detail.

Note that dispersion relations $\omega(\mathbf{k})$ are normally specified in dimensionless frequency units. These units make explicit use of the fact that no fundamental length scale is defined by Maxwell's equations [14]. This implies that the frequency of the bandgap scales directly with the lattice constant of the photonic crystal, as is easily seen from Bragg's law. This greatly facilitates the design of photonic crystals since any calculation can be scaled to the frequency of interest.

1.3 Theory of spontaneous emission

The concepts of spontaneous emission and photonic crystals are closely connected. If an atom is placed inside a photonic crystal no power can be radiated away if no light can propagate in the structure and spontaneous emission is thus completely inhibited. Classically, the influence of dielectric structures on spontaneous emission can be calculated by considering a point dipole that radiates away energy. If part of the energy is reflected back to the emitting dipole, interference effects occur that alter the amount of power radiated away. A quantum mechanical theory essentially gives the same result, but calculates a transition probability of a single atom. The experimentally observable decay of an excited atom is a statistical average over an ensemble of atoms. This quantum mechanical calculation can be done in a framework in which both the atom and the electromagnetic field are treated quantum mechanically, known as second quantization. The calculations of transition rates in this thesis are obtained from this quantum-mechanical description. The purpose of this section is to illustrate the basic principles, the use of Fermi's Golden Rule and the concept of local density of states (LDOS).

If an excited atom is placed inside a cavity, the energy it radiates away depends on the cavity. To give a proper description of such a system one needs to consider the hybrid system of the atom and cavity together. In such a picture the decay of the atom proceeds through the modes supported by the cavity. The number of modes in the cavity depend on the size of the cavity and on the reflectivity of the cavity walls. The decay rate of the atom scales with the amount of possible decay channels (modes) in the cavity. The LDOS counts the number of available modes between a frequency ω and $\omega + \mathrm{d}\omega$, at a position $\mathbf{r}$ in the cavity. The LDOS is thus a property that is directly related to the spontaneous emission probability of an atom at position $\mathbf{r}$.

As described above, the spontaneous emission of an atom is influenced by its surrounding. However, in the discussion above the macroscopic electromagnetic field is used. To directly calculate the emission rate the local field at the position of the atom is needed. In a bulk dielectric, this microscopic local field differs from the macroscopic field by a correction factor. This correction factor depends on the model used to describe the local field; i. e. empty-cavity, full-cavity or no-cavity model. Typically, the size of the cavity used in these models is comparable to the size of the electronic wave function associated with the transition of the atom itself. For all situations studied in this thesis the distance of the atom to the interface where the dielectric is modified is much longer than this length scale and the local field is only influenced through the macroscopic electromagnetic field of the structure under investigation. The microscopic electric field thus has a fixed relation to the macroscopic field, and the changes in spontaneous emission rate can be calculated and described via the concept of the LDOS.

1.3.1 Local density of states from normalized eigenfunctions

Let us consider an atom with a ground state and a single excited state that is of importance, reducing the atom system to a simple two-level system with states $|0\rangle$ and $|1\rangle$. We describe the coupling between atom and electro-magnetic field using the electromagnetic-dipole approximation, which leads to an interaction Hamiltonian of the form

$$\mathcal{H}_{int} = -\hat{\mu}(\mathbf{r}) \cdot \hat{\mathbf{E}}(\mathbf{r}), \tag{1.2}$$

where $\hat{\mu}(\mathbf{r})$ denotes the dipole moment operator of the atom at position $\mathbf{r}$ and $\hat{\mathbf{E}}(\mathbf{r})$ is the electric field operator. To continue further one needs to express the Hamiltonian in terms of creation and annihilation operators of the atom-radiation system;

$$\hat{\mathbf{E}}(\mathbf{r}, t) = \sum_{\lambda} \left(\frac{\hbar\omega_{\lambda}}{2\varepsilon(\mathbf{r})} \right)^{1/2} \left(i\hat{a}_{\lambda}^{\dagger}\varphi_{\lambda}(\mathbf{r})\mathrm{e}^{i\omega_{\lambda}t} + H.c. \right) \tag{1.3}$$

with $\varphi_{\lambda}(\mathbf{r})$ being the λ-th normalized eigenfunction of the classical Maxwell wave equation. By using time-dependent perturbation theory where one treats the atom-field interaction as a perturbation one can express the spontaneous emission rate to first order as

$$W(\mathbf{r}) = \frac{2\pi}{\hbar^2} \sum_{f} \left| \langle f|\mathcal{H}_{int}|i\rangle \right|^2 \delta(\omega_i - \omega_f) \tag{1.4}$$

a general result known as Fermi's Golden Rule. Combining Eqs. 1.2–1.4 results in

$$\begin{aligned} W(\mathbf{r}) &= \frac{\pi\omega}{\hbar\varepsilon(\mathbf{r})} \left| \langle 0|\hat{\mu}|1\rangle \right|^2 \sum_{\lambda} 2\omega\varphi_{\lambda}(\mathbf{r})\delta(\omega^2 - \omega_{\lambda}^2)\varphi_{\lambda}(\mathbf{r}) \\ &= \frac{\pi\omega}{\hbar\varepsilon(\mathbf{r})} |D|^2 \rho(\omega, \mathbf{r}) \end{aligned} \tag{1.5}$$

where $\rho(\omega, \mathbf{r})$ denotes the position dependent local density of states at the atomic transition frequency ω [8].

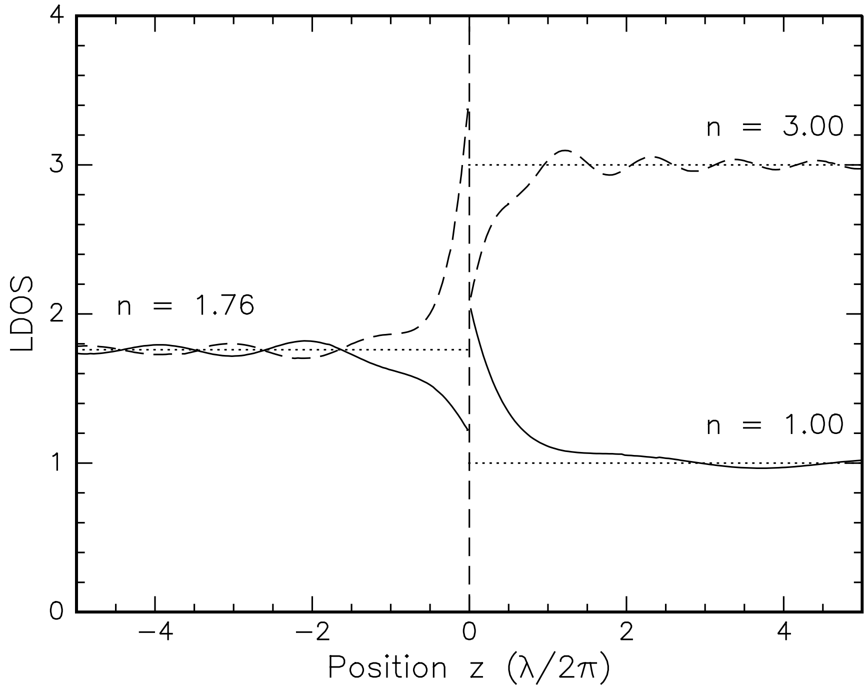

Figure 1.4: *An example of the calculated LDOS close to a dielectric interface positioned at z = 0. Two calculations are shown where the refractive index jumps from 1.76 at one side of the interface to 1.0 and 3.0 at the other side. The oscillations on both sides of the interface are due to interference of incoming and reflected waves. Note that the LDOS inside the medium with n = 1.76 is modified by changing the refractive index of the outside medium.*

1.3.2 Example: Local density of states near a dielectric interface

It is not difficult to show that the LDOS in a homogeneous dielectric is given by $\omega^2 n^3/c^3\pi^2$. This reduces the radiative rate in Eq. 1.5 to the Einstein A coefficient for spontaneous emission $\omega^3 n/\pi\hbar c^3\,|D|^2$. This reveals that the transition rate scales with ω^3 and depends linearly on the refractive index n of the medium[†]. To calculate the LDOS for a particular geometry involving dielectric interfaces one needs to find a complete set of normalized eigensolutions $\varphi_\lambda(\mathbf{r})$ of Maxwell's equations. A natural choice for stratified media is to use a complete set of plane waves, using reflection and refraction as given by the Fresnel coefficients. This procedure was describe for a single dielectric interface in Ref. [8]. The same technique was expanded in this thesis to the case of a thin dielectric film on a substrate involving two planar interfaces. The extension of the theory to problems involving more than two interfaces requires the definition and normalization of a complete set of eigensolutions to the problem which is a hideous and time-consuming task.

To illustrate the concept of LDOS, Fig. 1.4 shows a calculation of the LDOS close to an interface as function of the distance z from the interface. The factor $\varepsilon(\mathbf{r})$ appearing in Fermi's Golden Rule, Eq. 1.5, is taken into account in the LDOS[‡]. The distance is ex-

---

[†] As described in section 1.3, this is true only if contributions from the macroscopic E-field are considered. To calculate the decay rate from first principles, the local field correction needs to be evaluated.

[‡] In this thesis, the factor $\varepsilon(\mathbf{r})$ is always divided out and the resulting LDOS is denoted as f. Others have incorporated this factor directly in the LDOS and distinguish between the ordinary LDOS and the LDOS

pressed in units of the vacuum wavelength of the atomic transition. The calculated LDOS is averaged over both polarizations, assuming a collection of randomly oriented dipoles. As can be seen in Fig. 1.4, the LDOS and thus the spontaneous emission rate depends on the distance from the interface as a result of constructive and destructive interference between incoming and reflected radiation at the dielectric interface. This interference causes the oscillatory behavior of the LDOS at some distance from the interface. The period of the oscillations depends on the wavelength of the radiation in the material. Although such a planar interface between two dielectrics leads to changes in spontaneous emission rate that are relatively small compared to what could be achieved with a perfect cavity or photonic crystal, planar interfaces are frequently encountered in many experimental situations.

The theory of spontaneous emission is by now well understood and good agreement is found with experiments involving atoms close to metallic mirrors [6, 7] or a single dielectric interface [8]. An experiment with an atom close to a dielectric interface can thus be used to obtain some of the fundamental constants of the atom itself such as the radiative decay rate or emission cross section. The challenge is to calculate the LDOS for more complicated systems such as 1-D systems with more than one interface, 2-D and 3-D photonic crystals or microcavities. Experimentally, the LDOS can be probed in such complicated systems using atoms or molecules of which the radiative properties are first characterized using one of the well known systems.

1.3.3 Green's function approach to local density of states

A more versatile approach to calculating the LDOS is by using the dyadic Green's function, or Green tensor $\mathbf{G}(\mathbf{r};\mathbf{r}';\omega)$ of the problem. Such a Green's function might be easier to calculate for more complex systems where it is difficult to obtain a complete set of normalized eigenfuntions of the system. The Green tensor is defined via the Maxwell equation for the electric field and obeys the equation

$$\frac{1}{\varepsilon(\mathbf{r})}\nabla\times\nabla\times\mathbf{G}(\mathbf{r};\mathbf{r}';\omega)-\frac{\omega^2}{c^2}\mathbf{G}(\mathbf{r};\mathbf{r}';\omega)=\delta(\mathbf{r}-\mathbf{r}') \tag{1.6}$$

Note that in this case the differential operator defined by Maxwell's equations is indeed a time independent, linear, Hermitian differential operator relative to the inner product defined by the electromagnetic energy. In this case all eigenvalues of the problem are real and a formal solution of the above equation can be constructed in terms of a complete set of normalized eigenfunctions $|\varphi_n(\mathbf{r})\rangle$ with corresponding eigenvalues ω_n [38].

$$\mathbf{G}(\mathbf{r};\mathbf{r}';\omega)=\frac{c^2}{\varepsilon(\mathbf{r})}\sum_n\frac{|\varphi_n(\mathbf{r})\rangle\langle\varphi_n(\mathbf{r})|}{\omega^2-\omega_n^2} \tag{1.7}$$

The formal summation runs over all discrete eigenvalues and integrates over the continuous spectrum of eigenvalues. Note at this point that the formal solution of the Green's function is used to show the relation to the LDOS. The Green's function itself can be obtained by other means avoiding the need to find a complete set of normalized eigenfunctions. The solution given by the formal solution in Eq. 1.7 is not well defined if

---

for photons that differ by a factor $\varepsilon(\mathbf{r})$. Another alternative in literature is to represent calculations in terms of spontaneous emission enhancement, avoiding the concept of LDOS.

$\omega = \omega_n$ since the integrand has a pole at that point. The value can be found by considering the side limits of $\mathbf{G}(\mathbf{r};\mathbf{r}';\omega \pm \mathrm{i}s)$ as $s \to 0^+$. The side limits exist, but are different from each other causing a branch cut in $\mathbf{G}(\mathbf{r};\mathbf{r}';\omega)$ along the real ω-axis in the complex plane. If one introduces two related Green's functions by

$$\mathbf{G}^{\pm}(\mathbf{r};\mathbf{r}';\omega) = \lim_{s\to 0^+} \mathbf{G}^{\pm}(\mathbf{r};\mathbf{r}';\omega \pm \mathrm{i}s) \tag{1.8}$$

one finds that[§]

$$\mathbf{G}^{\pm}(\mathbf{r};\mathbf{r}';\omega) = \mathcal{P}\frac{c^2}{\varepsilon(\mathbf{r})}\sum_n \frac{|\varphi_n(\mathbf{r})\rangle\langle\varphi_n(\mathbf{r})|}{\omega^2-\omega_n^2} \mp \mathrm{i}\pi\frac{c^2}{\varepsilon(\mathbf{r})}\sum_n \delta(\omega^2-\omega_n^2)|\varphi_n(\mathbf{r})\rangle\langle\varphi_n(\mathbf{r})| \tag{1.9}$$

By definition the LDOS is given by

$$\rho(\omega,\mathbf{r}) \equiv \sum_n 2\omega\delta(\omega^2-\omega_n^2)|\varphi_n(\mathbf{r})\rangle\langle\varphi_n(\mathbf{r})| = \mp\frac{2\omega\varepsilon(\mathbf{r})}{\pi c^2}\mathrm{Im}\{\mathbf{G}^{\pm}(\mathbf{r};\mathbf{r}';\omega)\} \tag{1.10}$$

By applying Fermi's Golden rule, we can again relate the radiative rate of an atom at position $\mathbf{r}$ to the LDOS and arrive at (in terms of the Green's function)

$$W(\mathbf{r}) = \frac{2\omega^2\,|D|^2}{\hbar c^2}\mathrm{Im}\{\mathbf{G}^{-}(\mathbf{r};\mathbf{r};\omega)\} \tag{1.11}$$

Note that the Green's function approach gives exactly the same answer as the method using the complete set of normalized eigenfunctions described in the preceding section. However, the use of Green's functions does lead to a number of practical advantages. For many problems the Green's function is already known, since the real part of the Green's function is commonly used to obtain the electro-magnetic field in a certain structure. This solution is easily obtained, once the Green's function is known, by integration of the boundary conditions. In contrast to the method of normalized eigenfunctions, the Green's function approach does not require to find such a complete set of eigenfunctions. This is advantageous since the normalization of a complete set of eigenfunctions can be difficult and time consuming, even for relatively simple problems (such as a single interface). Finally, the Green's function of a complicated system can be found by a matrix multiplication involving several Green's functions of a much simpler system. For instance, such an approach was applied in the case of multilayer systems [39–41].

1.4 This thesis

This thesis is divided into three parts:

Part I deals with the design, microfabrication and optical properties of two-dimensional photonic crystals. The design of two-dimensional photonic crystals consisting of dielectric rods placed on a square lattice is discussed in Chapter 2. The photonic bandstructure is calculated for infinitely long cylinders. The existence of a photonic bandgap is investigated as function of dielectric constant and fill fraction of the rods. The structures considered in this thesis are all based on silicon because of its relatively high refractive

---

[§] $\lim_{y\to 0^+}\frac{1}{x\pm \mathrm{i}y} = \mathcal{P}\frac{1}{x} \mp \mathrm{i}\pi\delta(x)$

index and because the microfabrication of silicon is well known. It was found that a typical periodicity of 500 nm and a dielectric fill fraction of 10% is needed to fabricate structures with a photonic bandgap around the important telecommunication wavelength of 1.5 μm. Design rules based on the calculated effective refractive index were developed to design waveguide structures that confine the light vertically. Confinement using SiGe, silicon-on-insulator and amorphous silicon is discussed in Chapter 2.

Of these materials, amorphous silicon seems to be the most promising material. The fabrication of both crystalline and amorphous silicon structures is summarized in Chapter 3. The fabrication is achieved by careful tuning of an electron-cyclotron-resonance (ECR) driven anisotropic etch process using a SF_6/O_2 plasma. The temperature, O_2 flow, and bias voltage were independently varied to search for the optimum conditions to etch highly anisotropic vertical profiles. The fabrication of line defects such as waveguides and waveguide bends for near-infrared wavelengths was demonstrated, by leaving out a row of rods. Also the fabrication of Si photonic crystals in silicon-on-insulator substrates was shown.

The properties and limitations of amorphous silicon made by MeV Xe ion irradiation are discussed in Chapter 4. An optical absorption coefficient of 115 cm^{-1} (0.05 dB μm^{-1}) is found from transmission measurements on short length amorphous Si waveguides. Although this absorption coefficient is too large for waveguide applications on a centimeter length scale, amorphous silicon can be used for vertical confinement on the typical length scales ($<$100 μm) encountered in microphotonic circuits such as photonic crystal devices.

The incorporation of light emitters in silicon is difficult. Nevertheless, some photonic crystal devices, such as lasers or light emitting diodes, require optically active materials. A new coating method, in which optically active probe ions or molecules can be incorporated, was developed in Chapter 5. The coating method relies on a base catalyzed reaction using a mixture of tetra-ethoxy-silane, ethanol, ammonia and water. Typically 100 nm thick layers can be grown on a Si substrate or Si photonic crystals in a single step. Fluorescent species can be incorporated in the SiO_2 layer and thus lead to the incorporation of luminescent probes at a well-defined position in a 2-D photonic crystal.

Part II discusses spontaneous emission of atoms in several dielectric structures. The simplest case, where Cr ions are placed close to a dielectric interface is investigated in Chapter 6. The Cr ions are ion implanted in the near surface region of single-crystalline Al_2O_3 substrates and show typical ruby R-line luminescence around 694 nm. Samples of different Cr concentration (0.04 at.% to 0.28 at.% peak concentration) were made and the radiative and non-radiative decay rate of Cr^{3+} was determined. This was done by varying the reflectivity of the Al_2O_3-to-air interface by replacing the air with liquids of different refractive index and comparing the results to a calculation of local density of states (LDOS). Employing one of the simplest experimental geometries, the results from Chapter 6 provide a test for the concept of LDOS; the concept was then extended to include the concept of concentration quenching.

To probe the LDOS in spherical microcavities, erbium ions were ion implanted as probe ions in colloidal SiO_2 particles. First, Chapter 7 reports on the basic luminescent properties of 340-nm-diameter spherical SiO_2 particles implanted with Er ions. The dependence of the luminescence intensity and lifetime of the erbium ions as function of anneal temperature and erbium concentration is investigated. An extremely long luminescence lifetime of 17 ms is reported, suggesting a high quantum efficiency of the Er^{3+} ions. More detailed experiments on concentration quenching are reported in Chapter 8 and a comparison is made between decay rates of Er^{3+} in 175 nm and 340-nm-diameter particles. The data agree very well with the calculated difference in LDOS in these particles.

The spatial variation of the LDOS of spherical particles is further investigated in Chapter 9. The LDOS of a spherical SiO_2 cavity was calculated as function of the cavity diameter and reveals several maxima and minima as function of diameter. The maxima of the LDOS and their radial position correspond to the electric type Mie resonances of the sphere. Additional experiments and calculations were done using erbium implanted thin SiO_2 films that were grown with the method described in Chapter 5. The radiative rate of Er^{3+} in SiO_2 is found to be 54 s^{-1}. This information is then used to experimentally probe the LDOS in Er-doped spherical SiO_2 particles with and without index matching. In addition, the relation between the LDOS and Förster energy transfer is discussed.

The particles described in Chapters 7, 8 and 9 are doped with erbium by ion implantation which only allows for the fabrication of a limited number of particles. Chapter 10 introduces an alternative wet chemical method to fabricate rare earth doped colloidal particles using an acid catalyzed reaction. The resulting bulk rare earth doped particles are quite polydisperse and the properties of Er, Tb and Eu doped particles are discussed. The size polydispersity of the particles can be significantly reduced by using a seeded growth procedure in which a thin shell of silica doped with rare earth ions is grown on silica seed particles. Such particles can serve as optical probes in colloidal photonic crystals.

Finally, Part III describes several experiments on three-dimensional photonic crystals made from poly-crystalline Si rods made by Si microfabrication. Chapter 11 discusses the angle, polarization and surface orientation dependent spectrally resolved reflectivity of such crystals and results are compared to rigorous calculations. The reflectivity spectra depend on both the polarization of the incident light and the surface orientation of the finite-thickness photonic crystal. A superstructure present in the crystal is reflected in well-defined features in the reflectivity spectra, in good agreement with calculated spectra. Results on the modification of spontaneous emission in these Si woodpile crystals are described in Chapter 12. A broad luminescence feature is observed and is attributed to defect luminescence of the poly-crystalline Si itself. A strong decrease in luminescence intensity is observed for wavelengths that lie inside the photonic bandgap. The spectral changes are described by a model that takes into account both changes in the LDOS and the internal Bragg scattering in the crystal. It is shown that the quantum efficiency of the optical transitions determines the effect of the photonic crystal on spontaneous emission in an (initially) counter-intuitive way. A spectral attenuation of 5 dB per unit cell is derived from the data, consistent with theory and transmission data.

Part I

2-D

2

Design and optimization of 2-D photonic crystal waveguides based on silicon

The existence and properties of photonic bandgaps were investigated for a square lattice of dielectric cylinders in air. Bandstructure calculations were performed using the transfer matrix method as function of the dielectric constant of the cylinders and the cylinder radius-to-pitch ratio r/a. It was found that in the square lattice bandgaps exist only for transverse magnetic polarization, for a dielectric contrast larger then 3.8 (index contrast $>$ 1.95). The optimum r/a ratio is 0.25 for the smallest index contrast. For silicon cylinders (n = 3.45) the widest gap is observed for r/a = 0.18. Bandstructure calculations as function of r/a show that up to 4 gaps open for the silicon structure. The effective index was obtained from the bandstructure calculations and compared with Maxwell-Garnett effective medium theory. Using the bandstructure calculations we obtained design parameters for silicon based photonic crystal waveguides. The possibility and limitations of amorphous silicon, silicon germanium and silicon-on-insulator structures to achieve index guiding in the third dimension are discussed.

2.1 Introduction

A photonic crystal is composed of a periodic arrangement of dielectric material in two or three dimensions. If the periodicity and symmetry of the crystal and the dielectric constants of the materials used are chosen well, the bandstructure of such a crystal shows a photonic bandgap for one or both polarizations, i. e. at particular frequencies light propagation is prohibited in any direction in the crystal. The possible applications of these photonic crystals are numerous, including inhibition and enhancement of spontaneous emission [42, 43], fabrication of sharp waveguide bends [11, 12], waveguide couplers and filters [44].

In three dimensions the fabrication of photonic crystals for optical frequencies relies mainly on self-assembly techniques. In two dimensions, lithography and anisotropic etching techniques can be used. Two-dimensional (2-D) photonic crystals can be integrated with existing planar optical waveguide technology in which lithography and etching are used routinely for the fabrication of waveguides and other devices.

In two dimensions the only simple structure that offers a full photonic bandgap, i. e. a bandgap overlapping for both transverse magnetic (TM) and transverse electric (TE) polarization, is a triangular array of holes [45]. However, this structure is relatively difficult to fabricate with high aspect ratio because little open space is available in the lattice for the volatile etching products to escape. Therefore we will focus on the inverse structure; i. e. dielectric cylinders in air. The possibility to fabricate a 90 degree waveguide led to the choice of a square lattice [11, 12, 46, 47]. In a square lattice of cylinders bandgaps only open up for TM polarization (E-field along the cylinder axis); for the TE polarization no bandgaps are expected [14].

In this chapter we describe calculations of the photonic properties of 2-D photonic crystals based on a square lattice of dielectric cylinders in air. We explore the minimum requirements and tolerances for fabrication of devices based on silicon as a base material, operating around the standard telecommunication wavelength of 1.5 μm. Slab waveguides can be designed using the calculated properties of the square lattice of cylinders. In these waveguides, vertical confinement is provided by index guiding using either amorphous silicon (a-Si) or SiGe sections in the pillars, or by using silicon-on-insulator (SOI) materials. Waveguide properties are calculated based on dielectric waveguide theory in which the photonic crystal is incorporated using the effective dielectric constant derived from the calculated bandstructures.

2.2 Bandstructure calculations

Bandstructure calculations were performed for infinitely long cylinders placed on a square lattice, using the transfer matrix method [34]. The structure considered in our calculations is shown in Fig. 2.1. The cylinder radius r and pitch a are shown in the upper left corner of the figure. The right part shows the definition of TM and TE polarizations. The lower left corner shows the square unit cell in reciprocal space used for the bandstructure calculations. The **Γ**, X and M points of high symmetry in reciprocal space are shown. Due to the discretization method used in the calculation scheme, we have only calculated the bandstructure along the **Γ**X and XM directions. We will consider dielectric cylinders of dielectric constant ε embedded in a background with $\varepsilon = 1.0$.

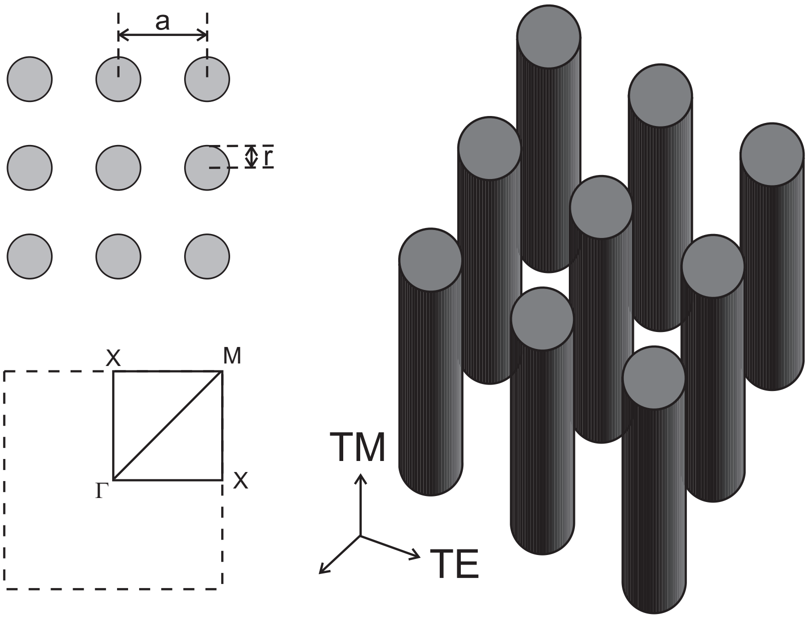

Figure 2.1: *Square lattice of dielectric cylinders. Indicated are the definition of the cylinder radius r and the pitch a. The $\mathbf{\Gamma}$, X and M points of symmetry in the square Brillouin zone are indicated in the figure. The transverse electric (TE) and transverse magnetic (TM) polarizations are indicated in the right part of the figure, where the arrows indicate the direction of the electric field vector.*

Figure 2.2 shows the result of a bandstructure calculation for a square lattice of silicon cylinders (ε = 11.8, refractive index n = 3.45) in air. The radius-to-pitch-ratio r/a was chosen to be 0.18 in this case. The vertical frequency scale is given in dimensionless units. These can be converted to ordinary units by specifying the pitch a. Note that the use of dimensionless frequency is natural in the case of Maxwell's equations, because these equations do not define a fundamental length scale. Due to the high index contrast a wide gap opens between the first and second band for TM polarization. The gap extends from $\omega a/2\pi c$ = 0.30 to 0.44, consistent with similar calculations for GaAs [14].

For TE polarization no bandgaps are observed. This can be explained by considering the polarization of a cylinder induced by an external field. If the external electric field is directed along the long axis of the cylinder the cylinder is easily polarized resulting in a strong interaction of the cylinders with TM polarized waves, whereas for TE polarization the polarizability of the cylinder is small [48].

Although we have calculated the bandstructure along the **Γ**X and XM directions only, the behavior along the **Γ**M direction can be predicted for the lower lying bands. Minima and maxima of a certain band are expected only at points of high symmetry in the reciprocal space. Therefore the part of the band along the missing **Γ**M direction varies smoothly between the minima and maxima already calculated at the **Γ**, X and M points. To design structures that operate around 1.5 μm wavelength, the pitch a should be chosen such that the desired wavelength falls in the bandgap region. For a pitch of 570 nm, the midgap frequency corresponds to a wavelength of 1.536 μm.

Figure 2.3 shows the dependence of the bandgap frequencies on the pillar radius-to-pitch ratio r/a, extracted from bandstructure calculations as shown in Fig. 2.2. The solid dots indicate the maxima and minimima observed in the bands of the calculated

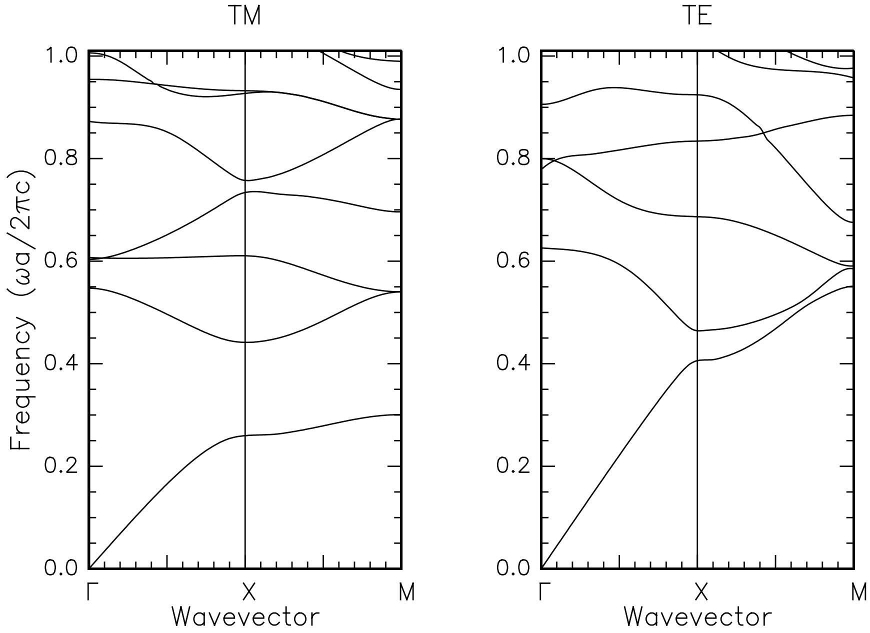

Figure 2.2: *Calculated bandstructure along the* ΓX *and* XM *directions for a square lattice of silicon cylinders (*ε *= 11.8) in air with* r/a *= 0.18, for TM and TE polarization. Due to the high index contrast a wide gap opens between the first and second band for TM polarization. For TE polarization no bandgap is observed.*

bandstructures for various values of r/a. The lines are smooth curves through the points to guide the eye. The area enclosed by the drawn lines indicates a bandgap region. The first two bandgaps could be mapped out in this way. Two higher bands for larger r/a are observed but not all points to map out the bands were calculated. The result of Fig. 2.3 can be compared to calculations for GaAs [14, 45] and are found to be similar, because the refractive indices at 1.5 μm of GaAs and Si are similar.

The widest bandgap for a square lattice of silicon cylinders (ε = 11.8) is observed for r/a = 0.20, with a relative gap width of 38% (defined as the midgap frequency divided by the gap width). To find the minimum dielectric constant required for a bandgap to occur in a square lattice for TM polarization, first a calculation as in Fig. 2.3 was repeated for cylinders with ε = 4.0. It was found that the widest gap in this case is observed for a r/a ratio of 0.25 (relative gap width 4%). Next, repeated bandstructure calculations as function of the dielectric constant of the cylinders at a fixed r/a of 0.25 were done. Figure 2.4 shows the maximum frequency of the first band and the minimum frequency of the second band as function of ε. The region enclosed by the drawn lines gives the gap between the first and second band. To find the minimum dielectric constant the solid lines were extrapolated, resulting in a minimum dielectric constant of 3.8 (n = 1.95) for gaps to open for a square lattice of cylinders (dashed lines). The inset shows the same data plotted as relative gap width. The upper frequency of the bandgap, i. e. the minimum of the second band at the M point, decreases linearly with the ε of the cylinders.

The refractive index requirement of at least 1.95 for a gap to occur for the square lattice is just out of reach of standard polymers and glasses. The use of silicon as a base material for 2-D photonic crystals seems natural because of its high refractive index

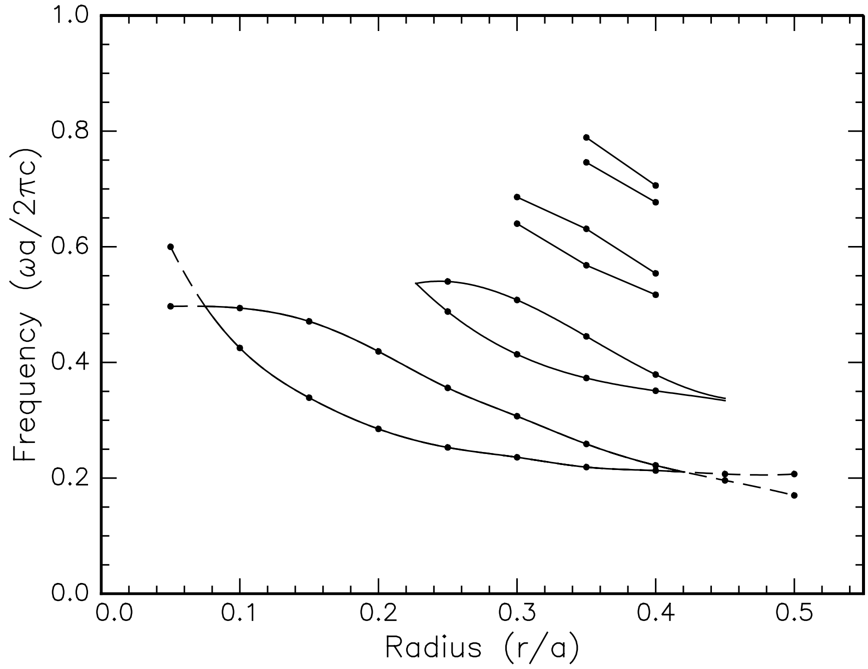

Figure 2.3: *Position of the bandgaps for TM polarized light calculated for a square lattice of silicon cylinders in air. The positions of the gaps were extracted from bandstructure calculations at various values of* r/a*, depicted by the dots.*

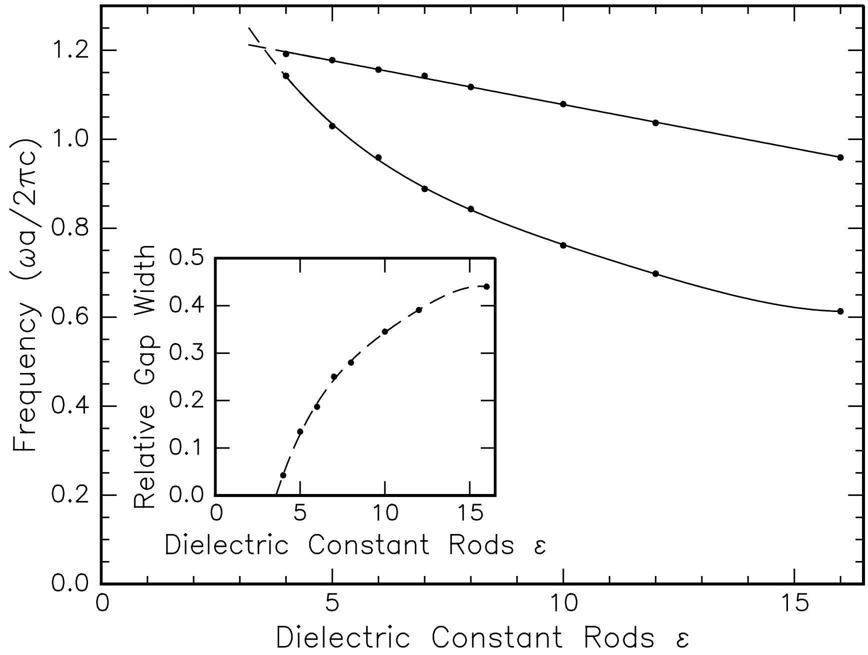

Figure 2.4: *Bandgap between the first and second band for TM polarization for a square lattice of cylinders in air with* $r/a = 0.25$ *as function of the dielectric constant. A minimum dielectric constant of 3.8 (*$n = 1.95$*) is needed for gaps to open. The inset shows the same data plotted in terms of the relative gap width, defined as the gap width divided by the midgap frequency.*

(n = 3.45) and because the microfabrication technology for this material is well characterized. For instance Si can be etched anisotropically to high precision using reactive ion etching [49–51] as will be shown in Chapter 3. The electronic bandgap of silicon is 1.1 eV, corresponding to a wavelength of $\sim$1.1 μm in vacuum, so that silicon is transparent in the near-infrared.

2.3 2-D photonic crystal waveguides

The structures discussed so far all consisted of cylinders of infinite length. For practical applications of a 2-D photonic crystal, it must be incorporated into a waveguide structure. The photonic crystal effects then take place in the plane perpendicular to the rods, similar as in the case of infinitely long cylinders. At the same time, index guiding in the dielectric waveguide structure may be used to provide confinement of the light out of the plane of the photonic crystal. In this section we will describe the design of such structures using 2-D bandstructure calculations combined with dielectric waveguide theory. Although this approach gives a good idea of the typical sizes and design parameters involved, only a full three-dimensional calculation can resolve the more detailed characteristics of such a device [52–55]. However, such a direct calculation of the entire structure gives less insight in the origin of coupling losses and differences in the optical response for different polarization of the incoming light.

To treat a photonic crystal using ordinary waveguide theory, the effective index of a square lattice of silicon cylinders was evaluated as function of the fill fraction $f = \pi$ (r/a)^2 of cylinders. The effective index is obtained in the long-wavelength limit from the linear part of the calculated dispersion relation near the zone center (k = 0):

$$n_{eff} = \lim_{k \to 0} c(\frac{\partial \omega}{\partial k})^{-1} \tag{2.1}$$

As can be seen in Fig. 2.2 there is a large difference in effective index for TM and TE waves because of the difference in slope of the linear part of the dispersion relation near k = 0. Figure 2.5 shows the calculated effective dielectric constant (left hand vertical axis) and effective refractive index (right hand axis) as obtained numerically from bandstructures calculated at various r/a ratios. Values are given as a function of fill fraction for the two polarizations. Data are shown for TM (dots) and TE polarization (circles). The dashed lines correspond to the Maxwell-Garnett effective medium theory for the two polarizations. As can be seen, ε_{eff} for TM polarization increases linearly with fill fraction, in perfect agreement with effective medium theory although the theory is only exact for small fill fractions. The data for TE polarization show an initial slow increase with fill fraction, roughly equal to what effective medium theory predicts, followed by a much stronger increase for fill fractions above 0.5.

Similar calculations as in Fig. 2.5 were also performed for dielectric constants of the rods between 1.0 and 16.0. It was found that a linear increase in ε_{eff} was observed for TM polarization in all cases; the result for TE polarization was found to depend on both the fill fraction of rods and the dielectric contrast of the lattice. For r/a values above 0.5 a lattice of star shaped holes should be considered instead of dielectric cylinders.

To achieve (effective) index guiding in a 2-D photonic crystal, it must be sandwiched between two layers of lower dielectric constant. In waveguide theory, TE and TM modes

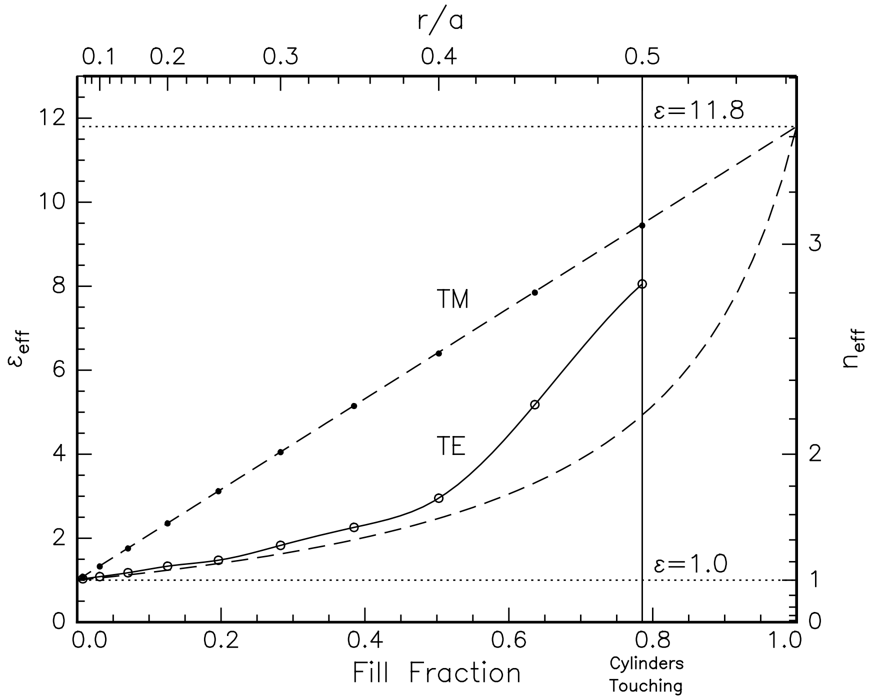

Figure 2.5: *Effective dielectric constant for a square lattice of silicon cylinders (ε = 11.8) in air (ε = 1.0). The effective dielectric constant was derived from separate bandstructure calculations at each fill fraction. The values obtained for TM polarization are shown by the solid dots, while the open circles show the results for TE polarization. The dashed lines indicate the effective ε as calculated from Maxwell-Garnett effective medium theory. The drawn line through the points for TE polarization is a guide to the eye.*

are defined as having their electric field (TE) or magnetic field (TM) transverse to the interfaces of the sandwich. Following this definition of waveguide modes for planar waveguide structures, the TE waveguide mode corresponds to the TE modes of the photonic crystal. For TM waveguide modes the electric field is nearly parallel to the long axis of the cylinders. However, there is a small component ($<$10%) that is perpendicular to the cylinders. This can be seen directly when using the ray optic approach for waveguide modes in which the light is confined by total internal reflection of the rays. To calculate the effective index for TM waveguides we have neglected this small effect.

While the in-plane propagation of electromagnetic waves is predominantly described by the photonic bandstructure, the index guiding in the vertical direction is governed by the polarizability of the cylinders [48]. The average polarizability is given by the effective index calculated in the long wavelength limit. We can get an estimate of the vertical index guiding using the effective index calculated from the bandstructure as long as a significant amount of the electric field is contained in the dielectric cylinders, making our approach most valid for the first dielectric band. Although many practical devices make use of the bandgap itself, where no propagating modes exist, our results can be used to estimate mode mismatch and coupling losses for devices with only a few rows of rods, or devices making use of the strong dispersion near the band-edge where propagating modes do exist. Our model gives a simple estimate of the required minimum length of the cylinders to prevent the light from leaking to the substrate in such a case. For devices employing higher lying bands our approach overestimates the index guiding, since a large fraction of the electric field is concentrated outside the dielectric cylinders.

In the following we will discuss three materials systems based on silicon in which index guiding in a 2-D photonic crystal may be achieved. The first two rely on creating a spatial variation of the index along the Si pillars using either a-Si or SiGe. The third makes use of a silicon-on-insulator substrate where the Si pillars are placed on a planar insulator (SiO_2) layer, which has a significantly lower refractive index. For all these materials waveguiding in a channel waveguide was shown experimentally [56–58].

2.3.1 Amorphous silicon

Amorphous silicon (a-Si) can be made by ion irradiation of single crystalline Si (c-Si). We have studied 4 MeV Xe irradiation at 77 K that creates a 2 μm thick a-Si layer on c-Si. Structural relaxation at 500 °C for 2 hrs in a vacuum furnace was performed to remove point defects and to relax the a-Si network structure [59]. The refractive index of the a-Si layer was measured by variable angle spectroscopic ellipsometry (see Fig. 4.2) and is 3.73 at 1.5 μm, significantly higher than that of c-Si (n = 3.45). This result is similar to that found for a-Si made by ion irradiation using other ions [60]. Ellipsometry and transmission measurements on 2 μm thick amorphous layers gave no indication for measurable optical absorption, from which we estimate that the absorption coefficient of a-Si at 1.5 μm is smaller than $\sim$100 cm^{-1}. Hence, a-Si would be a suitable waveguide material in a photonic crystal with dimensions in the order of 10 μm. However the optical loss is significant for cm long input/output waveguides integrated with the photonic crystal as is discussed in more detail in Chapter 4.

Using an a-Si top section of the pillars in a photonic crystal, the a-Si thickness and the pillar length (etch depth) should be chosen such that there is a minimal coupling from guided modes to the bulk Si substrate. Considering only TM modes, the effective index of c-Si cylinders at the optimum r/a of 0.18 is 1.45, as obtained from Fig. 2.5. Similarly the effective index for a-Si pillars with r/a = 0.18 is found to be 1.52.

Calculations were done to determine the existence and propagation constants (Fig. 2.6) of optical modes in a photonic crystal slab waveguide as function of a-Si layer thickness. The corresponding field distribution in the vertical direction is shown in Fig. 2.7 for three values of the layer thickness. Figure 2.6a) shows the solution of the propagation constant β, i. e. the component of the wavevector in the direction of propagation, for TM modes as function of the a-Si guiding layer thickness. The waveguide structure consists of c-Si pillars (n_{eff} = 1.45) with an a-Si section (n_{eff} = 1.52), in air (n = 1.00). For an a-Si layer thickness up to 2.5 μm the planar waveguide structure only supports a single TM mode. The corresponding propagation constants in a planar waveguide made of amorphous silicon on top of c-Si are shown in Fig. 2.6b). Because of the large refractive indices and relatively large index contrast, such a planar waveguide supports many modes and has propagation constants that differ very much from that of the photonic bandgap waveguide.

The field distribution of the zeroth order modes in the photonic crystal waveguide are shown in Fig. 2.7. Modes are compared for three different a-Si thicknesses of 1.0, 2.0 and 2.5 μm. The modes were normalized such that the power flow for all the modes is the same. It can be seen from the figure that for a 1.0 μm thick a-Si layer the mode penetrates deep into the substrate. Thicker a-Si layers show better confinement for the zeroth order

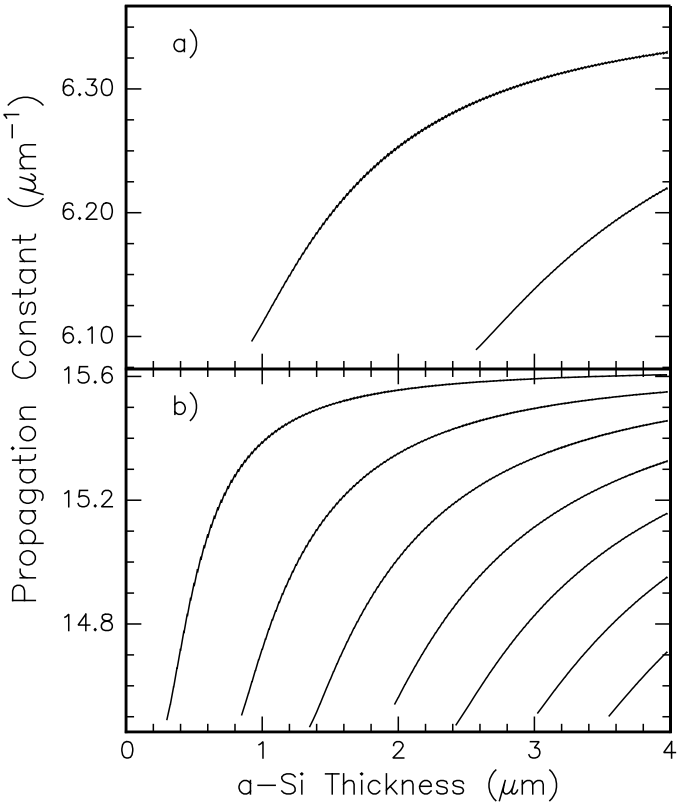

Figure 2.6: *Calculated propagation constant and waveguide modes for an a-Si/c-Si photonic crystal waveguide structure. a) propagation constant for the photonic crystal waveguide, using effective indices of 1.52 and 1.45, as function of a-Si thickness. b) propagation constant for a planar waveguide of a-Si on c-Si as function of a-Si thickness.*

mode, such that almost all energy is confined within a layer of 5 μm long cylinders.

For practical applications one should keep in mind that deep anistropic etching for the PBG structures is limited to an etch depth of ~5 μm [51]. Amorphization up to a depth of 2 μm can be done using e. g. 4 MeV Xe ion irradiation into a planar Si wafer. Subsequently pillars can be etched, resulting in crystalline Si pillars with an a-Si top section. Thus, in principle, the fabrication of a structure based on a-Si is possible.

As discussed earlier the propagation constant of the planar a-Si waveguide differs from that of the PBG waveguide. Because practical devices will most likely combine both planar waveguides and PBG waveguides it is important to consider the power coupling efficiency η between the planar waveguide and the PBG waveguide. We have assumed a butt-end coupling of the two waveguides. In that case the coupling efficiency η is given by [61]:

$$\eta = \left| \frac{2\beta_i\beta_t}{(\beta_i + \beta_t)} \frac{1}{2\omega\mu_0} \int_{-\infty}^{\infty} E_i(x)E_t^*(x)\mathrm{d}x \right|^2 \tag{2.2}$$

where β_i and β_t are the propagation constants of the incoming and transmitted waveguide mode. E_i and E_t are the normalized electrical field amplitudes of the modes.

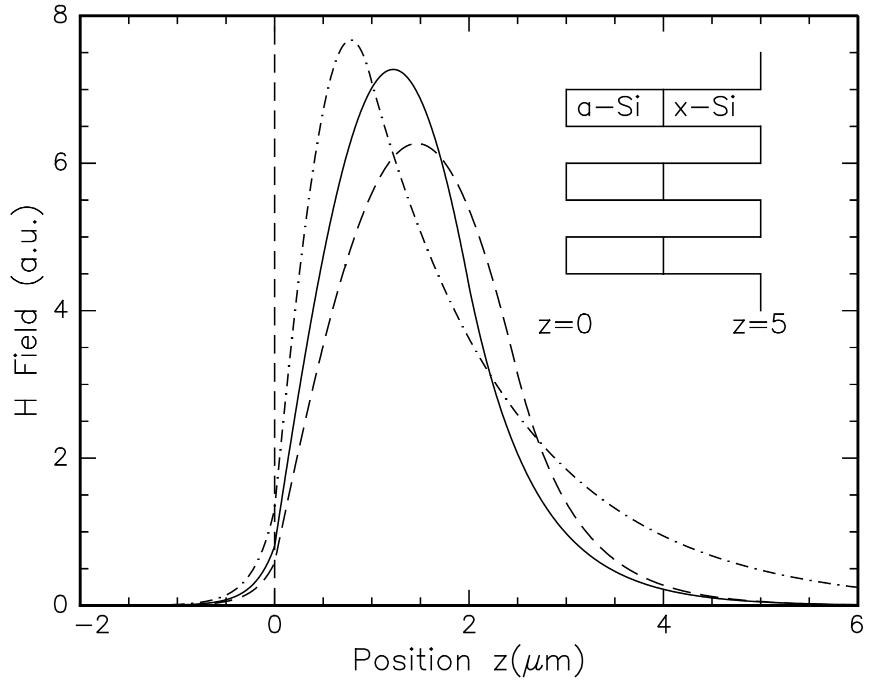

Figure 2.7: *Field strength of the calculated waveguide modes for a-Si thicknesses of 1.0 μm (dashed-dotted line), 2.0 μm (drawn line) and 2.5 μm (dashed line). The modes were normalized such that the power flow is the same for each mode.*

Using the calculated propagation constants for both the photonic crystal waveguide and the planar waveguide the coupling efficiency between the fundamental modes was calculated for a 1.0 μm and a 2.0 μm thick a-Si waveguide. The calculated coupling losses expressed in dB are summarized in Table 2.1. As can be seen the coupling losses are larger for the 1.0 μm thick guide. This can be explained from the fact that in the photonic crystal waveguide a large fraction of the mode propagates outside the guiding layer (mode confinement = 0.45, see Table 2.1) where the planar waveguide shows good confinement. The coupling losses for the 2.0 μm thick waveguide of -1.3 dB is partly due to reflection (-0.9 dB) caused by the difference in (effective) refractive index between the guiding layer of the incoming planar waveguide and the photonic crystal waveguide*.

The remainder of this Chapter summarizes the possibilities and coupling losses for similar structures, made using either SiGe on Si or silicon-on-insulator as a waveguide material. These results are summarized in Table 2.1 as well.

2.3.2 Silicon germanium

Silicon-germanium dielectric waveguides have been fabricated and show excellent transparency at 1.5 μm [56], making SiGe an interesting candidate for photonic crystal waveguides. Here we consider the case similar as in section 2.3.1 with pillars composed of a SiGe guiding top section on top of a Si pillar. The refractive index of the SiGe layer is

---

*We have only considered coupling losses between the fundamental modes, because coupling from a higher order mode to the fundamental mode leads to much higher coupling losses.

Table 2.1: *Comparison of the calculated coupling efficiencies η in dB for a-Si, SiGe and SOI photonic crystal waveguide structures. The table shows the coupling efficiency and mode confinement for various values of the guiding layer thickness. The modes with good confinement have smaller coupling losses. The remaining coupling loss is mostly due to reflection.*

Waveguide material	r/a	Layer thickness d (μm)	Coupling efficiency η (dB)	Mode confinement Γ
a-Si	0.18	1.0	-3.6	0.45
	0.18	2.0	-1.3	0.90
$Si_{0.75}Ge_{0.25}$	0.18	2.0	-3.0	0.54
	0.18	4.0	-1.3	0.89
SOI	0.20	2.0	-1.1	0.90
	0.20	1.5	-1.9	0.70

higher than that of pure Si and depends on the atomic fraction of Ge. The bandgap energy depends on the relative Si/Ge concentration and varies between the bandgap of pure silicon (1.15 eV) and pure Ge (0.74 eV) for fully relaxed layers [62].

To fabricate structures with a similar index contrast as discussed for a-Si, a Ge atomic fraction of 50 at.% is needed. It is very difficult to fabricate SiGe waveguide layers with such a high Ge content on one hand and have low optical losses on the other hand [56]. We have therefore limited the atomic fraction of Ge to 25%. For a Ge content of 25 at.%, the $Si_{0.75}Ge_{0.25}$ layer has a refractive index of 3.53 and a bandgap of 1.06 eV, corresponding to a wavelength of 1.17 μm in vacuum and will hence be transparent at 1.5 μm. For a photonic crystal structure with r/a = 0.18 the effective index of the SiGe layer is 1.47, giving a relatively small index contrast with the pure Si pillars underneath (n_{eff} = 1.45).

Consequently the mode size for a 2.0 μm thick $Si_{0.75}Ge_{0.25}$ waveguide is larger than that of a 2.0 μm thick amorphous waveguide and the mode is less well confined in the photonic crystal waveguide. Therefore a 2.0 μm thick SiGe waveguide leads to a relatively high coupling loss of -3.0 dB. The reflection loss of -0.8 dB is comparable to that of the a-Si waveguides. To improve the coupling the SiGe layer thickness can be increased to 4.0 μm giving a comparable coupling loss as the 2.0 μm thick amorphous silicon waveguide as shown in Table 2.1. However, to avoid coupling to the substrate a total etch depth of 8 to 10 μm is required, making the fabrication of these SiGe structures less attractive.

2.3.3 Silicon-on-insulator

Silicon-on-insulator (SOI) is a commercially available material of high optical quality, consisting of a single crystal Si layer separated from a Si substrate by a SiO_2 layer. Photonic crystals can be made by etching cylinders in the thin Si layer only, leaving the SiO_2 layer intact. As already pointed out, the effective refractive index of a square array of crystalline Si cylinders is 1.45 for $r/a = 0.18$. The refractive index of SiO_2 is 1.45, which means that no index guiding can be achieved in an array of silicon pillars on SiO_2 with r/a smaller than 0.18. To achieve similar modes as calculated for amorphous silicon one has to increase r/a such that the effective index increases to 1.52, corresponding to $r/a = 0.20$.

Commercially available silicon-on-insulator wafers, made using the "smartcut" process, typically have a maximum oxide thickness of 3 μm. The thickness of the Si layer on top is limited to 1.5 μm, although it can be grown thicker using epitaxial growth. For our calculations we used a thickness of 2.0 μm as a starting point to compare the waveguiding properties with that of the a-Si structures. The results of the calculation are shown in Table 2.1. A 2.0 μm thick SOI layer with $r/a = 0.20$ has similar waveguide modes as an amorphous silicon structure with $r/a = 0.18$. Therefore the mode overlap is the same. The difference in coupling efficiency with the amorphous silicon structure is entirely due to a somewhat smaller reflection coefficient of -0.7 dB. For a layer thickness of 1.5 μm the mode confinement is smaller resulting in larger coupling losses.

For SOI structures the coupling losses can be further reduced by increasing the fill fraction of silicon. In this way the index contrast between the guiding layer and surroundings is increased leading to better confined modes with better overlap. In addition, the reflection loss is also reduced, because the refractive index difference between the incoming planar waveguide and the photonic crystal waveguide is reduced. For example for a 1.5 μm thick SOI layer with $r/a = 0.25$, the coupling loss is reduced to -0.6 dB, while the reflection is -0.5 dB. It should be noted however, that in this case both incoming and photonic crystal waveguides are multimode so that coupling between higher order modes should be considered. By definition these modes are less well confined (having a smaller propagation constant) and thus higher losses. In all the structures discussed we only considered propagation of TM polarized modes, because all layer thicknesses are still below the cut-off condition for TE modes in the photonic crystal waveguide.

2.4 Conclusions

Using the transfer matrix method we have explored the existence of photonic bandgaps for a square lattice of cylindrical dielectric rods. Bandgaps were only observed for TM polarization. By calculating the bandstructure as function of both the pillar radius-to-pitch ratio r/a and the dielectric constant of the cylinders it was found that a minimum refractive index of 1.95 ($\varepsilon = 3.8$) is needed for a bandgap at the optimum $r/a = 0.25$. For a higher dielectric constant of 11.8, corresponding to the dielectric constant of Si at 1.5 μm, the largest bandgap was observed for $r/a = 0.20$, with a relative gap-width of 38%. Bandstructure calculations as function of r/a revealed up to four photonic bandgaps for TM polarization in a square lattice of silicon rods.

To design photonic crystal waveguides, the effective index was derived from the bandstructure calculations. For TM polarization the effective index corresponds to the result obtained from Maxwell-Garnett effective medium theory. We have calculated and compared waveguiding properties of photonic crystal waveguides operating around 1.5 μm using waveguide theory. Index guiding was achieved using a-Si, $Si_{0.75}Ge_{0.25}$ or SOI as waveguide core material. It was concluded that the fabrication of a-Si and SOI structures is possible, while fabrication of SiGe structures is difficult because of the large etch depths needed. The coupling losses for butt-end coupling of a planar waveguide to a photonic crystal waveguide were found to vary between -1.1 and -3.6 dB, which can be explained from the difference in mode confinement of the photonic crystal waveguide. Part of the coupling loss is due to reflection losses which were found to vary between -0.9 dB for a-Si structures and -0.7 dB for SOI structures. Full 3-D mode calculations are required to study the mode propagation and coupling in more detail.

3

Fabrication of two-dimensional photonic crystals at 1.5 μm in silicon by deep anisotropic dry etching

A fabrication process for two-dimensional silicon photonic crystals is developed. A two-dimensional photonic crystal of 5 μm long, 205 nm diameter pillars placed on a square lattice with a pitch of 570 nm is fabricated. The fabrication of a waveguide bend is demonstrated by removing a row of pillars. Using similar process conditions, square arrays of pillars were fabricated in silicon-on-insulator (SOI) substrates with a 1.5 μm thick Si layer. To meet the severe nano-tolerance requirements in the two-dimensional photonic crystals, the SF_6/O_2 electron-cyclotron resonance (ECR) driven plasma process at reduced temperature is tailored to extreme profile control. The impact of main plasma parameters - i. e. temperature, oxygen/fluorine content and ion energy - on the sidewall passivation process is unraveled in detail. A crystallographic orientation preference in the etch rate is observed. This preference leads to a pyramidal footprint for pillars etched in (100) oriented Si substrates. For pillars fabricated in SOI this footprint can be removed by overetching the structure.

3.1 Introduction

In the last decade ongoing research has demonstrated the great potential of photonic crystal structures for unprecedented control of light propagation in a broad range of novel optoelectronic devices. The basic 2-D structure typically exists of an array of pillars or holes. The diameter of the individual elements and the pitch of the array should be comparable to the wavelength scale of interest.

Search for photonic devices in the micron and submicron wavelength regime (IR and near-IR) has intensified greatly now that appropriate nanofabrication becomes more and more available. Most investigations deal with photonic structures in III-V compounds like GaAs [25], GaAs/AlGaAs [63], AlGaAs [26], GaAsP [25] and InP [27, 28]. Fabrication is achieved using chlorinated plasmas, either by reactive ion etching (RIE) or chemically assisted ion beam etching (CAIBE). Photonic operation is somewhat hampered by the limited vertical confinement due to a moderate etch depth.

Silicon is the most widely used semiconductor material today and the processing and microfabrication of Si are well known. Since Si is transparent for near infrared wavelengths and has a high refractive index (n = 3.45 at λ = 1.45 μm) it is an ideal material to fabricate photonic crystals. However, the Si material system, has attracted rather limited attention so far. Very steep and deep macroporous silicon structures for 5 μm wavelength operation have been realized by Grüning et al. [64] using a wet electrochemical process. An in-plane 2-D TE/TM beam splitter in a structured SiO_2/Si multilayer [65] and photonic bandgap microcavities in a Si waveguide for 1.5 μm wavelength have been reported recently [24].

In this Chapter, we develop a fabrication process for 2-D photonic crystal structures for the important telecommunication wavelength of 1.5 μm. The crystals considered are composed of a square lattice of dielectric rods and the design of such structures was discussed in detail in Chapter 2. The widest photonic bandgap for this structure is obtained for a radius-to-pitch ratio r/a = 0.18 (see Fig. 2.3). In this case, the fabrication of a photonic crystal for 1.5 μm requires etching of 205 nm diameter rods that are placed on a square lattice with a lattice constant of 570 nm. After the experimental details (section 3.2) the process development is considered in section 3.3. The plasma-substrate interaction process is first tailored on individual Si pillars to optimize the etch parameters so that the stringent requirements needed for the fabrication 2-D photonic crystals can be met. Strong evidence of a crystallographic orientation preference in the silicon etch rate shows up which has not been observed before under RIE conditions. Finally, the patterning process is used to fabricate photonic crystal devices. The fabrication of a sharp waveguide bend defined by removing a row of rods is demonstrates and the processing is extended to fabrication of structures using silicon-on-insulator substrates is Section 3.4.

3.2 Experimental

Mask patterns are prepared either in thermal silicon oxide or in resist. On samples that have a 2 μm thick amorphous Si top layer, the SiO_2 mask is grown prior to ion irradiation in order not to exceed the thermal budget of a-Si (550 °C, 30 min). All samples are coated with a resist double layer consisting of a 400 nm thick bottom layer of hardbaked AZ S1813 photoresist (Shipley) with an overlying 80 nm thick silicon containing negative tone electron-beam resist SNR (Toyo Soda). After electron-beam exposure (Leica EBPG05, 100 kV, 100 μC cm^{-2}) the pattern is developed in xylene for 20 s and dipped in isopropyl alcohol for 30 s. The pattern is then anisotropically transferred into the bottom photoresist layer by low pressure (0.3 Pa) oxygen RIE plasma at low RF power density of 0.07 W cm^{-2} (DC bias of -170 V). In case of an oxide mask, an additional CHF_3 plasma at 0.8 Pa and 0.33 W cm^{-2} RF power (DC bias -260 V) is applied. All patterning processes are *in situ* controlled by laser interferometry.

The Si etch process development is accomplished with a distributed electron cyclotron resonance driven plasma setup (Alcatel DECR200), operating at 2.45 GHz, with He gas flowing at the back side of the substrate for appropriate temperature control (range -150 °C to 150 °C) [50]. The substrate is RF driven (13.56 MHz) for independent ion energy control towards the sample. The gas mixture used is a SF_6/O_2 mixture, with the SF_6 flow fixed at 22.5 sccm at pressures around 0.2 Pa. A microwave power of 400 W is used unless stated otherwise.

Anisotropic etching in SF_6/O_2 high density plasmas (ECR driven [49] or inductively coupled [66]) can be taken as standard now. For the delicate sidewall passivation a strong coupling between the temperature and oxygen flow settings exists. Taking -80 °C and 3 sccm O_2 as a start position, with the standard DC bias setting on -13 V, we focus on the plasma-substrate interactions required for extreme profile control. In this context temperature (range -105 °C to -65 °C), oxygen flow (2–4 sccm) and DC bias (-50 V to 0 V) are the most important parameters in the process development. The dependence of the etch profile on these parameters was investigated using a mask of 450 nm diameter circular rods placed on a square lattice with a relatively large distance between the rods. Mask selectivity, both siliconoxide and resist, is almost infinite at these process conditions. Note that such a low ion energy in combination with a long mean free path of centimeters accesses plasma-substrate interactions that are not available in conventional RIE.

In order to confine light vertically in photonic crystals, amorphous silicon (a-Si) was proposed as a waveguide material (see Chapter 2) because it has a higher refractive index than that of crystalline silicon (c-Si). Etching experiments were performed on a-Si/c-Si double layers that were obtained by amorphization of the top layer of a c-Si(100) substrate by irradiation with 4 MeV Xe ions at 77 K to a dose of 2×10^{15} cm^{-2} followed by an anneal at 500 °C for 1 hr to reach a thermally stable state with low optical absorption at 1.5 μm. After thermal annealing a 1.93 μm thick a-Si layer results as measured by ellipsometry in the 1200–1700 nm wavelength range. Transmission electron microscopy analysis of Si-implanted samples shows the a-Si/c-Si transition to be smooth within 10 nm. Such a gradient has a negligible impact on the light confinement and photonic device operation.

3.3 Anisotropic etching of silicon

Figure 3.1 (bottom) shows SEM images of Si pillars etched at three different values of the DC bias of the substrate electrode. The inset shows the ion current towards the substrate as a function of DC bias. The ion current plot indicates that beyond -20 V all positive ions available from the plasma are captured. After a sharp increase of the etch rate from zero to 390 nm min^{-1} for increasing bias in the 0 to -20 V region the rate saturates for higher voltages. The strong etch rate increase coincides with the increase of the ion current in the 0 to -20 V bias region (see inset). Apparently, atomic fluorine is available in great

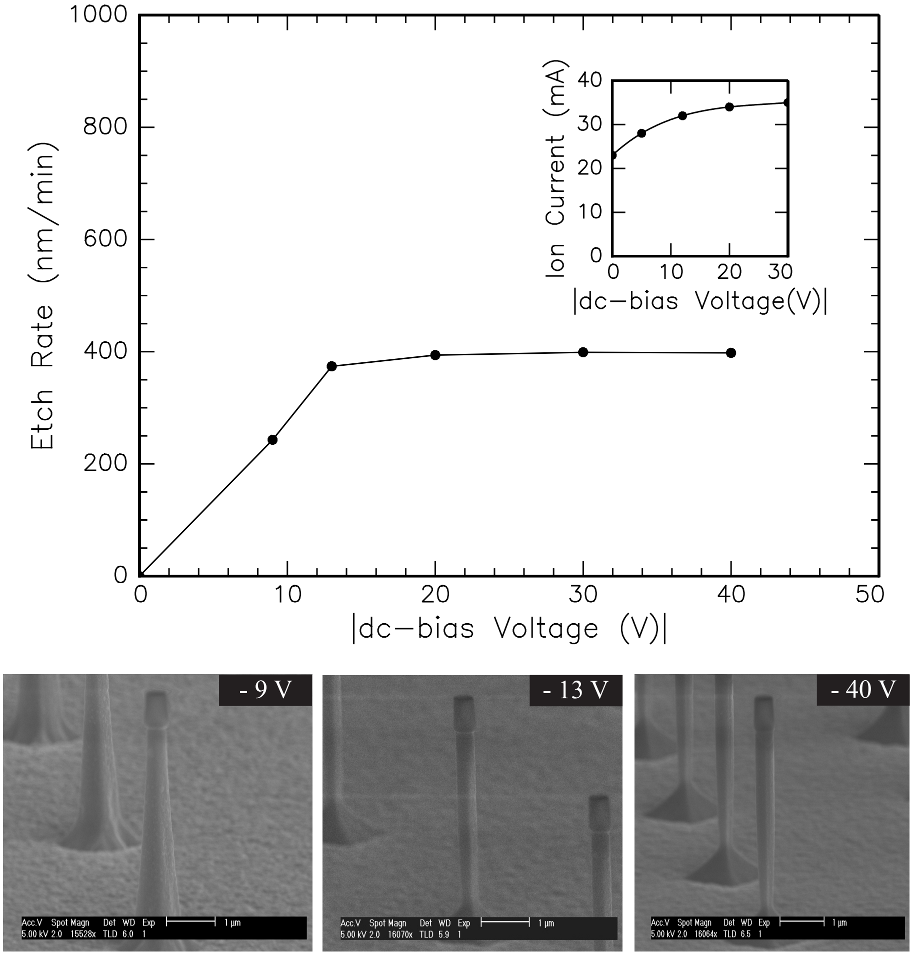

Figure 3.1: *Si etch rate as a function of the substrate DC bias (top), with the other process parameters on their standard setting (see text). The inset shows the ion current as a function of DC bias. SEM images of the resulting etch profiles (bottom). The 450 nm wide resist mask is visible on top of the pillars.*

excess and just ion flux (not the ion energy) is the etch rate limiting factor.

For increasing bias, the slope of the side-wall of the etched pillars turns gradually from positive to negative (see SEM images in Fig. 3.1). Considering the long mean free path (centimeters) compared to dark space thickness (around 100 μm) in the plasma, the ion flux enters perpendicularly to the substrate. Ion deflection towards the sidewall cannot explain lateral erosion at increasing DC bias. In grating structures processed under the same process conditions we observed an increasingly negative slope for a larger clearing area around a given ridge. In the absence of spontaneous etching (there is negligible isotropic mask undercut) the negative slope is then probably due to ions scattered back from the horizontal surface [67]. For effective etching/sputtering of siliconoxyfluorides at the sidewalls an energy threshold around 10–30 eV exists, i. e. in the same range but certainly lower than the threshold of 35 eV measured for silicon oxide [68]. In separate x-ray photoelectron spectroscopy (XPS) inspections of surfaces etched at 0 V and -20 V DC bias we indeed observed an increased removal of the lower (with less oxygen) oxyfluoride products at higher bias. It is pointed out that the actual ion energy is larger than the DC bias setting suggests because ions are accelerated from positive plasma potential

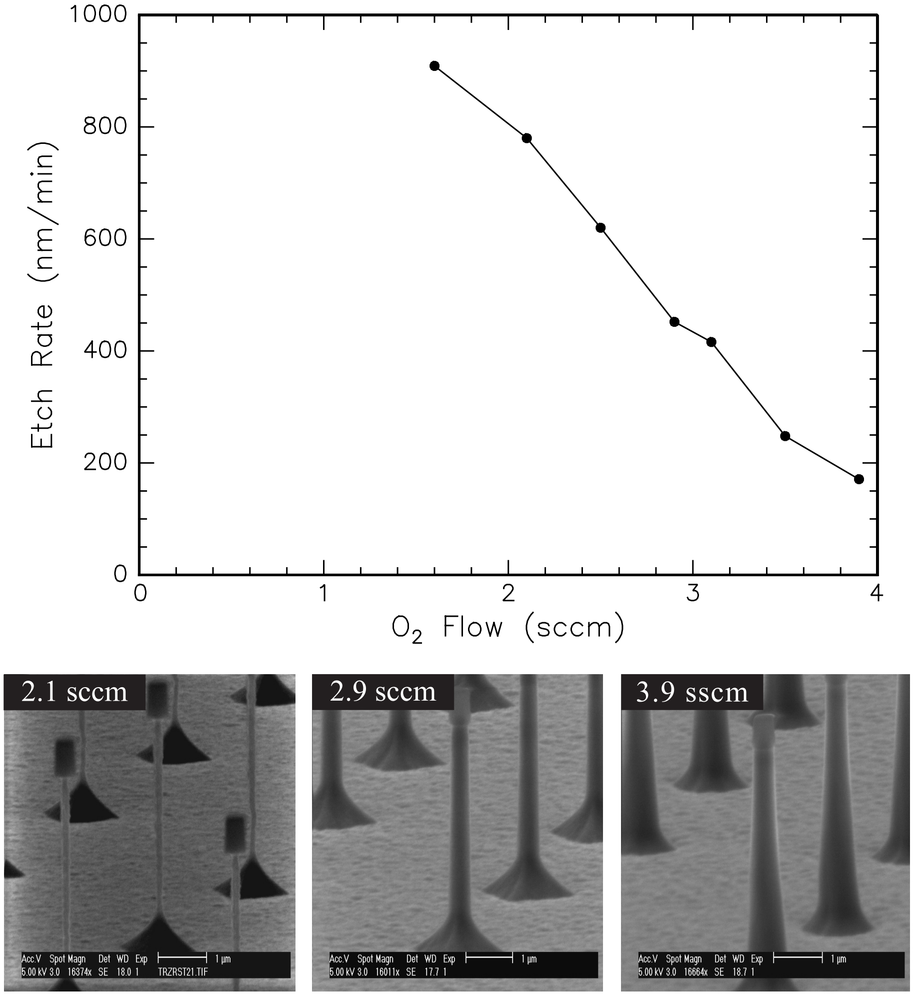

Figure 3.2: *Si etch rate (top) and SEM images of the resulting etch profiles (bottom) as function of the oxygen flow, with the other process parameters on their standard setting (see text). The 450 nm wide resist mask is visible on top of the pillars.*

region (on the order of +10 V). Finally, as can be seen in Fig. 3.1, substantial facetting at the Si pillar footprint shows up (most clearly visible for the pillars made at -40 V). Anticipating results shown below, this observation is reminiscent of crystallographic orientation preference in the dry etch process.

The etch behaviour of individual c-Si pillars as a function of oxygen flow is shown in Fig. 3.2. Etch rates (top) show a sharp drop with O_2 flow from 900 nm min^{-1} at 1.6 sccm to 180 nm min^{-1} at 3.9 sccm. The large sensitivity is attributed to the moderate ion energy (DC bias -16 V) which is exactly in the range of the sputter thresholds of the oxyfluoride etch products. The SEM images show Si pillars etched at different O_2 flows. At 3.9 sccm the tapered profile points to a significant sputter component. At 2.9 sccm the profile is almost perfectly anisotropic, probably because an ion-induced chemical etch component is most dominant. At 2.1 sccm a negative slope is observed. Apparently, for smaller oxygen flow lower oxygen content in the sidewall oxyfluoride builds up and greater sensitivity for parasitic ion exposure results. However, a slight, more or less homogeneous (over the full height) lateral pillar narrowing is also observed. Moreover the facetting at the footprint has steadily increased for lower oxygen flows. Altogether the actual profile development is a combination of a vertical process and facetting at the footprint, on which a slight lateral component is superimposed. This lateral component may be partly attributed to erosion from reflected ions.

Figure 3.3 shows the temperature behaviour of the Si pillar etching process in the range of -105 °C to -65 °C. The etch rate as a function of temperature (top) shows a continuous decrease for decreasing temperature; a minimum in etch rate is reached around -97 °C. At the lowest temperature a tapered profile is observed, without any underetch, which points to a process being highly sputter controlled. The horizontal surface is rough probably because of oxidic condensates acting as a mask. On close inspection the rough surface predominantly consists of tiny pyramids suggesting the crystallographic preference noted previously. The pillar profile behaviour for increasing temperature is more or less the same as observed in the series for decreasing oxygen flow; an ion-induced chemical process, enhanced facetting at the footprint and at the highest temperature of -65 °C an observable homogeneous lateral pillar narrowing. At higher temperatures the sidewall starts to roughen, possibly because sidewall passivation is hampered due to weak spots.

The substantial facetting at the footprint, homogeneous lateral narrowing and pyramidal surface roughness prompts a more accurate look at crystallographic preferences of the etch process. In Fig. 3.4 etch profiles (bottom) are compared for Si pillars etched in silicon substrates of different surface orientations etched simultaneously in the same experiment. Fig. 3.4 (top) shows the ratio of etch rates for Si(100) over Si(111). Over a broad temperature range from -105 °C up to 20 °C the etch rate of Si(100) is larger than that of Si(111), with a maximum ratio of 2.04 at around -80 °C. The etch profiles for different Si orientations show several characteristic differences. In Si(111) and Si(110) the facetting at the footprint is absent; it is present in Si(100) because etching of Si(111) planes is rate limiting. In both Si(111) and Si(110) the homogeneous lateral pillar narrowing is quite pronounced. Si(111) shows by far the largest initial mask undercut introduced at the start of the process in all samples (See Figs. 3.1, 3.2 and 3.3). All samples show the same negative slope attributed to the effect of parasitic ions.

The higher etch rate of Si(100) agrees well with the XPS observation [69] that at the Si(100) surface more SiF_2 species evolve than at Si(111), which is attributed to the different number of dangling bonds per Si surface atom (2 and 1, respectively). SiF_2 is considered to be the essential intermediate etch species to form the SiF_4 end product in consecutive disproportionation reactions [70]. For etching of Si(111) along the SiF_2 intermediate state a Si-Si bond should be broken, with inherently a higher activation energy and thus resulting in a lower etch rate.

3.4 Device fabrication

3.4.1 Crystalline and amorphous silicon

Two-dimensional Si photonic crystal structures designed to have a bandgap at 1.5 μm were dry etched using ECR plasma etching at optimized conditions: SF_6/O_2 (7.3:1) at 0.1 Pa pressure, -97 °C substrate temperature, 400 W RF power and -12 V DC bias. The etch rate was $\sim$150 nm min^{-1}. Figure 3.5a) shows a SEM image of a square array of Si pillars that were etched to have a length of 5 μm and a diameter of 205 nm. The

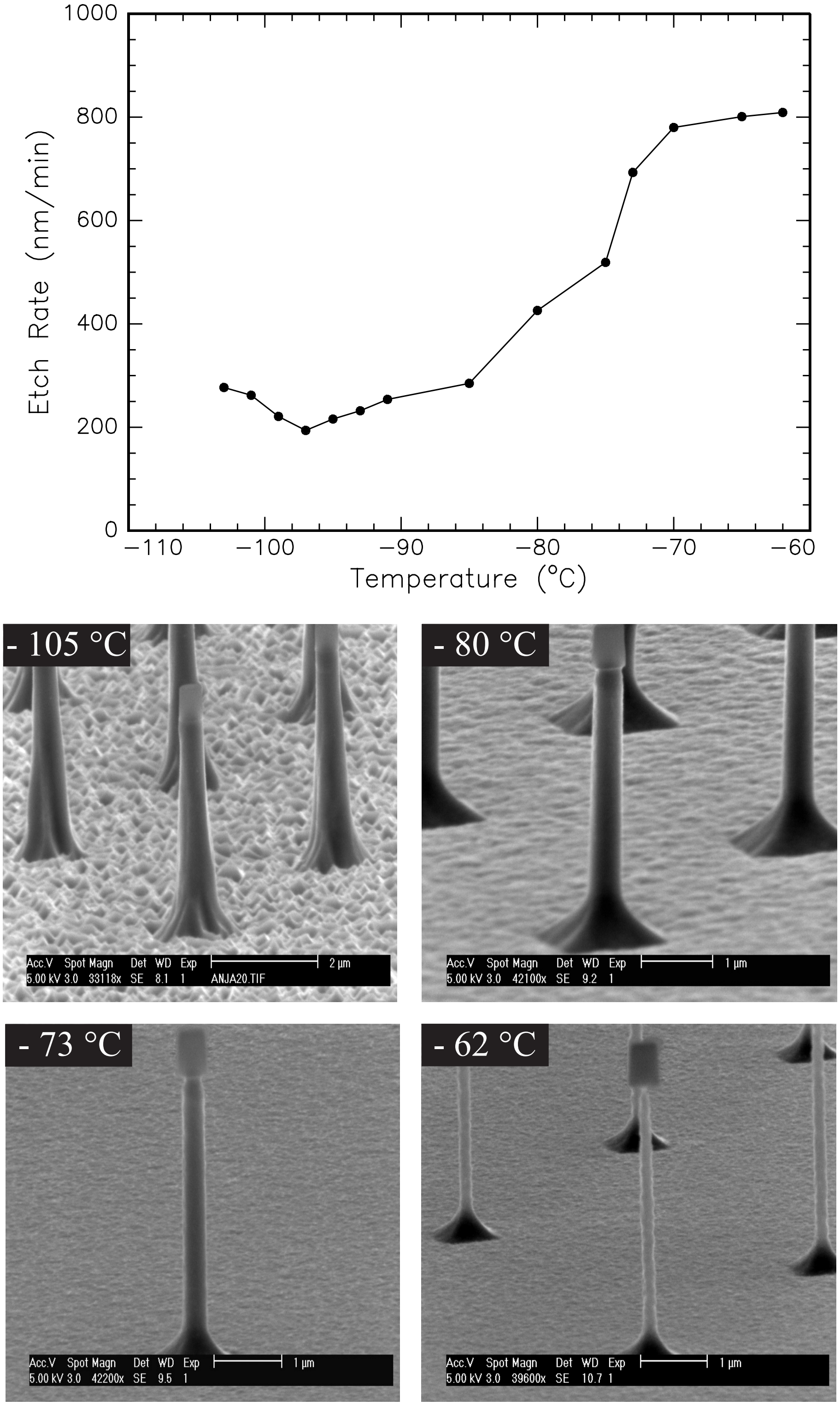

Figure 3.3: *Si etch rate (top) and SEM images of resulting etch profiles (bottom) as function of temperature, with the other process parameters on their standard setting (see text). The 450 nm wide resist mask is visible on top of the pillars.*

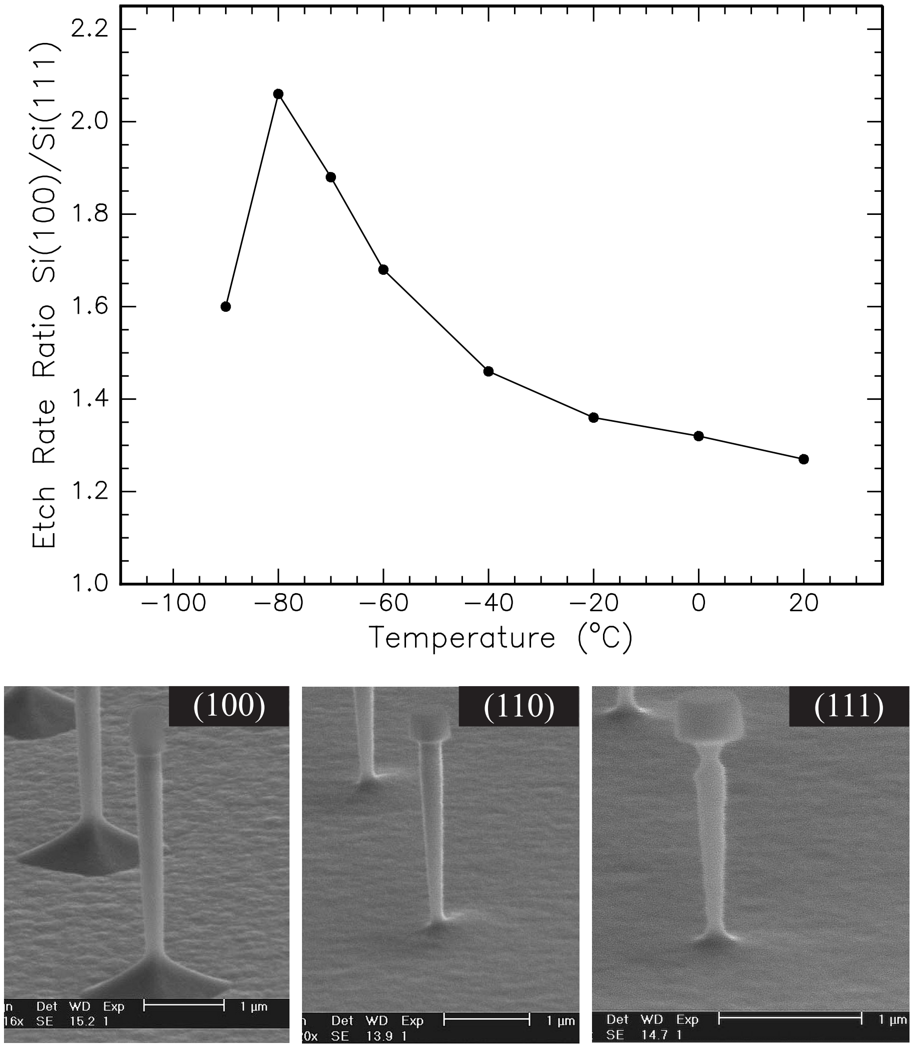

Figure 3.4: *Comparison of the etch for (100) and (111) crystallographic orientations of the Si surface as a function of temperature (top). SEM images of etch profiles (bottom) for (100), (110) and (111) orientations show the occurrence of a pyramidal footprint for (100) oriented samples only.*

image clearly demonstrates that by careful tuning of the important parameters the ECR etch technique is well suited to fabricate densely packed structures with high aspect ratio. To study the latter Fig. 3.5b) show a single pillar that was broken off the crystal. Good thickness uniformity was achieved over the entire etch depth. Note that the pressure was reduced to 0.1 Pa pressure, compared to Section 3.3 to enable the fabrication of dense arrays (up to $r/a = 0.18$).

A more complex geometry that can be made is shown in Fig. 3.6. It shows an SEM image of an array of 205 nm wide and 5 μm high c-Si-pillars in Si(100). A row of rods was removed to form a line defect. Such a defect introduces propagating modes in the photonic crystal that can be used to guide light. In this way a very small waveguide bend may be made that has near 100% transmission [11, 12]. The aspect ratio of individual pillars is about 50. The mask undercut is shown in the inset. The uniform etch depth agrees with the rate limiting step being related to surface kinetics rather than limited

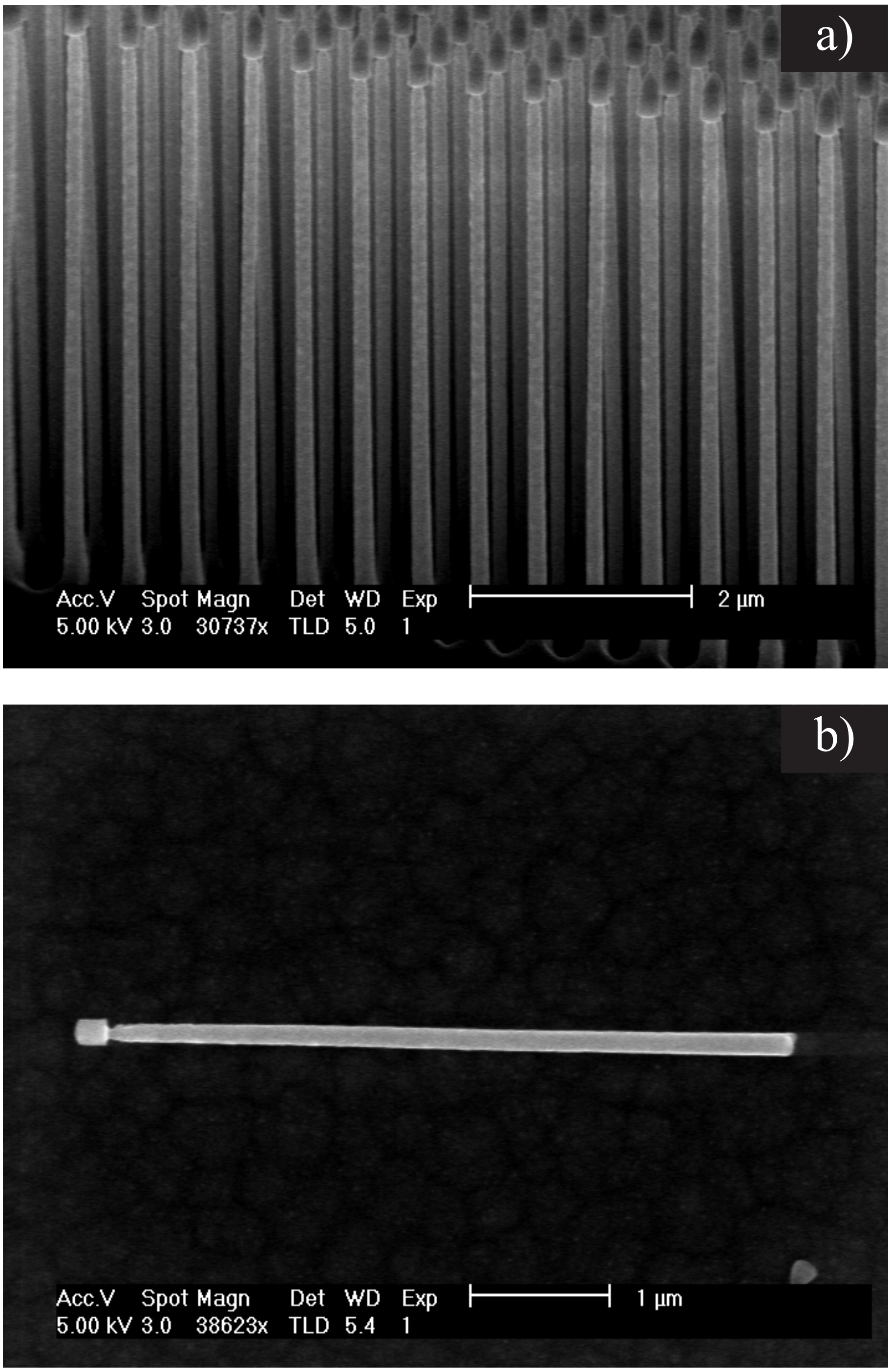

Figure 3.5: *Fabrication of a square array (a) of Si pillars using the ECR etching technique. The photonic crystal is designed for a wavelength of 1.5 μm and consists rods that are 205 nm in diameter and are placed on lattice with a pitch of 570 nm. The thickness of the etched pillar is uniform over the entire etch depth of 5 μm as demonstrated in (b).*

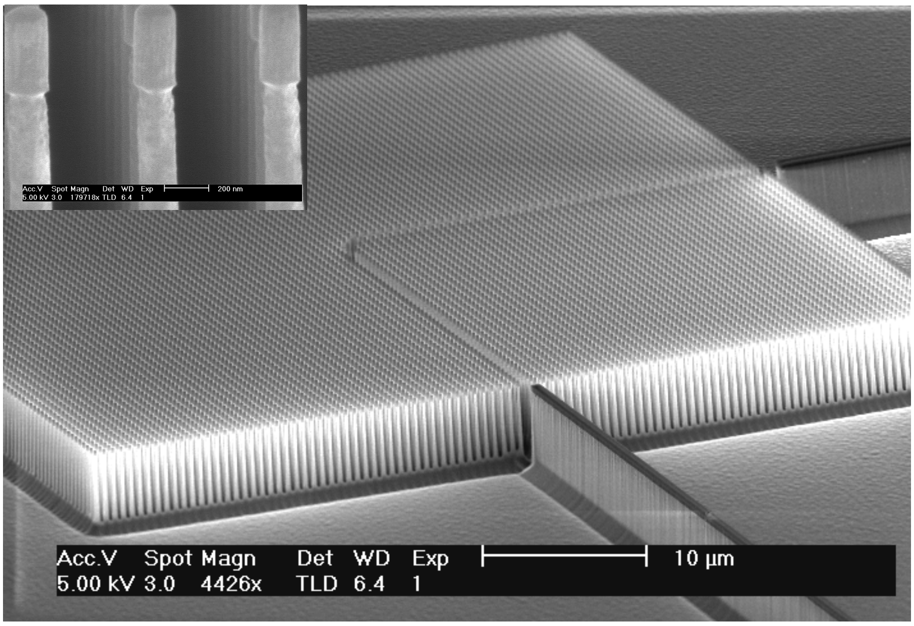

Figure 3.6: *Fabrication of 2-D photonic waveguide bend in silicon for 1.5 μm wavelength light. The etch depth is 5 μm, the individual rods are 205 nm in diameter and are placed on a square lattice with a pitch of 570 nm. The image shows a full device with input and output waveguides fabricated in c-Si.*

by in- and outdiffusion of the reactive species in the deep etched cavities. Figure 3.6 also demonstrates that input and output waveguides can be integrated with the photonic crystal. They were defined using the same mask.

We tested the etch process for an a-Si layer on a c-Si substrate. The SEM image of the resulting etch profile is shown in Fig. 3.7. The slight gray tone transition (indicated by dashed line) corresponds to the a-Si/c-Si interface as its position occurs at the expected depth of $\sim$1.9 μm. The c-Si bottom part of the pillars tends to a slightly negative slope, while the a-Si part is almost perfectly homogeneous in thickness. The a-Si layer has a 30% lower etch rate compared to (100)-oriented c-Si. Given the oxygen flow results shown in Fig. 3.2 both profile and rate observations can be explained by the buildup of a slightly higher oxygen content at the etched surface and the sidewalls of the a-Si pillars. In the crossover at the a-Si/c-Si interface the oxyfluoride balance on both the horizontal surface and the sidewalls then shifts to a lower oxygen content and so to enhanced sensitivity to ion exposure. A more quantitative understanding could be obtained from XPS measurements of the O/F ratio in the sidewall passivation under the various process conditions, as was previously done for SiGe [71].

Optical measurements on structures as in Fig. 3.6 that have a 2 μm thick a-Si top layer were so far unsuccessful due to the large intrinsic absorption losses of the mm long amorphous silicon input and output waveguides. This absorption will be quantified and discussed in detail in Chapter 4. In the particular structure of Fig. 3.6 this problem may be solved by fabricating a waveguide grating into the input waveguide, which would enable free-space coupling of light into the waveguide.

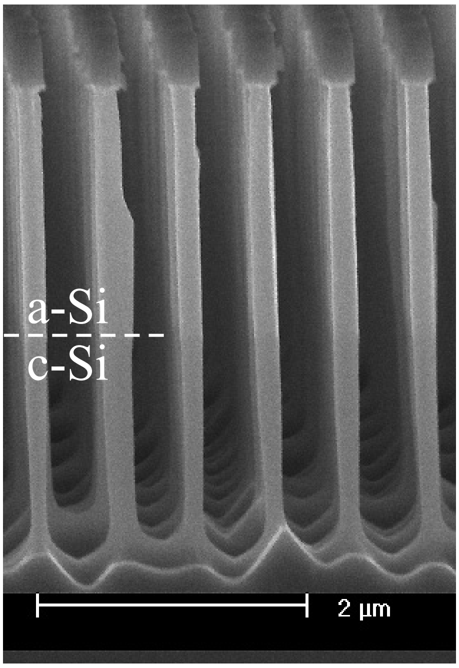

Figure 3.7: *Cubic array of pillars etched in an a-Si/c-Si double layer. A slight contrast is observed between the a-Si and c-Si regions; the interface is indicated by the dashed line.*

3.4.2 Silicon-on-insulator

An alternative way to vertically confine light in two-dimensional photonic crystal devices is to build the device on a low index substrate. Commercially available silicon-on-insulator (SOI) substrates that have a 1.5 μm thick c-Si(100) layer on a 3.0 μm thick SiO_2 layer on a c-Si substrate can be used for this purpose. In this case the 3.0 μm thick SiO_2 layer provides the low index substrate, and vertical confinement is provided by index guiding in the c-Si pillars. The details of the design using SOI substrates are reported in Chapter 2. It was found that in order to prevent light from leaking to the c-Si substrate, the r/a ratio of the photonic crystal should be at least 0.25. In this case the effective refractive index for TM polarization is sufficient to confine the light in the top 1.5 μm c-Si. Note that based on the effective refractive index, TE polarized light is not guided by the same structure. The etching of higher density arrays (higher r/a values) is more difficult, since less open space is available for etch products to escape. However, at the same time the aspect ratio of the pillars needed for the SOI structure is lower (the Si thickness is only 1.5 μm) which facilitates the fabrication process. Using the knowledge from the sections 3.3 and 3.4 the ECR etching process was tailored in order to fabricate square arrays of Si pillars in SOI.

Mask patterns are prepared in a resist double layer consisting of a 300 nm thick bottom layer of hardbaked AZ S1813 photoresist (Shipley) with an overlying 50 nm thick layer of hydrogen silsesquioxane (Dow Corning) that acts as a negative tone electron-beam resist. After electron-beam exposure (Leica EBPG05, 100 kV, 850 μC cm^{-2}) the pattern is developed in MF322 (Shipley) for 2 min, dipped in a MF322:H_2O mixture (1:9) for 15 s and finally rinsed in H_2O for 15 s. The pattern is then anisotropically transferred into the bottom photoresist layer by a low pressure (0.3 Pa) oxygen RIE plasma at a low RF power density of 0.07 W cm^{-2} (DC bias of -170 V). After dipping the substrates in hydrofluoric acid, ECR etching in a SF_6/O_2 plasma, as described in section 3.2, was used to transfer the

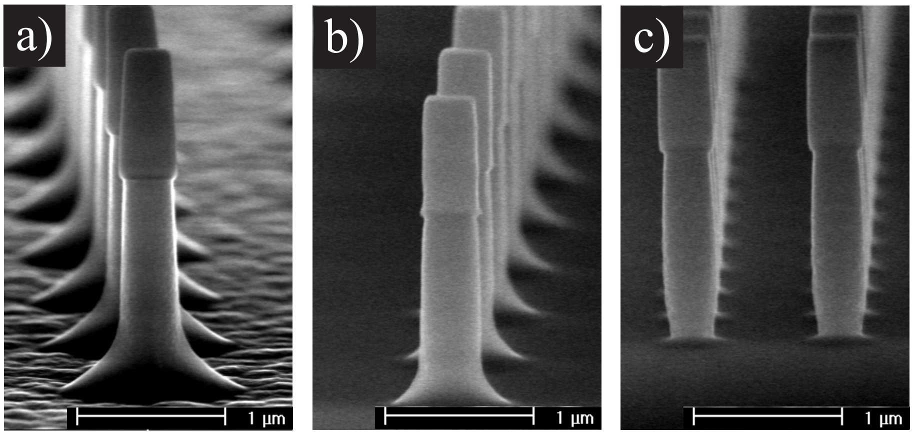

Figure 3.8: *Fabrication of pillars on SOI substrates using ECR etching in a SF_6/O_2 plasma. a) reference pillar etched in c-Si(100). b) similar pillar fabricated in SOI (1.5 μm thick Si layer). The etching was stopped when the underlying SiO_2 was reached. c) Same as b) etched for an additional 60 s. The 380 nm wide etch mask is visible on top of the pillars.*

pattern to the SOI substrates. A SF_6 flow of 11.5 sccm was used in combination with an O_2 flow of 1.3 sccm O_2, resulting in a pressure of 0.1 Pa. A RF power of 400 W was used in combination with a DC bias of -13 V. The substrate temperature was kept at -97 °C resulting in an etch rate of 300 nm min^{-1}. After ECR etching the remaining resist layer was stripped off using O_2 RIE (20 sccm O_2, p = 20 Pa, -100 V bias, 25 W RF power).

Figure 3.8 shows SEM images of Si pillars fabricated in Si(100) (Fig. 3.8a)) and SOI (Fig. 3.8b) and c)). The pillars in Fig. 3.8a) and b) were etched at the same time. The etch process was monitored *in situ* on an unpatterned area of the SOI sample and the etching was stopped after 370 s when the underlying SiO_2 was reached. The etch depth in the c-Si reference sample (Fig. 3.8a)) is 1.55 μm, slightly deeper than the thickness of the c-Si layer of the SOI substrate. The pyramidal footprint of the pillars, caused by a difference in etch rate between Si(111) and Si(100) planes (see Fig. 3.4), can be removed for SOI pillars by additional etching. This is illustrated in Fig. 3.8c) which shows pillars on a SOI sample that were etched for an additional 60 s after etching through the top c-Si layer. As can be seen this additional etch successfully removes the pyramidal footprint. At the same time slight additional etching at the base of the pillar occurs. Note that under the process conditions etching of the underlying SiO_2 is negligible.

Figure 3.9 shows device structures in which square photonic crystals are integrated with input and output waveguides. The photonic crystal consists of a square lattice of Si pillars and the waveguides are ~5 μm wide. The pillars are 230 nm wide and placed on square lattice with a lattice constant of 460 nm (r/a = 0.25). Figure 3.9a) shows a device with an array of 10 rows of 20 pillars. Figure 3.9b) shows a similar array rotated by 45°, keeping the width of the input and output waveguides comparable to the width in Fig. 3.9a). As can be seen in Fig. 3.9 the etching of such devices is possible. Looking at the details of the etching process, two effects are observed. First, the etching of pillars close to the input and output waveguide is different. This is related to the amount of open space surrounding the pillar, which is different close to the waveguide facets. Second, while the pillars in Fig. 3.9a) are connected at the base, the pillars in Fig. 3.9b) are clearly separated. Since the pyramidal footprint forms due to a difference in etch rate between Si(100) and Si(111) lattice planes, this difference can be explained by the orientation of

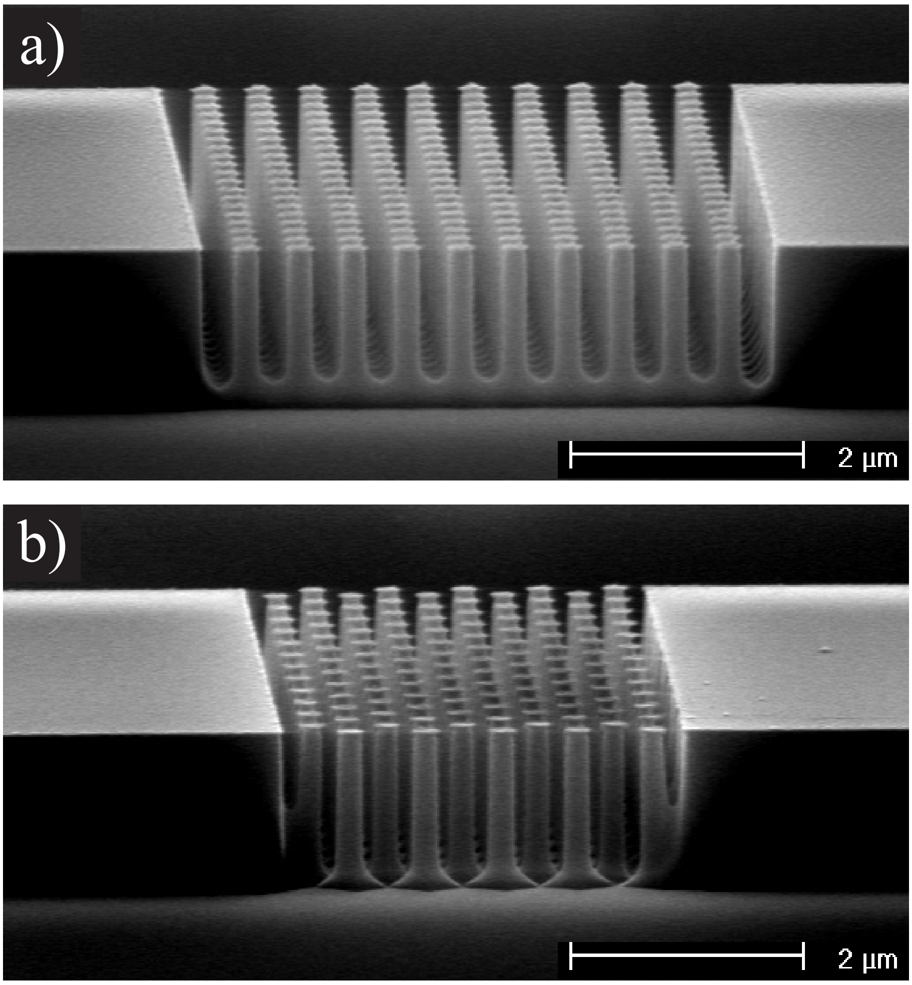

Figure 3.9: *Devices fabricated in SOI. The devices consist of a square lattice of c-Si pillars in between two waveguides that serve as input and output waveguides. a) Device with 10 rows of 20 pillars. The pillars are 230 nm in diameter and placed at a distance of 460 nm (r/a = 0.25). b) Similar device, with a 45° rotated square lattice. The mask on top of the pillars was removed by O_2 RIE.*

the square lattice relative to the (100) and (111) lattice planes of the c-Si.

The lattice constant and r/a value are chosen such that the calculated bandgap of the photonic crystal is centered around a wavelength of 1.5 μm and that the effective refractive index is sufficient to guide the light in the top 1.5 μm thick layer of pillars. Preliminary optical measurements on these devices have been performed. The light was coupled into the mm-long input waveguide using a tapered fiber and collected at the output waveguide using a 40× microscope objective (NA = 0.65). An InGaAsP diode laser operating at 1.49 μm was coupled to a single mode fiber and serves as a light source within the bandgap of the devices under study. Mode images of the output waveguide, taken with an IR sensitive camera, indicate that light is guided through the structures and can be collected at the output waveguides. By controlling the input polarization (extinction ratio $\leq$ 30 dB), polarization dependent transmission measurements were done for the samples in Fig. 3.9 and samples with a smaller number of pillar rows. For each waveguide two reference waveguides exist, one straight waveguide and one waveguide that has an air gap with a length equal to that of the photonic crystal. It was found that the overall transmission of the devices decreases with increasing size of the crystal for both polarizations. For TM polarized light this is consistent with the existence of a bandgap at 1.49 μm. For TE polarized light this is consistent with the fact that TE modes are not guided in the (square) photonic crystals studied (see Chapter 2). For the reference samples (gap without photonic crystal) the decreased transmission with gap width is attributed to the decreased collection of light diffracted off the output facet of the input waveguide. Spectrally resolved measurements of the transmission of TM polarized light through the photonic crystal are required to fully identify the effect of the photonic crystal on the transmission.

3.5 Conclusions

A new process for the etching of Si pillar structures with extremely high aspect ratios is developed. It uses an ECR driven SF_6/O_2 plasma at low temperature. Very high control in the sidewall profile is achieved. Depending on the actual setting of ion energy (by virtue of DC bias), fluorine/oxygen ratio and substrate temperature the etch profile can varied from positively to negatively sloped. The latter is attributed to the impact of ions reflected from the horizontal surface. At the low ion energies used (0–50 eV) a crystallographic orientation preference in the Si etch rate is found.

Cubic arrays of pillars with high aspect ratio were made, as well as more complex structure involving line defects as well as a-Si/c-Si double layer geometries. It is also demonstrated that the anisotropic etch process can be used to fabricate structures in silicon-on-insulator substrates. Using these Si pillars with extreme aspect ratio, it becomes possible to fabricate photonic crystals, crystals with well defined defects as well as randomly distributed photonic structures. All these structures may be of importance to study the propagation of optical modes, localization of light and modified spontaneous emission in two dimensions.

4

Amorphous silicon waveguides for microphotonics

Amorphous silicon a-Si was made by ion irradiation of crystalline silicon with 1×10^{15} *Xe ions cm*$^{-2}$ *at 77 K in the 1–4 MeV energy range. Thermal relaxation of the amorphous network at 500* $^\circ$*C for 1 hr leads to an amorphous layer with a refractive index of* n *= 3.73, significantly higher than that of crystalline silicon (*n *= 3.45 at* λ *= 1.55* μm*). a-Si can thus serve as a waveguide core in Si based optical waveguides. Channel waveguides were made by anisotropic etching of a 1.5* μ*m silicon-on-insulator structure that was partly amorphized. Transmission measurements of these waveguides as function of the amorphous silicon length show that the a-Si part of the waveguides exhibit a modal propagation loss of 70 cm*$^{-1}$ *(0.03 dB* μ*m*$^{-1}$*) and a bulk propagation loss of 115 cm*$^{-1}$ *(0.05 dB* μ*m*$^{-1}$*). Losses due to sidewall roughness are estimated, and are negligible compared to the modal loss. we conclude that a-Si waveguides are ideal for use in Si-based microphotonics applications on a* $\sim$*100* μ*m length scale.*

4.1 Introduction

Silicon is the most widely used semiconductor material in today's electronic devices, because of its excellent electronic properties. Single crystalline Si of high quality is available and the processing and microfabrication of Si are well known. Since silicon is transparent in the near infrared, Si is also an ideal optical material. Si-based waveguides may serve as optical interconnects on Si integrated circuits, or to distribute optical clock signals on a microprocessor. In such cases, using Si provides the advantage of integration with existing electronic circuits. So far optical waveguide technology in silicon is not well developed. Fabrication of waveguides in Si requires a core with a higher refractive index than that of crystalline Si (c-Si).

Amorphous Si (a-Si) is an interesting candidate as a core material. While the density of pure a-Si is 1.8% lower than that of c-Si [72], the refractive index of pure a-Si, at near-infrared wavelengths, is higher than that of c-Si [60, 73–75]. Amorphous silicon can thus be used as a waveguide core material on crystalline Si. As pure a-Si contains a large density of point defects and dangling bonds, the optical absorption at near-infrared wavelengths can be substantial. These point defects can be passivated to some extent by incorporation of hydrogen. In fact, hydrogenated a-Si made by deposition shows excellent electrical quality, and relatively low optical absorption [76].

Amorphous silicon has already received a lot of interest both from a fundamental point of view and because of its possible use in solar cells and optoelectronic devices. Hydrogenated a-Si films can be deposited using a number of different techniques, including plasma enhanced chemical vapor deposition (CVD), RF sputtering and hot-filament CVD. The hydrogen content, void density, structural properties as well as optical and electronic properties have been studied intensively and depend critically on the exact processing conditions. In contrast, a-Si made by ion irradiation of crystalline silicon has reproducible properties that are insensitive to the preparation details, while voids seem to be absent in this material [77]. Heat treatment of pure a-Si made by ion irradiation induces structural relaxation [78] and reduces the defect density, which leads to an improvement in the optical and electronic properties. Overall, it seems that hydrogenated a-Si has better transparency in the near-infrared than pure a-Si. However, pure a-Si can be made more easily in a Si processing sequence, as it requires a single ion implantation step. Furthermore, pure a-Si has larger thermal stability then hydrogenated a-Si. Given these pro's and con's of pure a-Si, it seems interesting to study its applicability in microphotonic integrated circuits. In this chapter we study the properties of amorphous silicon waveguides made using silicon-on-insulator (SOI) substrates and discuss the feasibility of a-Si waveguides for silicon microphotonic channel waveguides and optical interconnects, and as a guiding layer in two-dimensional photonic crystals.

4.2 Properties of amorphous silicon

To study the amorphization and structural relaxation of a-Si, (100) orienteded c-Si samples were mounted on a copper block that was kept at liquid nitrogen temperature. Samples were irradiated with 1×10^{15} Xe ions cm^{-2} in the 1–4 MeV energy range to form amorphous layers of different thickness. All irradiations were done with the ion beam incident under an angle of 7° with the surface normal to avoid ion channeling effects along

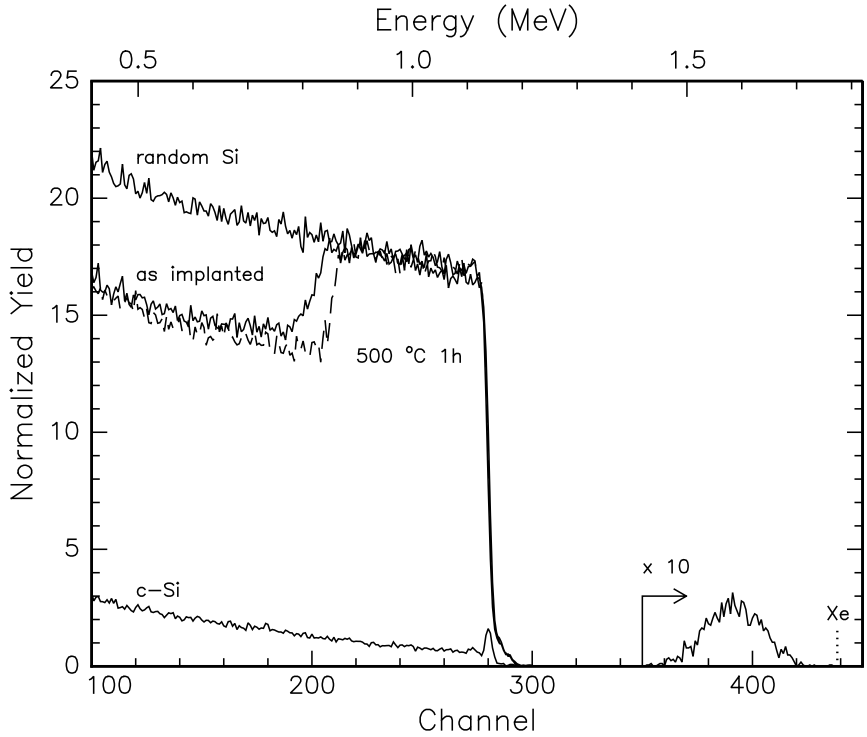

Figure 4.1: *RBS channeling spectra of amorphous silicon made by ion irradiation of crystalline Si with 1.0×10^{15} Xe ions cm^{-2}. The Xe ion energy was 1 MeV. Spectra are shown for the as implanted sample and for a sample annealed for 1 hr at 500 °C. For comparison a channeling spectrum of crystalline Si and a random Si spectrum are shown as well. The surface channel of Xe is indicated in the figure and the Gaussian distribution of Xe ions is clearly visible.*

the (100) crystal direction. After irradiation the amorphous silicon was heat treated at 500 °C for 1 hr in a vacuum tube furnace (base pressure $<10^{-6}$ mbar). The amorphous layer thickness was measured by Rutherford backscattering spectrometry (RBS) channeling measurements using 2 MeV He^{+} ions at a scattering angle of 165°. Variable angle spectroscopic ellipsometry in the 300–1700 nm wavelength was used to determine the refractive index of a-Si and to obtain independent information on the amorphous layer thickness.

The RBS channeling measurements for 1 MeV Xe irradiation are shown in Fig. 4.1. The data for ion irradiated samples are compared to channeling and random spectra of unirradiated crystalline Si. As can be seen the Si signal follows the random height starting from the Si surface channel around channel 280, up to a certain depth in the sample for both the as-implanted and the sample annealed at 500 °C for 1 hr. Annealing leads to the removal of point defects and amorphous pockets in the c-Si near the a-Si/c-Si interface, which sharpens the interface. In addition, solid phase epitaxial crystallization takes place at a growth rate of 0.083 Å/s at 500 °C [79, 80] leading to a shift of the interface. This explains the difference in channeling spectra between the as-implanted and annealed samples. The Gaussian shaped profile around channel 390 is due to the implanted Xe ions. The peak of the implanted Xe distribution is roughly at the center of the a-Si thickness, and the Xe peak concentration is ~0.08 at.%. From similar channeling measurements and

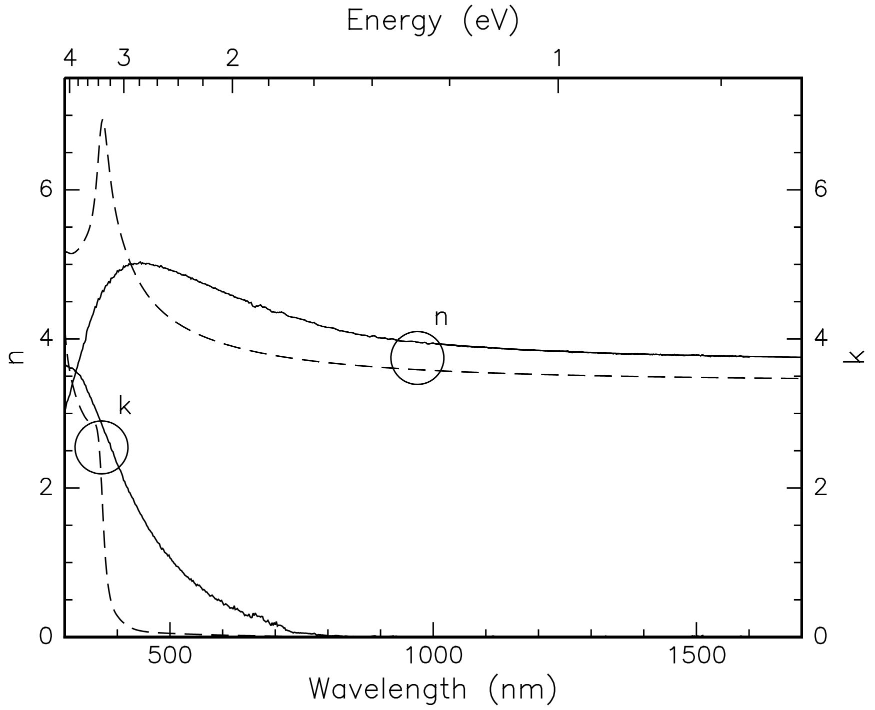

Figure 4.2: *Real (n) and imaginary (k) part of the index of refraction for relaxed amorphous silicon (drawn line) as function of wavelength, obtained from spectroscopic ellipsometry measurements. The index is compared to literature values for crystalline silicon (dashed lines) [81]. In the near-infrared part of the spectrum ($\lambda > 1100$ nm) the refractive index of amorphous is typically 0.3 higher than that of crystalline silicon, while the absorption is small.*

annealing studies we conclude that all samples irradiated with 1×10^{15} Xe ions cm^{-2} in the energy range 1–4 MeV, became amorphous up to the surface. The amorphous silicon thickness after annealing ranged from 0.6 μm for 1 MeV irradiation to 2.0 μm for 4 MeV irradiation.

Figure 4.2 shows the measured complex refractive index of amorphous silicon, made by 1 MeV Xe irradiation, after thermal relaxation (drawn line) compared to literature values for crystalline silicon (dashed line). After relaxation the ellipsometry data for wavelengths longer than 1.2 μm can be described with a lossless layer with a refractive index ~0.3 higher than that of crystalline silicon. To obtain the layer thickness accurately the ellipsometry data was first fitted to a model assuming a transparent layer in the range $\lambda > 1200$ nm*. The refractive index was then obtained for the entire wavelength range by point by point fitting of the complex refractive index, while keeping the layer thickness fixed. By comparing data for samples made using different Xe ion energies it was found that the optical properties are independent of layer thickness. Also, samples annealed for 2 hrs at 500 °C or for 1 hr at 550 °C gave the same results. The density of pure amorphous silicon is lower than that of crystalline silicon [72] and thus a density difference cannot explain the higher refractive index. Hence the high refractive index at infrared wavelengths

---

*To fit the ellipsometry data correctly, a 2.41 nm thick native oxide layer on top of the amorphous silicon was used in the model.

must be attributed to a difference in the electronic bandstructure. Such a difference is apparent from the data near the direct band-to-band transitions in the visible part of the spectrum as observed in Fig. 4.2. Ellipsometry as performed here is not sensitive to very small optical absorption. Given the experimental error on the ellipsometry data, an upper limit of the loss coefficient of amorphous silicon at 1.5 μm is found: 100 cm^{-1}.

4.3 Amorphous silicon waveguides

To further investigate the optical losses of a-Si, commercially available silicon-on-insulator (SOI) substrates with a 1.5 μm thick (100) oriented p-type (14–22 Ωcm) Si layer on a 3.0 μm thick SiO_2 layer grown by wet thermal oxidation were ion irradiated with 1×10^{15} 2 MeV Xe ions cm^{-2} at T = 77 K. The irradiation, followed by thermal relaxation at 500 °C for 2 hrs leads to the formation of a $\sim$1.2 μm thick amorphous silicon layer. During irradiation part of the SOI substrate was masked leading to a triangularly shaped amorphous silicon surface layer on the substrate (see inset in Fig. 4.4).

After irradiation, a series of 10 μm wide waveguides at a 50 μm repeat distance were defined using electron-beam lithography and deep anisotropic etching. Mask patterns were defined in a resist double layer consisting of a 400 nm thick hard baked photoresist layer (HPR 504), with a 80 nm thick silicon containing negative tone electron-beam resist (SNR) on top. After electron-beam exposure (100 kV, 150 μC cm^{-2}) the pattern was developed for 20 s in xylene and rinsed for 30 s in iso-propyl-alcohol. The pattern was then anisotropically transferred in the bottom photoresist layer by low pressure O_2 reactive ion etching at room temperature (p = 0.3 Pa, 0.07 W cm^{-2} RF power density, -180 V DC-bias). Before etching the underlying Si, a dip in hydrofluoric acid (4%) was used to remove the thin native oxide. The pattern was then transferred in the silicon by electron-cyclotron resonance (ECR) driven plasma etching using a low pressure (0.1 Pa) SF_6/O_2 gas mixture (5.6:1.0) at -95 °C. A microwave power of 400 W was used, combined with a -15 V DC-bias, resulting in an etch rate of $\sim$300 nm min^{-1} and anisotropic etch profiles [51]. All patterning processes were controlled *in situ* by laser interferometry. The Si was etched back till the etching stopped at the underlying oxide layer, resulting in 1.5 μm high Si profiles[†].

Fig. 4.3 shows bright field cross sectional transmission electron microscopy (TEM) images of the waveguides taken using 300 kV electrons. Cross sections were first saw cut to 0.5-1 mm thickness, then thinned to 15 μm thickness by mechanical grinding and polishing, and finally ion milled with 5 kV Ar ions to electron transparency. Figure 4.3a) shows the waveguide structure of the amorphous Si waveguide. The cross section shows a 1.06 μm thick amorphous Si region on top of a 0.45 μm crystalline Si layer on a 3.0 μm thick SiO_2 layer. As can be seen, the anisotropic ECR etching process has proceeded continuously through the a-Si/c-Si interface and leads to a similar side-wall angle for both materials. Figures 4.3b) and 4.3c) zoom in on the sidewalls of the a-Si waveguide and c-Si waveguide respectively. They show small sidewall roughness, as will be discussed further on.

[†] The a-Si layer has a 30% lower etch rate than the (100)-oriented c-Si. The etching process was controlled on the a-Si part of the sample, thus slightly overetching the c-Si part.

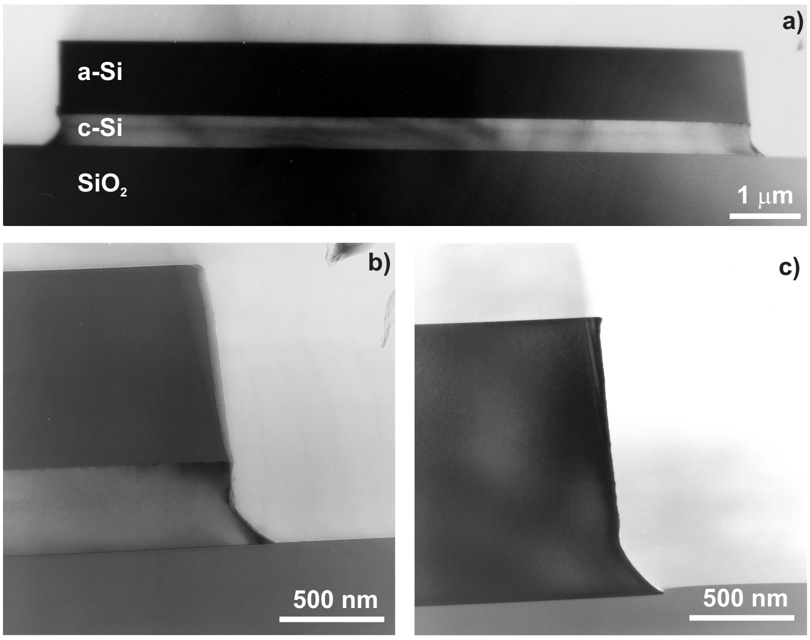

Figure 4.3: *Cross section TEM images of amorphous silicon channel waveguides on c-Si on SiO_2. (a) cross section of the amorphized crystalline region, (b) sidewall of a-Si guide and (c) sidewall of c-Si guide. The thickness of the cross-sections is 610 nm (b) and 310 nm (c).*

4.4 Results and discussion

For optical transmission measurements, waveguide samples were saw-cut to $\approx$7 mm length. The end faces were mechanically polished in order to attain an optimal light coupling into the waveguides. Transmission measurements at λ = 1.49 μm were performed by coupling an InGaAsP laser diode into the waveguides using a tapered optical fiber. 6% of the input power was split off to monitor the input power from the laser. The fiber alignment was controlled using piezo electric actuators. Mode images were obtained by imaging the light from the output facet on an infrared camera using a 10× microscope objective. For transmission measurements, the output mode was collected by a Ge diode detector and was compared to the input power monitored simultaneously on an identical Ge diode detector.

Figure 4.4 shows the measured transmission (open circles) for a series of 70 waveguides. A schematic of the measurement setup with the amorphous and crystalline parts of the waveguides indicated is shown in the inset. The first $\sim$12 waveguides are crystalline along their full length. By moving the input fiber along the horizontal direction on the sample, waveguides with an amorphous section of increasing length are probed. As can be seen, the measured transmission drops exponentially with increasing a-Si length. From the angle of the triangular amorphous region it is known that the amorphous silicon length increases by 25 μm per guide. This information was used to convert the horizontal scale to a length scale (top axis). The best fit to the data (dashed line in Fig. 4.4) results in an extinction coefficient of α = 70 cm^{-1} (0.03 dB μm^{-1}). This is consistent with the upper limit of 100 cm^{-1} derived from ellipsometry in section 4.2.

The transmission in Fig. 4.4 is measured relative to the input power in the tapered fiber and thus contains both the coupling loss and collection efficiency in our setup. The

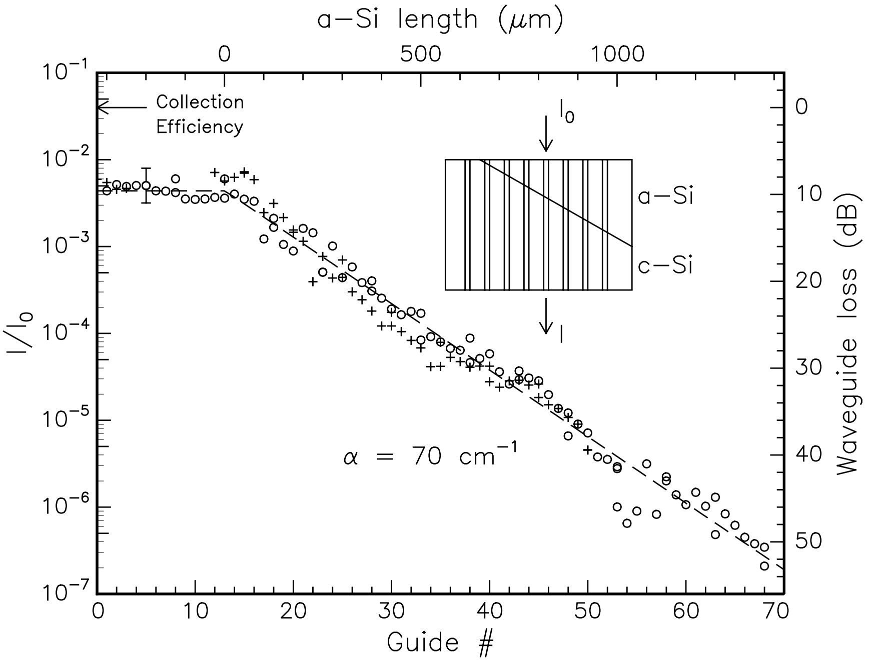

Figure 4.4: *Measured transmission (I/I_0) of c-Si waveguides with a short a-Si section as function of guide number (bottom axis) and a-Si length (top axis). The collection efficiency is estimated (see text) and is indicated on the left axis and is used as the 0 dB point of the waveguide loss indicated on the right axis. Measurements are shown after structural relaxation at 500 °c for 2 hrs (○) and after additional annealing at 500 °C for 1 hr in a forming gas (10% H_2 / 90% N_2) atmosphere(+). A schematic representation of the sample geometry is shown in the inset.*

collection efficiency was measured to be 4% by directly collecting the laser light from the tip of the tapered fiber without a waveguide. This value is indicated by the arrow in Fig. 4.4. The right axis in Fig. 4.4 shows waveguide loss in dB, corrected for this collection efficiency. The combined transmission and coupling losses through the 7 mm long crystalline waveguides (i. e. without a-Si) is less than 9 dB, which corresponds to $\alpha < 3$ cm^{-1}. This is insignificant compared to the value of 70 cm^{-1} measured for the a-Si waveguides.

In the remainder of this chapter we will discuss the nature of the optical loss of a-Si waveguides. Several loss mechanisms should be considered, including coupling losses, scattering losses due to sidewall roughness, and intrinsic material losses. Free carrier absorption can in our case be neglected since the experiments were carried out on lightly doped Si[‡].

Coupling loss occurs when coupling from the tapered input fiber to the waveguide and also when the mode crosses the junction between the c-Si and a-Si section of the waveguides as they have different optical mode sizes. Both types of coupling loss can be estimated from the mode overlap that can be calculated based on measured mode profiles. The measured output modes of the waveguides and the tapered fiber are both described

---

[‡] The free carrier concentration in the p-type Si waveguides (14–22 Ωcm) is $\sim 1.0\times10^{15}$ cm^{-3}. Using an absorption cross section of 0.64×10^{-17} cm^2 [82], this leads to a loss coefficient α $\sim 6\times10^{-3}$, so that free carrier absorption can be safely neglected.

satisfactorily by Gaussian shaped mode profiles. Assuming optimum alignment from fiber to waveguide, a lower limit of the coupling loss of 0.45 dB can be estimated. The loss occurring at the transition from the c-Si to a-Si part of the waveguide is calculated using the waveguide modes obtained from a finite element simulation. The loss due to mode mismatch is estimated to be 0.25 dB (94% transmission). Note that the coupling losses lead to a vertical shift of the data in Fig. 4.4 and do not affect the exponential decay observed.

To investigate scattering losses due to sidewall roughness, TEM images of the waveguide cross section (see Fig. 4.3b) and Fig. 4.3c)) and scanning electron microscopy (SEM) images (not shown) taken from the top and along the propagation direction were used to measure roughness of both the c-Si and a-Si waveguide sidewalls. A sidewall roughness (σ) of $\sim$5 nm for c-Si and $\sim$10 nm for a-Si is derived. These values are confirmed by the SEM images (resolution of $\sim$5 nm.) taken from the top. As can be seen in Fig. 4.3b) the roughness at the a-Si to c-Si interface is small, and is expected to be of atomic scale [83]. To calculate the scattering losses due to surface roughness, we use an expression derived by Tien [84] based on the Rayleigh criterion:

$$\alpha_s = (\frac{4\pi}{\lambda_2})^2 \left(\frac{1}{2}\frac{\sin^3\theta}{\cos\theta}\right)\left(\frac{1}{t_g + (1/p) + (1/q)}\right)\sigma^2 \tag{4.1}$$

where σ^2 is the variance of the surface roughness, λ_2 is the wavelength in the guiding layer, t_g is the thickness of the guiding layer. θ is the mode angle of the mode propagating in the waveguide and $1/p$ and $1/q$ are the penetration depths of the mode into the cladding. Using the calculated propagation constant of the waveguides as obtained from a finite element simulation and the measured values for σ, the scattering loss can be estimated to be 0.1 cm^{-1} (0.4 dB cm^{-1}) for the c-Si guide and 0.4 cm^{-1} (1.6 dB cm^{-1}) for the a-Si waveguide. These values are much lower than the loss of 70 cm^{-1} found from Fig. 4.4. In fact, a sidewall roughness of σ = $\sim$200 nm is needed to obtain a loss figure of 70 cm^{-1}, which would strongly disagree with the TEM data of Fig. 4.3. Therefore we conclude that the measured loss of the a-Si waveguide is mainly due to intrinsic absorption in the amorphous silicon itself. To convert the modal loss of 70 cm^{-1} to the intrinsic absorption coefficient of amorphous silicon, the confinement factor of the waveguide mode should be taken into account. Both from the experimentally measured mode and the finite element calculation a typical confinement factor of 60% is estimated. The absorption coefficient of amorphous silicon at 1.5 μm is thus estimated to be 115 cm^{-1} (0.05 dB μm^{-1}).

It is known that hydrogen can passivate point defects in a-Si and could thus reduce the absorption observed at 1.5 μm. To study this, the waveguide sample as described above was annealed in a forming gas atmosphere (10% H_2 / 90% N_2) at 500 °C for 1 hr. Given a typical diffusion constant of H_2 in silicon, hydrogen could diffuse $\sim$30 μm into the a-Si network and passivate defects inside the a-Si. Other experiments indicate that under these conditions concentrations of a few at.% atomic hydrogen can be incorporated in a-Si [85]. The + symbols in Fig. 4.4 show the transmission measured after this hydrogen treatment. It cannot be distinguished from the transmission measured before annealing in hydrogen. Apparently it is not possible to passivate defects responsible for absorption losses in a-Si made by MeV ion-irradiation by the thermal treatment described above.

The optical loss in a-Si waveguides described in this chapter (0.05 dB μm^{-1}) make a-Si an ideal waveguide core material in Si microphotonic circuits. With typical dimensions well below 100 μm, intrinsic losses on the scale of such devices would be quite

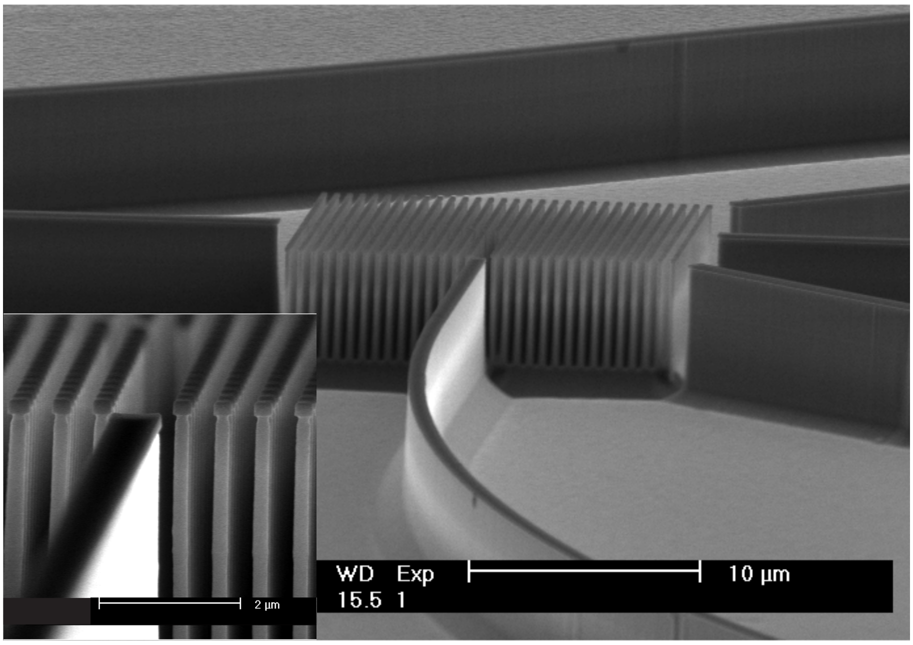

Figure 4.5: *Example of a Si photonic crystal device with a 2 μm thick a-Si top section to confine the light vertically. The device consist of an array of 205 nm diameter cylindrical Si rods placed on a square lattice with a lattice constant a = 570 nm. The rods are 5 μm long and have a 2 μm thick a-Si top section to confine the light vertically. The remaining photoresist is clearly visible on top of the pillars. A row of rods is removed from the array to define a 90° waveguide bend. Input and output channel waveguides to test the device are defined as well. The inset zooms in on the entrance of the photonic crystal waveguide and clearly shows the removed row of rods together with the input waveguide.*

tolerable. As the fabrication of a-Si using ion irradiation is fully compatible with Si microfabrication and integrated circuit processing this enables the fabrication of waveguides in Si, with the vertical confinement provided by the higher index a-Si. To keep the dimensions of these devices as small as possible and to obtain a high packing density requires waveguides that can make very small bends. With the high refractive index of a-Si a bending radius of order 1 μm may be achieved [86, 87]. Alternatively, 2-dimensional (2-D) photonic crystal structures have been proposed to achieve high transmission for 90° bends with very small radius of curvature [11, 12]. In the remainder of this chapter we will describe how a combination of a-Si waveguides and Si photonic crystal technology may be used to achieve such a small bending radius for the important telecommunication wavelength of 1.5 μm.

Figure 4.5 shows a SEM image of 2-D Si photonic crystal waveguide bend designed for operation at 1.5 μm wavelength. The device consist of an array of 205 nm diameter cylindrical Si rods placed on a square lattice with a lattice constant a = 570 nm. The rods are 5 μm long and have a 2 μm thick a-Si top section to confine the light in the vertical direction. Input and output channel waveguides to test the device are defined as well. The inset zooms in on the entrance of the photonic crystal waveguide and clearly shows the removed row of rods and the input waveguide. The mask pattern for this device was defined by electron-beam lithography and oxygen reactive ion etching following the same processing as for the channel waveguides discussed earlier and described in detail in Chapter 3 . The Si etch process was more carefully tuned because of the smaller feature sizes and higher aspect ratios involved. The photonic waveguide bend structures are dry etched in an ECR plasma of SF_6/O_2 (7.3:1) at a pressure of 0.1 Pa, a substrate temperature of -97 °C, a μwave power of 400 W and a DC bias of -12 V, resulting in an etch rate of about 150 nm min^{-1}. Details of the device fabrication procedure are published elsewhere [51].

The design of these devices is based on photonic bandstructure calculations of a square lattice of (infinitely long) Si rods. The vertical confinement in the top a-Si section is based on an effective index method as described in Chapter 2. The properties of a structure with rods of finite length that have a top section of higher refractive index show similar behavior as infinitely long cylinders if the top section is large enough [52]. To calculate the detailed optical response and vertical confinement in devices like the one depicted in Fig. 4.5 a three-dimensional calculation is needed.

The next challenge is to characterize the transmission characteristics of the bends. In this analysis, the main problem is the fact that the mm-long a-Si input and output waveguides suffer from high loss. This once again shows that in studies of microphotonic materials, the coupling to the outside macroscopic world is a matter of great importance and concern. In future microphotonic integrated devices, such problems can be minimized by integrating as many optical function as possible on a single optical chip.

4.5 Conclusions

We have fabricated amorphous silicon (a-Si) waveguides by combining MeV Xe ion irradiation with anisotropic etching techniques. Transmission measurements on 10 μm wide waveguides with different a-Si length revealed a modal absorption coefficient of 70 cm^{-1} (0.03 dB μm^{-1}) at a wavelength of 1.5 μm. Annealing of the waveguides in a hydrogen atmosphere did not improve the optical properties of the waveguides. The scattering loss of the waveguides due to sidewall roughness was calculated and found to be insignificant compared to the total modal loss. Taking the confinement factor of 60% into account the intrinsic absorption coefficient of a-Si made by ion irradiation is found to be 115 cm^{-1} (0.05 dB μm^{-1}). Since the processing of a-Si made by ion irradiation is compatible with standard Si microfabrication and integrated circuit technology, a-Si can be used to vertically confine light in microphotonic devices with dimensions well below 100 μm. As an example a 2-D photonic crystal device is presented in which the vertical confinement may be achieved by index guiding in a 2 μm thick a-Si top section.

5

Novel method for solution growth of thin silica films from tetra-ethoxy-silane

A novel method for solution growth of thin silica films is developed that can be applied to planar and non-planar structures such as photonic crystals. Typically ∼100 nm thick films can be grown from a reaction mixture containing tetra-ethoxy-silane, water, ammonia and ethanol. Under these conditions stable suspensions of monodisperse colloidal SiO_2 *spheres are also formed. The layer thickness as function of reaction mixture composition was investigated and compared to the size distribution of colloidal spheres that grow simultaneously in the solution. A seeded growth experiment was done, showing that after an initial nucleation step both the colloidal sphere radius and the layer thickness increase by the same amount. This clearly demonstrates that the growth occurs by addition of individual monomers and opens the possibility of nm control over the layer thickness by using a well characterized solution of seed particles in the growth. Finally we show that our method is applicable to coat lithographically defined micron-sized Si pillars with a thin* SiO_2 *layer. A luminescent dye was incorporated in the* SiO_2 *layer and the coating was studied in more detail using confocal microscopy imaging techniques.*

5.1 Introduction

Thin films of silicon dioxide find numerous applications in electronic and photonic technology. Several techniques have been developed to grow these layers, including sputter deposition, chemical vapor deposition and thermal oxidation. An alternative technique that is inexpensive, and does not require vacuum or high temperature, uses the sol-gel process [88]. This method relies on a wet chemical reaction leading to the formation of a gel that can, upon drying in a spin-coating process and subsequent sintering, transform into a relatively compact oxide. While the sol-gel technique is technically simple, it has an important disadvantage: it is not suited for the deposition on non-planar surfaces as it requires a spin-coating step of a precursor solution. In the sol-gel process, tetra-ethoxy-silane (TEOS) undergoes a hydrolysis and condensation reaction in which small colloidal particles are formed that are not stable and form a gel [88]. In the present method, we use a similar reaction, but now under base (ammonia) catalyzed conditions [89]. In a mixture of TEOS, water, ethanol and ammonia stable and monodisperse spherical colloidal particles are formed in the bulk of the solution. While this reaction has been thoroughly studied in the past few years with the aim to control the growth of colloids [90–93], it has not been explored for the formation of thin films. Early on in the reaction small sub-particles are formed that are not yet colloidally stable. These sub-particles aggregate until a size is reached where electric double layer interaction prevents further aggregation. Exactly when this happens depends on the surface potential and ionic strength that are sensitive and complicated functions of the amount of water, ammonia and the concentration of dissociated silanol groups. After this nucleation-aggregation stage, surface reaction limited growth takes over and the irregular shaped particles become smooth, spherical and more monodisperse by a condensation reaction of reactive monomers and small oligomers. The final size of the particles depends on the number of particles that result after the aggregation process and is hard to control with great accuracy experimentally. Nanometer control is possible though, if a seed suspension is used with well-characterized size and concentration. If the conditions are well chosen all monomers end up on the seeds and high control over the resulting size is possible [90–95].

In this Chapter we describe a different wet chemical method, based on the same precursors as in the sol-gel process, but under conditions that lead to the controlled growth of silica in solution. Nanometer control over the layer thickness is possible. The technique does not require spin-coating and can thus be used to coat surface features with large aspect ratio. We also demonstrate that the grown layers can be doped by chemical incorporation with optically active groups, making this method ideally suited for the coating of photonic structures with optically active probe ions or molecules.

5.2 Experimental

All chemicals were used as received, without further purification. TEOS (purity 99%) and ammonia solution (29.1 wt%) were supplied by Fluka Chemie AG, KOH and (3-aminopropyl)-triethoxysilane (APS) were supplied by Aldrich and eosin-5-isothiocyanate (eosin-ITC) was supplied by Molecular Probes. Ethanol (Merck) was of analytical grade.

Two types of silicon substrates were used for silica deposition. To study the grown layer thickness, Si substrates ((100) oriented, 5×10 mm^2) covered with a 535 nm thick

SiO_2 film grown by wet thermal oxidation were used. Silicon pillars fabricated using deep anisotropic etching of a Si(100) wafer with a SF_6/O_2 plasma [51] were used to study the coating process on a non-planar surface. Prior to deposition, the substrates were cleaned in a 2 M KOH ethanol solution for 15 minutes and rinsed with pure ethanol. The substrates were then placed in a closed bottle containing TEOS, ethanol, water and ammonia. As an example, the quantities used for the layer growth on the silicon pillars were: 7.925 g ethanol, 0.805 g water, 0.697 g ammonia solution and 0.376 g TEOS. For incorporation of a fluorescent dye in the silica layer [94, 95], 12.52 mg eosin-ITC was first reacted with 41.8 mg APS in 2.2 g dry ethanol by stirring for 16 hrs. 0.250 g of this reaction mixture was added to a solution containing 7.641 g ethanol, 0.809 g water, 0.699 g ammonia. Finally, 0.380 g TEOS was added to the solution. All reactions took place at room temperature and under continuous stirring. In the growth experiments on the silicon wafers the water and ammonia concentrations were varied. Concentrations were calculated assuming additivity of the individual volumes. The reaction time varied between 25 minutes and 12 hrs. After removing the samples from the solution the planar samples were wiped with lens Chapter and rinsed with ethanol to remove colloidal particles. Early and preliminary results of the method described in this Chapter were obtained in the deposition of thin layers of silica on phosphor particles and plant materials [96, 97].

Rutherford Backscattering Spectrotroscopy (RBS) using 2 MeV He^+ at a scattering angle of 165° was used to determine the relative silicon and oxygen composition and total areal density of silica of the grown layer. A variable-angle spectroscopic ellipsometer was used to determine the thickness of the film and the refractive index in the spectral range between 300 nm and 1700 nm. Scanning electron microscopy (SEM, Philips XL30FEG) with an acceleration voltage of 10 kV was used to determine the radius of the silica colloids that were simultaneously grown in the solution. For this aim the solution containing the silica colloids was dried on a silicon substrate. SEM was also used to determine the thickness of the grown silica layer on the silicon pillars. Fluorescence confocal microscopy (Leica TCS NT, 100x lens with NA 1.4) at excitation wavelengths of 476 nm and 488 nm was used to image the eosin-ITC coated silicon rods.

5.3 Results and discussion

To investigate the thin film growth technique, a thermally oxidized (535 nm) silicon wafer was used as a model substrate. Three 5×10 mm^2 samples were simultaneously immersed in a solution containing 7.891 g ethanol, 0.805 g water, 0.693 g ammonia solution (29.1 wt%) and 0.376 g TEOS (total volume 11.9 ml; concentrations 6.1 M water, 1.0 M ammonia and 0.15 M TEOS). After 135 minutes of continuous stirring (all TEOS was then consumed), one sample and 76 mg of the solution containing colloidal particles were taken out. Next, 0.375 g TEOS was added and after 130 minutes of continuous stirring, a second sample and 74 mg solution were taken out. This step was repeated once more. In Fig. 5.1 the insets show typical SEM images of the colloids that formed in the bulk and that were collected from the solution after each reaction step was finished. The images were used to determine the colloid radius distribution. The SiO_2 layer thickness increase for the three samples was determined using ellipsometry. The results are indicated in Fig. 5.1.

After the first growth step (Fig. 5.1a), the grown silica layer thickness was determined

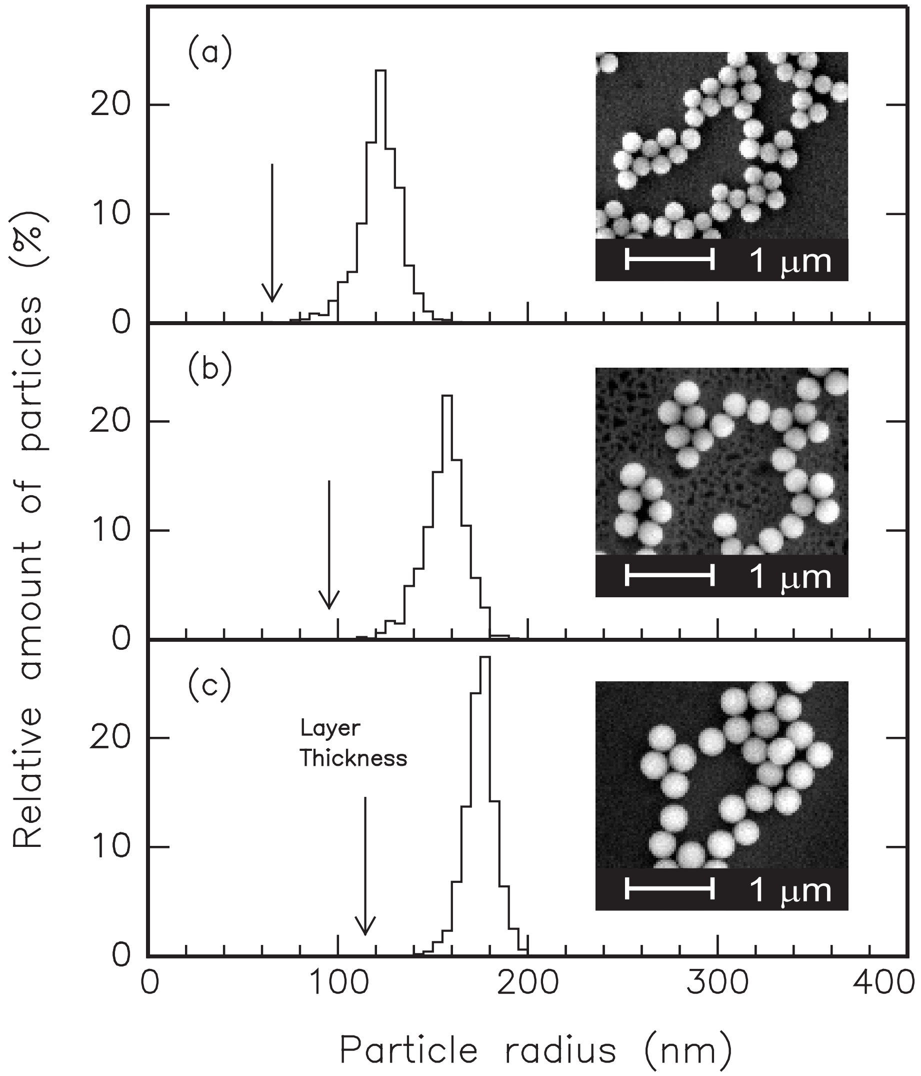

Figure 5.1: *Thickness of the grown silica layer (vertical arrow) and distribution of the radii of the colloids (histogram binsize 5 nm) grown in an ethanol solution containing 7.891 g water, 0.805 g ammonia solution (29.1wt%) and 0.376 g TEOS (a), after adding 0.375 g TEOS (b), and after adding another 0.37 g TEOS (c). The insets show typical SEM images of the colloids grown in solution.*

to be 65 nm and the mean colloid radius was found to be 122 nm. After the second growth step (Fig. 5.1b) the layer thickness and the mean radius increased to 95 nm and 156 nm respectively; after the third step (Fig. 5.1c) they increased to 114 nm and 175 nm. In the second and third growth step (where only TEOS was added) the increase in layer thickness was found to be the same as the increase in the mean radius of the colloids within ± 4 nm. From this it can be concluded that the silica layer grows with the same surface-reaction limited growth mechanism as the colloids do, because only in a surface-reaction limited growth the absolute increase in radius is independent of the particle size [92]. It can also be seen from Figs. 5.1b and 5.1c that under these conditions after adding additional TEOS no new nucleation reaction took place because no new (small) particles were formed. This implies that it is possible to obtain nanometer control over the layer thickness by immersing a substrate in a solution containing a known number of colloids with a known

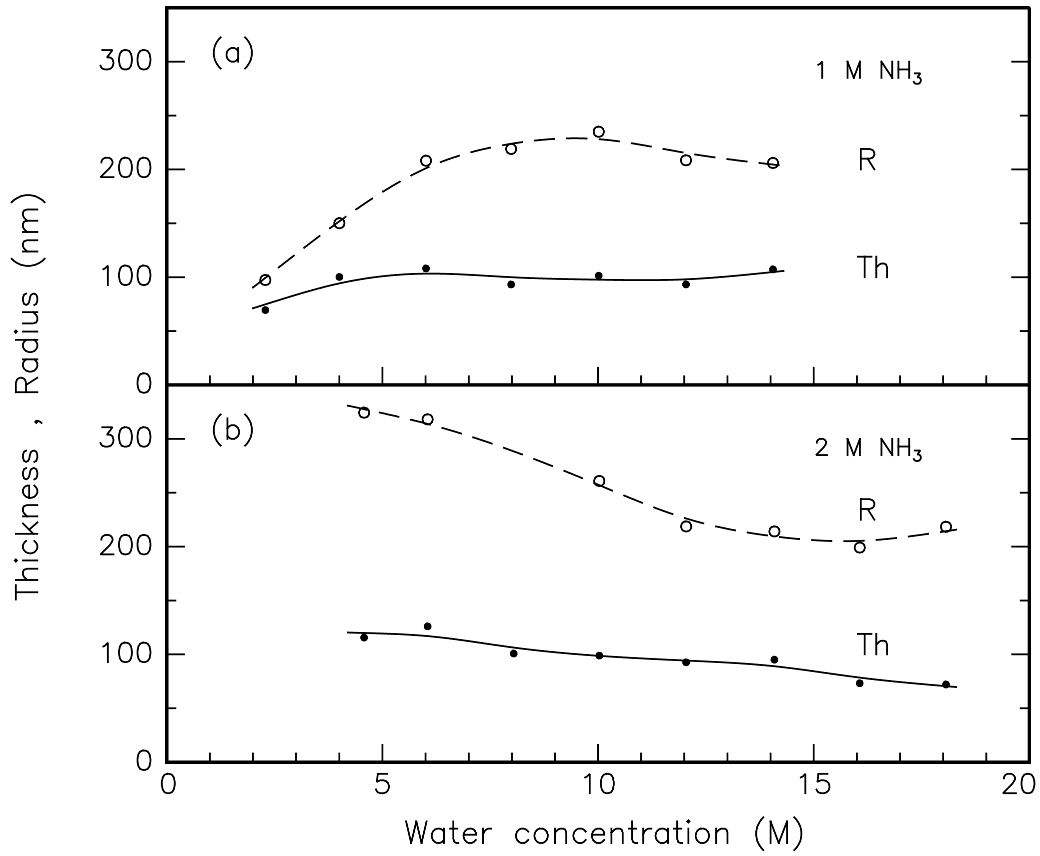

Figure 5.2: *Layer thickness (solid dots) of the grown films as derived from ellipsometry, and the mean colloid radius (open circles) as measured from SEM images. The TEOS concentration was kept constant at 0.15 M, while varying the water concentration between 2.0 M and 18.0 M. Results are shown for 1 M ammonia solutions (a), and 2 M ammonia solutions (b).*

radius. Under the above mentioned reaction conditions, the added amount of TEOS then very accurately determines the (equal) increase in colloid radius and layer thickness.

Although nanometer control over the layer thickness is possible, care has to be taken in preparing and characterizing the seed suspension used. Growing a silica layer without seeds is also possible (as shown in Fig. 5.1a), but then there is an uncertainty in layer thickness (and colloid radius). To investigate the dependence of the layer thickness and the mean colloid radius on the initial reaction conditions, the water concentration was varied from 2.0 to 18.0 M, while the TEOS concentration was kept constant at 0.15 M. Figures 5.2a and 5.2b show the layer thickness (Th) and the mean colloid radius (R) for ammonia concentrations of 1.0 M and 2.0 M respectively. In the 1 M ammonia case the smallest layer thickness (70 nm) was found for a water concentration of 2.3 M. For higher water concentration (4–14 M) the layer thickness is roughly constant at ∼100 nm. The colloid radius also shows an initial increase with water concentration and then a saturation for water concentrations above 6 M. For the 2.0 M ammonia solution, the silica layer thickness was ∼120 nm for the lowest water concentration of 4.6 M and then shows a steady decrease with increasing water concentration. A similar trend is observed for the colloid radius as a function of water concentration [91]. For both ammonia concentra-

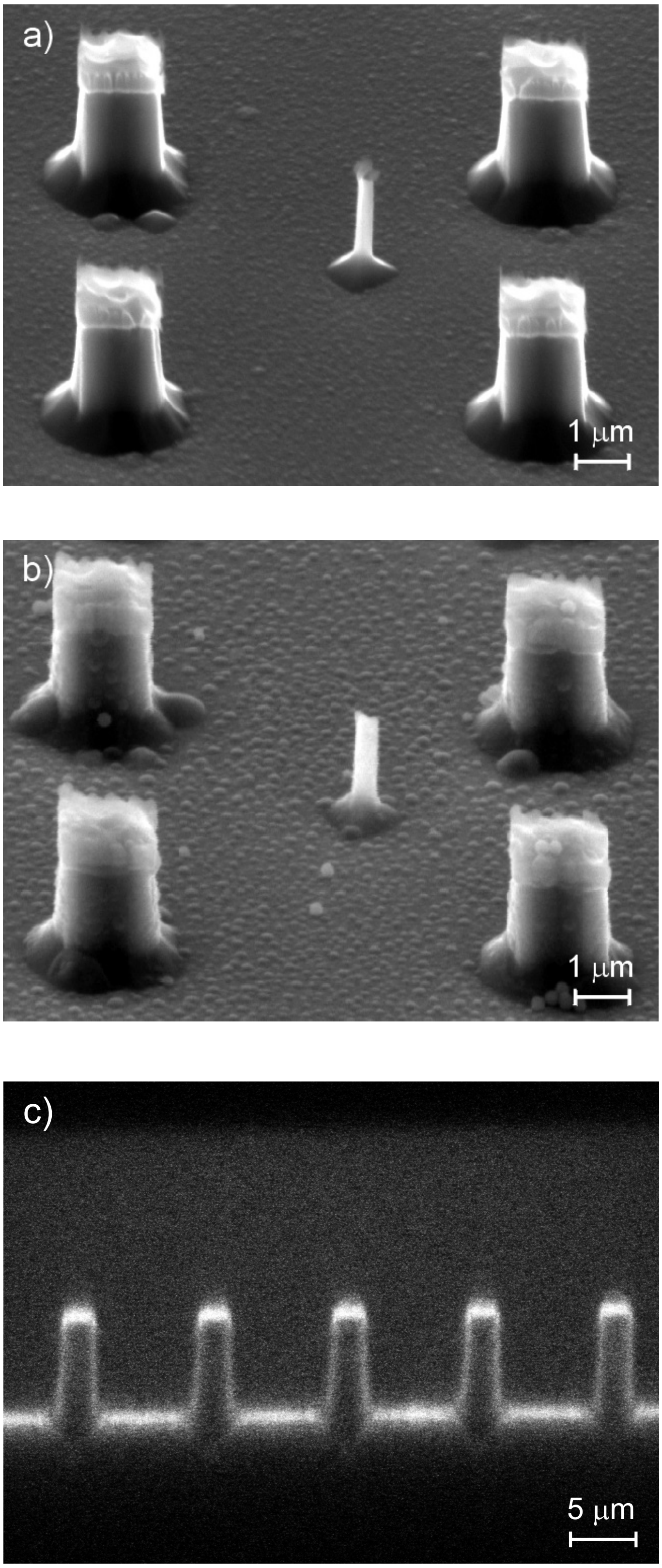

Figure 5.3: *SEM images of silicon pillars etched in silicon using deep anisotropic ion etching with a* SF_6/O_2 *plasma (a), and of the same array of pillars after coating with a silica layer (b). Cross section of silicon pillars coated with a eosin-labeled silica coating, obtained by fluorescence confocal microscopy (c).*

tions, the layer thickness and the colloid radius follow the same trend. The layer thickness is not a sensitive function of the water concentration although for one given set of concentrations, there is a variation of about 10% in the layer thickness, as can be seen from the apparent scattering of the data around the smooth lines. Variation of the initial reaction conditions can thus give some control over the silica layer thickness, but high accuracy is only possible with seeded growth.

The silicon to oxygen ratio in the grown films determined from Rutherford Backscattering Spectrotroscopy (RBS) measurements is 1:2. The density of the film, calculated using the film surface coverage obtained by RBS and the layer thickness determined by ellipsometry is found to be 2.0 g cm^{-3}. This is lower than the value of 2.2 g cm^{-3} typical for thermally grown SiO_2 [98]. This suggests that the films have a porous structure. Indeed, the refractive index of the films is found to be in the range from 1.42 to 1.44 at 1000 nm, significantly lower than that of the thermal oxide (n = 1.45 at 1000 nm), and characteristic for a porous structure that is not fully condensed, similar as has been found for the colloids grown in this way [99, 100].

Next, we will show how this novel method can be used to grow thin silica films on a predefined surface structure. Figure 5.3a shows a SEM image of an array of silicon pillars with a diameter of 1.5 μm and a height of 2.2 μm, placed at a distance of 6.5 μm apart. The top "hat" on the silicon pillars is a leftover from the silica mask used during the etching process. The etched structure was immersed in an ethanol solution containing 6.0 M water, 1.0 M ammonia and 0.15 M TEOS. Figure 5.3b shows the same array of pillars after the reaction. As can be seen the pillar diameter has increased, and the deposited film thickness is determined to be 45 ± 10 nm. The layer thickness appears to be quite uniform over the full height of the pillars.

Finally, we show that the grown silica layer can be doped with fluorescent dye. Eosin-5-isothiocyanate (eosin-ITC) was first coupled to (3-aminopropyl)-triethoxysilane (APS) and then added to the TEOS solution [94, 95]. Figure 5.3c shows a cross section of an array of silicon pillars coated with a silica layer obtained by fluorescence confocal microscopy. From this image it is visible that the full surface structure is covered with a fluorescent layer. The higher intensity on top of the pillars and on the substrate is because the pillars are not transparent in the visible. Therefore the sides are only partially imaged due to the high numerical aperture of the lens used in the confocal microscope. We have also performed preliminary experiments on doping these oxide films with erbium by ion implantation. Clear photoluminescence at 1.5 μm is observed with high quantum efficiency, indicating that these oxide layers are an excellent host for erbium as well [101].

5.4 Conclusion

We have developed a novel and simple method for solution growth of thin silica films using tetra-ethoxy-silane (TEOS). The films are grown on macroscopic surfaces from TEOS in a mixture of ethanol, water and ammonia. The silica growth is found to take place through a surface-reaction limited process. The grown layer thickness is not a very sensitive function of the water and ammonia concentrations. The layer thickness varies by $\sim$10%, for a given set of reaction conditions. Nanometer control over the layer thickness is possible using a seeded-growth process in which a known number of particles with known radius is introduced in the reaction that serve as nucleation sites. Finally, this new method can be applied for the coating of highly anisotropic, micron-sized silicon pillars and fluorescent dyes can be chemically incorporated.

Part II

1-D

6

Luminescence quantum efficiency and local optical density of states in thin film ruby made by ion implantation

Single crystal, (0001) oriented, sapphire samples were implanted with 150 keV Cr ions at fluences between 6.0×10^{14} *and 4.0×*10^{15} *Cr cm*$^{-2}$*. The peak concentrations ranged from 0.04 to 0.28 at.%. Characteristic photoluminescence of the* R *lines at 694.3 and 692.9 nm was observed. Annealing at 1450* $^{\circ}$*C for 2 hrs increased the luminescence intensity by a factor 45, due to the increasing fraction of substitutional Cr ions as confirmed by Rutherford backscattering spectrometry. The Cr luminescence decay rate in an annealed sample implanted with 3.0×*10^{15} *at. cm*$^{-2}$ *at 300 K is 299 s*$^{-1}$*. Decay rates were also measured for samples covered with a range of transparent liquids (refractive index* n *= 1.33-1.57), showing a clear increase with increasing refractive index of the liquid. This effect is explained by the increase of the local optical density of states in the Cr-implanted region. By comparing the measured data with the calculated optical density of states the radiative decay rate is found to be 164 ± 10 s*$^{-1}$ *and the internal quantum efficiency ∼50%. The quantum efficiency decreases slightly for increasing Cr concentration.*

6.1 Introduction

The spontaneous emission rate of an atom can be influenced by placing it close to a dielectric interface, within the scale of the emission wavelength, as first noted by Purcell [5]. Several experiments that demonstrate this concept have been performed and involve rare-earth ions or dyes in solution in contact with a dielectric or a mirror [6, 102–104], erbium ions implanted near a glass surface [8] and excitons recombining in a slab bound by two dielectrics [105].

A theoretical description of the change in emission rate requires the quantization of the electromagnetic field and results in an expression of the decay rate in terms of a local density of states (LDOS) of the (classical) Helmholtz equations [106, 107]. In spatially inhomogeneous geometries the LDOS changes from its free ($\varepsilon = 1$) value. For the case of a dielectric interface it can be calculated using a complete set of normalized plane waves of the problem [8, 108–111].

While the simple case of a dielectric interface has now been well studied and understood, it appears challenging to study the modification of spontaneous emission in more complicated cases, involving e. g. absorbing layers, strongly scattering systems, or photonic crystals. In order to do this, well-defined probes to measure the change in spontaneous emission rate are required. In this Chapter we study the fabrication of thin film ruby (Al_2O_3:Cr^{3+}) layers that can be used as probes in such experiments.

The optical properties of transition metal ions in solids have been studied for many years. Because the optical transitions of these ions occur in the outer lying 3d electronic levels of the ion, a strong coupling between these levels and the local crystal field of the surrounding atoms in the solid exists. If Cr^{3+} ions are incorporated into α-Al_2O_3 as substitutional atoms on the Al sublattice (known as ruby), characteristic R line luminescence is observed at well defined wavelengths of 692.9 and 694.3 nm. The energy levels are well understood in terms of ligand-field-theory [112–114] and the luminescence was studied intensively since the introduction of the ruby laser [115, 116]. Apart from its use as a laser, ruby can be used as a high-pressure or stress sensors. Here the pressure-induced frequency shift of the R lines, caused by a change in the local crystal field, is used for pressure or stress determination [117–120].

Ion implantation is a relatively simple technique to introduce Cr ions in the near-surface region of Al_2O_3. In the past much work has been done on the implantation of Cr ions to study surface hardening of Al_2O_3 [121–123]. However these ion-implanted samples were never characterized by luminescence measurements. Luminescence of Cr ions close to a dielectric interface was studied in thin film ruby layers formed by epitaxial growth, that were used as stress sensors [124, 125]. In this case no attention was paid to luminescent lifetimes.

In this Chapter we study Al_2O_3 implanted with Cr^{3+} ions in the near-surface region, resulting in characteristic photoluminescence at wavelengths around 694 nm [114]. Subsequently the spontaneous emission is influenced by bringing liquid films with different refractive index in contact with the Cr-doped Al_2O_3 surface. The aim of this Chapter is to determine the radiative lifetime and quantum efficiency of the R line luminescence for ion implanted samples. Once characterized these samples can be used as probes of the LDOS in more complicated photonic systems operating at 694 nm.

6.2 Experimental

Single crystalline, (0001) oriented α-Al_2O_3 substrates of 1 mm thickness with low Cr content (<1 ppb), were implanted at room temperature with 150 keV Cr^+ ions to fluences of 0.6, 1.6, 2.5, 3.0 and 4.0×10^{15} at. cm^{-2}. The samples were rotated 7° with respect to the incoming Cr ion beam to avoid ion channeling in the [0001] crystal direction. The beam was electrostatically scanned on the sample to obtain a homogeneous implantation over the sample surface. The current on the sample during implantation was kept below 0.1 μA cm^{-2}. After implantation, the samples were annealed for two hours at 1450 °C in air. One set of samples, implanted with 3.0×10^{15} Cr cm^{-2} was first annealed at 1200 °C for 1 hr, and then at 1450 °C for 1 hr.

Rutherford backscattering spectrometry (RBS) in combination with ion channeling was used to study the crystal structure before and after annealing, as well as the Cr depth distributions. A 2.0 MeV $^4He^+$ beam was used at a scattering angle of 165°. Photoluminescence (PL) measurements were performed at room temperature, using the 457.9 nm line of an Ar-ion laser as a pump source. Typical pump powers of 15 mW in a 0.3 mm diameter spot were used. The luminescence signal was detected using a 48-cm monochromator and a thermo-electrically cooled GaAs photomultiplier tube. The spectral resolution was 3.3 cm^{-1}. The pump beam was chopped at 13 Hz using an acousto-optic modulator and the signal was collected using standard lock-in techniques. Luminescence decay traces were recorded, at a spectral resolution of 8.3 cm^{-1}, using the GaAs photomultiplier tube in combination with a multichannel photon counting system. The overall time resolution was 400 ns.

Various liquids with different refractive index were brought in contact with the implanted front side of the samples by inserting a droplet of the liquid between the sample and a fused silica slide, placed at a distance of ~1 mm from the sample. The Cr ions were pumped through the back side of the Al_2O_3 sample and the PL signal was collected from the back as well. The transparent liquids used are water (n = 1.33), a mixture of glycerol and water (n = 1.45), microscope immersion oil (n = 1.51) and 2-methoxy-4-propenylphenol (n = 1.57).

6.3 Results and discussion

Figure 6.1 shows RBS channeling measurements along the [0001] direction of Al_2O_3 samples implanted with 3.0×10^{15} Cr cm^{-2} before and after annealing. The dashed line shows a channeling spectrum of the as implanted sample. A random spectrum (closed circles) is shown for reference. The dotted line shows the channeling spectrum after annealing at 1200 °C for one hour. Annealing at 1450 °C for one hour resulted in a spectrum (drawn line), similar to that of a virgin sample (not shown). To show the implanted Cr distribution, the yield of the random and channeling spectra for the sample annealed at 1450 °C was multiplied by a factor 25 for energies above 1.22 MeV.

Comparing the channeling spectrum of the as implanted sample with the random spectrum shows that the implantation has caused a disordered region, but has not completely amorphized the Al_2O_3. The depth of maximum damage in the Al sublattice is around 100 nm, while the near-surface region is relatively damage free. Although clear channeling is observed in the Al sublattice, no channeling is observed in the O sublattice. This

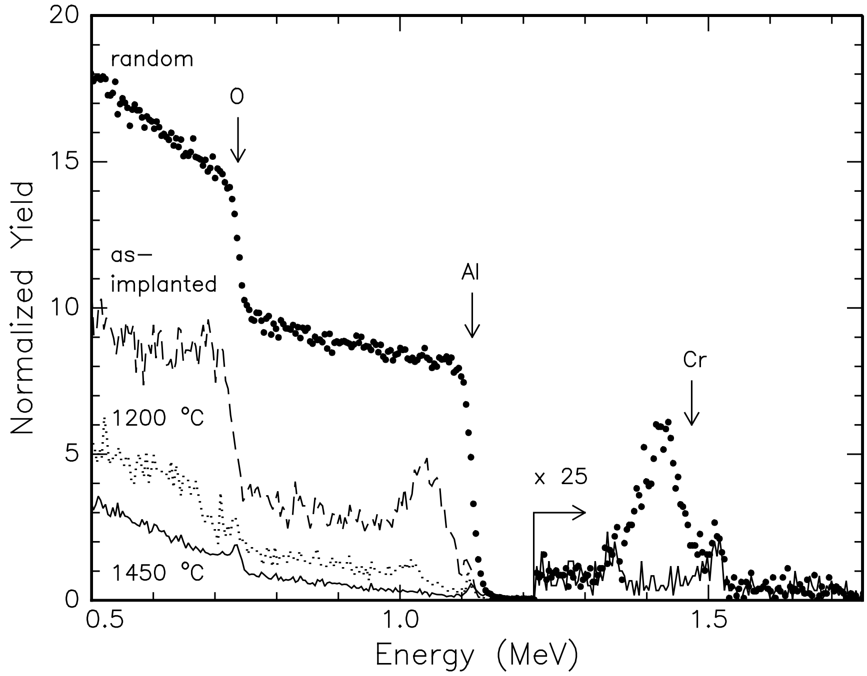

Figure 6.1: *RBS spectra of Cr-implanted (3.0×10*^{15} *Cr cm*$^{-2}$*) Al*$_2$*O*$_3$*. Channeling spectra are shown for the as-implanted sample and samples annealed at 1200 °C and 1450 °C. A random spectrum after 1450 °C annealing is also shown. The Cr section in the spectrum is enlarged by a factor 25 and is only shown for the random and channeling spectrum of the sample annealed at 1450 °C.*

implies that the O sublattice, contrary to the Al sublattice, has been amorphized by the ion implantation. This difference between the Al and O sublattices was observed before in the annealing behavior of ion implanted Al_2O_3 [121–123]. Figure 6.1 shows that annealing at 1200 °C for one hour partly removes damage made by the implantation (in both the Al and O sublattices). The damage is completely removed after subsequent annealing at 1450 °C for 1 hr.

The random spectrum in Fig. 6.1 shows a Gaussian-shaped implanted Cr distribution, peaking at a depth of 70 nm and with a full width at half-maximum (FWHM) of 115 nm. Using this distribution and the density of α-Al_2O_3 (1.17×10^{23} at cm^{-3}), the peak concentrations corresponding to implanted doses of 0.6, 1.6, 2.5, 3.0 and 4.0×10^{15} Cr cm^{-2},are 0.04, 0.11, 0.18, 0.21 and 0.28 at.% respectively. Note that diffusion of Cr in Al_2O_3 can be neglected for temperatures up to 1600 °C [121, 122]. The small peak to the right of the surface energy of Cr is possibly due to a small amount of Fe (surface energy 1.51 MeV) either at the surface or coimplanted with the Cr. A comparison between the random and channeling RBS spectra for the Cr section in Fig. 6.1 shows that after annealing at 1450 °C the minimum yield of the Cr ions almost vanishes, indicating that the Cr ions are substitutional. The peak observed in the channeling spectrum around 1.33 MeV is most likely due to Cr ions that are not substitutional after annealing due to end-of-range damage caused by the Cr implantation. Our results indicate that at least 95% of the Cr ions are substitutional, in agreement with existing literature [121, 122]. To summarize the RBS results, the first two columns of Table 6.1 list the minimum yield of the Al sublattice

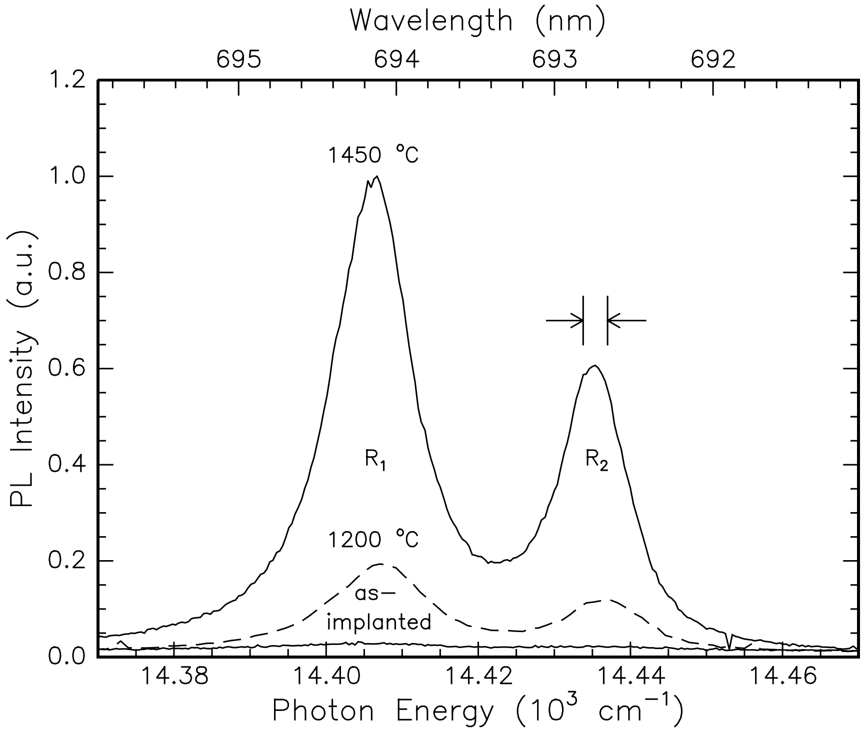

Figure 6.2: *Room temperature PL spectra of Al_2O_3 implanted with 3.0×10^{15} Cr cm^{-2} for various anneal treatments. Data are shown for the as-implanted sample, after annealing for one hour at 1200 °C, and after an additional anneal for one hour at 1450 °C. Clear R line luminescence is observed peaking at 14,403 (694.3 nm) and 14,432 cm^{-1} (692.9 nm). The spectral resolution is indicated by the arrows. The pump wavelength is 457.9 nm, the pump power is 15 mW in a 0.3 mm diameter spot.*

and the integrated minimum yield of the Cr distribution for the as-implanted sample and the samples annealed at 1200 and 1450 °C.

Figure 6.2 shows PL spectra measured at room temperature of Al_2O_3 samples implanted with 3.0×10^{15} Cr cm^{-2}, after implantation and after annealing at 1200 °C and 1450 °C. All spectra show two distinct peaks at energies of 14,403 and 14,432 cm^{-1} (corresponding to wavelengths of 694.3 and 692.9 nm respectively); often identified as the R_1 and R_2 lines respectively. The lines can be very well fitted with a sum of two Lorentzian line shapes [126]. For the sample that was annealed at 1200 °C, the FWHM of the 14,403 cm^{-1} peak (R_1 line) is 15.2 cm^{-1} and the FWHM of the 14,432 cm^{-1} peak (R_2 line) is 11.4 cm^{-1}. After annealing at 1450 °C, the FWHM reduces to 12.7 and 9.72 cm^{-1} (corresponding to 0.61 and 0.47 nm).

The R_1 and R_2 lines at 694.3 and 692.9 nm are characteristic for Cr^{3+} ions that are substitutional on the Al sublattice [114]. The 457.9 nm line of the pump source is absorbed in the $^4T_1$ and $^4T_2$ broad bands [127]. Subsequently, rapid non-radiative relaxation to the first excited (^2E) state occurs, followed by a radiative transition to the ground state ($^4A_2$) [115, 116, 127]. The broadening of the R lines is caused by Cr-lattice interaction. The FWHM measured in Fig. 6.2 is somewhat larger than that measured for bulk Al_2O_3:Cr. A possible explanation for this could be that the Al_2O_3 lattice contains residual damage or stress from the ion implantation that was not annealed completely [122] (but

Table 6.1: *Minimum yield from RBS channeling measurements for the Al sub-lattice (χ^{Al}) and integrated over the Cr depth distribution (χ^{Cr}), measured after different anneal treatments. The normalized PL intensities and lifetimes measured at 694.3 nm (R_1 line) are also shown.*

	χ^{Al} (%)	χ^{Cr} (%)	I_{PL} (R_1)	W_{PL} (s^{-1})
as-implanted	53	50	0.02	495
1200 °C	13	70	0.26	361
1450 °C	4	3	1.00	303

is invisible in RBS).

From Fig. 6.2 it is clear that the PL intensity increases with increasing anneal temperature. Although hard to identify in the figure, the as-implanted sample shows two clear R lines, superimposed on a broad background. This is consistent with channeling measurements [122], that show evidence for a small substitutional Cr fraction after implantation. Annealing at 1200 °C enhances the intensity by a factor 12; subsequent annealing at 1450 °C yields an intensity that is a factor 45 higher than that of the as-implanted sample. An increase in intensity may be explained by an increase in concentration of substitutional Cr as well as by an increase in luminescence quantum efficiency. Luminescence lifetime measurements were performed at 694.3 nm to study the latter. The measured decay rates are 495, 361 and 303 s^{-1} for the as-implanted, 1200 °C and 1450 °C annealed samples respectively. The decay rates are listed in Table 6.1 together with the peak luminescence intensity of the R_1 line at 14,402 cm^{-1}. The measured decay rate decrease upon annealing of only a factor 1.6, which implies that the 45-fold increase in PL intensity is mainly due to an increase in the concentration of substitutional Cr after annealing.

Due to additional non-radiative processes the measured decay rate will be higher than the radiative decay rate. It is known that ion implantation introduces defects and lattice strain in the crystal [122] which may not be completely removed by thermal annealing, leading to line broadening as in Fig. 6.2 and non-radiative decay channels. The total decay rate W can be written as the sum of radiative (W_{rad}) and non radiative decay ($W_{non-rad}$):

$$W = W_{rad} + W_{non-rad} \tag{6.1}$$

In order to study the luminescence quantum efficiency of the R line luminescence, PL decay measurements were done for samples brought into contact with liquids with a different refractive index. Figure 6.3 shows decay traces measured at a wavelength of 694.3 nm (R_1 line), for an Al_2O_3 sample implanted with 3.0×10^{15} Cr cm^{-2} annealed at 1450 °C for 2 hrs, for the sample in air (n = 1.00), and the sample in contact with 2-methoxy-4-propenylphenol (n = 1.57). The experimental configuration is shown in the inset of Fig. 6.3. A clear increase in the decay rate from 299 to 314 s^{-1} is observed upon adding the liquid.

We have performed similar measurements of the decay rate of the R_2 line at a wavelength of 692.9 nm and found no difference in decay rate between the R_1 and R_2 lines. This agrees with the notion that at room temperature the R lines are expected to be in thermal equilibrium, due to the small energy difference of 29 cm^{-1}. We have also performed temperature dependent measurements of the PL intensity and PL decay rate (not

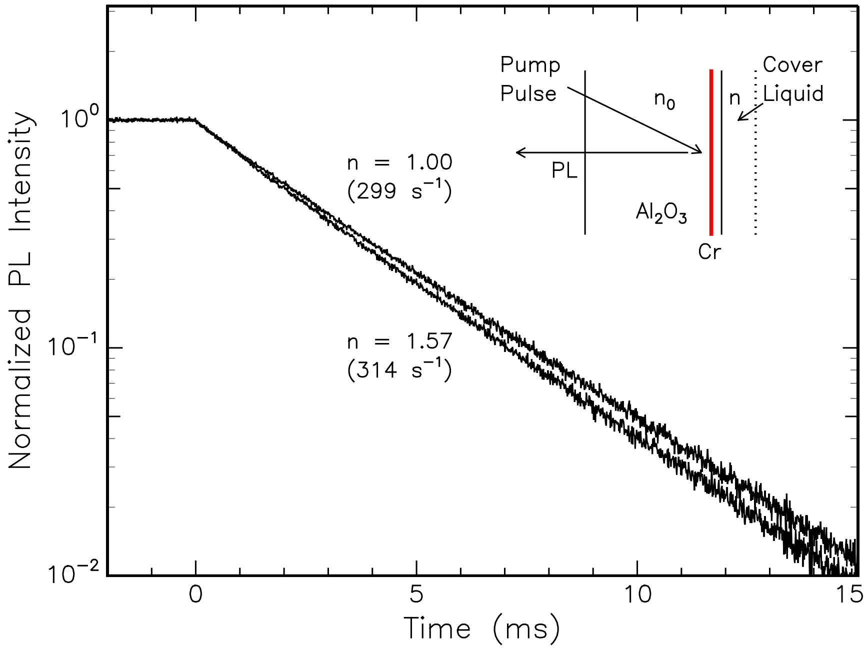

Figure 6.3: *Decay traces (λ = 694.3 nm) for a Al_2O_3 sample implanted with 3.0×10^{15} Cr cm^{-2} (annealed two hours at 1450 °C), measured in air and when in contact with 2-methoxy-4-propenylphenol (n = 1.57). The PL was collected from the back of the sample as shown in the inset. The curve measured in air (n = 1.00) shows a decay rate of 299 s^{-1}. An increase in the decay rate to 314 s^{-1} is observed if the sample is covered with the liquid. The 457.9 nm pump light is switched of at t=0.*

shown), which indicated that the R lines are in full thermal equilibrium for temperatures above 150 K as observed earlier [127].

Figure 6.4 shows measured decay rates for samples in air and brought in contact with liquids with refractive indices of 1.33, 1.45, 1.51 and 1.57, respectively. Decay rates were measured for samples implanted with 0.6, 1.6, 2.5, 3.0 and 4.0×10^{15} Cr cm^{-2} that were annealed at 1450 °C for 2 hrs. As can be seen the decay rate increases with refractive index of the liquid and, for a given index, the decay rate increases for increasing Cr concentration.

The increase with index can be explained by calculating the local optical density of states for the Cr ions close to the interface, where the presence of the liquid modifies the optical surrounding of the atom. Local field effects can play a role on length scales between wavelength and atomic scales. In our calculation we have assumed that the presence of the liquid at the interface does not affect the local field around the Cr ions [128, 129]. Since the outer 3d-shell of the Cr ion is involved in the optical transition, the transition frequency is determined by the field at the position of the atom and is extremely sensitive to the local field. In the experiment we did not observe spectral shifts or changes in the line shape, suggesting that the local field is not influenced by the liquids. This is also expected based on the relatively large distance between the Cr ions and the surface.

Using the dipole approximation, the spontaneous emission rate can be obtained from Fermi's Golden Rule [8, 110]:

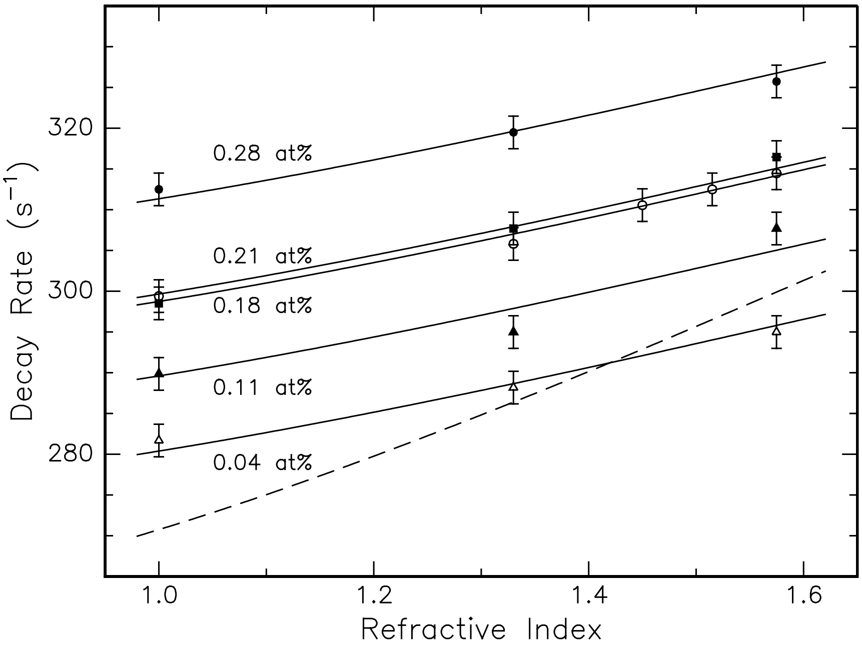

Figure 6.4: *Measured R line decay rate as a function of the refractive index of the covering liquid. Data are shown for samples with a Cr peak concentration of 0.04, 0.11, 0.18, 0.21 and 0.28 at.% annealed at 1450 °C for 2 hrs. The dashed line shows the calculated decay rate as function of refractive index of the liquid, based on the calculated optical LDOS, assuming purely radiative decay of 310 s^{-1} for bulk sapphire. The drawn line is a fit to all data points assuming a constant radiative decay rate for all samples independent of concentration but a different non-radiative decay rate for each sample.*

$$W_{rad}(z) = \frac{\pi\omega}{\hbar\varepsilon(z)}|D|^2\rho(\omega, z) \tag{6.2}$$

where D is the dipole matrix element of the ${}^2E \rightarrow {}^4A_2$ electronic transition at a frequency ω. ρ is the polarization- and angle-averaged LDOS [8, 111] at a distance z from the interface, and $\varepsilon(z)$ is the position-dependent dielectric constant. The matrix element D depends on the local environment of the emitting Cr ions and is not influenced by the optical properties of the interface or the presence of a liquid. Therefore the only parameter varied in our experiments is the LDOS $\rho(\omega, z)$ at a fixed frequency determined by the R line.

The radiative decay rate W_{rad} can be expressed more conveniently in terms of an optical LDOS $f_{1.76}$, which differs by a factor ε from the LDOS [43] introduced earlier. This optical LDOS is normalized to the LDOS for bulk Al_2O_3 with a refractive index of 1.76. The total decay rate $W(n, z)$ for a Cr ion at position z, with the sample covered by a liquid with index n, can now be written as:

$$W(n, z) = f_{1.76}(n, z)W_{rad}^{1.76} + W_{non-rad} \tag{6.3}$$

where $W_{rad}^{1.76}$ is the radiative decay rate in bulk Al_2O_3. The non-radiative decay rate is assumed to be independent of z and n.

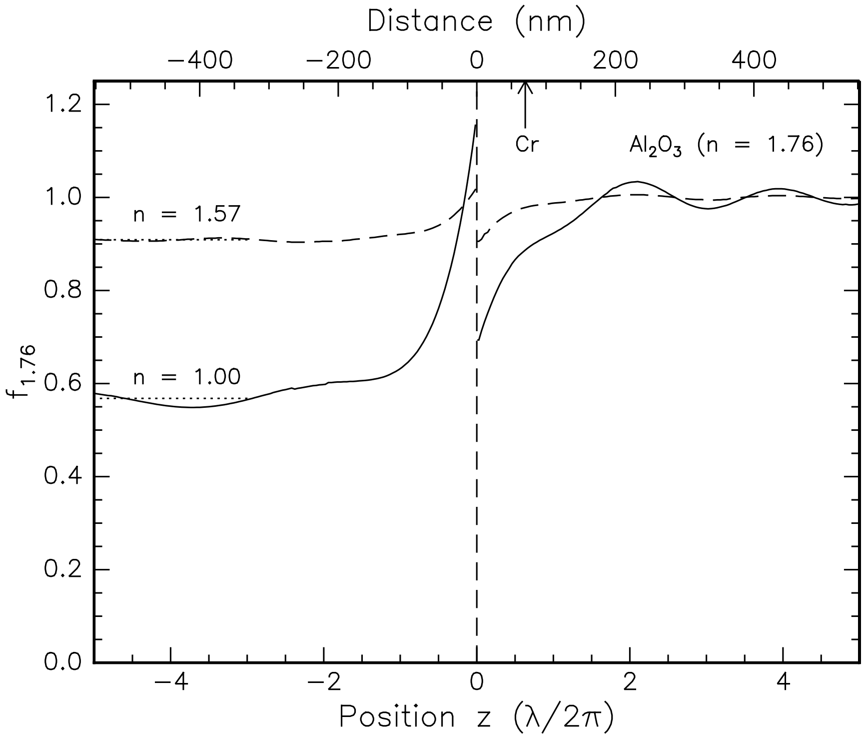

Figure 6.5: *Polarization- and angle-averaged optical LDOS $f_{1.76}$, as function of position, calculated for an Al_2O_3 sample in contact with air (n = 1.00, drawn line), and with a liquid of refractive index 1.57 (dashed line). The optical LDOS is normalized to the optical LDOS in bulk sapphire (n = 1.76). The position of the peak of the ion-implanted Cr distribution is indicated by the arrow.*

Figure 6.5 shows a calculation of the optical LDOS $f_{1.76}$ as a function of the distance z from the dielectric interface. The drawn line shows the result of a calculation for a system with an infinite half space of Al_2O_3 (n = 1.76) and an infinite half space of air (n = 1.00). We have neglected the effect of the Cr ions on the refractive index in our calculations, because for the highest Cr concentration of 0.3 at.% the change in refractive due to the Cr is less than 0.01. The interface is positioned at z = 0. The dashed line shows the calculation for Al_2O_3 in contact with a medium with a refractive index of 1.57, the highest value used in this experiment. In both cases, the optical LDOS is discontinuous at the interface due to a discontinuity in the E-field component that is parallel to the interface. The oscillations on both sides of the interface are caused by interference between incoming and reflecting waves and have a periodicity of $\sim \lambda/2n$. The position of the peak of the Cr distribution is indicated by the arrow. Figure 6.5 shows that the radiative decay rate is suppressed towards the interface compared to the bulk value. At the position of the Cr ions the rate increases for increasing refractive index of the liquid. This observation is supported by the data in Figs. 6.3 and 6.4.

To calculate the overall effect of the change in LDOS on the Cr decay rate, we integrated the effect of the optical LDOS over z using the measured Cr distribution from Fig. 6.1, for refractive indices in the range 1.00–1.76. The result of this calculation is shown by the dashed line in Fig. 6.4 assuming only radiative decay ($W_{non-rad} = 0$) and a radiative decay rate for bulk Al_2O_3 of 310 s^{-1}. Note that the latter is just a scaling factor

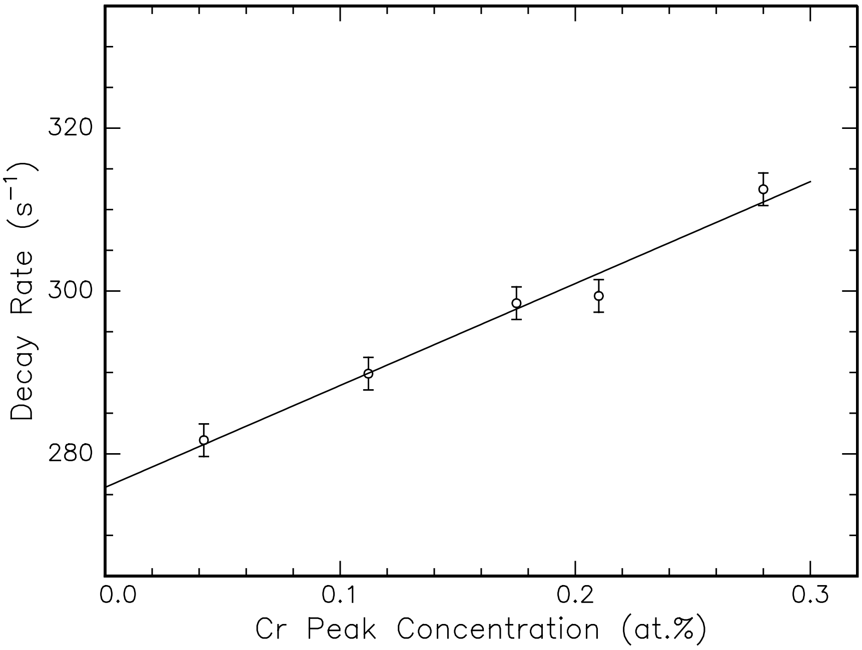

Figure 6.6: *PL decay rate as a function of Cr peak concentration, after annealing at 1450 °C for 2 hrs. The drawn line is a linear fit through the data. The extrapolated PL decay rate for zero Cr concentration is 276* s^{-1}.

in the calculation; in this example the value of 310 s^{-1} is chosen such that the calculated relative variation with refractive index can be compared to the data.

By comparing the dashed line in Fig. 6.4 with the measured data, which show a much weaker increase with n, it is clear that the data cannot be described by assuming radiative decay only. The data can be fitted if a non-radiative decay component, that is independent of the liquid refractive index n, is introduced as given by equation 6.3 [8]. The drawn lines show a single fit to all data in Fig. 6.4 assuming the same bulk radiative rate for all concentrations, but a different non-radiative rate for each sample. This results in $W_{rad}^{1.76}$=164±10 s^{-1} for the radiative decay rate in bulk sapphire. The radiative rate at the position of the implanted Cr ions is 143±10 s^{-1} and is lower than the bulk value due to the reduced LDOS near the interface. The non-radiative rates are 137±10, 146±10, 156±10, 155±10 and 168±10 s^{-1} for the samples implanted with 0.6, 1.6, 2.5, 3.0 and 4.0×10^{15} Cr cm^{-2} respectively, corresponding to internal quantum efficiencies ranging from 46% to 51% for bulk sapphire.

Fig. 6.6 shows the PL decay rate (measured in air) as a function of Cr peak concentration, after annealing at 1450 °C for 2 hrs. The decay rate increases linearly with Cr concentration, which can be explained by assuming an energy migration process between Cr ions that leads to non-radiative decay (“concentration quenching”) [130, 131]. Extrapolating the PL decay rate to zero Cr concentration, where no energy migration takes place, leads to a decay rate of 276±10 s^{-1}. This value is higher than the radiative decay rate of Cr ions near the interface as found above (143±10 s^{-1}). Note that reabsorption of the R line luminescence which could lengthen the observed decay, can be neglected for our samples due to their thin film geometry in combination with a small absorption coefficient (~10 cm^{-1}), as was observed earlier for Cr doped Al_2O_3 samples of different thickness [132]. We also note that PL spectra were identical for all Cr concentrations, suggesting that an increased Cr concentration does not change the local field, nor does it lead to significant Cr–Cr pair formation.

A possible explanation for this difference is the existence of non-radiative decay channels that are associated with defects remaining from the ion implantation, independent of Cr concentration. Alternatively, it could be that for concentrations lower than studied in Fig. 6.6 the decay rate does not depend linearly on Cr concentration and would in fact extrapolate to the measured value of W_{rad}. Such an effect was found earlier in Er implanted alkali-borosilicate glasses [130], where ion beam induced defects introduced additional non-radiative decay paths of which the density depends on the implanted fluence.

Our experimentally determined radiative decay rate of 164±10 s^{-1} is lower than the value of 250 s^{-1}, corresponding to a lifetime of 4.0 ms, reported in literature [127, 132]. This could be due to a difference in the local environment of the Cr in our ion-implanted samples compared to bulk sapphire doped with Cr ions using different methods. This observation is supported by the line broadening as observed in Fig. 6.2, which might be due to residual stress or defects that are not completely annealed out after implantation.

6.4 Conclusion

Ion implantation followed by thermal annealing can be used to dope a well-defined near-surface region of sapphire with optically active Cr^{3+} ions. Thermal annealing at 1450 °C is required to remove all implantation damage and leads to the incorporation of at least 95% of the Cr ions on a substitutional position, presumably in the Al sublattice.

Photoluminescence decay rates at a wavelength of 694 nm were measured in air, and as a function of refractive index for a range of transparent liquids (n = 1.33–1.57) covering the sample. The decay rate was found to increase with the refractive index of the liquid. From a comparison of the measured decay rates with calculations of the local optical density of states, the radiative decay rate was determined to be 164±10 s^{-1} independent of Cr concentration. A concentration-dependent non-radiative decay rate was found, that ranged from 137±10 s^{-1} for 0.04 at.% Cr to 168±10 s^{-1} for 0.28 at.% Cr. These well-characterized samples can now be used to probe the optical LDOS in more complicated photonic systems such as strongly absorbing media, scattering media or photonic crystals.

7

Erbium-implanted silica colloids with high luminescence quantum efficiency

Silica colloids with a diameter of 240–360 nm, grown by wet chemical synthesis using ethanol, ammonia, water, and tetra-ethoxy-silane, were implanted with 350 keV Er ions, to peak concentrations of 0.2–1.1 at.% and put onto a silicon substrate. After annealing at 700–900 °C the colloids show clear room-temperature photoluminescence at 1.53 μm, with lifetimes as high as 17 ms. By comparing data for different Er concentrations, the radiative lifetime is estimated to be 20–22 ms, indicating a high quantum efficiency of about 80%. This high quantum efficiency indicates that, after annealing, the silica colloids are almost free of –OH impurities.

7.1 Introduction

Integrated optics is becoming increasingly important in modern telecommunication technology. One important field of research is the study of rare-earth doped solid state planar optical amplifiers. Rare earth ions show sharp absorption and emission bands and relatively long luminescence lifetimes. Particularly the rare earth ion erbium (Er) is of interest due to its intra 4f-transition from the first excited state to the ground state around 1.53 μm ($^4I_{13/2} \rightarrow {}^4I_{15/2}$), which is one of the standard telecommunication wavelengths. Planar amplifiers have been realized based on rare earth doped silica, Al_2O_3, phosphate glasses, and $LiNbO_3$ [133, 134].

Polymer optical technology is an emerging field, and it is therefore interesting to fabricate Er-doped polymer waveguides. Organic rare earth complexes which can be dissolved in a polymer matrix [135–137] have been studied, but most of these complexes contain C–H bonds of which the second vibrational overtone can quench the rare earth luminescence [138, 139]. Therefore an alternative approach to encapsulate Er in a polymer is desired. Silica is an excellent host for rare earth ions yielding long luminescent lifetimes [140, 141]. A blend of polymer and small silica particles doped with erbium can be used as active medium.

Alternatively, erbium ions may be used as optical probe ions in silica colloidal crystals. Such colloidal crystals can be grown by self-assembly from highly monodisperse spherical SiO_2 particles. In this case, the colloidal crystal provides a host that has a periodic variation in refractive index. For a certain range of wavelengths, depending on the diameter of the spherical building blocks, Bragg reflection occurs. If an atom is placed inside such a crystal, the emission probability of that atom is influenced by the crystal. If a considerable amount of the total 4π solid angle is blocked by Bragg reflections in all directions, the emission can be strongly inhibited. This can be achieved only for large index contrasts. In these cases silica particles can still be used as impurities in crystals that have a larger index contrast, e. g. a crystal made from ZnS particles. However, before studying the emission of erbium ions from such complicated system, the influence of a single particle on the erbium emission should be characterized.

In this chapter we study the optical doping of colloidal silica particles with Er using ion implantation. The influence of Er concentration and anneal temperature on the luminescence intensity and lifetime is determined. It is found that the silica colloids are an excellent host for Er, yielding a quantum efficiency as high as 80%.

7.2 Sample preparation and characterization

Silica colloids with a diameter of 240 or 360 nm were synthesized as described by van Blaaderen et al. [98] Solutions of 10 ml ethanol, 0.7 ml NH_3 (28 wt.% in water), 0.8 ml H_2O and 0.4 ml tetra-ethoxy-silane (TEOS, 99%) were mixed and stirred for 1 hr at room temperature, resulting in the nucleation and growth of silica colloids with a diameter of 244 ± 10 nm, as measured using scanning electron microscopy (SEM). In one set of samples, the diameter of the spheres was increased to 360 nm by subsequent addition of TEOS to the reaction vessel [142]. After the reaction, the suspension was centrifuged and the remaining colloids were dissolved in pure ethanol. Droplets of the solution were then put onto a silicon substrate or a microscope cover glass (cleaned with a 1 M KOH in ethanol solution). After evaporation of the ethanol, a thin layer of colloids remained. Next, the samples were irradiated with 350 keV Er ions at various fluences ranging from 0.9×10^{15} to 5.5×10^{15} ions cm^{-2}. The projected range of 250 keV Er in silica is 160 nm. Implantation of these ion fluences into a planar film would result in a Gaussian Er distribution with a full width at half maximum (FWHM) of 34 nm. It is obvious that in these non-uniform, colloidal layers a less well-defined concentration profile builds up. After implantation the samples were annealed in vacuum at 100 °C for one hour and then for another hour at different temperatures in the range 700–1000 °C.

In order to study the Er incorporation in the colloids, Rutherford backscattering spectroscopy (RBS) measurements were performed, using a 2 MeV He^{+} beam at a scattering angle of 165°. Scanning electron microscopy (SEM) was performed at an electron energy of 10 keV. Photoluminescence (PL) measurements were performed using the 488 nm and 515 nm lines of an Ar ion pump laser at a power density of 50–60 mW mm^{-2} for excitation. The laser beam was modulated with an acousto-optic modulator. The PL signal was focused into a 48 cm monochromator and detected with a liquid-nitrogen-cooled Ge detector, using standard lock-in techniques, yielding a spectral resolution of 6 nm. Lifetime measurements were performed by monitoring the decay of the luminescence after switching off the light source. A digitizing oscilloscope was used to average the decay curves. Optical transmission measurements were performed at normal incidence using a spectrometer at wavelengths ranging from 300–1700 nm.

Figure 7.1 shows an RBS spectrum of a Si sample covered with a single layer of 360 nm diameter colloids, implanted with 9×10^{14} Er cm^{-2}. The dashed line shows an exact simulation of a single layer of 360 nm diameter colloids covering about 45% of the surface, treating the colloids as if they are submerged into the Si substrate [143, 144]*. For reference, a simulation for a 360 nm pure SiO_2 layer on a Si substrate is shown (dashed-dotted line). The surface channels of Er, Si and O are indicated by the arrows. The Si content at the surface is almost similar to the Si content in pure SiO_2, indicating that the substrate is almost completely covered with colloids. The Si yield then increases with decreasing energy, as a result of the spherical shape of the colloids. The Si yield coincides with that of the simulation at channel 245, consistent with the colloid diameter of 360 nm. The signal between channel 400 and 500 is due to the implanted Er. The peak concentration is 0.18 at.%. Note that a small fraction of the implanted Er has entered the Si substrate, as is evident from the Er tail near channel 400. The inset in Fig. 7.1 shows a SEM image of the deposited colloids (360 nm diameter), showing a rather unordered array of particles extending over several layers. To our knowledge, this is the first report of using RBS to measure the coverage, composition and doping of colloidal particles on a planar substrate.

The samples used for PL measurements consisted of about 3–4 layers of silica colloids, as determined from RBS simulations and SEM. The implantation and annealing caused no deformation of the silica spheres. Figure 7.2 shows the PL spectrum of colloidal silica particles implanted to a peak concentration of 1.1 at.% and annealed at 950 °C for 1 hr. The spectrum shows typical Er^{3+} luminescence around 1.53 μm due to transitions from the $^4I_{13/2}$ to the $^4I_{15/2}$ level. The two peaks result from Stark splitting of the Er^{3+}

---

[*] A spherical particle on a substrate can be described by a depth distribution $C(z)$ of the form $C(z) \propto \sqrt{f(1-(z/d)^2)}$, where d is the sphere diameter and f is the fraction of the surface covered by the spherical particles ($f \leq 0.74$). Incorporating this as an impurity distribution leads to a good approximation of the RBS spectrum.

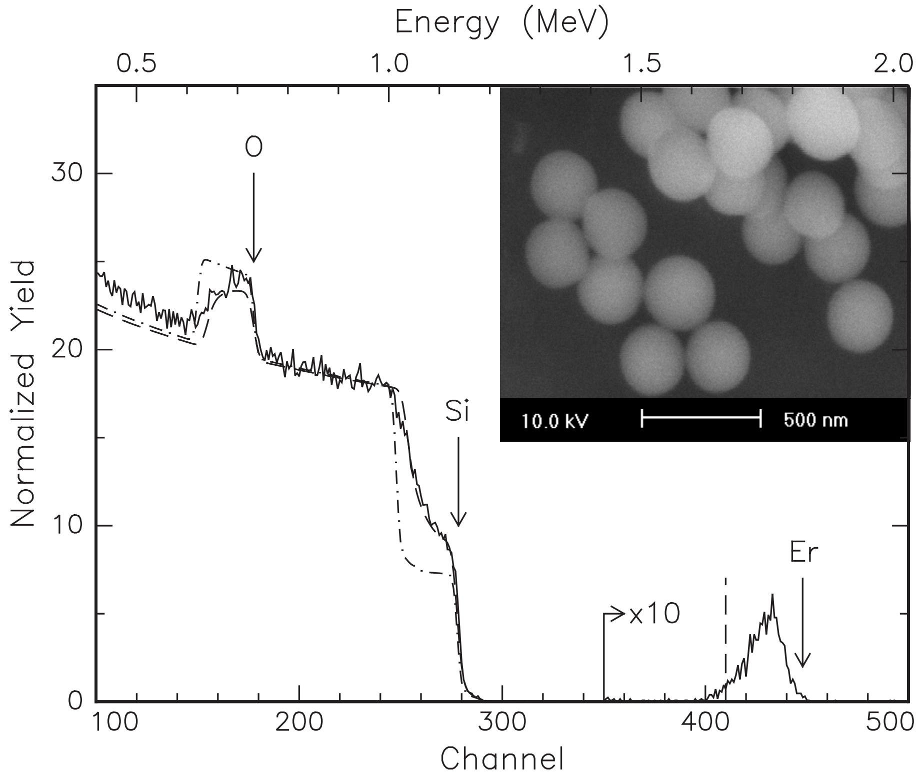

Figure 7.1: *RBS spectrum of a single layer of Er-implanted (350 keV, 9×10^{14} Er cm^{-2}) silica colloids on a Si substrate (drawn line). A 2 MeV He^+ beam was used at a scattering angle of 165°. The dashed line shows a simulation of a single layer of 360 nm diameter colloids covering about 45% of the surface. A simulation of a planar 360 nm thick SiO_2 film on a silicon substrate (dashed dotted line) is shown for reference. The dashed line at channel 410 indicates the position of the SiO_2/Si interface for Er. The inset shows a SEM image of the colloids on the sample.*

levels and are characteristic for Er^{3+} in SiO_2 [133]. The width (32 nm FWHM) is due to the thermal distribution over the Stark levels and homogeneous and inhomogeneous broadening. It is difficult to compare PL intensities for different implanted samples as the colloid coverage varies from sample to sample, and because of the fact that the pump beam is strongly scattered by the silica spheres, which results in non-uniform pumping. However, on average the intensity increases for increasing doping concentration up to at least 1.1 at.%.

7.3 Annealing behavior

Figure 7.3(a) shows the peak PL intensity of samples implanted with 0.2 at.% Er, annealed at various temperatures for 1 hr. Below 700 °C, no measurable PL was observed. This might be due to water that is physisorbed on the surface or trapped in the pores of the silica matrix. Water is known to quench the Er^{3+} luminescence, as the first overtone of the O–H vibration (E_0 = 3400 cm^{-1}) is strongly resonant with the Er^{3+} transition (E = 6500 cm^{-1}). Indeed, work by Fan et al. [145] and Tien et al. [146] on bulk silica samples, grown in a similar way as the colloids, shows that between room temperature and 200 °C, weakly

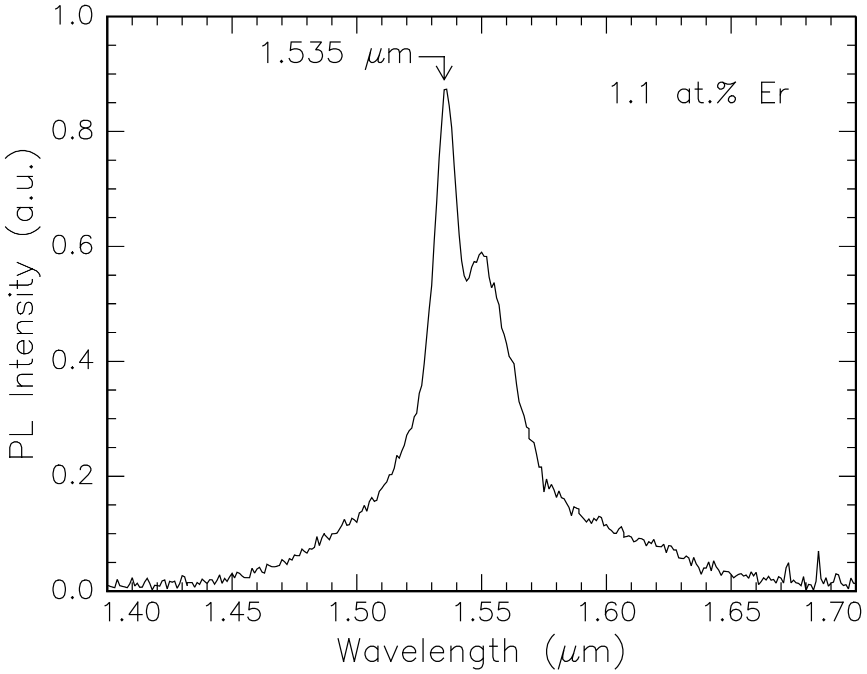

Figure 7.2: *Photoluminescence spectrum for a thick layer of colloids, implanted with Er (1.1 at.%), taken using 515 nm pump light at a power of 60 mW/mm^2.*

bound water and residual organic molecules vaporize, followed by the removal of chemically bound molecular water between 300 and 800 °C. Figure 7.3(a) shows a large scatter in the data above 700 °C, but the general trend is a decrease in PL intensity, certainly for temperatures above 900 °C. This may be due to the precipitation of Er, as has been observed before in Er implanted SiO_2 [140]. Figure 7.3(b) shows luminescence lifetime measurements as a function of anneal temperature for an Er^{3+} concentration of 0.2 at.%. For anneal temperatures below 700 °C the PL intensity was too low to perform lifetime measurements. The lifetime for anneal temperatures between 750 and 1000 °C is about 17 ms and is almost independent of anneal temperature. We have also performed lifetime measurements for samples implanted at higher doses, and found that increasing the Er concentration from 0.2 to 1.1 at.% results in a decrease in the luminescence lifetime from 17 to 10 ms. These lifetimes are among the highest observed in silica glass. Assuming that the decrease in lifetime is due to concentration quenching, we can estimate the radiative lifetime by linearly extrapolating to zero Er concentration and find τ_{rad} = 20–22 ms [130]. The long lifetimes observed in this work show that the silica glass made by wet chemical synthesis is an excellent host for Er. It indicates that the water impurity content in this glass after annealing is very small ($<$ 1 ppm) [130]. We note that the long radiative lifetime can be partly attributed to the fact that the Er-implanted colloids are partly surrounded by air, causing the local optical density of states in the colloids to be lower than that of bulk SiO_2 [8, 103]. To test this idea, we have deposited 0.2 at.% Er-implanted colloids on a Si substrate (n = 3.45). Indeed, they show a reduced luminescence lifetime of about 12 ms.

Two months after the first PL measurements on the Er-implanted colloidal particles, we performed the same measurements again and found that the luminescence intensity

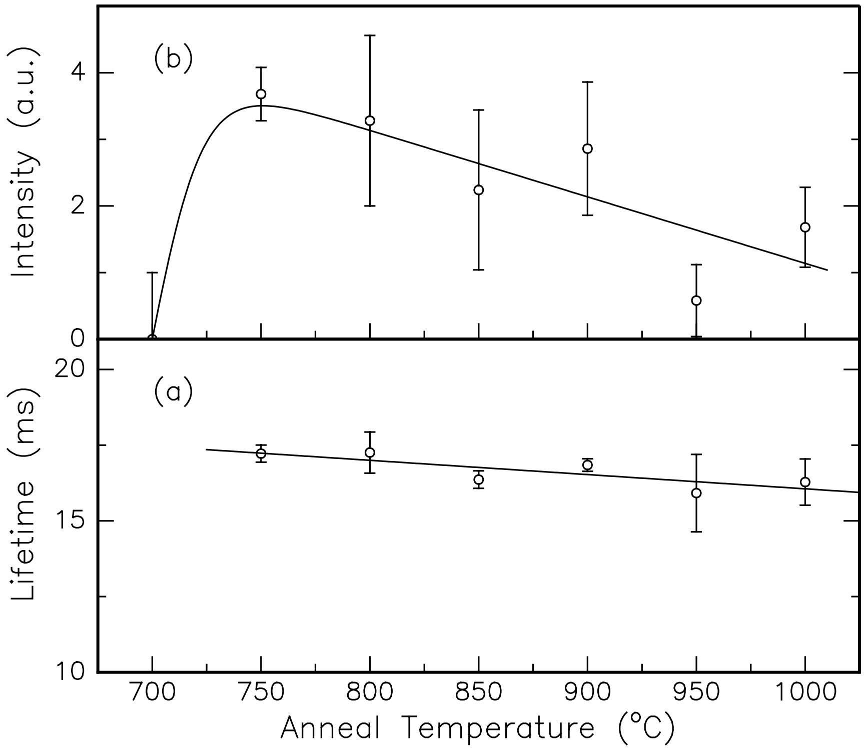

Figure 7.3: *(a) Average peak photoluminescence intensity at 1.535 μm as a function of anneal temperature for Er-implanted silica spheres (0.2 at.%). Pump wavelength 488 nm, pump power 50 mW. The large error bars are due to the large variation in colloid coverage over the surface. (b) Luminescence lifetime of Er-implanted silica spheres (0.2 at.%) as a function of anneal temperature.*

and lifetime were strongly reduced. After annealing at 475 °C, both the luminescence intensity and lifetime returned to the level observed after the initial anneal. This suggests that some time after the anneal, a thin film of water covers the colloids, this can be avoided by coating the silica spheres with a protective layer, e. g. a polymer.

7.4 Conclusions

Silica colloids on a planar Si substrate were implanted with Er ions to peak concentrations in the range 0.2–1.1 at.%. RBS was used for the first time to identify colloid coverage, composition and impurity content. Room temperature luminescence at 1.5 μm is observed from Er-implanted silica colloidal spheres. Thermal annealing at 750 °C is required to optimize the PL. The luminescence lifetime of Er is about 17 ms, and the quantum efficiency 80% for an Er concentration of 0.2 at.%.

8

Concentration quenching and local density of states in erbium-doped SiO_2 spherical colloids

Spherical SiO_2 *colloids with two different diameters (175 nm, 340 nm) were doped with erbium at different concentrations. The spheres show sharply peaked photoluminescence centered at 1.535* μ*m, due to intra-*$4f$ *transitions in* Er^{3+}*. From measurements of the Er decay rate for different Er concentrations the decay rate of isolated Er ions (i. e. in absence of concentration quenching) was determined for the two colloid diameters. The data were compared to spontaneous emission rates derived from calculations of the local optical density of states in the colloids. The calculation predicts a large difference in the spontaneous emission rate for both colloid sizes (61* s^{-1} *vs. 40* s^{-1}*), in perfect agreement with the measured data.*

8.1 Introduction

Erbium-doped dielectric materials find many applications in optical components, due to their sharp optical emission at 1.5 μm, the standard wavelength in optical telecommunications technology. Recently, Er-doped colloids [101] and microspheres [147] are being investigated. Small ($\sim$100 nm diameter) colloids can find applications in novel nanocomposit materials that can be used to fabricate a polymer optical amplifier, [148] while larger colloids or microspheres ($>$10 μm) can be used to fabricate whispering gallery mode lasers operating at 1.5 μm. Optically active colloids can also find applications as probes in photonic crystals, in which they can be used to probe the (local) optical density of states.

Two important parameters determine the gain performance of Er-doped colloids: the stimulated emission cross section and the emission quantum efficiency. The Er^{3+} intra-4f transitions at 1.53 μm are in principle forbidden by the parity selection rule, but mixing with other-parity states makes them slightly allowed. Hence, the transitions have a relatively small optical cross section, and consequently, the excited state of Er^{3+} has a long luminescence lifetime.

For a given material, a measurement of the luminescence lifetime can be made relatively easily, thus providing a quick identification of the emission cross section. However, in practice the lifetime is not only determined by radiative emission, but also by non-radiative processes such as multiphonon relaxation, coupling to defects, or interactions between Er ions [131, 149], that can all quench the excited state. Furthermore, the radiative emission rate is not a fixed property for a given material, but depends on the optical surrounding of the Er ions. For example, the presence of dielectric boundaries changes the local electric field fluctuations and modifies the spontaneous emission rate [8, 103]. Changes in decay rate can be determined by calculating the local optical density of states (LDOS) and then applying Fermi's Golden Rule. The radiative decay rate can then be written in terms of a local LDOS $\rho(\omega, r)$ as:

$$W_{rad}(\mathbf{r}) \;=\; \frac{\pi\omega}{\hbar\varepsilon(\mathbf{r})}|D|^2\rho(\omega,\mathbf{r}), \tag{8.1}$$

where $\varepsilon(r)$ is the position-dependent dielectric constant, ω is the transition frequency and $|D|^2$ the dipole matrix element of the transition involved. This matrix element is determined by the interaction of Er^{3+} ions with the coordinating matrix, while the macroscopic $\rho(\omega, r)$ and $\varepsilon(r)$ are determined by the optical surroundings.

In this Chapter, we study the modified spontaneous emission of Er ions implanted into spherical SiO_2 colloids. In such small particles, there is a strong interaction between excited Er ions and the colloid-air interface. Using a combined analysis of concentration quenching phenomena and LDOS effects in colloids with two different diameters, we are able to determine absolute values of the radiative and non-radiative decay rates. We find that the spontaneous emission rate for the two sizes differs by 50% and determine the emission cross section.

8.2 Concentration quenching

SiO_2 colloids with a diameter of either 175 or 340 nm (±5%) were made in a reaction between tetra-ethoxy-silane, ammonia, ethanol and water as described in Ref. [98]. The

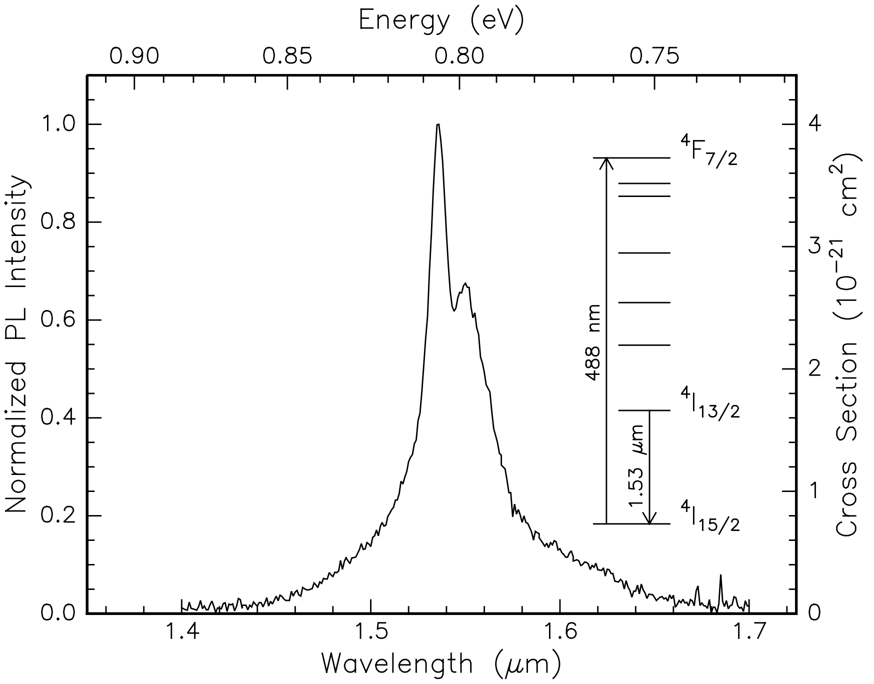

Figure 8.1: *PL spectrum of Er-implanted SiO_2 colloids (340 nm diameter, 0.2 at.% Er), measured at room temperature under 488 nm excitation.*

spheres were deposited on Si(100) substrates that were cleaned for 15 min. in a 1.0 M KOH solution in ethanol. A droplet of the spheres dissolved in ethanol was put on the substrate and the ethanol was let to evaporate. The 175-nm SiO_2 colloids were implanted at room temperature with 70 keV Er^+ ions to fluences of 3.4×10^{14} ions cm^{-2} or 9.1×10^{14} ions cm^{-2}. The ion range of 70 keV Er in silica is r = 48 nm, and the straggle σ = 11 nm. The Er peak concentration is 0.2 or 0.5 at.% for the two fluences, respectively. The 340-nm colloids were implanted with 350 keV Er^+ ions (r = 160 nm, σ = 34 nm) at fluences of 9.0×10^{14}, 2.5×10^{15}, or 4.0×10^{15} ions cm^{-2} (peak concentrations 0.2, 0.5 or 0.8 at.%). After implantation the samples were annealed in a vacuum furnace (pressure $< 5\times10^{-7}$ mbar) at 100 °C for 1 hr and at 900 °C for another hour. A scanning electron microscopy (SEM) image of the 340 nm-diameter colloids can be found in Fig. 9.1.

Photoluminescence (PL) measurements were performed using excitation with the 488-nm line of an Ar ion laser. The pump beam was modulated at 13 Hz using an acousto-optic modulator. The PL signal was focused onto the entrance slit of a 48-cm grating monochromator and detected with a liquid-nitrogen cooled Ge detector employing standard lock-in techniques. The spectral resolution of the system was 6 nm. PL decay traces of the luminescence were recorded at the peak of the Er luminescence at 1.535 μm and averaged using a digitizing oscilloscope. The overall time response of the system was measured to be 30 μs. All decay traces showed single-exponential behavior.

Figure 8.1 shows a PL spectrum of 340-nm colloids implanted to a peak concentration of 0.2 at.% Er. The Er ions are excited into the $^4F_{7/2}$ level as shown in the inset. The emission is due to transitions from the first excited state ($^4I_{13/2}$) to the ground state ($^4I_{15/2}$), peaking at a wavelength of 1.535 μm. Figure 8.2 shows PL decay rates measured as a function of Er peak concentration for both the 175-nm colloids (open circles) and the

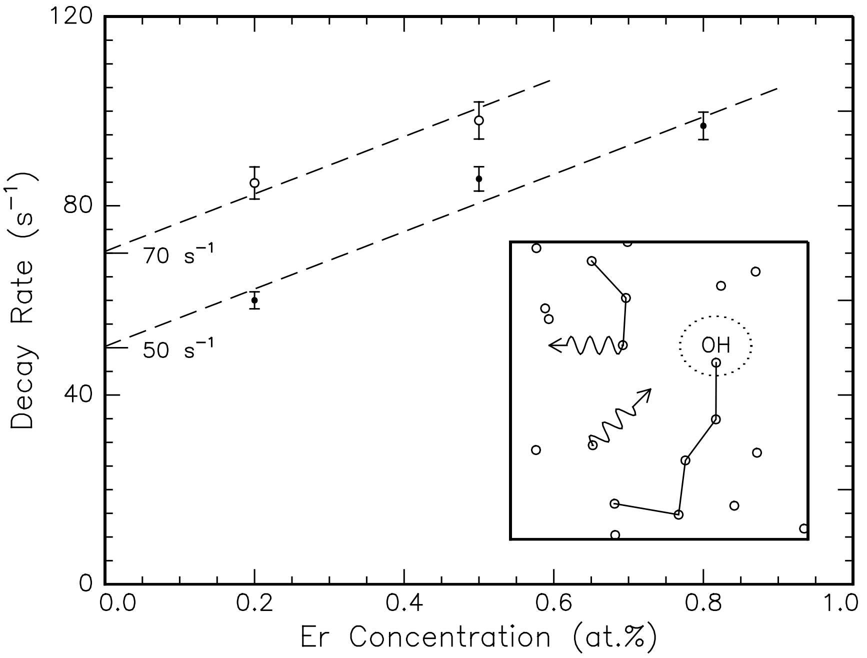

Figure 8.2: *PL decay rates measured at 1.535 μm for Er implanted colloids as function of Er peak concentration. Data are shown for 175-nm colloids (open circles) and 340-nm colloids (closed circles). The dashed lines are fits to the data according to Eq. 8.1 assuming an identical slope for both data sets, but different vertical offsets. The inset shows a schematic of the concentration quenching process: excitation migration among Er ions followed by quenching at an –OH impurity.*

340-nm colloids (closed circles). For both diameters the PL decay rate increases with Er concentration, an effect that is generally known as concentration quenching [130, 131]. It is due to an increased coupling to quenching sites as a result of excitation migration at high Er concentration (see inset in Fig. 8.2). For example, in silica glasses it is well known that small quantities of –OH impurities can act as a quencher for excited Er. This is due to the fact that the first overtone of the O-H stretch vibration is resonant with the $^4I_{13/2} \rightarrow ^4 I_{15/2}$ transition in Er^{3+}. For low quencher concentration, the decay rate can be written as:

$$W = W_{rad} + W_i + 8\pi C_{Er-Er}[Er][Q] \tag{8.2}$$

with W_{rad} the radiative rate, W_i the internal non-radiative rate e. g. due to multiphonon relaxation or coupling to defects, C_{Er-Er} a coupling constant, and $[Er]$ and $[Q]$ the Er and quencher concentration, respectively. The dashed lines in Fig. 8.2 are fits using Eq. 8.2, assuming the same slope but a different offset for each type of sample. The fact that both data sets can be described by the same slope indicates that the quencher concentration in 175-nm and 340-nm colloids is the same, which is expected, as the fabrication procedure for the two sizes is similar. Using a typical value for C_{Er-Er} from the literature (10^{-39} cm^6 s^{-1}) [150] we find a quencher concentration of 100 ppm. Assuming the dominant quencher is –OH this is a reasonable value, as the colloids were prepared in a wet-chemical reaction.

The vertical intercepts of the fits in Fig. 8.2 represent the Er decay rates in the ab-

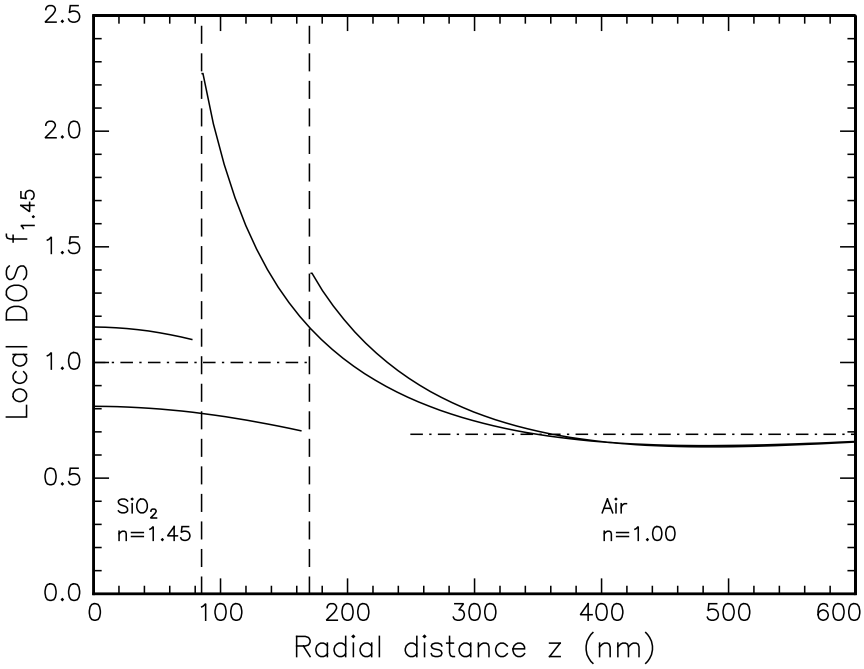

Figure 8.3: *Polarization-averaged local optical density of states as function of radial position for SiO_2 colloids (n = 1.45) in air (n = 1.00), calculated at a vacuum wavelength of 1.535 μm. Data are shown for colloid diameters of 175 nm and 340 nm.*

sence of concentration quenching (W_{rad}+W_i): they are 70.4 s^{-1} (14.2 ms) and 50.3 s^{-1} (19.9 ms) for 175-nm and 340-nm colloids respectively, and are listed in Table 8.1 under $W_{tot}^{[Er]=0}$. These rates can now be compared to calculated values of W_{rad} that can be derived as described below.

8.3 Local density of states

Figure 8.3 shows a calculation of the local optical density of states (LDOS) in spherical silica colloids, calculated using a Green's function approach [40]. The factor $\varepsilon(r)$ is included in the definition of the LDOS (see Eq. 8.1), making the LDOS directly proportional to the radiative decay rate. Since the polarization of the emitted radiation is randomly oriented, due to the amorphous structure of the silica glass network, integration over both polarizations is done.

In Fig. 8.3, the local LDOS is plotted for a vacuum wavelength of 1.535 μm as a function of radial distance for the two different colloid diameters. The colloids (refractive index n = 1.45) are surrounded by air (n = 1.00), and the LDOS is normalized to the LDOS in bulk silica (defined as $f_{1.45}$ = 1). As can be seen, the value of the LDOS inside the colloid differs strongly between spheres of different size. Depending on the size, the LDOS is smaller or larger than the LDOS for bulk SiO_2. For a given size, not much variation in the LDOS is observed inside the sphere. This can be explained by the fact that for both colloid sizes $2\pi r \leq \lambda_0/n$ (with r the colloid radius), hence no Mie resonances are observed. Assuming that the Er ions are distributed homogeneously over the SiO_2 sphere, the effect of the sphere on the radiative rate can be calculated by integrating the

Table 8.1: *Measured and calculated Er luminescence decay rates for two different colloid diameters (175 nm, 340 nm).*

Colloid diameter	$f^i_{1.45}$	$W_{tot}^{[Er]=0}$ (s^{-1})	W_{rad} (s^{-1})	$W_i^{[Er]=0}$ (s^{-1})
175 nm	1.13	70	61	9
340 nm	0.74	50	40	10

LDOS in Fig. 8.3 over the sphere volume. For a 175-nm sphere the calculation yields $f_{1.45}$ = 1.13, while for a 340-nm sphere a value of $f_{1.45}$ = 0.74 is found. These data are also listed in Table 8.1.

Using these two LDOS factors, the radiative rates in the colloids can be calculated, using as input the radiative rate of Er in bulk SiO_2 (54±10 s^{-1}) that we have previously determined (see Chapter 9) [151]. An identical rate (55±5 s^{-1}) was derived from our analysis of data by Vredenberg et al., [152] also described in Chapter 9 [151]. From the fact that the PL spectrum for the colloids in Fig. 8.1 is identical to that of the Er-implanted SiO_2 in our previous work [151] we conclude that the local environment in both materials is similar, and that therefore the bulk decay rate of 54 s^{-1} can also be applied to the silica glass used for the colloids. Multiplying this decay rate with the LDOS factors of 1.13 and 0.74 found above gives the purely radiative decay rate in the two types of colloids: W_{rad} = 61 s^{-1} (175-nm spheres) and W_{rad} = 40 s^{-1} (340-nm spheres). These data are summarized in Table 8.1. The Fuchtbauer-Ladenberg equation relates the radiative rate to the cross section; i. e.

$$W_{rad} = \frac{8\pi n^2}{c^2} \int \nu^2 \sigma(\nu) \mathrm{d}\nu, \tag{8.3}$$

where n is the host refractive index (n = 1.45), c is the speed of light and n is the optical frequency of the transition involved. Using the radiative rate for Er in bulk SiO_2 and Eq. 8.3 we can derive a peak cross section of 4.0×10^{-21} cm^2. This value was used to provide a cross-section scale in Fig. 8.1.

Several conclusions can be drawn by comparing these numbers with the data in Fig. 8.2. First, the vertical separation between the two linear curves through the data for the two types of colloids is equal to 20±5 s^{-1}, which is identical to the difference between the radiative rates calculated above (21 s^{-1}). This provides clear evidence that the data can be consistently described by the LDOS model. Second, subtracting for the two colloid diameters the measured decay rate in absence of concentration quenching ($W_{tot}^{Er=0}$) from the calculated radiative rate (W_{rad}) (see Table 8.1), we find the intrinsic non-radiative decay rate; it amounts to 9 s^{-1} or 10 s^{-1} for the 175-nm and 340-nm colloids respectively (see Table 8.1). The relative error on these values is ±5 s^{-1}, the absolute error ±10 s^{-1}. These values are consistent with the fact that identical intrinsic non-radiative decay rates are expected for both colloid diameters as they are fabricated in an identical way. This again shows that the data in Fig. 8.2 can be consistently described by the LDOS model.

Finally, we determine the luminescence quantum efficiency (QE) of excited Er. Although the QE has a relatively large error bar (± 10-20%) due to the uncertainty in W_i, it can be concluded that 1) in absence of concentration quenching the QE is on the order of 80%, 2) the 175-nm colloids have larger QE than the 340-nm colloids, and 3) increasing the Er concentration from zero to e. g. 0.5 at.% reduces the quantum QE by some 20%.

8.4 Conclusion

In conclusion, we have doped silica colloids with optically active Er ions emitting at 1.535 μm. Photoluminescence decay measurements as a function of Er concentration are consistent with a concentration quenching model that simultaneously fits the data for both colloid sizes. From the data, the Er decay rate in absence of concentration quenching was determined. This decay rate was compared with the radiative decay rate derived from calculations of the local optical density of states (LDOS) in the colloids. The LDOS calculation predicts a large difference in the radiative decay rate for both sizes (61 s^{-1} vs. 40 s^{-1}), in perfect agreement with the measured data. This Chapter shows that by careful consideration of changes in the local LDOS it is possible to achieve an accurate quantitative determination of radiative and non-radiative decay processes of Er in silica glass.

9

Local optical density of states in SiO_2 spherical microcavities: theory and experiment

The local optical density of states (LDOS) in 340 nm diameter SiO_2 spherical microcavities was calculated and probed experimentally by measuring the luminescence decay rate at 1.54 μm of erbium ions implanted in the colloids. To separate the effect of non-radiative processes, first the radiative decay rate of Er^{3+} in bulk SiO_2 was determined. This was done by varying the LDOS in an Er doped planar SiO_2 film by bringing the film into contact with liquids of different refractive index in the range n = 1.33–1.57. By comparing the calculated LDOS with the observed changes in decay rate with index the radiative rate was found to be 54±10 s^{-1} (τ = 18±3 ms) in bulk SiO_2. This value was then used to analyze the difference in decay rate in colloids surrounded by air or immersed in an index matching liquid. Within the experimental error, agreement was found between the calculated and experimentally probed LDOS in the colloids. Finally, a full determination of the LDOS in larger ($2\pi R/\lambda$ = 0.1–6.9) SiO_2 microcavities is presented, which shows the appearance of a number of maxima, corresponding to the position of the electric type resonances inside the microcavity.

9.1 Introduction

The spontaneous emission rate of an atom is not a property of the atom only, but depends on the local optical surrounding as well. Recently, there has been a growing interest in the use of dielectric structures such as microcavities and photonic bandgap materials, to modify the rate of spontaneous emission. Such modifications were observed for Rydberg atoms [153, 154], for atoms placed in microcavities [152, 155, 156], in thin films [157], close to a mirror or dielectric interface [6–8, 158], in liquid microdroplets [159–161] and photonic crystals [42, 162, 163].

The changes in decay rate can be determined by calculating the local density of states (LDOS) and then applying Fermi's Golden Rule to obtain the radiative decay rate. It has been shown that the radiative decay rate is proportional to this LDOS, both in a scalar approximation [43] and for the full Maxwell equations [106, 164]. For relatively simple geometries the LDOS can be calculated using either a full set of eigenfunctions of the Helmholtz wave equation [108–110] or by using Green's functions [40, 165]. Luminescent ions can be used to experimentally probe the LDOS. In general, the measured changes in decay rate cannot be compared directly to theoretical results because non-radiative processes that occur parallel to the radiative decay must be taken into account. Therefore, in an experimental determination of the LDOS, accurate and reproducible methods are needed so that the non-radiative and radiative decay rates can be determined independently.

Trivalent rare-earth ions are excellent candidates to probe the LDOS, since the optical transitions occur in the visible and near-infrared part of the spectrum and they have excited state lifetimes in the millisecond range with high quantum efficiencies [7, 8, 101]. The transition frequency is almost insensitive to the host material and resembles that of the free ion, due to the fact that the optical transitions take place in the 4f shells that are shielded from interactions with the host material by the 5s and 5p electrons. Ion implantation of rare-earth elements can be used to put the atoms at a well-defined depth in almost any host material [133].

In this Chapter, we study the radiative decay rate of optically active Er^{3+} ions incorporated in SiO_2 colloidal spheres, which serve as small spherical microcavities. To separate radiative and non-radiative components in the decay, experiments were also done on an erbium implanted SiO_2 thin film on a silicon substrate. By changing the LDOS in the film by bringing it in contact with liquids with different refractive indices, and monitoring the change in the decay rate of the erbium ions, the radiative and non-radiative decay rates of Er^{3+} ions in bulk SiO_2 were determined. This resulted in the first experimental determination of the radiative decay rate of Er^{3+} in pure SiO_2. These data were then used to analyze experimentally observed changes in decay rate for Er^{3+} doped SiO_2 colloids upon immersing the colloids in an index matching liquid. A large effect is observed if the Er^{3+} is incorporated in a 340 nm diameter spherical microcavity, which is fully attributed to the variation in LDOS in the microcavity.

9.2 Experiment

SiO_2 colloidal spheres were made using a wet chemical reaction from tetra-ethoxy-silane (TEOS), ethanol, ammonia and water. The sphere diameter obtained was 340 nm at a size-polydispersity of 5%. The colloids were deposited on Si(100) substrates that were cleaned for 15 min in a 1.0 M KOH solution in ethanol and rinsed in pure ethanol before use. A droplet of the spheres dissolved in ethanol was put on the substrate, and the ethanol was let to evaporate, leading to the formation of 3–4 layers of stacked spheres.

A SiO_2 layer of 100 nm thickness was grown on a Si(100) substrate in two consecutive steps using a reaction mixture of TEOS, ethanol, ammonia and water; a process described in detail in Chapter 5. The substrates were put into the reaction mixture and the layer was grown for 2 hrs under continuous stirring of the mixture. Details of the synthesis procedure and characterization of the layers and the spheres are published elsewhere [90–93, 142].

The 100 nm thick SiO_2 film was implanted with 70 keV Er^+ ions to fluences of 3.4×10^{14} ions cm^{-2} and 9.1×10^{14} ions cm^{-2} at room temperature. The 340 nm diameter spheres were implanted with 350 keV Er^+ ions to fluences of 0.9×10^{15} and 2.5×10^{15} at cm^{-2}. Both implantation conditions were chosen to lead to the same nominal Er peak concentrations of 0.2 and 0.5 at.%. After implantation all samples were annealed in a vacuum furnace (pressure $\leq5\times10^{-7}$ mbar) at 100°C for 1 hr and at 900°C for 1 hr. Rutherford backscattering spectrometry (RBS) measurements were done using a 2 MeV He^+ beam incident along the surface normal at a scattering angle of 83.8°.

Scanning electron microscopy (SEM) images of the colloids were taken using 5 keV electrons at a resolution better than 5 nm. Photoluminescence (PL) spectra were obtained using the 488 nm line of an Ar ion laser as a pump source. The pump beam was modulated at a frequency of 13 Hz using an acousto-optic modulator. The PL signal was focused onto the entrance slits of a 96 cm grating monochromator and detected by a liquid nitrogen cooled Ge detector employing standard lock-in techniques. The spectral resolution of the system was 6 nm. PL decay traces of the luminescence were recorded at the peak of the Er^{3+} luminescence at 1.536 μm and averaged using a digitizing oscilloscope. The overall time response of the system was measured to be 30 μs. Transparent liquids of different refractive index (n = 1.33 to 1.57) were brought into contact with the sample surface, while the luminescence signal was collected from the (unpolished) back-side of the Si substrate. Since silicon is transparent for wavelengths longer than 1.1 μm, the Er^{3+} luminescence around 1.54 μm can be collected without difficulties. The pump laser beam was directed onto the sample surface through the liquid films. The liquids used in our experiments are water (n = 1.33), a microscope immersion oil (Merck, according to DIN 58884, n = 1.51) and iso-eugenol (n = 1.57). An index matching liquid (n = 1.45) was prepared by mixing water and ethylene glycol in the right proportions.

9.3 Results and discussion

9.3.1 Synthesis and photoluminescence

Figure 9.1 shows a SEM image of the 340 nm silica colloids. A layered structure composed of 3–4 layers can be determined from the SEM image. The layer thickness was found more accurately in Rutherford backscattering spectrometry (RBS) measurements [101]. RBS spectra of the SiO_2 film implanted with 70 keV Er ions are shown in Fig. 9.2 showing a Gaussian Er depth distribution peaking at a depth of 39 nm with a standard deviation σ = 11 nm. The peak concentrations are 0.2 at.% (solid dots) and 0.5 at.%

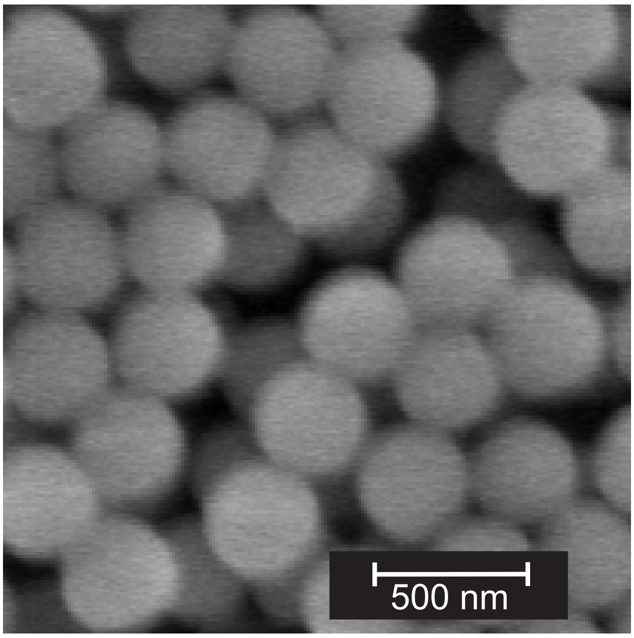

Figure 9.1: *SEM image of SiO_2 colloidal spheres (diameter 340 nm) deposited on a Si substrate.*

(open circles) respectively. Spectroscopic ellipsometry measurements (not shown) on the annealed Er implanted film indicate that the SiO_2 layer thickness is 100 nm, and the refractive index equals that of pure SiO_2 made by thermal oxidation (n = 1.45).

The PL spectrum of a sample with 3–4 layers of 340 nm spheres annealed at 900 °C is shown in Fig. 9.3. The Er^{3+} ions are excited into the $^4F_{7/2}$ level as shown in the inset. The emission is due to transitions from the first excited state ($^4I_{13/2}$) to the ground state ($^4I_{15/2}$), peaking at a wavelength of 1.536 μm. Other samples, implanted to higher erbium fluences even if annealed at different temperatures, as well as the 100 nm thick SiO_2 layers, show the same PL spectrum. This spectrum is similar to the PL spectrum of erbium ions implanted into thermally grown SiO_2 [140]. Since the shape of the PL spectrum is determined by the Stark splitting of the ground state and first excited state induced by the local environment around the atom, this suggests that the local environment of the Er^{3+} ions in all samples discussed in this Chapter is comparable.

In the next two sections we will first describe experiments to determine the radiative decay rate of Er^{3+} in planar SiO_2 films and compare this value with existing literature. We will then use these data to study the LDOS in colloidal particles.

9.3.2 Luminescence lifetime and local density of states in an Er^{3+} doped SiO_2 layer

Figure 9.4 shows luminescence decay rates of Er^{3+} measured at a wavelength of 1.536 μm for the SiO_2 film implanted to a peak concentration of 0.2 at.% Er. Decay rates were measured for the sample in air, and in contact with liquids with refractive indices n of 1.33, 1.45 (index matching case), 1.51 and 1.57. A clear increase of the decay rate from 184 s^{-1} to 205 s^{-1} is observed as the refractive index of the liquid is increased. A similar (absolute) increase in the decay rate was observed for a sample with a peak concentration

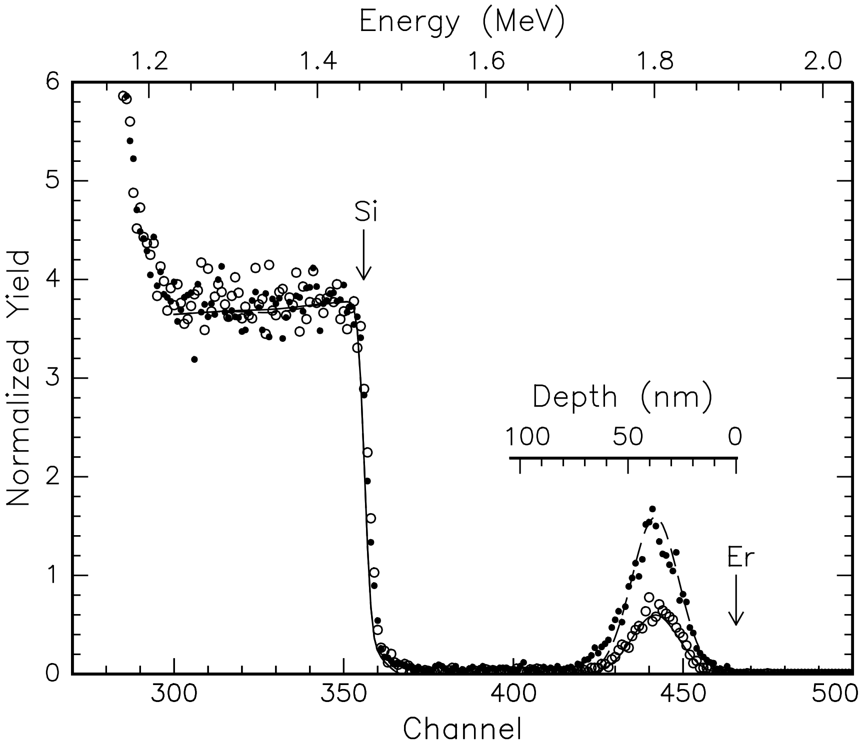

Figure 9.2: *RBS spectra for 100 nm thick SiO_2 layers implanted with 70 keV Er ions to fluences of 3.4×10^{14} ions cm^{-2} (open circles) and 9.1×10^{15} ions cm^{-2} (solid dots). The dashed and drawn lines correspond to fits of the data to obtain the Er depth distribution. The surface channels for Er and Si are indicated by the arrows and the Er depth scale is indicated. The increased yield at channel 280 is due to both the increased Si concentration from the substrate, and the oxygen surface edge.*

of 0.5 at.% (not shown).

As was shown before, for the simpler case of a single interface between two dielectric media of infinite thickness [8, 158], the increase in decay rate with refractive index of the covering liquid can be understood by considering the local optical LDOS for the SiO_2 film in contact with liquids of different refractive index. According to Fermi's Golden rule the radiative decay rate can be written in terms of a LDOS ρ as [8, 110]:

$$W_{rad}(\mathbf{r}) = \frac{\pi\omega}{\hbar\varepsilon(\mathbf{r})}|D|^2\rho(\omega,\mathbf{r}), \tag{9.1}$$

where $\varepsilon(\mathbf{r})$ is the position dependent dielectric constant, ω is the transition frequency and $|D|^2$ is the atomic dipole matrix element of the transition involved. This matrix element is not influenced by the optical properties of the interface. Thus the macroscopic ρ and $\varepsilon(\mathbf{r})$ are the only parameters in Eq. 9.1 that are varied in our experiments.

The LDOS ρ can be calculated as function of position $\mathbf{r}$. For a dielectric slab this calculation is done by quantizing the electromagnetic field using a complete set of normalized eigenvectors of the classical Maxwell problem [110]. For this calculation the complete set of incoming plane waves at a single frequency is summed, using reflection and refraction of the waves as given by the Fresnel coefficients of the layered system. Since the ions are incorporated in an amorphous matrix, an integration over all angles

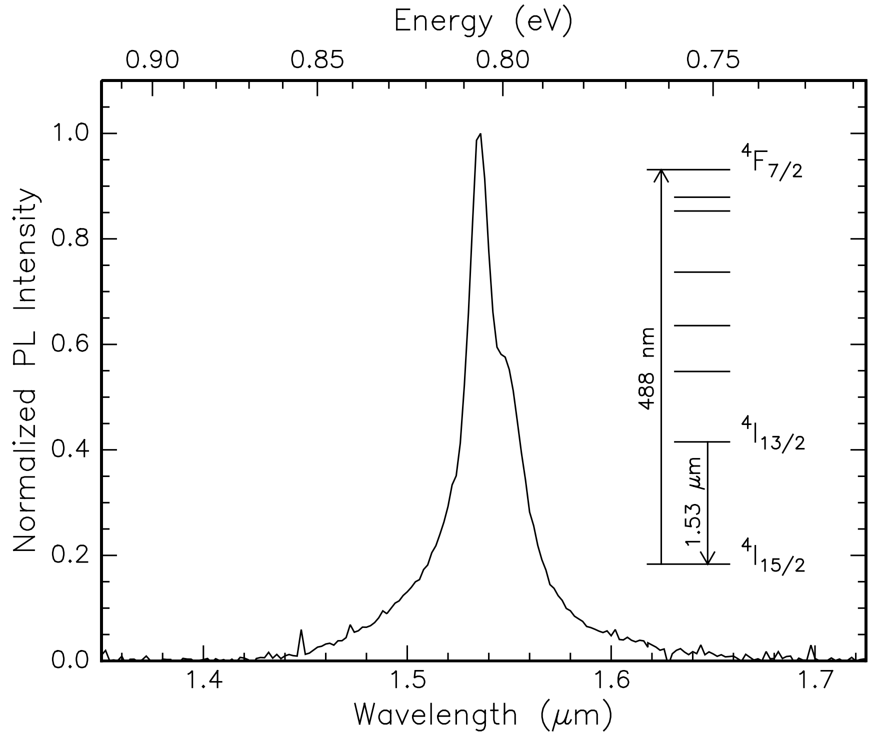

Figure 9.3: *PL spectrum for Er implanted SiO_2 colloids of 340 nm diameter on a silicon substrate. The 488 nm emission line from an Ar ion laser was used as an excitation source. The PL spectrum peaks at a wavelength of 1.536 μm corresponding to the $^4I_{13/2} \rightarrow {}^4I_{15/2}$ transition of Er^{3+}.*

and both polarizations was done. For an absolute determination of the radiative rate the microscopic local field should be used in the calculation. This local field seen by the atom is due to the microscopic environment of the atom and differs from the macroscopic field. With the liquid films in our experiment, we only influence this microscopic local field through the macroscopic field since the Er^{3+} ions are relatively far away from the interface*.

Figure 9.5 shows a calculation of the LDOS $f_{1.45}$ for a 100 nm thick SiO_2 slab (n = 1.45) on a Si substrate (n = 3.45) normalized to the LDOS for a bulk medium of refractive index n = 1.45. The calculation was done for a wavelength of 1.54 μm, corresponding to the peak of the Er^{3+} emission. The factor $\varepsilon(\mathbf{r})$ in Eq. 9.1 is included in the definition of $f_{1.45}$ making this LDOS directly proportional to the radiative decay rate. The position z = 0 corresponds to the position of the Si/SiO_2 interface.

The dashed line shows the calculated LDOS for a sample in air (n = 1.00) and the drawn line shows the LDOS for an index matched film (n = 1.45). The Er depth distribution is indicated in the figure as well. The oscillations in the local LDOS on both sides of the interface are caused by interference between incoming and reflected waves and have a periodicity of $\sim \lambda/2n$. Such oscillations are invisible in the SiO_2 film because the film thickness is much smaller than the emission wavelength (thickness< λ/4n). Clearly, for

---

[*] This assumption can be justified by analysis of measured changes in the radiative decay rate of Er ions in sodalime silicate glass incorporated at two different depths [8], comparable to the depth scales in our experiments. In these experiments, the changes in lifetime were fully described by changes in the LDOS.

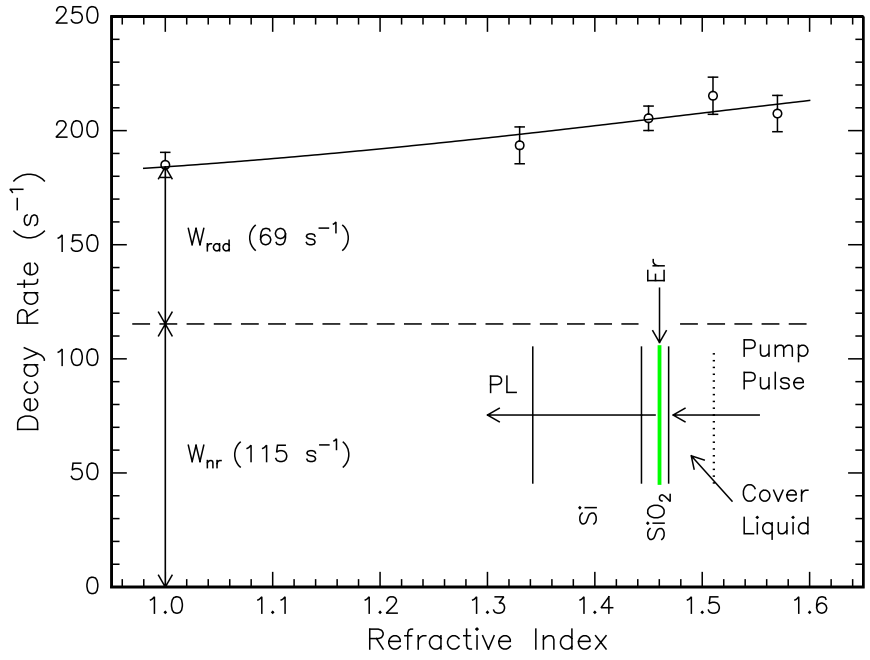

Figure 9.4: *Measured decay rate of Er^{3+} ions in a 100 nm thick SiO_2 layer as function of refractive index of the covering liquid (0.2 at.% Er). The Er^{3+} ions were excited through the liquid using the 488 nm line of an Ar ion laser, while the PL signal was collected from the back through the Si substrate (see inset).*

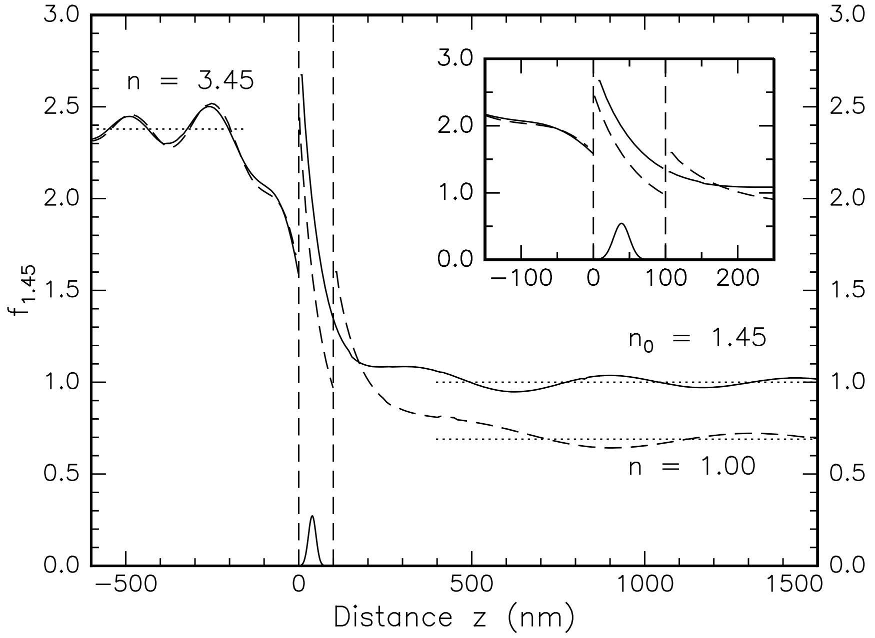

Figure 9.5: *Polarization- and angle-averaged local optical density of states for a 100 nm thick SiO_2 layer (n_0 = 1.45). The layer is sandwiched between a Si substrate (n = 3.45) and an ambient with n = 1.00 (dashed line) or $n = n_0$ = 1.45 (drawn line). The Er depth distribution is also indicated. All calculations were done for a vacuum wavelength of 1.54 μm. The inset shows the LDOS in the SiO_2 layer in more detail.*

both curves in Fig. 9.5 the LDOS in the SiO_2 film is enhanced compared to that for bulk SiO_2 ($f_{1.45}$ = 1.00) which is due to the presence of the high index Si substrate. The inset of Fig. 9.5 shows the LDOS in the SiO_2 layer in more detail, which clearly shows that the LDOS in the film increases with increasing index of the outside medium (n = 1.00 to 1.45). According to Eq. 9.1 this qualitatively explains the increase of the decay rate with refractive index as observed in Fig. 9.4.

The change in decay rate with refractive index can be calculated quantitatively by considering:

1. the calculated LDOS
2. the measured depth profile
3. the standing wave pattern of the pump light in the film, which causes an uneven excitation of Er ions throughout the film

By integrating these effects over the film thickness we find that the observed relative increase in decay rate is much smaller than that found in the calculation that assumes that the decay process is purely radiative. Therefore non-radiative processes that are independent of the optical properties of the interface must be included. The total decay rate is the sum of the radiative and non-radiative decay rates:

$$W = W_{rad} + W_{nonrad}. \tag{9.2}$$

Using Eq. 9.1 the total decay rate can be rewritten in terms of the local LDOS $f_{1.45}$:

$$W(n,z) = f_{1.45}(n,z)W_{rad}^{1.45} + W_{nonrad}, \tag{9.3}$$

where $f_{1.45}$ is the LDOS normalized to the LDOS in a bulk material with n = 1.45 and $W_{rad}^{1.45}$ is the radiative decay rate of Er^{3+} ions in bulk SiO_2. The drawn line in Fig. 9.4 is a fit of Eq. 9.3 to the measured data, resulting in $W_{rad}^{1.45}$ = 54±10 s^{-1} and W_{nonrad} = 115±10 s^{-1}. The radiative and non-radiative rates are separated by the dashed line in Fig. 9.4. Note that the radiative rate for the index matching case (n = 1.45) is found to be W_{rad} = 69 s^{-1} for the SiO_2 thin film. The fact that this is higher than the radiative rate in bulk SiO_2 (54 s^{-1}) is due to the fact that the Er^{3+} ions are close to the high refractive index Si substrate, which enhances the radiative decay rate due to the increased LDOS (see Fig. 9.5. Our analysis uses refractive index values n_D at λ = 590 nm. As the index dispersion between 590 nm and 1.5 μm is less than 2% and the LDOS is sensitive to the difference in index between SiO_2 and the liquid, this introduces an error <1% in the LDOS[†].

9.3.3 Comparison with literature

The radiative rate of 54±10 s^{-1} (τ = 18±3 ms) for Er^{3+} in bulk SiO_2 found in the preceding section is identical to the lifetime measured for 10 μm thick SiO_2 layers grown by wet thermal oxidation of Si that are implanted with 3.5 MeV Er ions [140]. In that case the distance between the interfaces and the Er^{3+} ions is so large that the LDOS is equal to

---

[†] Using spectroscopic ellipsometry measurements we found that indices at 1.5 μm are typically 0.01–0.02 lower than the values at 590 nm, both for SiO_2 and the liquids.

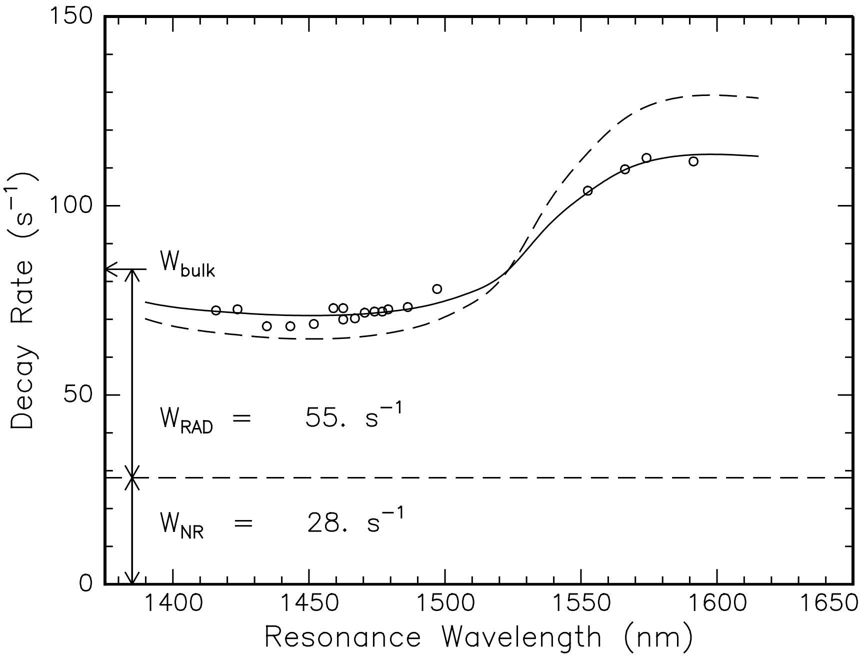

Figure 9.6: *Measured decay rate at 1.536 μm of Er ions embedded in a Fabry-Perot cavity built from alternating Si/SiO$_2$ layers (from Ref. [152]), as function of resonance wavelength of the cavity. The Er ions are positioned in the central SiO$_2$ layer of the cavity. The dashed line shows the calculated decay rate assuming only radiative decay. The solid line is a best fit to the data assuming both radiative and non-radiative decay.*

that of bulk SiO$_2$ within a few percent and a lifetime of 17 ms was reported (W = 59 s^{-1}). We note that the radiative lifetime of 18±3 ms determined here is larger than the lifetime found in several other studies of Er-doped SiO$_2$ [140, 141, 152] indicating that non-radiative decay plays an important role in those studies.

Our result can also be compared with measurements of the decay rate of Er^{3+} in a Si/SiO$_2$ Fabry-Perot microcavity studied by Vredenberg and coworkers in Ref. [152]. The experimental data are reproduced in Fig. 9.6. The active SiO$_2$ region was doped with Er^{3+} ions using Er ion implantation. The authors find that the emission rate enhancement and suppression effects in such cavities are smaller than predicted by theory. One explanation of this effect, also indicated by the authors, is that there is a non-radiative component in the decay. The data in Fig. 9.6 can be fitted using Eq. 9.3, with f equal to the cavity enhancement factor, given by the dashed line in Fig. 9.6, taken from Ref. [152]. A best fit of the cavity data is represented by the drawn line in Fig. 9.6 and results in values of W_{rad} = 55 s^{-1} and W_{nonrad} = 28 s^{-1}. This value for W_{rad} is in perfect agreement with the value obtained above for bulk SiO$_2$.

The radiative rate that we have found for Er in bulk SiO$_2$ (54 s^{-1}) can be compared to the radiative decay rate of Er implanted in silica sodalime glass which was determined to be 45 s^{-1} [8]. The difference is likely to be due to a difference in the local environment of the Er ions, which is also reflected in the difference in PL spectra.

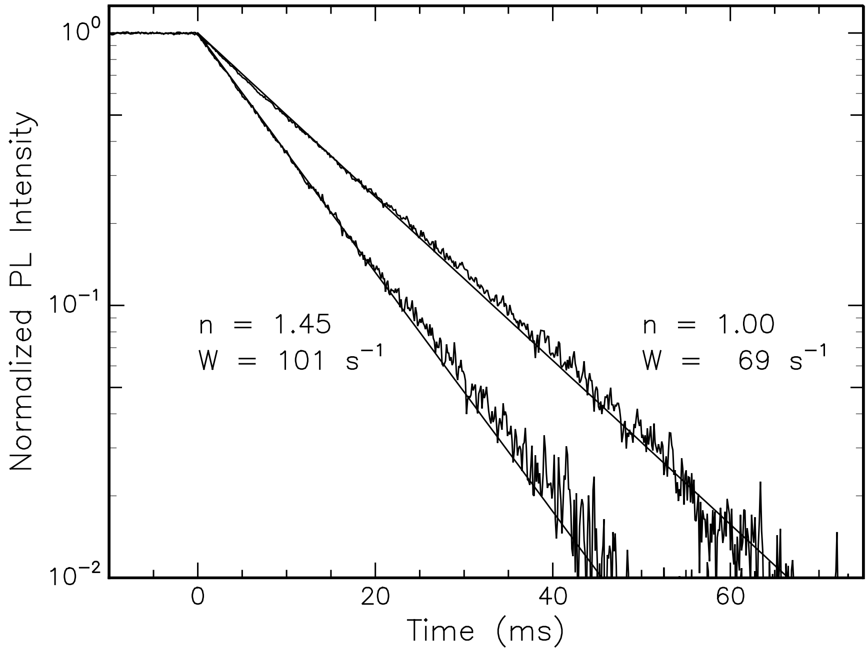

Figure 9.7: *Photoluminescence decay traces plotted on a logarithmic scale for 340 nm diameter SiO_2 spheres implanted with Er to a peak concentration of 0.2 at.%. Decay traces for the sample in air (n = 1.00), and immersed in an index matching liquid (n = 1.45) are shown. The straight lines correspond to single exponential fits with decay rates of 69 s^{-1} and 101 s^{-1} respectively.*

9.3.4 Luminescence lifetime in Er^{3+} doped SiO_2 spherical microcavities

Now that we have determined the radiative lifetime of Er^{3+} in bulk SiO_2, this result can be used to study changes in the luminescence lifetime of Er^{3+} in SiO_2 colloidal spheres. The SiO_2 spheres are grown using a similar process as the thin SiO_2 layers described in section 9.3.2 [142]. Therefore the local environment is likely to be the same and hence the radiative lifetime of the Er ions is the same in both cases. Figure 9.7 shows Er^{3+} luminescence decay traces measured at λ = 1.536 μm for SiO_2 spheres of 340 nm diameter (as in Fig. 9.1) implanted with 350 keV Er ions to a fluence of 0.9×10^{15} ions cm^{-2} (0.2 at.%) and annealed at 900 °C for 1 hr. Two luminescence decay traces are shown: one for the spheres in air, and one for the spheres in an index matching (n = 1.45) liquid. A large increase in the decay rate from 69 to 101 s^{-1} is observed due to the index matching. After removing the index matching liquid and drying the sample for several minutes, the decay rate returned to the original value of 69 s^{-1}, showing that the index matching process is reversible. We have repeated the experiment using di-methyl-sulfoxide (DMSO) (n = 1.48) and fully deuterated DMSO-d6 and found the same increase by 30 s^{-1} for both cases. This excludes the possibility that the increase is due to non-radiative processes owing to –OH and –CH groups in the liquid, as the quenching rate for the two liquids should then have been very different [138, 139]. This indicates that the effect on decay rate is purely caused by the higher refractive index of the liquid.

In the index matched case, the LDOS in the colloids is identical to that for the SiO_2

film on Si in contact with the index matching liquid, as given by the drawn line in Fig. 9.5. In the present geometry with the substrate covered with 3–4 layers of 340 nm spheres the implanted Er^{3+} ions are placed 700–1000 nm away from the Si interface. As can be seen in Fig. 9.5, for these distances the LDOS differs by less than 7% from the bulk value. Therefore the radiative decay rate of the Er^{3+} ions inside the index matched spheres must be close to the rate in bulk SiO_2 of 54±10 s^{-1}. The difference with the measured rate of 101 s^{-1} is then attributed to a non-radiative decay process at a rate of 47±10 s^{-1} (101 - 54 = 47). Having now determined the non-radiative decay rate in these colloids, we can derive the radiative decay rate in the colloids in air by subtracting the measured non-radiative rate from the measured total rate in air. This results in a radiative decay rate of 22±15 s^{-1} (69 - 47 = 22) for a 340 nm diameter sphere surrounded by air.

This experimentally determined value can be compared with theoretical calculations of the LDOS for a spherical particle. The LDOS is obtained by using the imaginary part of the Green function $G(\mathbf{r}, \mathbf{r}; \omega)$ of the Helmholtz equation at a given frequency ω [166, 167]. The LDOS is defined as [39, 40, 165]:

$$\rho(\omega, r) = -\frac{2}{\pi}\mathrm{Im}G(\mathbf{r}, \mathbf{r}; \omega). \tag{9.4}$$

Using the definition of Eq. 9.4 the relation between the LDOS and the radiative decay rate is again given by Eq. 9.1.

Figure 9.8 shows a calculation of the LDOS for a single spherical particle at a vacuum wavelength of 1.536 μm, as function of the radial distance, for spheres with a diameter of 175 nm (a), 340 nm (b) or 1600 nm (c). The density of states is normalized to the LDOS of a bulk medium with n = 1.45. For the 175 nm and 340 nm diameter spheres very little variation in the LDOS is observed inside the sphere. This can be explained by the fact that the emission wavelength is larger then the first Mie resonance in these spheres. Note that the average LDOS can be larger (Fig. 9.8a)) or smaller (Fig. 9.8b)) than the LDOS in bulk SiO_2, depending on the sphere diameter. For larger diameter spheres Mie resonances appear, leading to more pronounced variations in the LDOS as shown in Fig. 9.8(c) for 1600 nm spheres.

A complete representation of the LDOS for a single sphere with a refractive index n = 1.45 surrounded by air is shown in Fig. 9.9, as function of sphere diameter (horizontal axis) and the position within the sphere (vertical axis). The gray scale indicates the LDOS normalized to the LDOS for bulk SiO_2 (n = 1.45). The position within the sphere is normalized to the sphere radius such that r/R = 1 corresponds to the edge of the sphere, while r/R = 0 corresponds to the center of the sphere. A number of maxima and minima in the LDOS are observed as function of the sphere diameter, which can be compared to the position of Mie resonances or normal modes of the sphere. The size parameter ($2\pi R/\lambda$) at which these resonances appear is indicated on the top axis. The magnetic (electric) resonance are labeled as M_n^ℓ (E_n^ℓ), where n corresponds to the order of the resonance. ℓ = 1 corresponds to the ground tone of a resonance, while higher ℓ indicate the overtones.

By comparing the position of the maxima in Fig. 9.9 (indicated by the black circles) with the diameter at which the normal modes appear, we find that the maxima in the local LDOS correspond to the position of the electric type resonances. Depending on the order of the resonance the maximum in the LDOS occurs in the center of the sphere or more towards the perimeter of the sphere. As can be seen in Fig. 9.9 the decay rate of ions

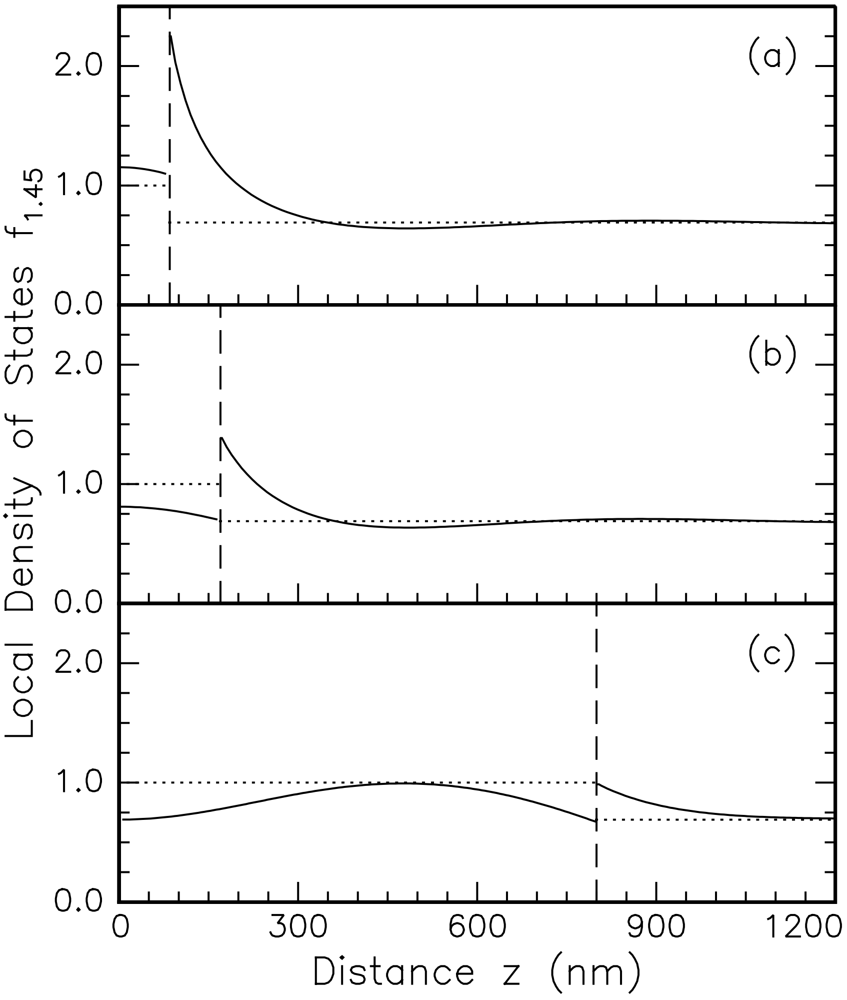

Figure 9.8: *Polarization- and angle-averaged LDOS as function of radial position for a SiO_2 sphere (n = 1.45) in air, calculated for a vacuum wavelength of 1.54 μm. Data are shown for spheres with a diameter of 175 nm (a), 340 nm (b), or 1600 nm (c).*

placed inside a sphere can thus be enhanced or reduced, depending on both the sphere diameter and the position of the ions within the sphere.

The Er doped SiO_2 spheres considered in this Chapter have a diameter of 340 nm which corresponds to a size parameter that lies below the size parameter of the lowest (magnetic) normal mode of the sphere. As can be seen in Fig. 9.9 the LDOS is a slowly varying function of the sphere diameter in this size range. Assuming a bulk radiative rate W_{rad} = 54±10 s^{-1} the calculation predicts a radiative decay rate in the range of (35–40)±10 s^{-1} depending on the distribution of the Er ions within the sphere. Within the errors, these values agree with the experimentally observed value of 22±15 s^{-1}. For small spheres, the electric field outside (but in close proximity to the sphere) is enhanced due to a strong dipolar contribution [168]. The LDOS scales with E^2, and is enhanced by a factor $1 + 6(\varepsilon_s - \varepsilon_h)/(\varepsilon_s + \varepsilon_h)$, with ε_s and ε_h being the sphere and host dielectric constant. Since local field effects will become important for small spheres as well, we did not perform calculations for spheres that are much smaller than those used in the

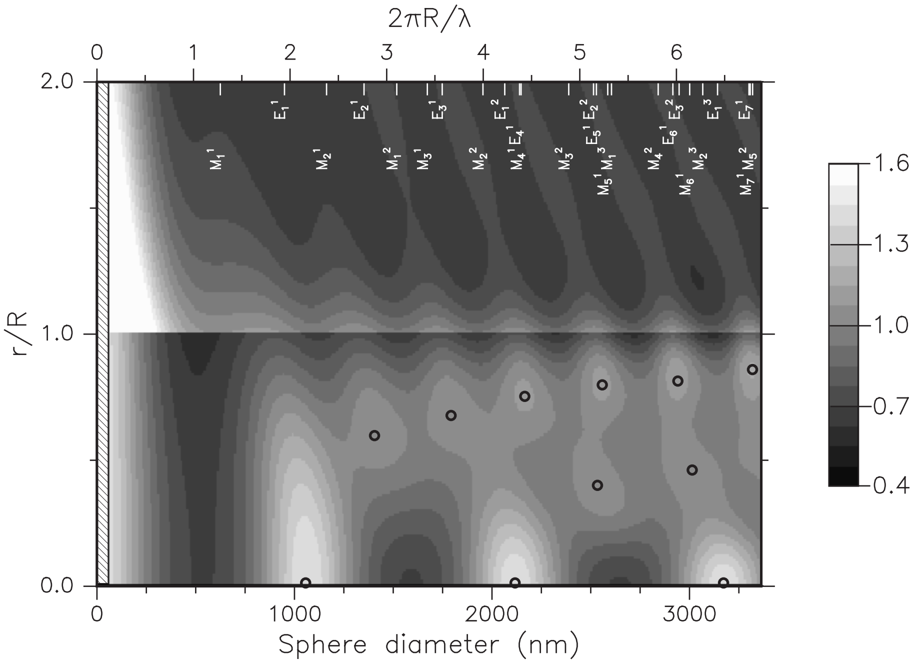

Figure 9.9: *Polarization- and angle-average LDOS for a SiO$_2$ sphere (n = 1.45) in air for a vacuum wavelength of 1.536 μm as function of normalized radial position (vertical axis) and sphere diameter (horizontal axis). The corresponding size parameter is indicated on the top axis. The LDOS is indicated by the gray scale on the right and was normalized to the density of states in bulk SiO$_2$. The observed maxima in the LDOS are indicated by the black circles. The magnetic (electric) resonances of the sphere are indicated on the top axis by M_n^ℓ (E_n^ℓ). No data were calculated in the cross hatched region for diameters $<$ 50 nm.*

experiment (hatched area in Fig. 9.9).

The measured and calculated Er luminescence decay rates for the SiO$_2$ layer and the 340 nm spheres are summarized in Table 9.1. The quantum efficiency, defined as the ratio of the radiative rate and the total decay rate, is also indicated in Table 9.1. Both for the film and the sphere the quantum efficiency increases for increasing index, because of the increased relative contribution of radiative decay to the total decay. As can be seen in the table, a large difference in the non-radiative rates exists between the spheres and the layer. Since the Er concentration is 0.2 at.% in both cases, this implies that the non-radiative processes that occur in our samples depend on material properties other than the Er concentration only. One possibility is a difference in the concentration of –OH quenchers incorporated in the SiO$_2$ material that act as centers for non-radiative decay [8, 131]. This could be due to a difference in annealing behavior for spheres and thin layers.

Finally, we note that in our analysis we have assumed that the spheres are isolated. This greatly facilitates the calculation of the LDOS since the different polarizations can be treated separately. In reality the spheres are touching and deposited on a substrate, which affects the calculated LDOS [169] and a full vector calculation of the Maxwell equations is needed. Since the error on the experimentally derived radiative decay rate in the SiO$_2$ colloids is rather large, we were unable to observe a significant difference between the measured data and calculations of the LDOS for an isolated sphere. Since our experiments were done spheres with a diameter that is small compared to the emission wavelength, the effect of neighboring spheres is expected to be limited. For larger spheres,

Table 9.1: *Measured and calculated decay rates for Er^{3+} doped SiO_2 samples (0.2 at.% Er). Results are given for a 100 nm thick SiO_2 layer and for 340 nm diameter spherical microcavities, both either in contact with air or an index matching liquid (n = 1.45). As discussed in the text, measurements of the decay rate in a SiO_2 film as a function of refractive index were first made (W_{exp}). From a comparison with LDOS calculations W_{rad} and W_{nonrad} were then determined for the layer. The radiative rate of Er in bulk SiO_2 was then determined to be 54 s^{-1}. Next, from the measured decay rate of the index matched spheres the non-radiative rate in the colloids was found (47 s^{-1}). From this the radiative decay rate of the colloids in air was found (22 s^{-1}). The calculated radiative rate in the colloids (40 s^{-1}) was derived from a LDOS calculation combined with the bulk radiative rate of 54 s^{-1}. For each geometry the quantum efficiency (QE) is also indicated.*

Sample	Calculated W_{rad} (s^{-1})	W_{exp} (s^{-1})	W_{rad} (s^{-1})	W_{nonrad} (s^{-1})	QE
SiO_2 layer (n = 1.00)	69	184	69	115	37%
SiO_2 layer (n = 1.45)	90	205	90	115	44%
340 nm sphere (n = 1.00)	40	69	22	47	32%
340 nm sphere (n = 1.45)	54	101	54	47	53%

the surroundings will greatly influence the resonances observed in Fig. 9.9.

9.4 Conclusions

The radiative decay rate at 1.535 μm of Er^{3+} ions implanted at a well defined position in a thin SiO_2 layer on Si was determined by bringing the layer into contact with liquids of different refractive index in the range between 1.33 and 1.57. The decay rate was found to increase with refractive index, an effect that is explained by a change in the local optical density of states at the position of the Er^{3+} ions in the film. Radiative and non-radiative components in the decay were separated and the radiative decay rate for Er in bulk SiO_2 was determined to be 54 ± 10 s^{-1}.

The LDOS for spherical SiO_2 microcavities was calculated for various radii of the sphere. Depending on the sphere radius and the position of the Er ions in the sphere the radiative decay rate can either be enhanced or reduced relative to the decay rate in bulk SiO_2. A full determination of the LDOS as function of sphere diameter revealed that the maxima in the LDOS correspond to the electric type resonances of the spherical microcavity.

The experimentally obtained value for the decay rate in bulk SiO_2 was used to analyze decay rates measured for Er^{3+} implanted in 340 nm diameter SiO_2 colloidal spheres. By index matching the spheres a large increase in decay rate from 69 s^{-1} to 101 s^{-1} was observed. Radiative and non-radiative decay components were distinguished, and the data are well described by the calculated LDOS in a single spherical microcavity.

9.5 Appendix: Förster transfer and the local density of states

In this thesis, several experiments are described in which the decay rate of an atom is influenced by changing the local optical surrounding of these ions. The simplest geometry involves placing atoms close to a dielectric interface (see Chapter 6). The optical surrounding can then be changed relatively easily by replacing the air on one side of the interface by a liquid of refractive index n. More complex geometries including two interfaces and microspheres were discussed in detail in the present chapter. All data are analyzed by calculations of the local density-of-states (LDOS), which is related to the radiative decay rate of the atom by using Fermi's Golden rule (Eq. 9.1). In all experiments described in this thesis, measured changes in decay rate of optical probe ions as function of the refractive index n of the liquid, can only be described by assuming a non-radiative decay component that is independent of the LDOS.

It was argued that this non-radiative decay component is due to concentration quenching, typically observed in practical optical materials doped with high concentrations of the optically active species. In that case, energy transfer between the closely spaced ions takes place via Förster transfer. The migration of the excitation among the ions continues until a photon is emitted or until the energy is transferred to a quencher (e. g. an –OH impurity in the case of Er ions). This Förster transfer is assumed to be independent of the LDOS. Here, we reanalyze earlier experiments by Snoeks et al. on Er ions in sodalime silicate glass [8, 130], and provide data that support this assumption.

Using the same technique as described in Chapter 6, for sodalime silicate glass doped with Er to a peak concentration of 1.0×10^{20} Er cm^{-3}, the radiative and non-radiative rate were determined [8]. For n = 1.00 (sample in air), it was found that the total decay rate (85 s^{-1}) is composed of a radiative rate of 40 s^{-1} and a non-radiative rate of 45 s^{-1}. Additional data on similar samples implanted to different Er peak concentrations [130] reveal that the total decay rate increases linearly with Er concentration from 85 s^{-1} for the lowest concentration (1.0×10^{20} Er cm^{-3}) to 450 s^{-1} for a peak concentration of 1.3×10^{21} Er cm^{-3}. This linear increase is characteristic for concentration quenching, based on Förster transfer between Er ions. Extrapolating the decay rate to zero Er concentration yields an Er decay rate in absence of concentration quenching: 42 s^{-1}. The non-radiative rate due to concentration quenching for an Er concentration of 1.0×10^{20} Er cm^{-3} can then also be derived: 43 s^{-1}.

Combining these two analyses, we find that the non-radiative component not affected by the LDOS (45 s^{-1}) is with measurement inaccuracy equal to the non-radiative component attributed to concentration quenching (43 s^{-1}). These data indicate that, contrary to what was suggested elsewhere [170], Förster transfer over the nm distances between Er ions (the "Förster zone") is not affected by the LDOS.

Finally, we note that in general, energy transfer via dipole-dipole interactions between two ions strongly depends on the separation between the ions. Two limits can be defined:

1. The separation d between the ions is $\ll \lambda/2\pi$, with λ the emission wavelength and Förster energy transfer dominates. In this process, an excited donor is de-excited

by transferring its energy to a nearby acceptor ion through a non-radiative process.

2. For diluted systems, when $d \gg \lambda/2\pi$, donor-acceptor energy transfer primarily takes place via emission and reabsorption of a photon.

In the latter case, the energy transfer is affected by the LDOS. The fact that the relative contribution of radiative and non-radiative (Förster) processes can be influenced by changing the LDOS can lead to interesting novel concepts of nanoscale energy transfer. For example, if an erbium doped material is embedded in a photonic crystal with small LDOS Förster transfer becomes the main decay process. As it involves migration (but not necessarily annihilation) of the excitation Förster transfer can then lead to the diffusion of an excitation over very long distances.

10

Acid based synthesis of monodisperse rare earth doped colloidal SiO_2 spheres

Rare earth (Er^{3+}, Tb^{3+} and Eu^{3+}) doped spherical SiO_2 colloids were synthesized using an acid based wet chemical procedure by adding the appropriate rare earth chloride to a solution of tetra-ethoxy-silane, glacial acetic acid and water. Spherical SiO_2 particles of 2.2 μm diameter and a size polydispersity of $\sim$40% can be separated from the reaction mixture after stirring for 30 min. Rutherford backscattering spectrometry measurements reveal a typical rare earth concentration of 0.15–0.18 at.%. Erbium doped particles with very small size polydispersity were grown using a seeded growth process starting from monodisperse, 183 nm diameter, spherical SiO_2 colloids. Transmission electron microscopy images reveal the formation of a 5–6 nm thick (Er-doped) shell on the seed particles. After annealing for 30 min at 900 °C in flowing O_2 identical photoluminescence spectra were observed from both the bulk Er-doped particles and particles obtained from seeded growth. The luminescence lifetime of 13.2 ms indicates that particles can be grown with a high quantum yield of $\sim$70%. Visible luminescence from polydisperse Eu^{3+} and Tb^{3+} doped particles was observed with ms lifetimes from annealed and unannealed particles as well.

10.1 Introduction

Monodisperse colloidal spheres in solution can self-organize into a crystalline structure if their size polydispersity is low enough. In such a colloidal crystal the dielectric constant shows a periodic variation with position. If the length scale of this periodic variation is comparable to the wavelength of visible or near-infrared wavelengths, the structure can Bragg-reflect the light, leading to interesting optical properties. The properties of such a photonic crystal can be studied by placing luminescent probes inside the crystal [171]. For example, fluorescently labeled spheres can be used to study colloidal crystals in real-space by confocal microscopy [172]. Commonly, laser dyes are used for this purpose and are chemically incorporated into the SiO_2 particles during synthesis [98, 99]. However, to study the effect of the photonic crystal on spontaneous emission, or to probe the local optical density of states, dyes are impractical, as their emission spectrum is often broader than the photonic feature under study [99, 173]. In contrast, rare earth (RE) ions incorporated in SiO_2, display narrow-line intra-4f transitions that are to first order independent of the local environment. In addition, the luminescence from RE ions is often improved by thermal treatments, extending the experimental range of RE luminescent probes to sintered colloidal crystals. Also, RE ions do not exhibit photo bleaching commonly observed for laser dyes. Thus, RE-doped colloids appear ideal probes in photonic crystals.

So far, ion implantation was used to dope monodisperse spherical SiO_2 particles with Er^{3+} [101]. However, this technique only yields a limited amount of particles. In this chapter we describe a new method to dope SiO_2 particles with RE ions via an acid based wet chemical synthesis route by adding the appropriate RE-chloride to the reaction mixture. This method was explored recently to synthesize Pr^{3+} and Er^{3+} silica microspheres [174]. In addition, we also describe a seeded growth process in which a thin shell of Er^{3+} doped silica is grown on existing, monodisperse silica colloids. The growth and luminescence properties of the particles are studied using scanning electron microscopy (SEM), transmission electron microscopy (TEM), Rutherford backscattering spectrometry (RBS) and photoluminescence (PL) spectroscopy.

10.2 Experimental

All chemicals were used as received without further purification. Tetra-ethoxy-silane (TEOS) (purity $\geq$99%) was supplied by Fluka Chemie AG, KOH was supplied by Aldrich, glacial acetic acid was supplied by Biosolve. Ethanol (Merck) was of analytical grade. $ErCl_3$, $EuCl_3 \cdot 6\,H_2O$ and $TbCl_3 \cdot 6\,H_2O$ (purity 99.9%) were all supplied by Acros Organics.

SiO_2 colloids were produced by adding TEOS to a mixture of glacial acetic acid and water under stirring at room temperature. The molar composition of TEOS : CH_3COOH : H_2O was 1 : 4 : 4, which is described as the optimum composition for obtaining dense (density 2.14±0.02 g cm^{-3}) spherical SiO_2 colloids [175, 176]. Rare earth (RE) ions were incorporated in the SiO_2 by replacing the water by an aqueous solution of 1 wt.% $ErCl_3$, $EuCl_3 \cdot 6\,H_2O$ or $TbCl_3 \cdot 6\,H_2O$, respectively. After stirring the mixture for 30 minutes the SiO_2 particles were separated from the solution by centrifuging at 1000 rpm and washed at least twice with pure ethanol.

Seeded growth experiments were conducted using a slightly different molar composition TEOS : CH_3COOH : H_2O of 1 : 8 : 8 and using a 0.2 wt.% $ErCl_3$ solution. The total reaction time in this case was 45 min. The SiO_2 seed particles were made in a microemulsion [177, 178] and subsequently grown larger in a base catalyzed seeded growth procedure [92, 178]

Si(100) substrates were cleaned for at least 2 min. in a 2 M KOH in ethanol solution. Droplets of the SiO_2 particles suspended in ethanol were deposited on the Si substrate and the ethanol was let to evaporate, leaving a layer of particles on the substrate. Annealing of the particles was done at 900 °C for 30 min. under flowing oxygen (4 l min^{-1}) in a rapid thermal annealing furnace. Photoluminescence (PL) measurements were done on the particles on a Si substrate as well as on quartz cuvettes containing suspensions of the particles in an index matching mixture of dimethylsulfoxide (DMSO) and dimethylformamide (DMF) (n_D = 1.45).

The 465.8 nm (Eu^{3+}) and 488.0 nm (Er^{3+}, Tb^{3+}) lines of an Ar ion laser, modulated on-off at frequencies of 7–11 Hz with an acousto-optic modulator, were used as an excitation source for PL spectroscopy. The luminescence was focused on the entrance slits of a 48 cm grating monochromator and detected by a liquid nitrogen cooled Ge detector in the spectral region from 800 to 1700 nm or an AgOCs photomultiplier tube in the spectral region from 400 to 1100 nm employing standard lock-in techniques. Decay curves were recorded using a digitizing oscilloscope in combination with the Ge detector for Er^{3+} (time response 30 μs) or a multichannel scaler system in combination with the photomultiplier tube for Eu^{3+} and Tb^{3+} (time response 100 ns, limited by the AOM).

Scanning electron microscopy (SEM) images were taken at a resolution better than 5 nm using 5 keV electrons. Transmission electron microscopy (TEM) images were taken using 200 keV with particles dried from the suspension on standard Cu TEM grids. To determine the elemental composition of the rare earth doped colloids, Rutherford backscattering spectroscopy (RBS) of 2 MeV He^+ particles was used at a scattering angle of 165°.

10.3 Particle synthesis

Colloidal SiO_2 particles can be formed by either an acid catalyzed reaction [175, 176] or a base catalyzed (Stöber) reaction [89]. The base catalyzed reaction, using ammonia, ethanol, water and tetra-ethoxy-silane (TEOS), can be controlled to yield spherical SiO_2 particles with low size polydispersity. Seeded growth has been applied on these particles to grow larger particles, to incorporate laser dyes and to grow core-shell particles [92, 98, 99]. Unfortunately, the incorporation of RE ions by dissolving a RE salt in ethanol fails for the base catalyzed reaction since the RE ion immediately forms an insoluble RE hydroxide [148]. Attempts to synthesize RE-doped particles by using either tri-amino-propyl-tri-ethoxy-silane or N-(tri-methoxy-silyl-propyl)-ethylene-diamine, triacetic acid, tri-sodiumsalt were unsuccessful for the same reason [148].

A well established process to obtain RE-doped SiO_2 layers is spin coating of sol-gel solutions containing RE ions. This acid catalyzed process relies on the formation of a gel from a reaction mixture containing TEOS, ethanol, water and an acid [179, 180]. In an early stage of this reaction, spherical particles can be separated from such an acid catalyzed reaction mixture of TEOS, glacial acetic acid and water [175, 176]. The reaction results in the formation of micron sized spherical particles that are quite polydisperse. We have used this reaction, modified by the addition of $ErCl_3$, to form bulk Er-doped SiO_2 colloids.

Figure 10.1a) shows a SEM image of these particles after annealing (900 °C, 30 min). The inset shows a TEM image of one of the particles. Analyzing ∼100 particles reveals a broad size distribution (not shown) characterized by a mean diameter of 2.2 μm and a size polydispersity of $\sigma = 40\%$. The distribution is not Gaussian shaped and exhibits a tail extending to a diameter of ∼6 μm. Note that in this analysis the number density of small particles may be underestimated as they may not all be collected from the solution in the centrifugation step. After separation, the remaining reaction mixture develops into a stiff, ringing gel in a few days time, clearly demonstrating the fact that the particles studied form in an early stage of the reaction. Particle suspensions washed only once in pure ethanol eventually form a gel as well, albeit on a much longer time scale. The particles in this study were all washed at least twice, resulting in stable suspensions of particles in ethanol. No gelation was observed in these suspensions.

To use Er-doped colloids in photonic crystals and colloidal crystallization studies, the size polydispersity needs to be low and controllable. We achieve this by using a seeded growth process starting from 183-nm-diameter (undoped) silica seed particles. Figure 10.1b) and c) show TEM images of silica particles used before (b), and after (c) seeded growth in the Er-doped solution. The seeds used were grown by a base catalyzed reaction starting from particles grown in a microemulsion leading to the formation of 183 nm diameter particles with a 1% size polydispersity of ∼1% (Fig. 10.1b)). After seeded growth (Fig. 10.1c)) the particle diameter has increased to 194 nm by 11±2 nm, and the size polydispersity has increased to ∼3%. These data show that the particle diameter has increased by 11±2 nm using the seeded growth process. Furthermore, as the insets in Figs. 10.1b) and c) show, the roughness of the particle surface increases by seeded growth; the roughness being typically 2–3 nm. As the roughness in a base catalyzed seeded growth process is usually smaller [92], this indicates that the acid catalyzed reaction leads to a different growth mechanism. To obtain a successful seeded growth, the reaction conditions were chosen such that the reaction speed was lower than for the synthesis of the bulk Er-doped (polydisperse) particles in Fig. 10.1a). When seeded growth was carried out under the same conditions as used for the bulk particles, nucleation of new particles also occurred. The inset in Fig. 10.1a) shows that the roughness of the bulk Er-doped particles grown by the acid based reaction is much lower, which indicates that reduction of the surface roughness of particles grown by seeded growth may be possible by careful tuning of the reaction conditions.

The absence of large clusters of particles in Fig. 10.1c) indicates that seeded growth in the Er solution occurs on individual particles. Further evidence that mostly single particles are present in the solution is provided by the fact that uniform layers of the particles can be deposited on Si substrates by depositing a droplet of the solution on the substrate. Directly after synthesis the particles were mostly unaggregated. Storing the particles for a few weeks, however leads to large aggregates of particles which may be related to the reduced surface potential of the particles. In principle, long-term storage could be possible if the particles are covered with a thin outer shell of pure, undoped, silica. We note that the effect of (charged) RE ions on the stability of the particle suspension has been observed before. For instance, it is known that RE ions influence the viscosity of sol-gel solutions used in spin-coating studies [181].

RBS was done on bulk Er-doped SiO_2 particles on a Si substrate to determine the

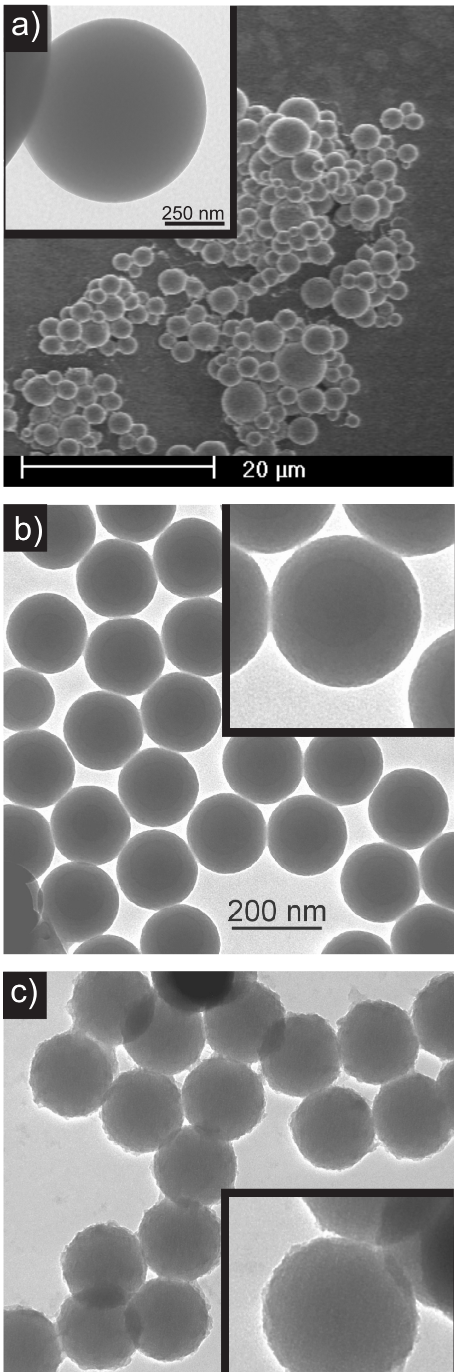

Figure 10.1: *a) SEM image of colloidal SiO_2 particles grown by the acid based route, b) TEM images of particles used for seeded growth experiments, and c) TEM images of seed particles after seeded growth using the acid based reaction. The insets zoom in on single particles and reveal an increase in both particle diameter and surface roughness by the seeded growth.*

elemental composition of the colloids (data not shown). It was found that the Si:O ratio is close to the stochiometric value for pure SiO_2. No carbon (detection limit 3 at.%) was observed in RBS. The Er concentration measured is typically 0.15–0.18 at.%. In studies on spin-coated SiO_2 layers containing Er ions it was found that the Er:Si ratio in the deposited layer is roughly equal to the Er:Si ratio in the solution [180, 181]. The solutions in our work have an Er:Si ratio of 1:60, while the Er:Si ratio in the particles is roughly 1:200 which is significantly lower. At present both the exact growth mechanism of the acid catalyzed silica growth and the incorporation mechanism of the Er ions are not known and need further study.

10.4 Photoluminescence

Figure 10.2 shows the normalized PL spectra of the bulk Er^{3+}-doped particles (see SEM image in Fig. 10.1a), and Er^{3+}-doped particles obtained by the seeded growth process (see TEM image in Fig. 10.1c), both annealed at 900 °C for 30 min. in a 100% oxygen flow. Annealing of the particles in a vacuum furnace leads to a discoloration most likely due to a small amount of carbon formed by cracking of remaining organic groups in the SiO_2 network at high temperatures. By annealing in pure oxygen any remainder of organic groups is burnt away and the particles do not change color upon annealing. No Er^{3+} related luminescence is observed from SiO_2 particles that are not annealed. This is most likely caused by the presence of C-H and O-H groups in the silica network of which the first vibrational overtones are known to be resonant with the ${}^4I_{13/2} \rightarrow {}^4I_{15/2}$ transition of Er^{3+} at 1.5 μm, causing the Er^{3+} luminescence to be quenched.

The PL spectra in Fig. 10.2 show typical luminescence from the ${}^4I_{13/2} \rightarrow {}^4I_{15/2}$ transition of Er^{3+} ions in SiO_2, peaking at 1.536 μm. The inset shows PL decay traces measured at the peak luminescence wavelength. The measured decay traces show single-exponential behavior characterized by a lifetime of 13.5 ms (decay rate 75 s^{-1}) for both samples. The measured decay of the particles obtained by seeded growth shows an initial fast decay component, attributed to the small background observed in the PL spectrum, and is therefore not related to Er^{3+}.

Comparing the PL lifetimes with earlier results on Er^{3+} doped colloidal particles by ion implantation (see Chapter 7), and taking into account the variation in local optical density of states in the spherical particles (see Chapter 9), we estimate the PL quantum efficiency to be $\sim$70% (the radiative decay rate of Er^{3+} in bulk SiO_2 is 54 s^{-1} [101, 151]). Comparing PL measurements for bulk-doped (polydisperse) Er-doped particles and the particles fabricated by seeded growth, with only a 5–6 nm thick Er-doped shell, it was found that the latter showed much lower absolute PL intensity. As the quantum efficiency (PL lifetime) for both types of particles is similar, the reduction in PL intensity for the particles made by seeded growth is fully attributed to the much lower total Er content of the particles made by seeded growth.

The monodisperse Er^{3+} doped particles synthesized here might find use as optical probes in photonic crystals with a bandgap centered around the important telecommunication wavelength of 1.5 μm. For applications in the visible range of the spectrum, other rare-earth ions, e.g., Eu^{3+} and Tb^{3+}, are of interest. We have synthesized bulk Eu^{3+} and Tb^{3+} doped particles using the acid based process using the corresponding RE-chloride. PL spectra of such polydisperse particles suspended in an index-matching mix-

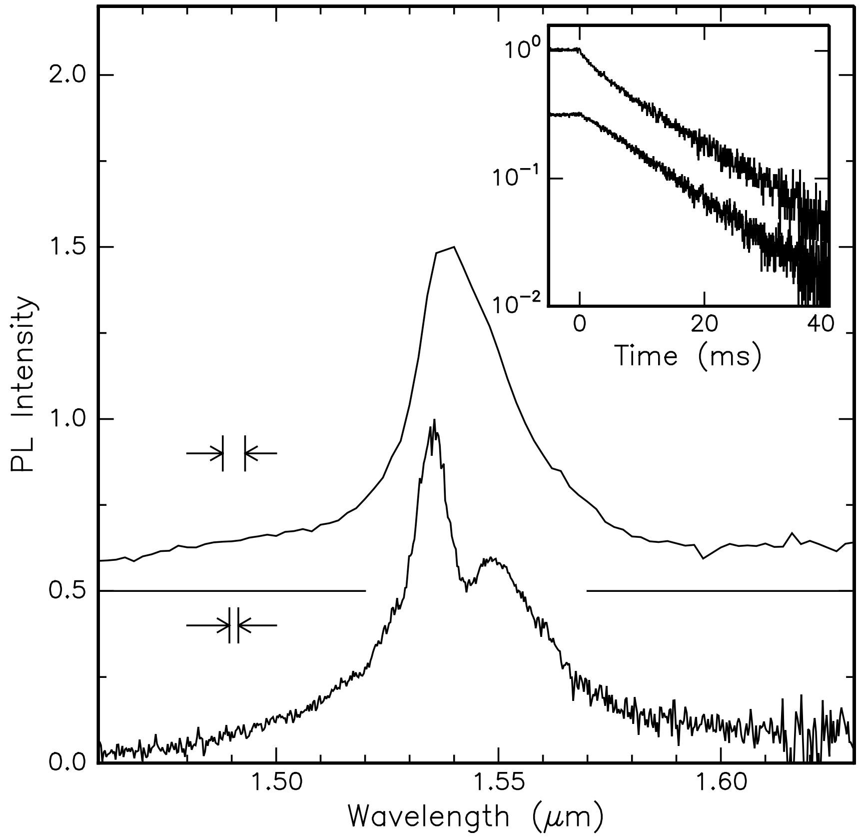

Figure 10.2: *Normalized PL spectra of bulk Er-doped particles (lower spectrum) and Er-doped particles obtained by seeded growth (upper spectrum, offset for clarity) after annealing for 30 min in pure oxygen at 900 °C. The arrows indicate the spectral resolution. The inset shows PL decay traces measured for the seeded growth particles (upper trace) and bulk doped particles (lower trace) at the peak emission wavelength.*

ture of dimethylsulfoxide (DMSO) and dimethylformamide (DMF) are shown in Fig. 10.3 for Tb^{3+} (a) and Eu^{3+} (b) ions. The Tb^{3+} ions are pumped directly into the $^5D_4$ level (λ = 488 nm) and show typical Tb^{3+} luminescence from transitions to the $^7F_5$, $^7F_4$, $^7F_3$, and $^7F_0$ levels as indicated in the level diagram in Fig. 10.3. The luminescence from the $^5D_4$ to $^7F_1$ and $^7F_2$ transitions is too weak to be observed. Luminescence from the $^5D_4$ manifold down to the ground state of Tb^{3+} cannot be measured because it coincides with the laser line used for excitation. Exciting the Eu^{3+} ions into the $^5D_2$ level (λ = 458.7 nm) leads to characteristic peaks in the luminescence related to transitions from the $^5D_0$ level to the $^7F_4$, $^7F_3$, $^7F_2$, $^7F_1$ and $^7F_0$ levels, as shown in Fig. 10.3b.

The PL spectra in Fig. 10.3 are measured on particles that were not annealed after synthesis. Decay traces of the luminescence from the $^5D_4$ level of Tb^{3+} and $^5D_2$ level of Eu^{3+} show single exponential decay curves. The measured lifetimes are summarized in Table 10.1 together with the measured lifetime of the Er^{3+} doped colloids. The measured lifetime of the Tb^{3+} $^5D_4$ level increases from 0.15 ms to 1.00 ms upon annealing at 900 °C and increases even further to 1.29 ms when the silica spheres are suspended in an index matching DMSO/DMF mixture. A similar trend is observed for the $^5D_2$ level of Eu^{3+}; in this case the lifetime of unannealed colloids is 0.66 ms, and increases to 1.15 ms

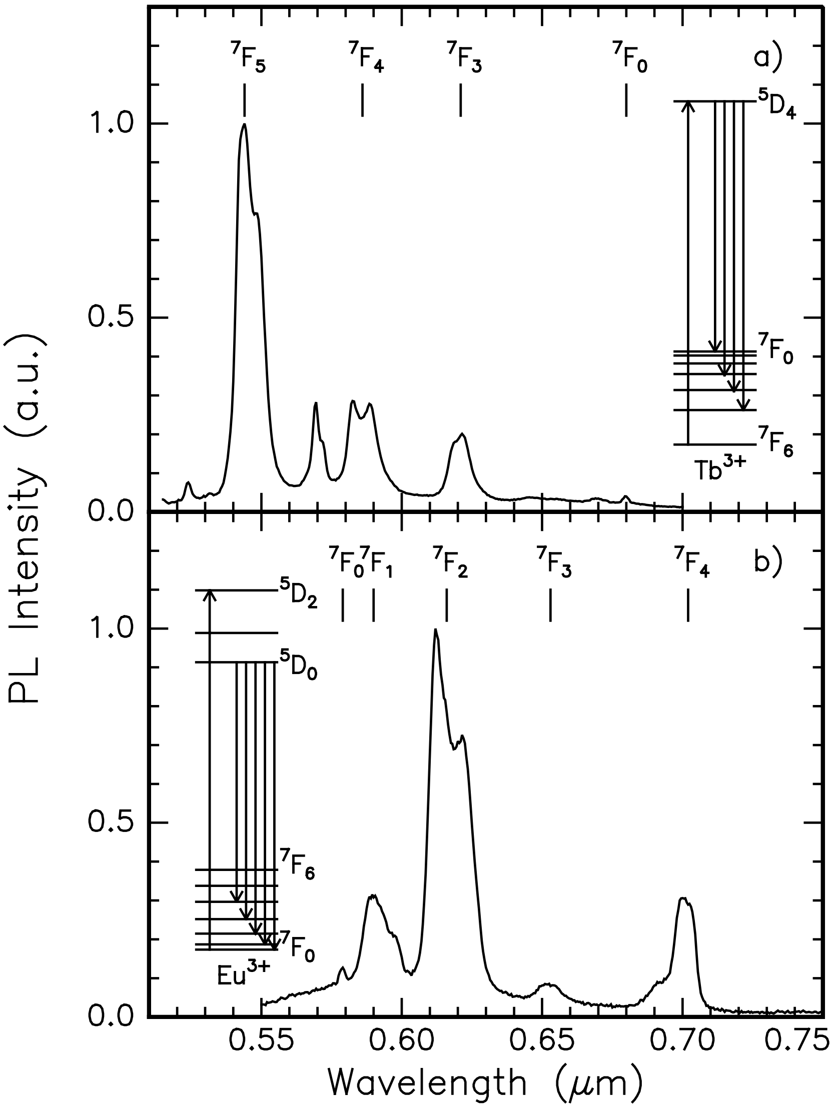

Figure 10.3: *PL spectra of a) unannealed Tb^{3+} and b) Eu^{3+} doped SiO$_2$ particles suspended in an index matching DMSO/DMF mixture. Excitation wavelengths of 488 nm (Tb^{3+}) and 465.7 nm (Eu^{3+}) were used. Level diagrams for Tb^{3+} and Eu^{3+} are shown as insets and the transitions from the initial $^5D_4$ (Tb^{3+}) and $^5D_0$ (Eu^{3+}) states to the final states are indicated by the arrows.*

and 2.43 ms for annealed particles and particles in DMSO/DMF respectively. As noted before, Er luminescence was observed for annealed particles only. The increased lifetime for Tb^{3+} and Eu^{3+} upon annealing is ascribed to the removal of quenching sites, such as (point) defects in the silica glass network, or impurities such as –OH and –CH [182]. Indeed the observed lifetime increase upon suspending the colloids in DMSO/DMF may be ascribed to the removal of –OH groups that interact with the RE ions.

Finally we note that during RBS measurements, using a 20 nA, 2 MeV He$^+$ beam in a 1 mm diameter spot, both the Eu^{3+} and Tb^{3+} doped colloids show red and green ionoluminescence respectively, that is clearly visible to the naked eye. This shows that the RE

Table 10.1: *Measured PL lifetimes of Er^{3+}, Eu^{3+} and Tb^{3+} ions. Lifetimes of the RE ions are tabulated for unannealed particles on a Si substrate, particles annealed for 30 min. at 900 °C under flowing O_2 and particles suspended in a DMSO/DMF mixture. Er^{3+} luminescence was observed only for the annealed particles.*

RE ion	not annealed	900 °C 30 min	DMSO/DMF solution
Er^{3+}	–	13.2 ms	–
Eu^{3+}	0.15 ms	1.00 ms	1.29 ms
Tb^{3+}	0.66 ms	1.15 ms	2.43 ms

ions in the SiO_2 particles can be excited by other means than optical pumping, paving the way to use for instance cathodoluminescence techniques to probe the properties photonic crystals.

10.5 Conclusions

In conclusion, we have successfully applied seeded growth in the synthesis of 194 nm diameter, monodisperse, Er^{3+}-doped colloidal particles using an acid based reaction. Without using seeded growth, bulk Er-doped spherical particles with an average diameter of 2.2 μm and a $\sim$40% polydispersity are formed. The typical Er concentration is 0.15–0.18 at.%. Identical photoluminescence spectra were observed from both the polydisperse and seeded growth particles after annealing for 30 min at 900 °C in flowing O_2. The luminescence lifetime is 13.2 ms, corresponding to a quantum yield as high as 70%. Visible luminescence from bulk-doped (polydisperse) Eu^{3+} and Tb^{3+} doped particles was observed, with lifetimes in the ms range for both annealed and unannealed particles. The particles described in this chapter might find future application as optical probes inside photonic crystals.

Part III

3-D

11

Superstructure and finite size effects in a Si photonic woodpile crystal

The reflectivity of finite-thickness silicon photonic woodpile structures was measured in the wavelength range from 0.9 μm to 1.7 μm. Polarization and surface orientation dependent measurements were performed as function of angle of incidence and the data were compared with rigorous calculations for the finite structure. Due to the finite size, the reflectivity near the stopgap edge is strongly orientation and polarization dependent. Clear stopgaps can be identified and good agreement with calculations is found. Outside the stopgap region, Fabry-Perot type resonances are observed that are related to the finite thickness of the photonic crystal. In the stopgap region clear dips are found that are not reproduced in the calculation for perfect, finite-size crystals. These are due an irregularity in the pitch of the woodpile structure as observed in electron microscopy images. This irregularity can be described in terms of a superstructure that introduces additional bands due to zone folding of the bandstructure. Calculations based on the superstructure successfully reproduce the major features in the experimental data.

11.1 Introduction

Photonic crystals are composite dielectric materials, that have a periodic variation in refractive index on a length scale comparable to the wavelength of light. Since their introduction [3, 4] these photonic crystals have attracted a lot of attention because of their special optical properties. For sufficiently high index contrast between the materials, photonic crystal structures can be made that do not allow light propagation in any direction in the structure for a limited range of frequencies. This range of frequencies is called the photonic bandgap and is commonly investigated by reflection and transmission measurements: no transmission and 100% reflection are expected in the bandgap region. Photonic crystals can be used to manipulate optical modes in a controlled way, to modify or inhibit spontaneous emission [4] or to localize light [3].

For optical and near-infrared wavelengths, photonic crystals require feature sizes of typically 100 nm. Such structures can be made by self assembly and infiltration techniques [20, 21] or by using microfabrication [29, 31, 32]. In this Chapter, we will focus on the microfabrication approach. The most amenable structure to microfabrication is a layer-by-layer structure built from layers of parallel dielectric rods (often called a “woodpile” crystal). Using high index semiconductor materials this structure can be made using advanced micromachining and integrated circuit processing techniques. This structure has been studied extensively both theoretically [183, 184] and experimentally [17, 29, 31, 185]. The photonic bandgap in this structure occurs between the first and second bands in the bandstructure and is thus relatively insensitive to such variations in the structure. Experimentally, the existence of a photonic bandgap for near-infrared wavelengths in woodpile crystals has been deduced from reflectivity and transmission measurements both on GaAs [31] and Si [29, 186] structures.

For near-infrared wavelengths existing data report on results with unpolarized light, while experiments with microwaves, on much larger crystals, show a strong polarization dependence [15, 17]. Thus, polarization dependent measurements on near-infrared woodpile structures are of great importance. The determination of a photonic bandgap at near-infrared wavelengths in an experimentally realizable structure is hampered by the finite number of layers in crystals made by microfabrication techniques. However, both the orientation and termination of the crystal surface are known exactly and this opens the unique possibility to study the effects of polarization and surface orientation in detail.

The photonic crystals in this study are made using the layer-by-layer approach [30, 183] and are designed to have a photonic bandgap around the important telecommunication wavelength of 1.5 μm. The crystals consist of 5 layers of stacked poly-crystalline Si bars and their reflective properties have been studied before [29, 30, 186]. We have done reflectivity measurements on these crystals for different polarizations and surface orientation as function of angle of incidence. The data are compared to calculations done for the finite crystal under study; a comparison that has not been made before. The experimental reflectivity is strongly dependent on both polarization and surface orientation of the crystal. In the stopgap region all data show near 100% reflectivity and good quantitative agreement with calculations is found. Outside the stopgap region, Fabry-Perot type of resonances occur due to the finite thickness. Electron microscopy images indicate that the structure under study is slightly different from the perfect woodpile structure. The experimental structure shows a variation in pitch between alternating rod pairs. A calculation, that includes this imperfection, shows additional features in the reflectivity that exactly match the experimental data. These additional features can be explained in terms of folding of the bandstructure of a superstructure.

11.2 Experimental structure

Photonic crystals are fabricated from poly-crystalline Si (p-Si) using lithography and ion etching techniques according to a layer-by-layer design, developed for Si by Lin and Fleming [30, 183]. The design uses layers of parallel one-dimensional rods of rectangular cross section. The layers are stacked such that the orientation of the rods on alternate layers is rotated by 90°. Between every two layers, the rods are displaced relative to each other by exactly half the pitch between the rods. In this way a structure is built that repeats itself every four layers and has a face-centered-tetragonal lattice symmetry. The crystals described in this work are composed of p-Si bars with a width of 170 nm and a height of 200 nm. The pitch between rods is $\sim$650 nm and the crystal in this study consists of 5 layers of stacked parallel rods. The volume fraction of dielectric (p-Si) is 0.28 in this case. The crystal is designed to have a complete photonic bandgap including the important telecommunication wavelength of 1.5 μm. Si is transparent at this wavelength and is thus well suited since it provides a high index contrast (n = 3.45 at λ = 1.5 μm [187]). Figure 11.1 shows scanning electron microscopy (SEM) images of the crystals used in this study, looking from the top (a) and under an angle of 80° (b). The individual rods of p-Si are clearly visible in Fig. 11.1 which shows both the 90° rotation of alternate layers (Fig. 11.1a)) and the displacement by half the pitch between every two layers (Fig. 11.1a) and b)).

The photonic crystal is fabricated on a 6 inch Si wafer using advanced silicon processing developed for the fabrication of micro-electro-mechanical systems and integrated circuits. First a $\sim$70 nm thick silicon nitride film is deposited on the substrate, followed by low-pressure chemical vapor deposition of a p-Si layer. The p-Si is then patterned to define the first layer of parallel rods. This requires the fabrication of feature sizes down to 170 nm and is achieved using a fillet process as described in detail elsewhere [30]. The essential steps are depicted in Fig. 11.2. In a fillet process the minimum feature size is determined by sidewall coverage of a deposited thin film. In this fillet process first a structure is defined that has a relatively large feature size (Fig. 11.2a)). Next, a thin film of p-Si is deposited over the structure (Fig. 11.2b)) and then subjected to isotropic reactive ion etching. As a result a thin sliver of p-Si remains on the sidewalls of the SiO_2 bars (Fig. 11.2c)). If the bar height is several times greater that the thickness of the deposited film, then the width of the fillet is equal (or at least proportional) to the film thickness. Using this procedure thus relaxes the requirements on the photopatterning, since the minimum feature size equals the pitch in between the rods (650 nm). After removing the SiO_2 bars, the remaining p-Si slivers are used as a mask for ion etching an underlying p-Si film.

After etching, the open space in between the rods is filled with SiO_2 and the layer is planarized and polished using chemical-mechanical-polishing (CMP). The planarization step is critical, since this prevents the topography generated in the first level from being replicated in the subsequent level. After CMP of the first layer a second layer of p-Si is deposited and patterned. The entire process is repeated until 5 layers of rods are fabricated. After completion of the entire structure the SiO_2 is removed by selective wet etching.

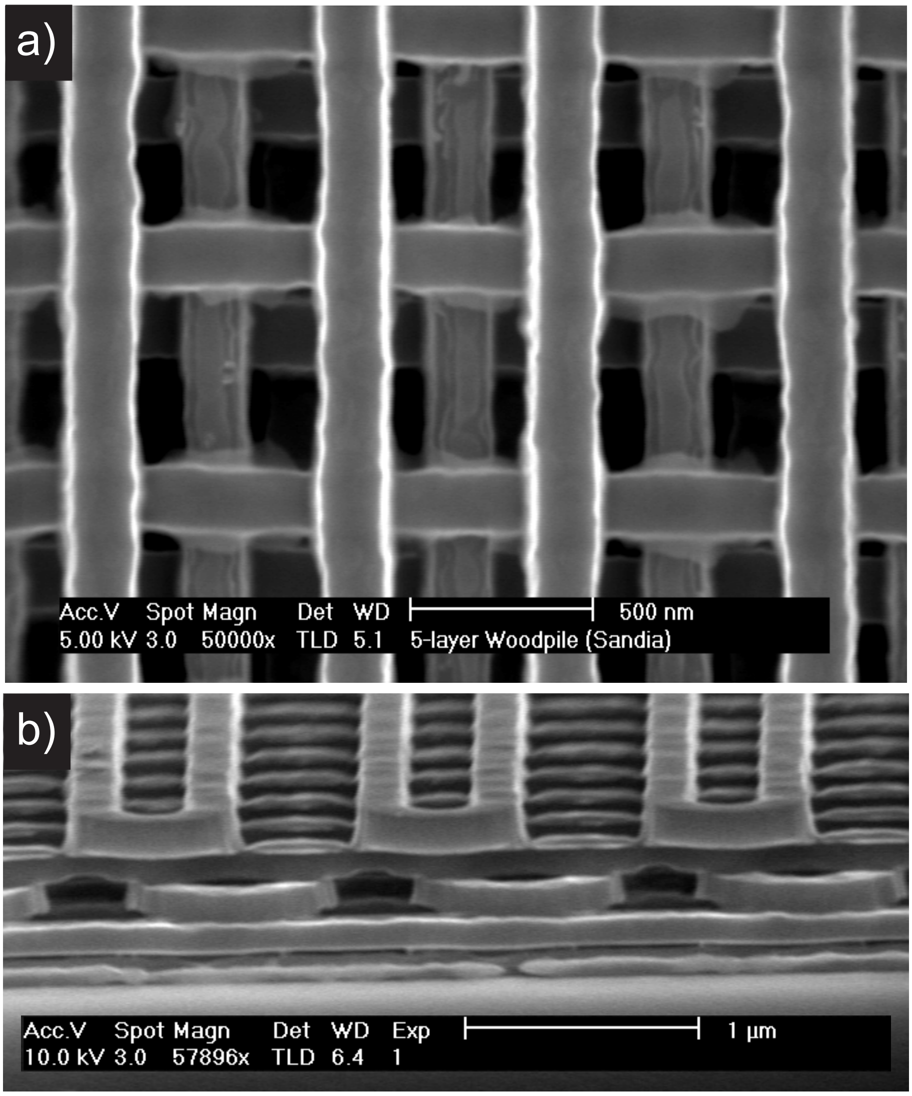

Figure 11.1: *SEM images of the 5-layer woodpile structure; (a) Top view and (b) side view. The rods are 170 nm wide and 200 nm high and the pitch between rods is targeted at 650 nm. As can be seen, there is a variation in the pitch between alternating rod pairs caused by the fillet process. However, the sum of two adjacent pitches is always 1300 nm.*

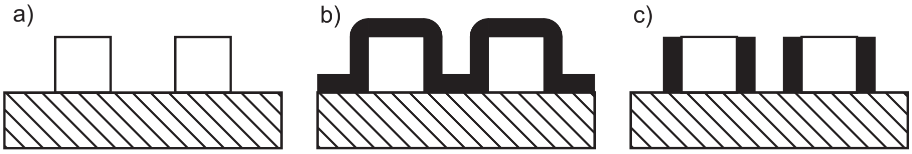

Figure 11.2: *Schematic representation of the essential steps in the fillet process (cross-section): a) Definition of an array of SiO_2 bars on a p-Si layer (hatched area) b) The bars are covered with a thin p-Si layer. c) After anisotropic etching of the structure in b) a thin sliver of p-Si material remains at the sidewall. The thickness of these slivers is equal (or at least proportional) to the thickness of the deposited layer. The slivers then serve as a mask for etching the underlying p-Si layer, and are much smaller than the originally patterned structure in a).*

As can be seen in Fig. 11.1 there is a slight variation in pitch between alternating rod pairs within each layer, which is a result of the fillet process. However, the sum of the two adjacent pitches is always exactly 1300 nm and is defined by the pitch of the SiO_2 bars used in the fillet process. Note that this variation in pitch is not intrinsic to the fillet process or other Si processing techniques in general. In principle, the variation in pitch observed here can be avoided with relative ease. The typical U-shaped profiles visible in Fig. 11.1b) occur at the edges of the crystal and are a consequence of the fillet process as well. The individual crystals on the wafer are 2×2 mm in size and the rods have the same alignment in all crystals covering the 6 inch diameter wafer. While the thickness of the crystals is finite (5 layers) the in-plane structure can be considered as infinite.

11.3 Numerical method and model

To calculate the spectral reflectivity of these finite woodpile crystals, a numerical method is employed that is based on the generalization of the method of "exact eigenvalues and eigenfunctions" used in the study of lamellar gratings [188–190]. The woodpile structure under consideration can be described as a stack of gratings. Using this method, the dielectric function is represented exactly and the electromagnetic field in each layer of rods (grating) is expanded in a suitable basis of "exact eigenfunctions". In this way, convergence problems associated to Gibbs phenomena in a Fourier approximation (plane wave method) are avoided. Next, the stable R-algorithm, developed by Li et. al [191], is used to obtain an expansion of the electromagnetic field in a stack of several grating layers. Finally, the electromagnetic fields in the homogeneous media above and below the stack of layers are expanded in a Fourier basis. In the far field, reflection and transmission of the incident wave are given by the reflected and transmitted fractions of the Poynting vector of the incident wave.

The structure modeled is identical to that described in the experimental section and is built up from layers of parallel rods of rectangular cross section. The rods are assumed to be non-absorbing p-Si with a (wavelength independent) refractive index of 3.45 (index of crystalline Si at λ = 1.5 μm [187]). Convergence of the calculations was verified by extending the number of eigenfunctions in the expansion, as reported in [192]. Since there is no absorption, energy conservation can also be checked by comparing the sum of the calculated transmission and reflection to the flux of the Poynting vector of the incoming plane wave. The observed difference is always less than 3%.

In this work we are mainly interested in the reflected field. The incident plane wave is characterized by the angle of incidence θ relative to the surface normal of the sample. The polarization of the incident plane wave can be specified and is either s or p-polarized. Also, the angle between the scattering plane and the long axis of the first row of rods (the sample azimuth) is specified. Thus, for each given angle of incidence four different reflectivity (and transmitivity) curves can be calculated.

The calculations are first done assuming an "ideal" crystal (i. e. without the superstructure observed in Fig. 11.1) based on the experimentally determined dimensions of the p-Si bars. In each layer the bars are 170 nm wide and 200 nm high and are placed on a pitch of 650 nm. The superstrate is air with a refractive index of 1.0. The substrate is modeled by an infinite layer of crystalline Si with n = 3.45. To model the structure correctly a homogeneous (unstructured) silicon nitride layer (n = 2.0) of 70 nm thickness is inserted in between the Si substrate and the 5-layer woodpile structure. The thickness of this layer, that was inserted as a buffer layer between the Si substrate and the woodpile structure, was determined using Rutherford backscattering spectrometry (not shown). The substrate can be modeled as being infinite since the backside of the supporting Si wafer is unpolished.

11.4 Reflectivity measurements and discussion

To probe the optical properties of the photonic crystal, the polarization dependent reflectivity was measured using a variable angle spectroscopic ellipsometer. White light from a Xe lamp was first led through a grating monochromator and then illuminates the sample under study with a parallel beam with a diameter of 1 mm. The angle of incidence, measured relative to the surface normal, can be varied between 20 and 80°. The reflected light was collected using a combined Si and Ge photodiode, covering the spectral range from 300 to 1700 nm. The incident beam is fixed, while the sample stage and detector rotate using a θ–2θ geometry. Polarization dependent measurements are done using two polarizers. One polarizer is mounted in the input beam to illuminate the sample with linearly polarized light. A second linear polarizer is mounted in front of the detector and analyzes the polarization of the reflected light. The extinction ratio of the polarizers is at least 30 dB. Reflectivity measurements are obtained by first measuring the (linearly polarized) white light spectrum of the lamp in a straight-through configuration. Next, the reflected light from the photonic crystal under study is measured. The reflectivity of the sample is then calculated by dividing the reflected intensity from the sample by the reference intensity of the lamp at each wavelength. The absolute accuracy of the reflectivity determined in this way is better than 10%.

The alignment of the first layer of rods on the surface relative to the scattering plane was verified by measuring the reflectivity for crossed polarizations, i. e. the incident light is p-polarized and the detector is configured to measure s-polarized light (or vice versa). On symmetry grounds the reflectivity for crossed polarization should be zero; experimentally this typically amounts to less than 3% (alignment is better than 2°). Figures 11.3 and 11.4 show the measured (drawn lines) and calculated (dashed lines) reflectivity spectra of the 5-layer photonic woodpile lattice at an angle of incidence $\theta = 20°$. Data are shown for s and p polarized light, as indicated by the s and p symbols in the figures. Figure 11.3 shows data for a crystal with the long axis of the first layer of rods aligned perpendicular to the scattering plane (defined by incoming and outgoing wave vectors). Measurements on the same sample, but with the long axis aligned in the scattering plane are shown in Fig. 11.4. The schematic above each figure shows the incoming and outgoing wave vectors of the light and a cross section of the woodpile defining the surface orientation. As can be seen in Figs. 11.3 and 11.4, all four possible combinations of surface orientation and polarization yield quite different reflectivity spectra.

Figs. 11.3 and 11.4 show that for wavelengths longer than $\sim$1.5 μm the reflectivity is near 100% for all four geometries, consistent with the calculated photonic stopgap at $\theta = 20°$ [183]. The observed stopgap extends into the infrared, well beyond the experimental limit of 1.7 μm, as expected from both our calculations and experiments with unpolarized light [29]. Comparing the measured reflectivity (drawn lines) and calculated values (dashed lines), good agreement is achieved for all four measurements in the region

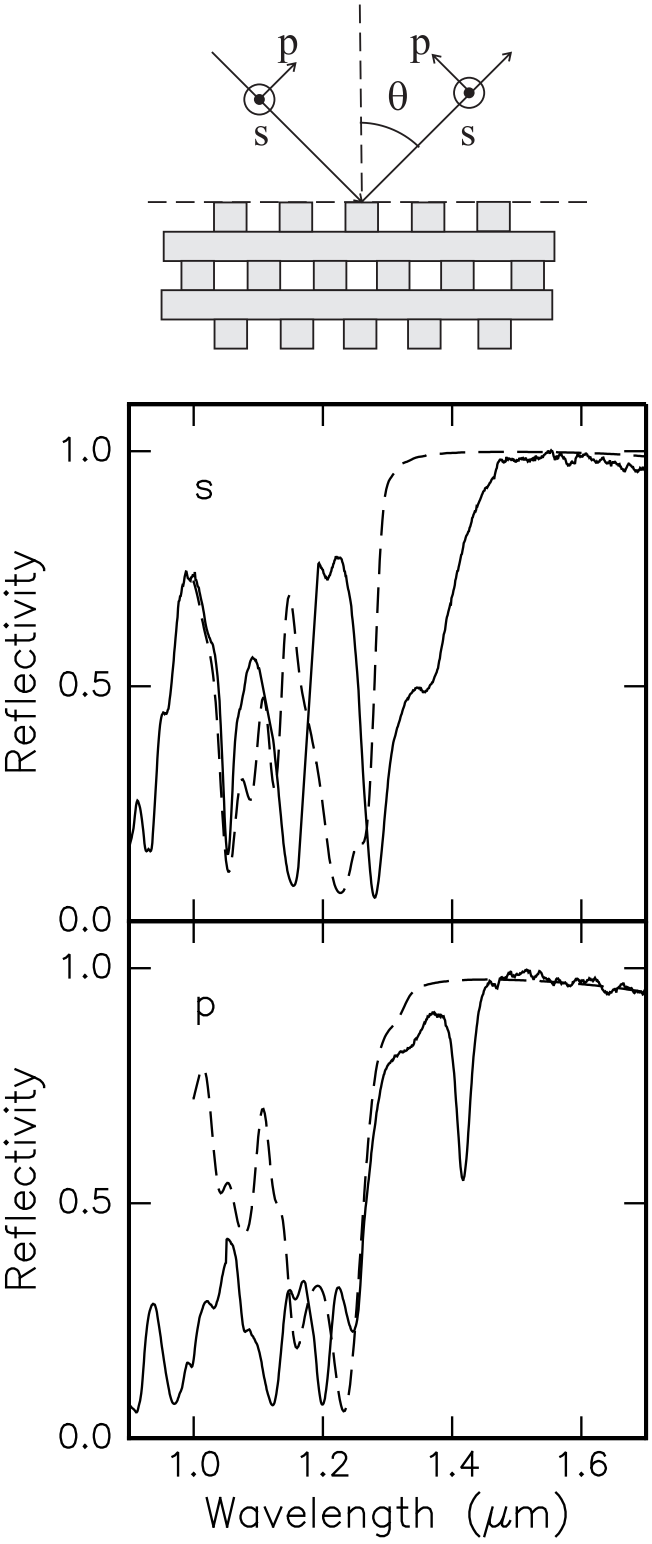

Figure 11.3: *Reflectivity spectra of the photonic woodpile lattice for s (top) and p (bottom) polarized light. The angle of incidence is $\theta = 20°$ and the long axis of the first row of rods is aligned perpendicular to the scattering plane. Both experimental data (drawn line) and calculated data (dashed line) are shown. The calculated data assume an ideal finite structure (see text).*

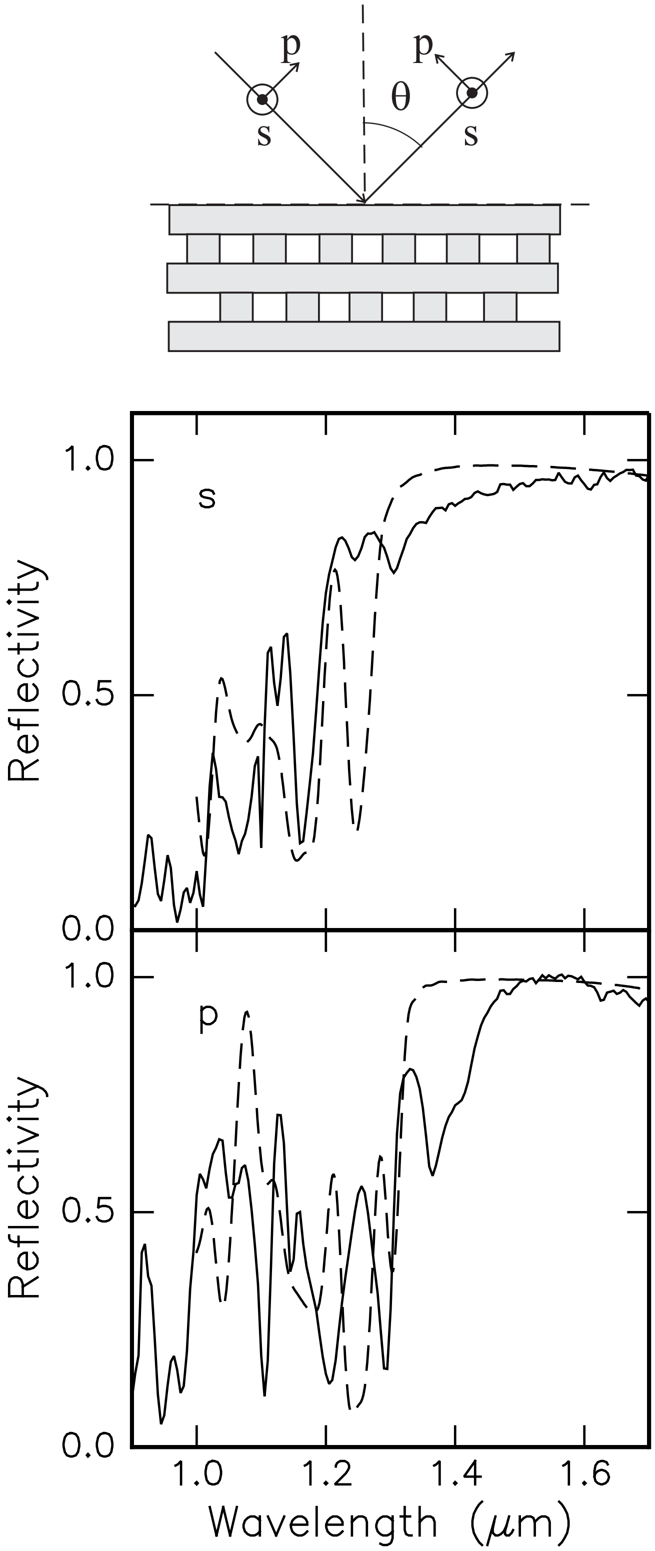

Figure 11.4: *Reflectivity spectra of the photonic woodpile lattice for s (top) and p (bottom) polarized light. The angle of incidence is θ = 20° and the long axis of the first row of rods is aligned parallel to the scattering plane. Both experimental data (drawn line) and calculated data (dashed line) are shown. The calculated data assume an ideal finite structure (see text).*

$\lambda > 1.5$ μm. The measured position of the short wavelength edge of the stopgap (defined as R = 50%) agrees well with calculations for p-polarized light, although the dips at ~1.41 μm (Fig. 11.3) and ~1.35 μm (Fig. 11.4) are not reproduced in the calculation. For s-polarized data the agreement is less satisfactory.

For wavelengths < 1.2 μm, a low reflectivity is observed since at these wavelengths no photonic stopgap exists and light can propagate in the photonic crystal. The structure in the spectra at shorter wavelengths is the result of Fabry-Perot type of resonances due to the finite thickness of the crystal. Note that in the wavelength range down to 1.15 μm (electronic bandgap of bulk Si) Si is fully transparent. For wavelengths down to 0.9 μm Si is only weakly absorbing (absorption length ~30 μm). Thus the comparison with calculations (that do not include absorption) is a valid one. For wavelengths below 0.9 μm, the specular reflectivity decreases (not shown), which can be explained by a combination of diffraction and absorption by the Si in that spectral range.

In order to optimize agreement between measured and calculated data, calculations were done for several slightly different structures. Both the width of the p-Si bars and the thickness of the silicon nitride buffer layer were varied. Decreasing the width of the bars leads to a shift of the band edge towards longer wavelength. Changing the silicon nitride thickness modifies the resonances in the short wavelength region. Best agreement between calculated data and experiment is found for the calculations in Figs. 11.3 and 11.4, that use 170 nm wide bars and a 70 nm thick silicon nitride buffer layer (see experimental section). Our data demonstrate that in particular at and below the bandgap region polarization is a key parameter determining the optical response of the photonic woodpile crystal.

Next, we discuss the angle dependence of the reflectivity for polarized light in order to experimentally determine the bandgap edge. So far, for optical and near-infrared wavelengths, experiments were only done using unpolarized light [29, 186]. Our data described above demonstrate that this is a severe limitation (see Figs. 11.3 and 11.4). Our data clearly shows a large stopgap at $\theta = 20°$, but these data confirm nor exclude the existence of a full photonic bandgap (i. e. stopgap in all direction). Figure 11.5 shows measured reflectivity spectra for three different angles of incidence (20, 50 and 80°). The reflectivity is measured for p polarized light, with the sample aligned such that the long axis of the first layer of rods is perpendicular to the scattering plane (see schematic of the geometry in Fig. 11.3). The reflectivity for wavelengths between 1.5 μm and 1.7 μm is close to 100% for all angles of incidence and a shift of the edge of the stopgap towards shorter wavelength (higher frequency) is observed for increasing angle. Clear dips in the reflectivity data are observed at $\lambda = 1.35$ and 1.42 μm for angles of incidence of 20° (as in Fig. 11.3) and 50° respectively. These dips are not reproduced by the calculation, as will be discussed later. The much broader feature around $\lambda = 1.4$ μm for an angle of incidence of 80° is also found in the calculations and has a different origin than the sharp dips observed for 20 and 50°.

Reflectivity measurements, similar to those in Fig. 11.5 were done for both polarizations and surface orientations. The angle of incidence ranged from 20° to 80°. At each angle the position of the stopgap was estimated by determining the wavelength at which the reflectivity drops below 50%. The experimental results are summarized in Fig. 11.6. Data are shown for both p polarization (solid symbols) and s polarization (open symbols). The different orientations of the first layer of rods relative to the scattering plane are indicated. ○, ● symbols indicate that the long axis of the first row of rods is perpendicular

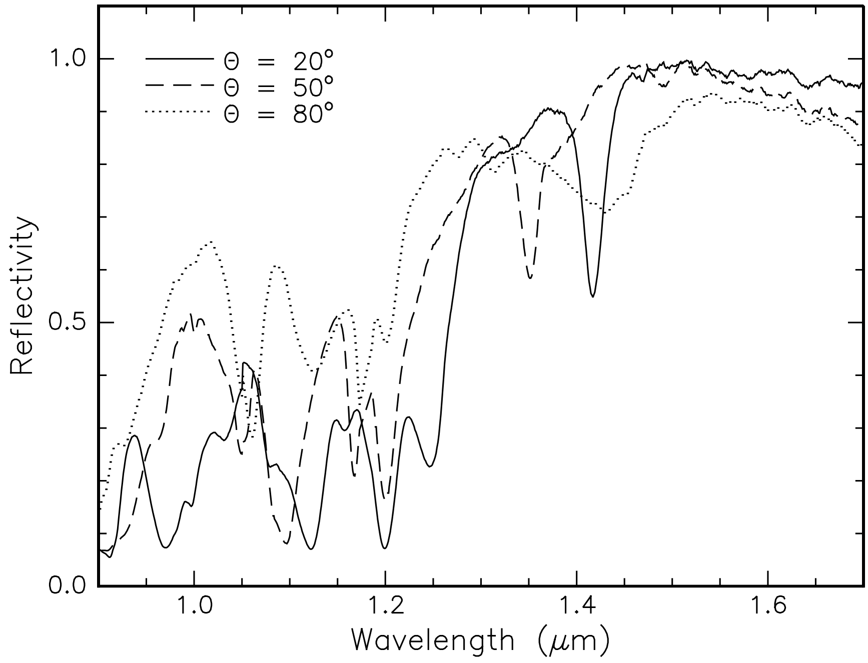

Figure 11.5: *Reflectivity spectra of the photonic woodpile lattice for p polarized light for three different angles of incidence. The long axis of the first row of rods is aligned perpendicular to the scattering plane. A clear shift of the "band edge" towards shorter wavelength is observed with increasing angle.*

to the scattering plane. △, ▲ symbols indicate that the long axis of the first row of rods is in the plane of measurement. The dashed lines connect the experimental data points and serve to guide the eye. As can be seen in Fig. 11.6 all four combinations of polarization and surface orientation lead to a different stopgap edge.

The data in Fig. 11.6 are compared to the calculated stopgap edge of a 32 layers thick crystal (drawn lines) as function of external angle. Calculations are shown for the two polarizations and are different because the coupling of the incoming plane wave to the crystal is different for the two polarizations. No difference is found for near-normal incidence as expected on symmetry grounds. In the calculations, the position of the calculated band edge as function of external angle was found to be independent of the surface orientation. This is expected, since for an infinite crystal the two orientations cannot be distinguished. Model calculations show that the effect of increasing the crystal thickness on the reflectivity is two-fold; the reflectivity in the stopgap regions further increases towards 100% and the edges of a photonic stopgap become sharper. Hence, from such a calculation the stopgap edge can be determined unambiguously.

Note that the "dispersion" curves in Fig. 11.6 are plotted as function of external angle, while a band structure is specified as function of Bloch-wave vector inside the crystal. The conversion can be made using Snell's law, i. e. the wave vector component in the direction parallel to the interface is conserved ($k_{\|} = \frac{2\pi}{\lambda}\sin\theta$). The perpendicular component of the wave vector propagating in the crystal is determined by the bandstructure.

As can be seen in Fig. 11.6 good agreement between the calculation and experimental data is observed for p polarized light with the long axis of the rods in the scattering

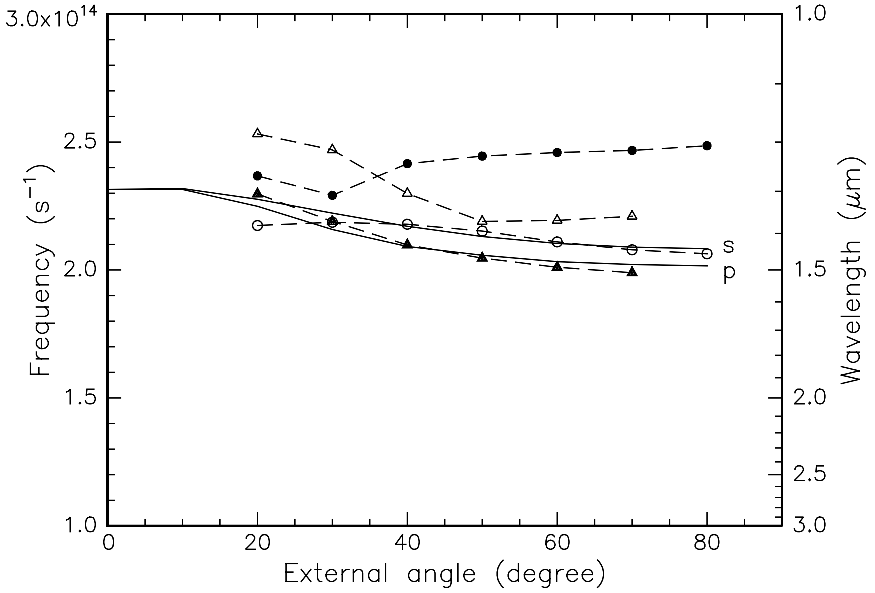

Figure 11.6: *"Dispersion" curves $\omega(k_{\|})$ obtained from reflectivity data as function of angle of incidence. The low-wavelength (high-frequency) stopgap edge is shown for p polarization (solid symbols) and s polarization (open symbols). The different surface orientation are studied: (△, ▲) indicate that the long axis of the first row of rods is in the scattering plane, (○, ●) indicate that the long axis of the first row of rods is perpendicular to the scattering plane. The dashed lines connect the experimental data points and serve to guide the eye. The drawn line shows the band edges calculated as function of external angle, obtained from a calculation on a thick crystal (32 layers). The s and p labels indicate s and p polarization for the theoretical curves.*

plane (▲ data) and for s polarized light with the long axis of the rods perpendicular to the scattering plane (○ data). In these two cases the long axis of the first, third and fifth layers of rods is aligned with (a component of) the E-field of the incoming light. Since rods are easily polarized when the E-field is in the direction of the long axis, the light effectively interacts with three layers. For the remaining two geometries, the agreement is less good, because in this case the E-field is aligned with the long axis of the rods for only two layers.

Based on bandstructure calculations that support the existence of a photonic bandgap for the present woodpile structure and the correspondence of calculated and experimental results in Fig. 11.6, we conclude that our data support the existence of a full photonic bandgap in these woodpile crystals (for an infinite crystal). The discrepancies between calculated and experimental data are due to the finite size of the crystal. In addition, the dips in the experimental reflectivity, unexplained by the theory discussed so far, make the determination of the bend edge less accurate. The remainder of this chapter discusses the origin of these dips and their influence on the bandgap in detail.

Measurements and theory on woodpile photonic crystals have mostly concentrated on the perfect structures. However, experimentally such crystal do not exist. In fact, a careful observations of the SEM images in Fig. 11.1 reveals a variation in pitch that finds its origin in the nature of the fillet process (see Fig. 11.2). So far, only a limited amount of

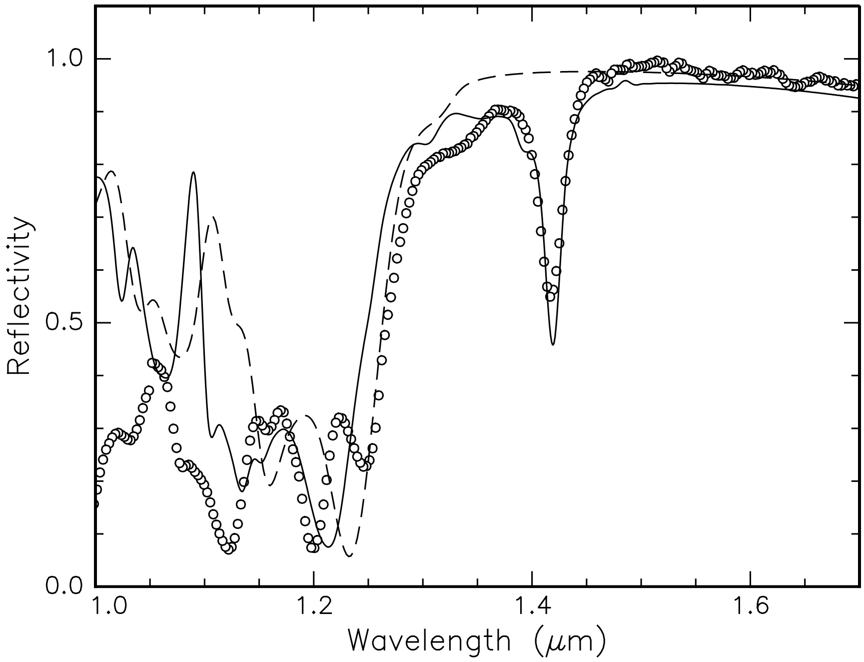

Figure 11.7: *Reflectivity spectra of the woodpile structure for p-polarized light at an angle of incidence of 20°. Experimental data (○) are compared to calculations of a perfect structure (dashed line) and structure that includes the experimentally determined superstructure in the (5-layer) crystal (drawn line). The calculation of the slightly perturbed structure gives a satisfactory description of the dip in the reflectivity at λ = 1.42 μm*

work is done to understand the effects of disorder on the photonic bandgap of woodpile structures [193, 194]. The imperfections considered typically shift or change the rods in the unit cell and thereby repeat the defect and the entire structure is still periodic. The effect of such imperfections can be calculated, since this involves a calculation of the bandstructure of a photonic crystal with a different unit cell (in our case a four times bigger unit cell is needed). Note that a clear distinction should be made between the periodic imperfections as found here, and that may lead to propagating (Bloch) modes, and random defects or disorder, that lead to localized states.

From the SEM images in Fig. 11.1 it is found that the pitch between alternating rod pairs is not constant in all layers of the structure. The pitch between rods alternates between 600 and 700 nm and creates a superstructure with a pitch of 1300 nm in both directions. Figure 11.7 shows the measured reflectivity (○) at an angle of incidence $\theta = 20°$, for p-polarized light. The long axis of the first layer of rods is perpendicular to the scattering plane (same data as in Fig. 11.3b)). Overlaid on the measurements are calculations of the reflectivity for two cases: a perfect structure (dashed line, same as in Fig. 11.3b)), and a calculation using the technique described in Section 11.3 that takes the variation in the pitch into account (drawn line). As can be seen, the distinct dip in the experimental data at 1.42 μm is very well reproduced by the calculation.

The origin of the dip in the spectra can be explained as follows. The structure that has a variation in pitch in both in-plane directions can be described using an unit cell (in real space) that is twice as large as that of the "ideal" structure. As a consequence, the irreducible part of the Brillouin zone (in reciprocal space) of this superstructure is twice as small in both directions. The bandstructure of this structure can be roughly obtained by a folding of the bandstructure of the “ideal” crystal. The result of this zone folding is that modes that exist on the edge of the Brillouin zone for a perfect crystal fold back to the center of the Brillouin zone in the case of the superstructure. In the perfect structure, modes from the second band are generally at lower energies (longer wavelength) at the edge of the Brillouin zone. The folding thus introduces propagating modes in the bandgap region and explains the observed dip in the reflectivity at $\lambda = 1.42$ μm in Fig. 11.7. Figure 11.5 shows that this dip shifts towards shorter wavelength for increasing angle of incidence. This effect too is reproduced in calculations (not shown). The remaining difference between calculation and experiment might be further improved by including the effect of index dispersion of the Si in the calculation.

11.5 Conclusions

Polarization and surface orientation dependent reflectivity spectra was measured on a Si photonic woodpile structure of finite thickness. The reflectivity was found to depend strongly on both polarization and surface orientation. In the stopgap region the reflectivity reaches a value close to 100% independent of polarization or surface orientation. A direct comparison between experimental data and calculations confirms the existence of photonic stopgaps. Comparing the experimentally determined stopgap edges with calculations yields good agreement for two combinations of polarization and sample azimuth. In the other two cases the agreement is less satisfactory. The agreement is best for measurement conditions that have a component of the E-field aligned with the first layer of rods, effectively increasing the interaction with the 5-layer crystal. The calculated position of the band edge for a 32 layer thick crystal was independent of surface orientation of the first layer. Hence, a measured orientation dependence is a result of the finite thickness of the crystal.

At shorter wavelengths, outside the stopgap region, the structure observed in the reflectivity data is a result of Fabry-Perot type resonances related to the finite thickness of the photonic crystal under study. These resonances depend on the vertical component of the Bloch-wave vector in the structure and are sensitive to small changes in the structure. Experimentally it was observed that the photonic woodpile structure has a variation in pitch, which introduces a superstructure. This superstructure was introduced in the calculation and results in better agreement with experimental data. In particular a distinct dip observed in the experimental reflectivity spectra is successfully reproduced by the calculation. To origin of the dip was explained in terms of new bands introduced in the bandstructure described by zone folding of the bandstructure.

12

Modified spontaneous emission from erbium doped photonic woodpile crystals

The spontaneous emission from luminescent Si photonic woodpile crystals doped with optically active erbium ions is studied. Erbium ions are implanted in the center of the 5-layer crystal. The polycrystalline Si shows a broad defect-related emission extending from 1.1–1.7 micron that serves as an ideal probe of the photonic bandstructure. A large band of reduced emission (1.4–1.7 μm*) is observed from the photonic crystal and also the Er emission collected from the crystal is strongly suppressed. The spectral changes are described by a model that takes into account both changes in the local density of states and the internal Bragg scattering in the crystal. It is shown that the quantum efficiency of the optical transition determines the effect of the photonic crystal on spontaneous emission in an (initially) counter-intuitive way. A spectral attenuation of* $\sim$*5 dB per unit cell is derived from the data, consistent with theory and transmission data. These measurements are the first demonstration of modified spontaneous emission from a Si photonic crystal at the important telecommunication wavelength of 1.5* μ*m.*

12.1 Introduction

A photonic crystal is a three-dimensional periodic arrangement of dielectric material that interacts strongly with light. Photonic crystals constitute a new class of materials that can be used to control spontaneous emission and to manipulate optical modes in ways that were impossible so far. A major challenge in photonic crystal design and fabrication is to realize a photonic crystal with a full photonic bandgap, i. e. a structure in which the propagation of light within a well-defined frequency range is forbidden in any direction in the crystal. This requires on the one hand the use of materials with sufficient refractive index contrast, and on the other hand a well-chosen crystal symmetry.

In the past few years, intense research has focused on the fabrication of photonic crystals for optical wavelengths. Several methods have been developed and two different techniques have appeared as particularly attractive. They are based on either self-assembly techniques leading to colloidal crystallization, or high-resolution lithography based on Si integrated circuit processing techniques. The first technique can lead to true three-dimensional crystals, though of limited size, and often with unintentionally incorporated defects or disorder. The bandgap in these inverted-opal type crystals is very sensitive to disorder as it appears between the eight and ninth bands. Using infiltration of a silica colloidal crystal, three dimensional Si photonic crystals can be made [21, 22]. These crystals show high reflectivity in the near-infared region of the spectrum related to the presence of a photonic bandgap at that wavelength [22]. Lithographic techniques, on the other hand, lead to large (up to 6 inch) crystals [29, 30] in two dimensions, but with the third dimension limited to several crystal lattice units. Lithography can be directly applied on materials such as Si or GaAs that possess the index contrast large enough to create a full photonic bandgap. Fleming et al. have demonstrated how a photonic woodpile lattice based on Si can be made using 0.35 μm optical lithography [30]. Noda et al. later showed similar results for the same structures based on GaAs [31]. The woodpile structure is rather robust against disorder as the photonic bandgap appears between the first and second bands.

With several routes to photonic crystal fabrication now successfully developed, the challenge is to demonstrate the existence of a true photonic bandgap in these crystals. So far, optical characterization of photonic crystals with a presumed full photonic bandgap mostly involves optical spectroscopy using external beams, probing reflectivity and transmission. From such measurements it is not possible experimentally to determine the full bandstructure in all directions in the irreducible part of the Brillouin zone. For example, reflectivity is often measured over a “full” range of angles from 0–90 degrees with respect to the surface normal. This, however, does not corresponds to a full range of angles inside the crystal. Also, surface roughness often present on colloidal crystals makes a precise determination of the reflectivity ambiguous.

A method to probe photonic bandstructure is to incorporate optical probes inside the photonic crystal and to study their spontaneous emission. In a true three-dimensional photonic crystal, no emission should be detected in any direction. Studies of spontaneous emission are also interesting in crystals with a partial gap (i. e. inhibition in a limited range of directions only), or in thin crystals that are not truly three-dimensional. In this case spontaneous emission can be actually observed and its spectroscopic and time-dependent properties can provide important information on the bandstructure as well as on the local optical density of states.

In this Chapter we present the first data on modified spontaneous emission of Si photonic woodpile crystals. The crystals are very large (compared to the wavelength) in two dimensions, and limited to 5 layers in the third dimension. This enables the detection of spontaneous emission in the third direction. We study optical emission both from well-defined atomic-scale defects that are intrinsic to the poly-crystalline Si base material, and of optically active Er ions that are ion implanted into the photonic crystal. Our data are the first to demonstrate large effects on spontaneous emission in a photonic crystal in the important telecommunication wavelength range around 1.5 μm.

12.2 Er ion implantation

The photonic crystal was fabricated as described elsewhere [30]. In short, a one-dimensional array of 180 nm wide and 200 nm high poly-crystalline Si (p-Si) bars is fabricated onto a Si substrate. The p-Si layer is deposited on the substrate using low-pressure chemical vapor deposition at 570 °C using silane as a source gas and annealed at 1040 °C to convert any amorphous silicon to poly-crystalline Si. The bars are etched into the p-Si layer using a fillet process that uses 650 nm wide SiO_2 bars [30]. The Si bar repeat period in each layer is 650 nm. After completion of a layer, the empty space between the bars is filled with SiO_2 and then planarized with chemical mechanical polishing. Next, a second layer of Si bars is formed, rotated by 90 degrees. This process is repeated five times to lead to a structure with 5 layers (2.5 primitive unit cells), as schematically indicated in Fig. 12.1. After completion of the full structure the SiO_2 is etched out using a wet chemical process. Bandstructure calculations for an infinite Si woodpile crystal show a large bandgap (relative bandwidth $\Delta\lambda/\lambda \approx 20\%$). Calculations and measurements on finite thickness woodpile crystals show an attenuation of roughly 5 dB per unit cell at 1.5 μm [29, 195]. This makes the present five-layer crystals ideal to study photonic bandstructure, as significant interaction with light is achieved, but at the same time light is still able to escape from the crystal.

915 keV erbium ions were implanted into the woodpile lattice at normal incidence at a temperature of 77 K to a dose of 1.5×10^{13} Er cm^{-2}. To activate the Er, oxygen was co-implanted to a dose of 1.5×10^{14} O cm^{-2} (Er:O ratio 1:10) at an energy of 145 keV to overlap the Er distribution. The projected range of 915 keV Er in bulk Si is 300 nm and the straggle (σ) of the distribution is 80 nm. The Er distribution is sketched in Fig. 12.1 (side view), showing that the Er is preferentially implanted in the 2^{nd}, 3^{rd} and 4^{th} layers. Part of the erbium (45%) is implanted in the crystalline Si (c-Si) substrate. However, given the large attenuation, at λ = 1.5 μm, luminescence from this depth will not be detected in our optical measurements. Planar p-Si samples were implanted with Er and O ions to the same doses as in the woodpile sample and serve as a reference. The p-Si samples were made by deposition of a 2 μm thick amorphous Si layer on a Si substrate covered with a 1 μm thick Si_3N_4 layer.

After implantation all samples were annealed at 600 °C for 3 hrs in a vacuum furnace at a base pressure better than 5×10^{-7} mbar, followed by a 1000 °C anneal for 60 s in flowing nitrogen using a rapid thermal annealer. Photoluminescence (PL) measurements were taken from the samples cooled to 12 K in a closed-cycle He cryostat using the 488 nm line of an Ar ion laser as a pump source. The laser beam was modulated on-off with an acousto-optic modulator at a frequency of 20 Hz. The laser power was kept constant at

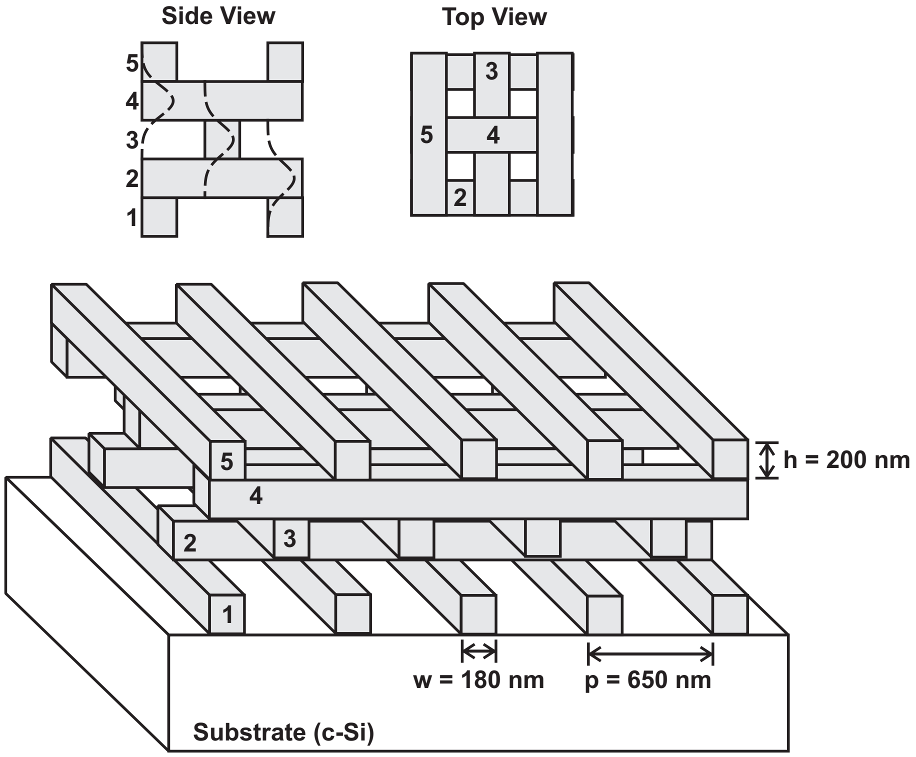

Figure 12.1: *Schematic 3-D drawing of the woodpile lattice showing the stacking of the 5 layers of poly-crystalline Si bars in the woodpile structure (2$\frac{1}{2}$ primitive unit cells). Top and side views of the structure are shown as well. The depth of the Er (O) implantation is indicated by the Gaussian shaped curves in the side view.*

10 mW in our experiments and was focused to a 1 mm diameter spot on the sample, under an angle of incidence of 20° from the surface normal. The luminescence was collected using a lens and focused on the entrance slits of a 48 cm grating monochromator, collecting a cone with a full angle of ~20° (a solid angle of 10 msr).

12.3 Photoluminescence

Figure 12.2a) shows the measured luminescence at 12 K from both the implanted woodpile lattice (——) and the p-Si reference sample (—×—). Luminescence measurements were made using both the 457 and 514.5 nm lines of the Ar ion laser and resulted in identical PL spectra. The broad luminescence band extending from the indirect electronic band edge of bulk Si (1.1 μm) to well beyond 1.7 μm is attributed to defect mediated optical transitions in the p-Si host material. This indicates that the luminescence from the p-Si material is electron-hole pair mediated. Superimposed on the defect band, a sharp peak is observed at a wavelength of 1.539 μm which is due to the $^4I_{13/2} \rightarrow ^4 I_{15/2}$ intra-4f transition of implanted Er ions. The broad defect luminescence band shows four broad features at a constant energy difference of ~0.07 eV peaking at wavelengths of 1.25 (0.99 eV), 1.35 (0.92 eV), 1.475 (0.84 eV) and 1.61 μm (0.77 eV). This broad luminescence band is observed in unimplanted samples and in samples implanted to different Er and O concentrations and is therefore not related to the ion-implantation itself nor to erbium or oxygen. Thermal annealing of the p-Si material leads to a decrease in luminescence intensity, but

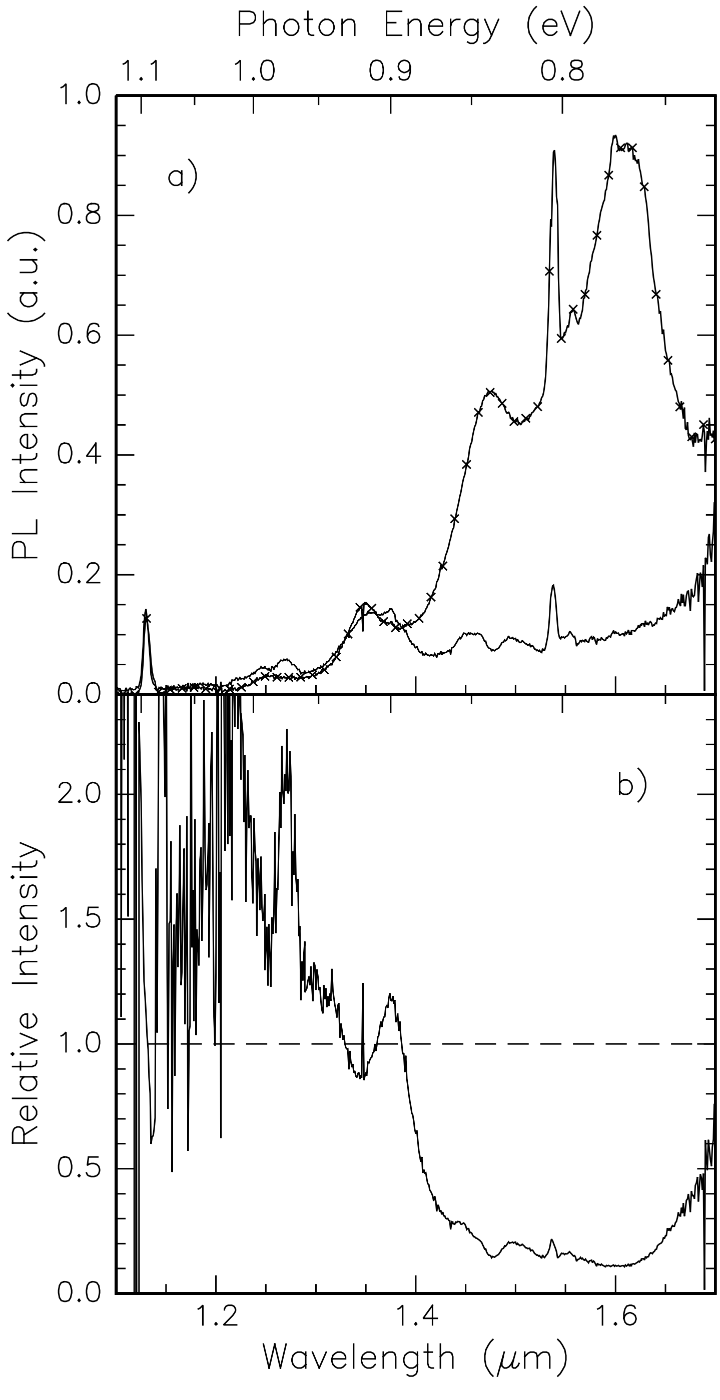

Figure 12.2: *(a) PL spectra measured at $T = 10$ K of an Er implanted photonic crystal (——) compared to the emission from the p-Si reference sample (—×—). (b) Relative intensity obtained by dividing the measured intensity from the photonic crystal by the intensity of the reference sample. A clear dip in the relative intensity is observed around 1.5 μm showing that the emission from the photonic crystal is suppressed inside the stop gap.*

does not alter the structure observed in the luminescence spectrum. Experiments on the same structure performed at temperatures up to 125 K show an overall decrease in PL intensity, which is attributed to thermalization of trapped carriers responsible for the luminescence of the p-Si. However, the ratio in PL intensity as in Fig. 12.2b) was found to be independent of temperature.

The two spectra for the photonic crystal and the reference sample, shown in Fig. 12.2a), are taken at the same pump power and the spectral intensities can thus be compared directly. As can be seen, the luminescence intensity collected from the two samples is similar for wavelengths shorter than 1.4 μm, while for longer wavelengths a much lower intensity is observed from the woodpile structure than for the p-Si reference. The ratio between the luminescence from the woodpile lattice and the p-Si reference is plotted in Fig. 12.2b). It shows a broad dip in the range from 1.4 to 1.7 μm, indicative of a photonic bandgap. Optical transmission and reflection measurements [29, 30, 186] (see Chapter 11) of the same crystal also show a gap in this wavelength region. In addition, our data are consistent with calculations of the emissivity of an electrical dipole in the middle layer of a finite-thickness woodpile lattice [195]. These calculations show that a reduced emission over this wavelength range is expected. Two peaks at wavelengths of 1.270 μm and 1.375 μm are observed in the ratio, while a dip is observed at 1.345 μm. These are possibly related to an increase and decrease, respectively, of the (local) density of states (DOS) at these wavelengths.

The intensity ratio observed in Fig. 12.2b) is determined by a photonic bandgap effect as well as by the distribution of the Ar pump laser light over the structure. The pump power distribution in the reference sample is relatively simple and decays exponentially in the p-Si because of the large absorption of Si in the visible (absorption length $\sim$ 1 μm). At the Ar laser wavelength of 488 nm the photonic crystal does not show a photonic bandgap and light can propagate through the structure. As the Si is strongly absorbing, most of the light is directly absorbed in the photonic crystal. This pumping mechanism explains the intensity ratio close to unity outside the bandgap region, since the areal density of e-h pairs generated (by optical absorption of laser light) is comparable for the photonic crystal and the reference sample.

Figure 12.2a) also shows a sharp luminescence peak at λ = 1.536 μm, related to intra-4f transitions of Er^{3+}, both in the PL spectra for the reference and the woodpile sample. The Er emission collected from the photonic crystal is strongly suppressed compared to that of the reference sample. Interestingly, the ratio between the spectra in Fig. 12.2b) shows a small Er related peak. This indicates that the effect of the photonic crystal on the Er ions is different than the effect on the defect luminescence. In the remainder of this chapter this will be discussed in more detail by combining the data in Fig. 12.2 with luminescence lifetime measurements.

Decay traces of the luminescence taken at the peak wavelength of the erbium emission (λ = 1.536 μm) are plotted in Fig. 12.3. The decay traces for both the reference sample and the woodpile structure show an initial fast decay component limited by the detector response time, followed by a slow component. Lifetime measurements at different wavelengths indicate that the fast component is related to the defect luminescence, while the slow component is related to the Er emission. The ratio between fast and slow components exactly matches the ratio between defect and Er luminescence at 1.536 μm observed in both the spectrum for the photonic crystal and reference sample in Fig. 12.2a). The slow component can be described by a single-exponential decay with lifetimes of 1.09 ms and

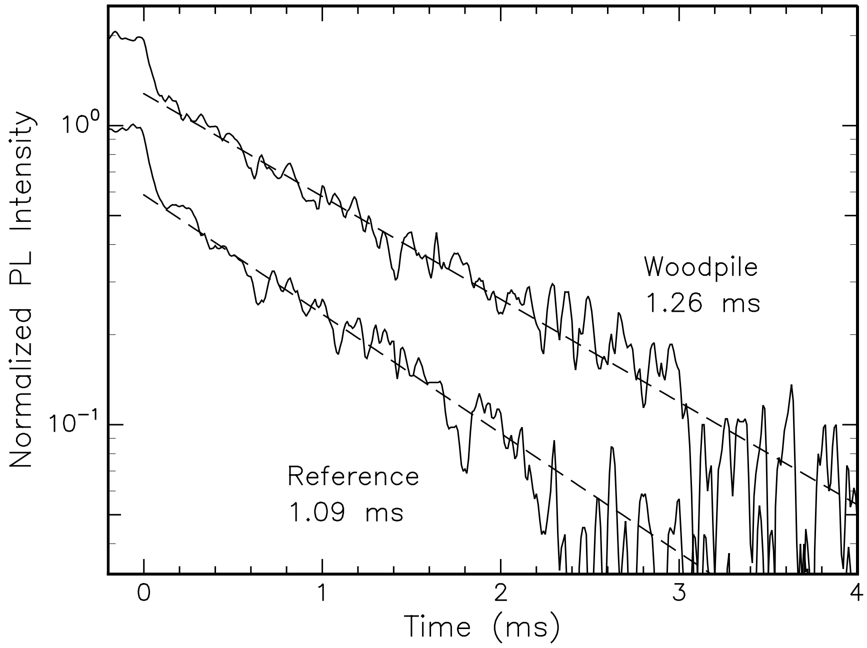

Figure 12.3: *Photoluminescence decay traces of the woodpile sample and the reference sample. Decay traces were measured at 10 K at a wavelength of 1.536 μm, corresponding to the peak of the Er luminescence. The luminescence shows an initial fast decay related to the defect emission and a slow component related to luminescence from erbium ions embedded in the p-Si.*

1.26 ms (W = 920±50 s^{-1} and 790±50 s^{-1}) for the reference sample and the photonic crystal sample respectively.

12.4 Results and discussion

The data reported in the preceding section clearly demonstrate that spontaneous emission is affected by the photonic bandgap of the woodpile lattice. The effect is twofold. First, radiation that is emitted from within a crystal can be Bragg reflected which leads to a dip in the spectra over the stopgap region. This effect is present in any photonic crystal and does not require a complete photonic bandgap nor does it require a high index contrast. The second effect is the inhibition of spontaneous emission and becomes important if a significant amount of the entire 4π solid angle can be blocked by Bragg reflections. If an atom is placed inside such crystal it cannot decay in all directions since propagation of light is forbidden. Even if the bandgap is incomplete the DOS can be strongly reduced and spontaneous emission is partly inhibited. To evaluate the exact effect of the photonic crystal on the spontaneous emission rate both the position of the optical probe and the local density of states (LDOS, see Part II of this thesis) must be evaluated.[*]

For any luminescent species, the total PL emitted over all directions depends on the steady-state population of luminescing species and the radiative rate, W_{rad}, of that species.

---

[*] Note that this LDOS, if integrated over the unit cell of a photonic crystal, differs by a factor $\varepsilon(\mathbf{r})$ from the conventionally used DOS [43].

The steady state population that can be achieved depends on the pump rate and the total decay rate, W_{tot}. This total decay rate contains a radiative contribution and a non-radiative contribution. For a simple two-level system in the low pump-power limit the total PL intensity emitted is given by:

$$I_{PL} \propto R_{pump} \frac{W_{rad}}{W_{tot}} N \tag{12.1}$$

where, R_{pump} denotes the pump excitation rate and N is the total number of excitable species. The factor W_{rad}/W_{tot} equals the internal quantum efficiency (QE). Both the Er and defect luminescence in Fig. 12.2 can be described using this simple two-level model. Next, the effect of Bragg reflection of the crystal must be included. Defining the fraction of light collected from the structure as η the ratio in PL intensity (I_{PC}/I_{ref}) (see Fig. 12.2b)) between the photonic crystal (PC) and the reference sample can be expressed as:

$$\frac{I_{PC}}{I_{ref}} = \frac{W_{rad,PC}}{W_{rad,ref}} \frac{W_{tot,ref}}{W_{tot,PC}} \frac{\eta_{PC}}{\eta_{ref}} \tag{12.2}$$

where $W_{rad,PC}$ $(W_{rad,ref})$ and $W_{tot,PC}$ $(W_{rad,ref})$ denote the radiative and total decay rate of the emitting species in the PC (reference) sample. η_{PC} and η_{ref} are the beforementioned collection efficiencies of the luminescence from the PC and reference sample respectively. Note that Eq. 12.2 holds for both the defect luminescence and the Er luminescence separately. This equation thus includes three important parameters that determine changes in the spontaneous emission collected from a photonic crystal:

1. changes in W_{rad} due to changes in the (local) DOS
2. internal quantum efficiency of the optical transition involved
3. collection efficiency / Bragg reflection effect

The importance of the quantum efficiency in Eq. 12.2 is obvious; in practical studies however it is often neglected, most often because it is unknown. Two extreme cases may be considered: For unit QE, the observed ratio in PL intensity is η_{PC}/η_{ref} (i. e. W_{rad} = W_{tot} for both reference and PC samples) and is thus a measure of the effect of Bragg reflection only. On the other hand, if the QE is very small, the ratio in PL intensity equals $(W_{rad,PC}/W_{rad,ref})$ (η_{PC}/η_{ref}) (i. e. $W_{tot,ref} \approx W_{tot,PC}$) and does contain the effect of the DOS on the radiative lifetime as well. This counterintuitive result is due to the fact that for transitions with high QE a reduced W$_{rad}$ will cause a higher steady state excited population in the crystal, whereas for transitions with low QE it will not.

With this model the data in Fig. 12.2b) can be analyzed quantitatively as follows. First the intrinsic p-Si defect luminescence is analyzed. Defect related transitions in Si are generally non-radiative in nature, and therefore the quantum efficiency for radiative emission is very small. From the data we can thus estimate $(W_{rad,PC}/W_{rad,ref})$ $(\eta_{PC}/\eta_{ref}) = 0.13$, the measured ratio at a wavelength of 1.536 μm. To separate the contribution of the defect luminescence from the Er luminescence at this wavelength we used the fast and slow components of the measured decay from Fig. 12.3.

The erbium luminescence can be treated in a similar way using the measured total decay rates from Fig. 12.3, effectively eliminating a difference in the observed intensity ratio due a difference in QE. Using Eq. 12.2 and the measured data for W_{tot} we again obtain the value of $(W_{rad,PC}/W_{rad,ref})\ (\eta_{PC}/\eta_{ref}) = 0.23$, which differs from the number found for the defect luminescence. The difference may be related to a difference in depth distribution of the luminescent species that affect both η and W_{rad} (through the LDOS).

The analysis above does not lead to an absolute determination of the important factor $(W_{rad,PC}/W_{rad,ref})$ that would directly give the modification of spontaneous emission by the photonic crystal under study. Assuming that the radiative rate of Er in Si is 500 s^{-1} (τ = 2 ms) [196] (being, to our knowledge, the longest lifetime of Er in c-Si reported thus far), we deduce that the non-radiative rate in the reference sample is ~420 s^{-1} (total decay rate is 920 s^{-1}). This non-radiative decay is most likely related to direct energy transfer from the erbium to electronic states in the p-Si host matrix and is thus expected to be equal in the reference and PC sample. Subtracting the non-radiative rate from the measured total decay rate a radiative rate in the PC of ~380 s^{-1} (800 s^{-1}-420 s^{-1}) is found. This value is suppressed by $25\pm10\%$ compared to that in the reference sample. Calculations show that in an infinite woodpile crystal of the dimensions used in our experiment the spontaneous emission around 1.536 μm should be fully suppressed (DOS = 0). The fact that this is not the case in our experiment is attributed to the finite size of the crystal. To compare this number to theoretical results requires knowledge of the exact depth distribution of the Er and the local DOS in the finite-thickness photonic crystal [197, 198].

Finally, using the value found for $(W_{rad,PC}/W_{rad,ref})$ (380/500), we evaluate that for the Er emission η_{PC} / η_{ref} = 0.3 (5 dB). This number represents the reduced emission from the crystal due to Bragg reflection. Transmission measurements as function of thickness of the crystal [29, 195] report a reduction in transmission of ~6 dB per primitive unit cell (= 2 layers). As the erbium ions are implanted in the 3^{rd} layer (implantation depth = 300 nm), leaving 2 layers on top, this is consistent with our found value of 5 dB.

12.5 Conclusion

The spontaneous emission collected from an Er-implanted Si photonic woodpile crystal is strongly modified compared to that of a planar reference sample. The intrinsic defect emission from the polycrystalline Si is reduced over a broad spectral range extending from 1.4–1.7 μm and the intra-4f emission from Er^{3+} at 1.535 μm is strongly reduced as well. These spectral modifications are due to 1) the change in spontaneous emission rate due to the modified local density of states, and 2) changes in the amount of collected light due to internal Bragg scattering in the crystal. Using a simple rate equation argument it is shown that, depending on the quantum efficiency of the optical transition, only the latter, or both of these effects must be taken into account to explain the modified spontaneous emission. The presence of the photonic crystal reduces the spontaneous rate of Er at 1.53 μm by 25%. Taking the reduced Er decay rate into account, a spectral attenuation of ~5 dB per primitive cell is found, consistent with theory and transmission measurements. These measurements are the first demonstration of modified spontaneous emission from a Si photonic crystal at the important telecommunication wavelength of 1.5 μm.

References

[1] J. Bardeen and W. H. Brattain, *The transistor, a semiconductor triode*, Phys. Rev. **74**, 230 (1948).

[2] W. Shockley, *The theory of p-n junctions in semiconductors and p-n junction transistors*, Bell Syst. Tech. J. **28**, 435 (1949).

[3] S. John, *Strong localization of photons in certain disordered dielectric superlattices*, Phys. Rev. Lett. **58**, 2486 (1987).

[4] E. Yablonovitch, *Inhibited spontaneous emission in solid state physics and electronics*, Phys. Rev. Lett. **58**, 2059 (1987).

[5] E. M. Purcell, *Spontaneous emission probabilities at radio frequencies*, Phys. Rev. **69**, 681 (1946).

[6] K. H. Drexhage, *Influence of a dielectric interface on fluorescence decay time*, J. Luminescence **1,2**, 693 (1970).

[7] R. M. Amos and W. L. Barnes, *Modification of the spontaneous emission rate of Eu*$^{3+}$ *ions close to a thin metal mirror*, Phys. Rev. B **55**, 7249 (1997).

[8] E. Snoeks, A. Lagendijk, and A. Polman, *Measuring and modifying the spontaneous emission rate of erbium near an interface*, Phys. Rev. Lett. **74**, 2459 (1995).

[9] S. Noda, A. Chutinan, and M. Imada, *Trapping and emission of photons by a single defect in a photonic bandgap structure*, Nature **407**, 608 (2000).

[10] M. Meier, A. Dodabalapur, J. A. Rogers, R. E. Slusher, A. Mekis, A. Timko, C. A. Murray, R. Ruel, and O. Nalamasu, *Emission characteristics of two-dimensional organic photonic crystal lasers fabricated by replica molding*, J. Appl. Phys. **86**, 3502 (1999).

[11] A. Mekis, J. C. Chen, I. Kurland, S. Fan, P. R. Villeneuve, and J. D. Joannopoulos, *High transmission through sharp bends in photonic crystal waveguides*, Phys. Rev. Lett. **77**, 3787 (1996).

[12] S.-Y. Lin, E. Chow, V. Hietala, P. R. Villeneuve, and J. D. Joannopoulos, *Experimental demonstration of guiding and bending of electromagnetic waves in a photonic crystal*, Science **282**, 274 (1998).

[13] R. F. Cregan, B. J. Mangan, J. C. Knight, T. A. Birks, P. S. J. Russell, P. J. Roberts, and D. C. Allan, *Single-mode photonic band gap guidance of light in air*, Science **285**, 1537 (1999).

[14] J. D. Joannopoulos, R. D. Meade, and J. N. Winn, *Photonic Crystals: Molding the Flow of Light*, Princeton University Press, Princeton, NJ, 1995.

[15] E. Yablonovitch, T. J. Gmitter, and K. M. Leung, *Photonic band structure: The face-centered-cubic case employing nonspherical atoms*, Phys. Rev. Lett. **67**, 2295 (1991).

[16] W. M. Robertson, G. Arjavalingham, R. D. Meade, K. D. Brommer, A. M. Rappe, and J. D. Joannopoulos, *Measurement of photonic band structure in a two-dimensional periodic dielectric array*, Phys. Rev. Lett. **68**, 2023 (1992).

[17] E. Özbay, A. Abeyta, G. Tuttle, M. Tringides, R. Biswas, C. T. Chan, C. M. Soukoulis, and K. M. Ho, *Measurement of a three-dimensional photonic band gap in a crystal structure made of dielectric rods*, Phys. Rev. B **50**, 1945 (1994).

[18] D. A. Kofke and P. G. Bolhuis, *Freezing of polydisperse hard spheres*, Phys. Rev. E **59**, 618 (1999).

[19] S. Auer and D. Frenkel, *Suppression of crystal nucleation in polydisperse colloids due to increase in free energy*, Nature **413**, 711 (2001).

[20] J. E. G. J. Wijnhoven and W. L. Vos, *Preparation of photonic crystals made of air spheres in titania*, Science **281**, 802 (1998).

[21] A. Blanco, E. Chomski, S. Grabtchak, M. Ibisate, S. John, S. W. Leonard, C. Lopez, F. Messeguer, H. Miguez, J. P. Mondia, G. A. Ozin, O. Toader, and H. M. van Driel, *Large-scale synthesis of a silicon photonic crystal with complete three-dimensional bandgap near 1.5 micrometers*, Nature **405**, 437 (2000).

[22] Y. A. Vlasov, X.-Z. Bo, J. C. Sturm, and D. J. Norris, *On-chip natural assembly of silicon photonic crystals*, Nature **71**, 289 (2001).

[23] A. van Blaaderen, *Opals in a new light*, Science **2**, 481 (1998).

[24] J. S. Foresi, P. R. Villeneuve, J. Ferrera, E. R. Thoen, G. Steinmeyer, S. Fan, J. D. Joannopoulos, L. C. Kimmerling, H. I. Smith, and E. P. Ippen, *Photonic-bandgap microcavities in optical waveguides*, Nature **390**, 143 (1997).

[25] C. C. Cheng and A. Scherer, *Fabrication of photonic band-gap crystals*, J. Vac. Sci. Technol. B **13**, 2696 (1995).

[26] T. F. Krauss, R. M. De La Rue, and S. Brand, *Two-dimensional photonic bandgap structures operating at near-infrared wavelengths*, Nature **383**, 699 (1996).

[27] T. Baba and M. Koma, *Possibility of InP-based 2-dimensional photonic crystal: An approach by the anodization method*, Jpn. J. Appl. Phys. **34**, 1405 (1995).

[28] H. Hatate, M. Hashimoto, H. Shirakawa, Y. Fujiwara, Y. Takeda, H. Nakano, T. Tatsuta, and O. Tsuji, *Fabrication of InP submicron pillars for two-dimensional photonic crystals by reactive ion etching*, Jpn. J. Appl. Phys. **37**, 7172 (1998).

[29] S.-Y. Lin, J. G. Fleming, D. L. Hetherington, B. K. Smith, R. Biswas, K. M. Ho, M. M. Sigalas, W. Zubrzycki, S. R. Kurtz, and J. Bur, *A three-dimensional photonic crystal operating at infrared wavelengths*, Nature **394**, 251 (1998).

[30] J. G. Fleming and S.-Y. Lin, *Three-dimensional photonic crystal with a stop band from 1.35 to 1.95 μm*, Opt. Lett. **24**, 49 (1999).

[31] S. Noda, K. Tomoda, N. Yamamoto, and A. Chutinan, *Full three-dimensional photonic bandgap crystals at near-infrared wavelengths*, Science **289**, 604 (2000).

[32] C. C. Cheng, A. Scherer, V. Arbet-Engels, and E. Yablonovitch, *Lithographic band gap tuning in photonic band gap crystals*, J. Vac. Sci. Technol. B **14**, 4110 (1996).

[33] L. P. Bouckaert, R. Smoluchowski, and E. Wigner, *Theory of Brillouin zones and symmetry properties of wave functions in crystals*, Phys. Rev. **50**, 58 (1936).

[34] J. B. Pendry and A. MacKinnon, *Calculation of photon dispersion relations*, Phys. Rev. Lett. **69**, 2772 (1992).

[35] P. M. Bell, J. B. Pendry, L. M. Moreno, and A. J. Ward, *A program for calculating photonic band structures and transmission coefficients of complex structures*, Computer Physics Comm. **85**, 306 (1995).

[36] M. Plihal, A. Shambrook, A. A. Maradudin, and S. Ping, *2-Dimensional photonic band structures*, Opt. Comm. **80**, 199 (1991).

[37] A. Moroz, *Density-of-states calculations and multiple-scattering theory for photons*, Phys. Rev. B **51**, 2068 (1995).

[38] E. N. Economou, *Green's functions in quantum physics*, Springer, Heidelberg, 1979.

[39] M. S. Tomaš, *Green's function for multilayers: Light scattering in planar cavities*, Phys. Rev. A **51**, 2545 (1995).

[40] A. Moroz, *Minima and maxima of the local density of states for one-dimensional periodic systems*, Europhys. Lett. **46**, 419 (1999).

[41] C. Hooijer, D. Lenstra, and A. Lagendijk, *Mode density inside an omnidirectional reflector is heavily directional but not small*, Opt. Lett. **25**, 1666 (2000).

[42] M. Megens, J. E. G. J. Wijnhoven, A. Lagendijk, and W. L. Vos, *Fluorescence lifetimes and linewidths of dye in photonic crystals*, Phys. Rev. A **59**, 4727 (1999).

[43] R. Sprik, B. A. van Tiggelen, and A. Lagendijk, *Optical emission in periodic dielectrics*, Europhys. Lett. **35**, 265 (1996).

[44] R. Stoffer, H. J. W. M. Hoekstra, R. M. de Ridder, E. van Groesen, and F. P. H. van Beckum, *Numerical studies of 2D photonic crystals: waveguides, coupling between waveguides and filters*, Opt. Quant. Elec. **32**, 947 (2000).

[45] J. N. Winn, R. D. Meade, and J. D. Joannopoulos, *Two-dimensional photonic band-gap materials*, J. Mod. Opt. **41**, 257 (1994).

[46] T. Baba, N. Fukaya, and J. Yonekura, *Observation of light propagation in photonic crystal optical waveguide with bends*, Elec. Lett. **35**, 654 (1999).

[47] M. Tokushima, H. Kosaka, A. Tomita, and H. Yamada, *Lightwave propagation through a 120° sharply bent single-line-defect photonic crystal waveguide*, Appl. Phys. Lett. **76**, 952 (2000).

[48] H. C. van de Hulst, *Light scattering by small particles*, Wiley, New York, 1957.

[49] S. Tachi, K. Tsujimoto, S. Arai, and T. Kure, *Low-temperature dry etching*, J. Vac. Sci. Technol. A **9**, 796 (1991).

[50] J. W. Bartha, J. Greschner, M. Puech, and P. Maquin, *Low temperature etching of Si in high density plasma using* SF_6/O_2, Microelectron. Eng. **27**, 453 (1995).

[51] T. Zijlstra, E. van der Drift, M. J. A. de Dood, E. Snoeks, and A. Polman, *Fabrication of two-dimensional photonic crystal waveguides for 1.5 μm in silicon by deep anisotropic dry etching*, J. Vac. Sci. Technol. B **17**, 2734 (1999), Chapter 3 of this thesis.

[52] S. G. Johnson, S. Fan, P. R. Villeneuve, and J. D. Joannopoulos, *Guided modes in photonic crystal slabs*, Phys. Rev. B **60**, 5751 (2000).

[53] V. N. Astratov, D. M. Whittaker, I. S. Culshaw, R. M. Stevenson, M. S. Skolnick, T. F. Krauss, and R. M. De La Rue, *Photonic band-structure effects in the reflectivity of periodically patterned waveguides*, Phys. Rev. B **60**, 16225 (1999).

[54] M. D. B. Charlton and G. J. Parker, *Visible photonic band gap waveguide devices*, Mat. Res. Soc. Symp. Proc. **486**, 87 (1998).

[55] M. D. B. Charlton, S. W. Roberts, and G. J. Parker, *Guided mode analysis, and fabrication of a 2-dimensional visible photonic band structure confined within a planar semiconductor waveguide*, Mat. Sci. Eng. B **49**, 155 (1997).

[56] R. M. Emmons, B. N. Kurdi, and D. G. Hall, *Buried-oxide silicon-on-insulator structures I: Optical waveguide characteristics*, IEEE J. Quant. Elec. **28**, 157 (1992).

[57] B. Schüppert and K. Petermann, *Integrated optic devices in silicon and silicon-on-insulator materials*, MRS Symp. Proc. **486**, 33 (1998).

[58] G. Cocorullo, F. G. D. Corte, R. de Rosa, I. Rendina, A. Rubino, and E. Terzini, *Amorphous silicon based waveguides and light modulators for silicon low-cost photonic integrated circuits*, MRS Symp. Proc. **486**, 113 (1998).

[59] S. Roorda, W. Sinke, J. Poate, D. Jacobson, S. Dierker, B. Dennis, D. Eaglesham, F. Spaepen, and P. Fuoss, *Structural relaxation and defect annihilation in pure amorphous-silicon*, Phys. Rev. B **44**, 3702 (1991).

[60] C. N. Waddell, W. G. Spitzer, J. E. Fredrickson, G. K. Hubler, and T. A. Kennedy, *Amorphous silicon produced by ion implantation: Effects of ion mass and thermal annealing*, J. Appl. Phys. **55**, 4361 (1984).

[61] C. R. Pollock, *Fundamentals of optoelectronics*, Irwin, Chicago, 1995.

[62] E. Kasper, *Properties of strained and relaxed Silicon Germanium*, INSPEC, 1995.

[63] J. R. Wendt, G. A. Vawter, P. L. Gourley, T. M. Brennan, and B. E. Hammons, *Nanofabrication of photonic lattice structures in GaAs/AlGaAs*, J. Vac. Sci. Technol. B **11**, 2637 (1993).

[64] U. Grüning, V. Lehmann, S. Ottow, and K. Busch, *Macroporous silicon with a complete two-dimensional photonic band gap centered at 5 μm*, Appl. Phys. Lett. **68**, 747 (1996).

[65] C. C. Cheng, A. Scherer, R.-C. Tyan, Y. Fainman, G. Witzgall, and E. Yablonovitch, *New fabrication techniques for high quality photonic crystals*, J. Vac. Sci. Technol. B **15**, 2764 (1997).

[66] J. K. Bhardwaij and H. Ashraf, *Advanced silicon etching using high density plasmas*, SPIE **2639**, 224 (1995).

[67] K. Tsutsui, E. L. Hu, and C. D. W. Wilkinson, *Controlling the profile of nanostructures*, J. Vac. Sci. Technol. B **11**, 2233 (1993).

[68] A. M. Manenschijn, E. van der Drift, G. C. A. M. Janssen, and S. Radelaar, *Cl_2 reactive ion etching mechanisms studied by in situ determination of ion energy and ion flux*, J. Appl. Phys. **69**, 7996 (1991).

[69] F. R. McFeely, J. F. Morar, N. D. Shinn, G. Landgren, and F. J. Himpsel, *Synchrotron photoemission: investigation of the initial stages of fluorine attack on Si surfaces: Relative abundance of fluorosilyl species*, Phys. Rev. B **30**, 764 (1984).

[70] J. A. Yarmoff and F. R. McFeely, *Mechanism of ion-assisted etching of silicon by fluorine atoms*, Surf. Science **184**, 389 (1987).

[71] E. van der Drift, T. Zijlstra, E. J. M. Fakkeldij, R. Cheung, K. Werner, and S. Radelaar, *XPS study on dry etching of Si/Ge_xSi_{1-x}*, Microelectron. Eng. **27**, 481 (1995).

[72] J. S. Custer, M. O. Thompson, D. C. Jacobson, J. M. Poate, S. Roorda, and W. C. Sinke, *Density of amorphous Si*, Appl. Phys. Lett. **64**, 437 (1994).

[73] G. K. Hubler, C. N. Waddell, W. G. Spitzer, J. E. Fredrickson, S. Prussin, and R. G. Wilson, *High-fluence implantations of silicon: Layer thickness and refractive indices*, J. Appl. Phys. **50**, 3294 (1979).

[74] M. Fried, T. Lohner, W. A. M. Aarnink, L. J. Hanekamp, and A. van Silfhout, *Determination of complex dielectric functions of ion implanted and implanted-annealed amorphous silicon by spectroscopic ellipsometry*, J. Appl. Phys. **71**, 5260 (1992).

[75] R. Reitano, M. G. Grimaldi, P. Baeri, A. Borghesi, and A. Sassella, *Spectroscopic ellipsometry study of the relaxation state of amorphous silicon*, Thin Solid Films **233**, 203 (1993).

[76] G. Cocorullo, F. G. D. Corte, I. Rendina, C. Minarini, A. Rubino, and E. Terzini, *Amorphous silicon waveguides and light modulators for integrated photonics realized by low-temperature plasma-enhanced chemical-vapor deposition*, Opt. Lett. **21**, 2002 (1996).

[77] D. L. Williamson, S. Roorda, M. Chicoine, R. Tabti, P. A. Stolk, S. Acco, and F. W. Saris, *On the nanostructure of pure amorphous silicon*, Appl. Phys. Lett. **67**, 226 (1995).

[78] K. Laaziri, S. Kycia, S. Roorda, M. Chicoine, J. L. Robertson, J. Wang, and S. C. Moss, *High-energy x-ray diffraction study of pure amorphous silicon*, Phys. Rev. B **60**, 13520 (1999).

[79] J. S. Custer, M. O. Thompson, and P. H. Bucksbaum, *Solid phase epitaxy of laser amorphized silicon*, Appl. Phys. Lett. **53**, 1402 (1988).

[80] G. L. Olson and J. A. Roth, *Kinetics of solid phase crystallization in amorphous silicon*, Mat. Sci. Reports **3**, 1 (1988).

[81] E. D. Palik, *Handbook of optical constants of solids; Vol. 1*, Academic Press, Boston, 1991.

[82] M. A. Green, *Silicon solar cells*, University of New South Wales, Sydney, 1995.

[83] M. Lohmeier, S. de Vries, J. S. Custer, E. Vlieg, M. S. Finney, F. Priolo, and A. Battaglia, *Interface roughness during thermal and ion-induced regrowth of amorphous layers on Si(001)*, Appl. Phys. Lett. **64**, 1803 (1994).

[84] P. K. Tien, *Light waves in thin films and integrated optics*, Appl. Opt. **10**, 2395 (1971).

[85] S. Acco, D. L. Williamson, P. A. Stolk, F. W. Saris, M. J. van den Boogaard, W. C. Sinke, W. F. van der Weg, S. Roorda, and P. C. Zalm, *Hydrogen solubility and network stability in amorphous silicon*, Phys. Rev. B **53**, 4415 (1996).

[86] E. A. J. Marcatili, *Bends in optical dielectric guides*, Bell Syst. Tech. J. **7**, 2103 (1969).

[87] R. L. Espinola, F. P. R. U. Ahmad, M. J. Steel, and R. M. Osgood Jr., *A study of high-index-contrast 90° waveguide bend structures*, Optics Express **8**, 517 (2001).

[88] C. F. Brinker and G. W. Scherer, *Sol-Gel Science*, Academic Press, San Diego, 1990.

[89] W. Stöber, A. Fink, and E. Bohn, *Controlled growth of monodisperse silica spheres in the micron range*, J. Colloid Interface Sci. **1**, 62 (1968).

[90] A. P. Philipse and A. J. Vrij, *Polydispersity probed by light scattering of secondary particles in controlled growth experiments of silica spheres*, J. Chem. Phys. **87**, 5634 (1987).

[91] G. H. Bogush, M. A. Tracy, and C. F. Z. IV, *Preparation of monodisperse silica particles: control of size and mass fraction*, J. Non-Cryst. Sol. **104**, 95 (1988).

[92] A. van Blaaderen, J. van Geest, and A. Vrij, *Monodisperse colloidal spheres from tetraalkoxysilanes - particle formation and growth-mechanism*, J. Colloid Interface Science **154**, 481 (1992).

[93] S.-L. Chen, P. Dong, and G.-H. Yang, *The size dependence of growth rate of monodisperse silica particles from tetraalkoxysilane*, J. Colloid Interface Sci. **189**, 268 (1997).

[94] A. Walcarius, C. Despas, and J. Bessière, *Molecular sieving with amorphous monodisperse silica beads*, Microporous and Mesoporous Materials **23**, 309 (1998).

[95] C. Despas, A. Walcarius, and J. Bessière, *Influence of the base size and strength on the acidic properties of silica gel and monodispersed silica beads: Interest of impedance measurements for the in situ monitoring of the ionization process*, Langmuir **9**, 3186 (1999).

[96] G. P. Kochanski, C. A. Murray, M. L. Steigerwald, P. Wiltzius, and A. van Blaaderen, (Lucent Technologies Inc.) US Patent Appl. Nr: US 1996 000 623 201, 1998.

[97] M. J. Hodson, R. J. Smith, A. van Blaaderen, T. Crafton, and C. H. Oneill, *Detecting plant silica fibers in animal tissue by confocal fluorescence microscopy*, Ann. Occup. Hyg. **2**, 149 (1994).

[98] A. van Blaaderen and A. Vrij, *Synthesis and characterization of colloidal dispersion of fluorescent, monodisperse silica spheres*, Langmuir **8**, 2921 (1992).

[99] N. A. M. Verhaegh and A. van Blaaderen, *Dispersions of rhodamine-labeled silica spheres - synthesis, characterization, and fluorescence confocal scanning laser microscopy*, Langmuir **10**, 1427 (1994).

[100] R. K. Iler, *The Chemistry of Silica*, Wiley, New York, 1979.

[101] L. H. Slooff, M. J. A. de Dood, A. van Blaaderen, and A. Polman, *Erbium-implanted silica colloids with 80% luminescence quantum efficiency*, Appl. Phys. Lett. **76**, 3682 (2000), Chapter 7 of this thesis.

[102] W. Lukosz and R. E. Kunz, *Changes in fluorescence lifetimes induced by variation of the radiating molecules' optical environment*, Optics Comm. **31**, 42 (1979).

[103] W. L. Barnes, *Topical review: Fluorescence near interfaces: the role of photonic mode density*, J. Mod. Opt. **45**, 661 (1998).

[104] R. R. Chance, A. Prock, and R. Silbey, *Decay of an emitting dipole between two parallel mirrors*, J. Chem. Phys. **62**, 771 (1975).

[105] E. Yablonovitch, T. J. Gmitter, and R. Bhat, *Inhibited and enhanced spontaneous emission from optically thin AlGaAs/GaAs double heterostructures*, Phys. Rev. Lett. **61**, 2546 (1988).

[106] A. Tip, *Canonical formalism and quantization for a class of classical fields with application to radiative atomic decay in dielectrics*, Phys. Rev. A **56**, 5022 (1997).

[107] H. T. Dung, L. Knöll, and D.-G. Welsch, *Three-dimensional quantization of the electromagnetic field in dispersive and absorbing inhomogeneous dielectrics*, Phys. Rev. A **57**, 3931 (1998).

[108] H. Khosravi and R. Loudon, *Vacuum field fluctuations and spontaneous emission in the vicinity of a dielectric surface*, Proc. R. Soc. Lond. A **433**, 337 (1991).

[109] H. Khosravi and R. Loudon, *Vacuum field fluctuations and spontaneous emission in a dielectric slab*, Proc. R. Soc. Lond. A **436**, 373 (1992).

[110] H. P. Urbach and G. L. J. A. Rikken, *Spontaneous emission from a dielectric slab*, Phys. Rev. A **57**, 3913 (1998).

[111] B. A. van Tiggelen and E. Kogan, *Analogies between light and electrons: Density of states and Friedel's identity*, Phys. Rev. A **49**, 708 (1994).

[112] R. M. MacFarlane, *Analysis of the spectrum of d^3 ions in trigonal crystal fields*, J. Chem. Phys. **39**, 3118 (1963).

[113] S. Sugano and M. Peter, *Effect of configuration mixing and covalency on the energy spectrum of ruby*, Phys. Rev. **122**, 381 (1961).

[114] S. Sugano, Y. Tanabe, and H. Kamikura, *Multiplets of transition-metal ions in crystals*, Academic, New York, 1970.

[115] T. H. Maiman, *Stimulated optical emission in fluorescent solids. I. Theoretical considerations*, Phys. Rev. **123**, 1145 (1961).

[116] T. H. Maiman, R. H. Hoskins, I. J. D'Haennens, C. K. Asawa, and V. Evtuhov, *Stimulated optical emission in fluorescent solids. II. Spectroscopy and stimulated emission in ruby*, Phys. Rev. **123**, 1151 (1961).

[117] J. H. Eggert, K. A. Goettel, and I. F. Silvera, *Ruby at high pressure. I. Optical line shifts to 156 GPa*, Phys. Rev. B **40**, 5724 (1989).

[118] J. H. Eggert, K. A. Goettel, and I. F. Silvera, *Ruby at high pressure. II. Fluorescence lifetime of the R line to 130 GPa*, Phys. Rev. B **40**, 5733 (1989).

[119] Y. Sato-Sorensen, *Measurements of the lifetime of the ruby R_1 line under high pressure*, J. Appl. Phys. **60**, 2985 (1986).

[120] W. L. Vos and J. A. Schouten, *On the temperature correction of the ruby pressure schale*, J. Appl. Phys. **69**, 6744 (1991).

[121] G. C. Farlow, C. W. White, C. J. McHargue, and B. R. Appleton, *Behaviour of implanted α-Al_2O_3 in an oxidizing annealing environment*, Mat. Res. Soc. Symp. Proc. **27**, 395 (1984).

[122] H. Naramoto, C. W. White, J. M. Williams, C. J. McHargue, O. W. Holland, M. M. Abraham, and B. R. Appleton, *Ion implantation and thermal annealing of α-Al_2O_3 single crystals*, J. Appl. Phys. **54**, 683 (1983).

[123] C. W. White, G. C. Farlow, C. J. McHargue, P. S. Sklad, M. P. Angelini, and B. R. Appleton, *Formation of amorphous layers in Al_2O_3 by ion implantation*, Nucl. Instr. Meth. B **7/8**, 473 (1985).

[124] Ning Yu, Q. Wen, D. R. Clarke, P. C. McIntyre, H. Kung, M. Nastasi, T. W. Simpson, I. V. Mitchell, and DeQuan Li, *Formation of iron or chromium doped epitaxial sapphire thin films on sapphire substrates*, J. Appl. Phys. **78**, 5412 (1995).

[125] Q. Wen, D. R. Clarke, Ning Yu, and M. Nastasi, *Epitaxial regrowth of ruby on sapphire for an integrated thin film stress sensor*, Appl. Phys. Lett. **66**, 293 (1995).

[126] D. E. McCumber and M. D. Sturge, *Linewidth and temperature shift of the R lines in ruby*, J. Appl. Phys. **34**, 1682 (1963).

[127] D. F. Nelson and M. D. Sturge, *Relation between absorption and emission in the region of the R lines of ruby*, Phys. Rev. **137**, A1117 (1965).

[128] G. L. J. A. Rikken and Y. A. R. R. Kessener, *Local field effects and electric and magnetic dipole transitions in dielectrics*, Phys. Rev. Lett. **74**, 880 (1995).

[129] F. J. P. Schuurmans, D. T. N. de Lang, G. H. Wegdam, R. Sprik, and A. Lagendijk, *Local-field effects on spontaneous emission in a dense supercritical gas*, Phys. Rev. Lett. **80**, 5077 (1999).

[130] E. Snoeks, P. G. Kik, and A. Polman, *Concentration quenching in erbium implanted alkali silicate glasses*, Opt. Mat. **5**, 159 (1996).

[131] H. C. Chow and R. C. Powell, *Models for energy transfer in solids*, Phys. Rev. B **21**, 3785 (1980).

[132] N. A. Tolstoi and Liu-Shun-Fu, *Luminescence kinetics of chromium luminors*, English transl. - Opt. Spectry. (USSR) **13**, 224 (1962).

[133] A. Polman, *Erbium implanted thin film photonic materials*, J. Appl. Phys. **82**, 1 (1997).

[134] P. G. Kik and A. Polman, *Erbium-doped optical waveguide amplifiers on silicon*, MRS Bulletin **23**, 48 (1998).

[135] S. Lin, J. Feuerstein, and A. R. Mickelson, *A study of neodymium-chelate-doped optical polymer waveguides*, J. Appl. Phys. **79**, 2628 (1996).

[136] L. H. Slooff, A. Polman, M. P. Oude Wolbers, F. C. J. M. van Veggel, D. N. Reinhoudt, and J. W. Hofstraat, *Optical properties of erbium-doped organic polydentate cage complexes*, J. Appl. Phys. **83**, 497 (1998).

[137] L. H. Slooff, A. Polman, S. I. Klink, G. A. Hebbink, F. C. J. M. van Veggel, D. N. Reinhoudt, and J. W. Hofstraat, *Optical properties of lissamine functionalized Nd^{3+} complexes in polymer waveguides and solution*, Opt. Mater. **14**, 101 (2000).

[138] G. Stein and E. Würzberg, *Energy gap law in the solvent isotope effect on radiationless transitions of rare earth ions*, J. Chem. Phys. **62**, 208 (1975).

[139] V. L. Ermolaev and E. B. Sveshnikova, *Application of luminescent kinetic methods to investigation of lanthanide ions complexation in solutions*, Russ. Chem. Rev. **63**, 905 (1994).

[140] A. Polman, D. Jacobson, D. Eaglesham, R. Kistler, and J. Poate, *Optical doping of waveguide materials by MeV Er implantation*, J. Appl. Phys. **70**, 3778 (1991).

[141] W. J. Miniscalco, *Erbium-doped glasses for fiber amplifiers at 1500-nm*, J. Lightwave Technol. **9**, 234 (1991).

[142] D. L. J. Vossen, M. J. A. de Dood, T. van Dillen, T. Zijlstra, E. van der Drift, A. Polman, and A. van Blaaderen, *Novel method for solution growth of thin silica films from tetraethoxysilane*, Adv. Mater. **12**, 1434 (2000), Chapter 5 of this thesis.

[143] W.-K. Chu, J. W. Mayer, and M.-A. Nicolet, *Backscattering Spectrometry*, Academic Press, New York, 1978.

[144] S. U. Campisano, G. Foti, F. Grasso, and E. Rimini, *Determination of concentration profile in thin metallic films: Applications and limitations of He*$^{+}$ *backscattering*, Thin Solid Films **25**, 431 (1975).

[145] X. Fan, M. Wang, and G. Xiong, *Study of Eu*$^{3+}$*-doped luminescence glasses prepared by a sol-gel process*, Mat. Sci. Eng. B **21**, 55 (1993).

[146] P. Tien and L.-K. Chau, *Novel sol-gel derived material for separation and optical sensing of metal ions: propyl-ethylenediamine triacetate functionalized silica*, Chem. Mater. **11**, 2141 (1999).

[147] M. Cai, O. Painter, and K. H. Vahala, *Observation of critical coupling in a fiber taper to a silica-microsphere whispering-gallery mode system*, Phys. Rev. Lett. **85**, 74 (2000).

[148] L. H. Slooff, *Rare-earth doped polymer waveguides and light emitting diodes*, PhD thesis, FOM-Institute for Atomic and Molecular Physics, Amsterdam, The Netherlands, 2000.

[149] J. C. Wright, in *Radiationless processes in molecules and condensed phases,* p. 239 ed. by F. K. Fong, Springer, Heidelberg, 1976.

[150] V. P. Gapontsev, A. A. Izyneev, Y. E. Sverchov, and M. Syrtlanov, *Mechanism and parameters of the quenching of luminescence of rare-earth ions by hydroxyl impurity groups in laser phosphate glass*, Sov. J. Quantum Electron. **11**, 1101 (1981).

[151] M. J. A. de Dood, L. H. Slooff, A. Polman, A. Moroz, and A. van Blaaderen, *Local optical density of states in SiO*$_2$ *spherical microcavities: Theory and experiment*, Phys. Rev. A **64**, 033807 (2001), Chapter 9 of this thesis.

[152] A. M. Vredenberg, N. E. J. Hunt, E. F. Schubert, D. C. Jacobson, J. M. Poate, and G. J. Zydzik, *Controlled spontaneous emission from Er*$^{3+}$ *in a transparent Si/SiO*$_2$ *microcavity*, Phys. Rev. Lett. **71**, 517 (1993).

[153] P. Goy, J. M. Raimond, M. Gross, and S. Haroche, *Observation of cavity-enhanced single-atom spontaneous emission*, Phys. Rev. Lett. **50**, 1903 (1983).

[154] R. G. Hulet, E. S. Hilfer, and D. Kleppner, *Inhibited spontaneous emission by a Rydberg atom*, Phys. Rev. Lett. **55**, 2137 (1985).

[155] M. Suzuki, H. Yokoyama, S. D. Brorson, and E. P. Ippen, *Observation of spontaneous emission lifetime change of dye-containing Langmuir-Blodgett films in optical microcavities*, Appl. Phys. Lett. **58**, 998 (1991).

[156] M. D. Tocci, M. Scalora, M. J. Bloemer, J. P. Dowling, and C. M. Bowden, *Measurement of spontaneous emission enhancement near the one-dimensional photonic band edge of semiconductor heterostructures*, Phys. Rev. A **53**, 2799 (1996).

[157] G. L. J. A. Rikken, *Spontaneous emission from stratified dielectrics*, Phys. Rev. A **51**, 4906 (1995).

[158] T. M. Hensen, M. J. A. de Dood, and A. Polman, *Luminescence quantum efficiency and local optical density of states in thin film ruby made by ion implantation*, J. Appl. Phys. **88**, 5142 (2000), Chapter 6 of this thesis.

[159] A. J. Campillo, J. D. Eversole, and H.-B. Lin, *Cavity quantum electrodynamic enhancement of stimulated emission in microdroplets*, Phys. Rev. Lett. **67**, 437 (1991).

[160] H.-B. Lin, J. D. Eversole, C. D. Merritt, and A. J. Campillo, *Cavity-modified spontaneous emission rates in liquid microdroplets*, Phys. Rev. A **45**, 6756 (1992).

[161] B. Y. Tong, P. K. John, Y. Zhu, Y. S. Liu, S. K. Wong, and W. R. Ware, *Fluorescence-lifetime measurements in monodispersed suspensions of polystyrene particles*, J. Opt. Soc. Am. B **10**, 356 (1993).

[162] J. Martorell and N. M. Lawandy, *Observation of inhibited spontaneous emission in a periodic dielectric structure*, Phys. Rev. Lett. **65**, 1877 (1990).

[163] E. P. Petrov, V. N. Bogomolov, I. I. Kalosha, and S. V. Gaponenko, *Spontaneous emission of organic molecules embedded in a photonic crystal*, Phys. Rev. Lett. **81**, 77 (1998).

[164] R. J. Glauber and M. Lewenstein, *Quantum optics of dielectric media*, Phys. Rev. A **43**, 467 (1991).

[165] L. Knöll, S. Scheel, and D.-G. Welsch, *QED in dispersing and absorbing media* in *Coherence and statistics of photons and atoms* ed. by J. Peřina, Wiley, New York, 2001.

[166] A. Tip, *Nonconducting electromagnetic media with rotational invariance: Transition operators and Green's functions*, J. Math. Phys. **38**, 3545 (1997).

[167] D. S. Jones, *Acoustic and electromagnetic waves*, Oxford University Press, Oxford, 1986.

[168] J. D. Jackson, *Classical Electrodynamics*, John Wiley & Sons, New York, 1975.

[169] P. A. Bobbert and J. Vlieger, *Light scattering by a sphere on a substrate*, Physica A **137**, 209 (1986).

[170] P. Andrew and W. L. Barnes, *Förster energy transfer in an optical microcavity*, Science **290**, 785 (2000).

[171] M. Megens, J. E. G. J. Wijnhoven, A. Lagendijk, and W. L. Vos, *Light sources inside photonic crystals*, J. Opt. Soc. Am. B **16**, 1403 (1999).

[172] A. van Blaaderen, R. Ruel, and P. Wiltzius, *Template-directed colloidal crystallization*, Nature **385**, 321 (1997).

[173] A. Imhof, M. Megens, J. J. Engelberts, D. T. N. de Lang, R. Sprik, and W. L. Vos, *Spectroscopy of fluorescein (FITC) dyed colloidal silica spheres*, J. Phys. Chem. B **103**, 1408 (1999).

[174] C. E. Moran, G. D. Hale, and N. J. Halas, *Synthesis and characterization of lanthanide-doped silica microspheres*, Langmuir **17**, 8376 (2001).

[175] G. De, B. Karmakar, and D. Ganguli, *Hydrolysis-condensation reactions of TEOS in the presence of acetic acid leading to the generation of glass-like silica microspheres in solution at room temperature*, J. Materials Chemistry **10**, 2289 (2000).

[176] B. Karmakar, G. De, D. Kundu, and D. Ganguli, *Silica microspheres from the system tetraethyl orthosilicate – acetic acid – water*, J. Non-Cryst. Sol. **135**, 29 (1991).

[177] F. J. Arriagada and K. Osseoasare, *Synthesis of nanometer-sized silica by controlled hydrolysis in reverse micellar systems*, in *Colloid Chemistry of Silica* (Amer. Chemical Soc., Washington) **234**, 113 (1994).

[178] A. van Blaaderen, K. P. Velikov, J. P. Hoogenboom, D. L. J. Vossen, A. Yethiraj, R. Dullens, T. van Dillen, and A. Polman, *Manipulating colloidal crystallization for photonic applications: From self-organization to do-it-yourself organization*, in *Proceedings of the NATO advanced study institute on photonic crystals and light localization, Crete, Greece, June 18–30, 2000* ed. by C. M. Soukoulis , 239 (2001).

[179] L. C. Klein, *Sol-gel processing of silicates*, Ann. Rev. Mater. Sci. **15**, 227 (1985).

[180] L. H. Slooff, M. J. A. de Dood, A. van Blaaderen, and A. Polman, *Effects of heat treatment and concentration on the luminescence properties of erbium-doped sol-gel films.*, J. Non-Cryst. Sol. **296**, 158 (2001).

[181] S. Bruynooghe, A. Chabli, F. Bertin, F. Pierre, and G. Leflem, *Preparation and characterization of* Nd^{3+} *and* Er^{3+}*-doped silica sol-gel coatings by Rutherford backscattering spectroscopy and spectroscopic ellipsometry*, J. Mater. Res. **12**, 2779 (1997).

[182] J. L. Kropp and M. W. Windsor, *Enhancement of fluorescence yield of rare-earth ions by heavy water*, J. Chem. Phys. **39**, 2769 (1963).

[183] K. M. Ho, C. T. Chan, C. M. Soukoulis, R. Biswas, and M. Sigalas, *Photonic bandgaps in three dimensions: New layer-by-layer periodic structures*, Solid State Commun. **89**, 413 (1994).

[184] H. S. Sozuer and J. P. Dowling, *Photonic band calculations for woodpile structures*, J. Mod. Opt. **41**, 231 (1994).

[185] M. C. Wanke, O. Lehmann, K. Müller, Q. Wen, and M. Stuke, *Laser rapid prototyping of photonic band-gap microstructures*, Science **275**, 1284 (1997).

[186] S.-Y. Lin and J. G. Fleming, *A three-dimensional photonic crystal*, IEEE J. Lightwave Technol. **17**, 1944 (1999).

[187] E. D. Palik, *Handbook of optical constants of solids; Vol. 2*, Academic Press, Boston, 1991.

[188] R. Petit, editor, *Electromagnetic theory of gratings*, Springer Verlag, Berlin, 1980.

[189] L. C. Botten, M. S. Craig, R. C. McPhedran, J. L. Adams, and J. R. Andrewartha, *The dielectric lamellar diffraction grating*, Optica acta **28**, 413 (1981).

[190] L. Li, *A modal analysis of lamellar diffraction gratings in conical mountings*, J. of Mod. Optics **40**, 553 (1993).

[191] L. Li, *Formulation and comparison of two recursive matrix algorithms for modeling layered diffraction gratings*, J. Opt. Soc. Am. A **13**, 1024 (1996).

[192] B. Gralak, S. Enoch, and G. Tayeb, *From scattering or impedance matrices to Bloch modes of photonic crystals*, J. Opt. Soc. Am. A **(in press)** (2002).

[193] S. Ogawa, K. Tomoda, and S. Noda, *Effects of structural fluctuations on three-dimensional photonic crystals operating at near-infrared wavelengths*, J. Appl. Phys. **91**, 513 (2002).

[194] A. Chutinan and S. Noda, *Effects of structural fluctuations on the photonic bandgap during fabrication of a photonic crystal*, J. Opt. Soc. Am. B **16**, 240 (1999).

[195] D. M. Whittaker, *Inhibited emission in photonic woodpile lattices*, Opt. Lett. **25**, 779 (2000).

[196] R. Serna, Jung H. Shin, M. Lohmeier, E. Vlieg, A. Polman, and P. F. A. Alkemade, *Incorporation and optical activation of erbium in silicon using molecular beam epitaxy*, J. Appl. Phys. **79**, 2658 (1996).

[197] T. Suzuki and P. K. L. Yu, *Emission power of an electric dipole in the photonic band structure of the fcc lattice*, J. Opt. Soc. Am. B **12**, 570 (1995).

[198] Z.-Y. Li, L.-L. Lin, and Z.-Q. Zhang, *Spontaneous emission from photonic crystals: Full vectorial calculations*, Phys. Rev. Lett. **84**, 4341 (2000).

Summary

Photonic crystals are materials that show a periodic arrangement of dielectric material on a length scale comparable to the wavelength of light. By virtue of this periodicity, such crystals can Bragg reflect light for a certain wavelength range and thereby substantially influence the propagation of light. If the refractive index contrast is high enough, the light is unable to penetrate in any direction in the crystal due to this Bragg reflection. In this case, a photonic bandgap exists and light can be localized inside the crystal or light emission from atoms inside the crystal can be inhibited. This inhibition of spontaneous emission can be used to increase the efficiency of lasers or light emitting diodes. Even without a complete photonic bandgap, photonic crystals can be used to manipulate the propagation of light. In this perspective, especially two dimensional structures are appealing since they can be integrated with existing planar integrated optical devices used for telecommunication purposes.

Silicon is an excellent material for photonic crystal structures that operate around the important telecommunication wavelength of 1.5 μm. At this wavelength Si is transparent, has a high refractive index and its processing technology is well developed. This thesis studies the fabrication of silicon photonic crystals and the propagation of light in these structures by using external as well as internal light sources. The effect of dielectric structures on spontaneous emission is studied in more detail using relatively simple structures such as a dielectric interface, a thin dielectric film on a substrate or an isolated microsphere. From these experiments it is possible to unravel radiative and non-radiative contributions to the decay of an atom. This information is essential if one uses these atoms to probe the effect of a photonic crystal on spontaneous emission.

Part I of this thesis studies the design and fabrication of two-dimensional photonic crystal structures in silicon and silicon-based materials. The transfer matrix method is employed to calculate the properties of two-dimensional photonic crystals that consist of a square array of dielectric rods. The existence, width and position of photonic bandgaps depends on the dielectric contrast, the fill fraction of rods and the lattice spacing (see Chapter 2). An index contrast of at least 1.95 is needed at the optimum radius-to-pitch ratio (fill fraction) $r/a = 0.25$. To obtain structure that have large bandgaps a much higher index contrast is needed. The structures in this thesis focus on designs that have photonic bandgaps around the important telecommunication wavelength of 1.5 μm. Silicon is an ideal material to fabricate such structure since Si is transparent at near-infrared wavelengths ($>$1.1 μm), has a high refractive index ($n = 3.45$ at $\lambda = 1.5$ μm) and its microfabrication is well known from semiconductor industry. To fabricate such structures in Si, typically 200 nm diameter pillars are needed that are placed on a lattice with a periodicity of 570 nm.

Chapter 3 shows how these arrays of pillars can be fabricated using an electron-cyclotron resonance driven SF_6/O_2 plasma process at reduced temperature. The main

plasma parameters, O_2 flow, dc-bias voltage and temperature were all tuned to etch highly anisotropic vertical profiles. Vertical confinement of the light in silicon based structures may be achieved by embedding the photonic crystal in a waveguide structure, using either amorphous silicon or silicon-on-insulator materials. The fabrication of photonic crystal structures in both materials is demonstrated.

The use of amorphous silicon as a guiding layer is further investigated in Chapter 4. Amorphous silicon is made by ion irradiation of crystalline silicon with MeV Xe ions followed by thermal relaxation of the amorphous network. A transparent layer with a refractive index of n = 3.73 is formed, on top of the crystalline silicon substrate (n = 3.45 at λ = 1.55 μm). Using silicon-on-insulator substrates, transmission measurements on waveguides as function of amorphous silicon length show that at 1.5 μm wavelegnth amorphous silicon exhibits an intrinsic loss of 115 cm^{-1} (0.05 dB μm^{-1}).

A novel method for solution growth of thin silica films is developed in Chapter 5. Typically, $\sim$100 nm thick films can be grown from a reaction mixture containing tetraethoxysilane, water, ammonia and ethanol. Under these conditions stable suspensions of monodisperse colloidal SiO_2 spheres form. After a nucleation stage, a silica layer grows on the substrate by addition of individual monomers. This method is applicable to coating of non-planar surfaces, and opens a possibility to coat photonic crystals, made from small Si pillars, with a thin SiO_2 layer. Optical probes, such as laser dyes or erbium ions, can be inserted in the silica layer and optically active photonic crystal structures can be made.

Part II discusses spontaneous emission of atoms in several dielectric structures. The simplest case, where Cr ions are placed close to a dielectric interface is investigated in Chapter 6. The Cr ions are ion implanted in the near surface region of single crystalline Al_2O_3 substrates and show typical ruby R-line luminescence around 694 nm. Samples of different Cr concentration (0.04 at.% to 0.28 at.% peak concentration) were made and the radiative decay rate of all samples was determined (299 s^{-1}). This was done by varying the reflectivity of the Al_2O_3 to air interface by replacing the air with liquids of different refractive index. The decay rate is found to increase with the refractive index of the liquid. A comparison of the experimental results with a calculation of the local density of states (LDOS) yields the radiative and non-radiative contributions to the decay. Being one of the simplest experimental geometries, the results from Chapter 6 provide a test for the concept of LDOS, and were expanded to include the concept of concentration quenching.

To probe the LDOS in spherical microcavities, erbium ions were ion implanted as probe ions in colloidal SiO_2 particles. First, Chapter 7 reports on the basic luminescent properties of 340-nm-diameter spherical SiO_2 particles implanted with Er ions. The dependence of the luminescence intensity and lifetime of the erbium ions on anneal temperature and erbium concentration is investigated. An extremely long luminescence lifetime of 17 ms is reported, suggesting a high quantum efficiency of the Er^{3+} ions. More detailed experiments on concentration quenching and the local density of states are reported in Chapter 8 and a comparison is made between decay rates of Er^{3+} in 175 nm and 340-nm-diameter particles. The data agree very well with the calculated difference in LDOS in these particles.

The spatial variation of the LDOS of spherical particles is further investigated in Chapter 9. The LDOS of a spherical SiO_2 cavity was calculated as function of the cavity diameter and reveals several maxima and minima as function of diameter. The maxima of the LDOS and their radial position correspond to the electric type Mie resonances of the sphere. Additional experiments and calculation were done using erbium implanted thin

SiO_2 films that were grown with the method described in Chapter 5. The radiative rate of Er^{3+} in a variety of different SiO_2 structures is consistently found to be 54 s^{-1}. This information is then used to experimentally probe the LDOS in Er-doped spherical SiO_2 particles with and without index matching. In addition, the relation between the LDOS and Förster energy transfer is discussed.

The particles described in Chapters 7, 8 and 9 are doped with erbium by ion implantation which only allows for the fabrication of a limited number of particles. Chapter 10 introduces an alternative wet chemical method to fabricate rare earth doped colloidal particles using an acid catalyzed reaction. The resulting bulk rare earth doped particles are quite polydisperse and the properties of Er, Tb and Eu doped particles are discussed. The size polydispersity of the particles can be significantly reduced by using a seeded growth procedure in which a thin shell of silica doped with rare earth ions is grown on silica seed particles. Such particles can serve as optical probes in colloidal photonic crystals.

Finally, Part III describes several different experiments on three-dimensional photonic crystals made from polycrystalline Si rods made by Si microfabrication (so called photonic woodpile crystals). Chapter 11 discusses the angle, polarization and surface orientation dependent spectrally resolved reflectivity of such crystals and the results are compared to rigorous calculations. The reflectivity spectra depend on both the polarization of the incident light and the surface orientation of the finite-thickness photonic crystal. A superstructure present in the crystal is reflected in well-defined features in the measured reflectivity spectra, in good agreement with calculated spectra. Results on modified spontaneous emission in these Si woodpile crystals are described in Chapter 12. A broad luminescence feature is observed and is attributed to defect luminescence of the poly-crystalline Si itself. A strong decrease in luminescence intensity is observed for wavelengths that lie inside the photonic bandgap. The spectral changes are described by a model that takes into account both changes in the LDOS and the internal Bragg scattering in the crystal. It is shown that the quantum efficiency of the optical transitions determines the effect of the photonic crystal on spontaneous emission in an (initially) counter-intuitive way. A spectral attenuation of 5 dB per unit cell is derived from the data, consistent with theory and transmission data.

Samenvatting

Fotonische kristallen zijn materialen met een periodieke variatie in de brekingsindex op een lengteschaal vergelijkbaar met de golflengte van licht. Dergelijke fotonische kristallen kunnen voor een beperkt golflengte gebied efficiënt licht reflecteren. Dit treedt op als in een bepaalde richting en voor een bepaalde golflengte wordt voldaan aan de Bragg conditie. Als het verschil in brekingsindex tussen de materialen groot genoeg is, dan kan men kristallen maken die de voortplanting van licht in alle mogelijke richtingen verbieden. In dit geval spreekt men van een volledige fotonische bandkloof. Dergelijke materialen zijn interessant omdat ze de mogelijkheid bieden om licht op te sluiten of om de spontane emissie van atomen geheel te onderdrukken. Deze onderdrukking van spontane emissie kan worden toegepast om bijvoorbeeld lasers of licht emitterende diodes (LED's) efficiënter te maken. Ook zonder een volledige bandkloof zijn fotonische kristallen toepasbaar als materialen die het voorplanten van licht sterk kunnen beïnvloeden. Dit is vooral interessant in het geval van tweedimensionale kristallen omdat deze relatief eenvoudig te integreren zijn met (planaire) geïntegreerde optische schakelingen die worden gebruikt in telecommunicatietoepassingen.

Silicium is een uitstekend basis materiaal voor de fabricage van fotonische kristallen die werken rond de belangrijke telecommunicatiegolflengte van 1.5 μm. Silicium is bij deze golflengte transparant, heeft een hoge brekingsindex en de siliciumtechnologie die nodig is voor het maken van kleine structuren is goed ontwikkeld. Dit proefschrift beschrijft de fabricage van fotonische kristallen en hun interactie met licht. De invloed van dielectrische structuren op spontane emissie in het algemeen wordt bestudeerd aan de hand van relatief eenvoudige structuren zoals een enkel grensvlak, een dunne laag op een substraat en voor kleine SiO_2 colloiden. Met behulp van deze experimenten is het mogelijk om stralende als niet-stralende bijdragen aan het atomair verval te scheiden. Deze informatie kan op zijn beurt weer worden gebruikt om het effect van een ingewikkelder structuur (zoals een fotonisch kristal) op spontane emissie te bestuderen.

In deel I van dit proefschrift worden zowel het ontwerp als de fabricage van tweedimensionale fotonische kristallen besproken. Kristallen in silicium en in een aantal op silicium gebaseerde materialen worden beschouwd. De optische eigenschappen van een structuur van ronde paaltjes geplaatst op een vierkant rooster worden uitgerekend in Hoofdstuk 2 met behulp van de transfer matrix methode. De berekeningen laten zien dat de positie en breedte van de fotonische bandkloven afhangen van het verschil in brekingsindex, de volume fractie van paaltjes en de roosterconstante. Een verschil in brekingsindex groter dan 1.95 is nodig om een fotonische bandkloof te krijgen bij de optimale volumefractie van paaltjes (19%). Om structuren te maken met grote bandkloven is een aanzienlijk hoger index contrast nodig. De structuren die worden besproken in dit proefschrift zijn alle ontworpen zodat ze een fotonische bandkloof hebben rond de voor telecommunicatietoepassingen belangrijke golflengte van 1.5 μm. Uit de berekeningen blijkt dat om een Si fotonisch kristal te maken paaltjes nodig zijn van $\sim$200 nm diameter geplaatst in een vierkant rooster op een onderlinge afstand van $\sim$570 nm.

Hoofdstuk 3 laat zien dat dergelijke structuren ook daadwerkelijk kunnen worden gemaakt door gebruik te maken van een anisotroop etsproces in een SF_6/O_2 plasma. Om structuren te maken gebaseerd op het ontwerp van Hoofdstuk 2 wordt het etsproces systematisch onderzocht. De belangrijkste parameters, de instroom van O_2, de electrische spanning over het plasma en de temperatuur, worden geoptimaliseerd om zo verticaal mogelijk te etsen. De structuur van paaltjes kan men integreren met een dielectrische lichtgeleider om zo het licht op te sluiten in de “verticale” richting. Dit kan men doen door paaltjes te maken met een bovenkant met een materiaal met een hogere index, zoals amorf Si, of door paaltjes te maken in een silicium-op-isolator substraat. De fabricage van fotonische kristallen in beide materialen blijkt mogelijk.

De beperkingen en mogelijkheden van amorf Si als materiaal voor lichtgeleiders wordt nader onderzocht in Hoofdstuk 4. Het amorf Si wordt gemaakt door middel van bestraling van kristallijn Si met MeV Xe ionen. Na bestraling wordt het amorf Si netwerk thermisch gerelaxeerd. Het resultaat is een transparante, amorfe toplaag met een brekingsindex van 3.73 op een ondergrond van kristallijn Si (n = 3.45 bij λ = 1.55 μm). Optische transmissiemetingen aan lichtgeleiders van amorf Si laten zien dat amorf silicium bij 1.5 μm een intrinsieke absorptie coefficiënt heeft van 115 cm^{-1} (0.05 dB μm).

Hoofdstuk 5 bespreekt een nieuwe methode om dunne SiO_2 films op een substraat te groeien. Met deze methode kan men films van $\sim$100 nm dikte groeien in een een mengsel van tetra-ethoxy-silaan, water, ammonia en ethanol. In het mengsel vormt zich een stabiele suspensie van colloïdale SiO_2 bollen. De reactie verloopt, na een eerste nucleatie stadium, via de aangroei van SiO_2 monomeren. Deze aangroei vindt plaatst op zowel de bolletjes als op de wanden van het reactievat en dus ook op een substraat dat in het mengsel wordt gehouden. Dankzij het mechanisme waarbij monomeren SiO_2 aangroeien kan deze methode ook worden toegepast op substraten die niet vlak zijn, zoals bijvoorbeeld fotonische kristallen gemaakt van Si paaltjes. Voor een aantal toepassingen van fotonische kristallen is het nodig om een lichtbron in te bouwen in het kristal. Echter, het inbouwen van een efficiënte lichtbron in Si is moeilijk. De dunne SiO_2 laag kan worden gebruikt om bijvoorbeeld een laser dye of erbium ionen in te bouwen om op die manier optisch actieve fotonische kristallen te maken.

Deel II behandelt de invloed van dielectrische structuren op de spontane emissie van atomen. Het eenvoudigste geval, waarbij Cr atomen dicht bij een dielectrisch grensvlak zijn geplaatst, wordt onderzocht in Hoofdstuk 6. De Cr atomen zijn door middel van ionen implantatie vlak onder het oppervlak van een Al_2O_3 kristal gebracht. Na een warmtebehandeling vertonen deze samples typische R-lijn luminescentie van robijn bij golflengten rond 694 nm. Cr ionen in preparaten met verschillende Cr piek concentraties (0.04 at.% – 0.28 at.%) hebben alle dezelfde stralend vervalsnelheid van 299 s^{-1}. Deze vervalsnelheid wordt bepaald door de luminescentie levensduur te meten voor samples in contact met een reeks van vloeistoffen met verschillende brekingsindex. Hierdoor veranderen de dielectrische eigenschappen van het grensvlak en daarmee de vervalsnelheid van de Cr ionen. Uit het experiment blijkt dat de vervalsnelheid toeneemt met toenemende brekingsindex van de vloeistof. Door de metingen te vergelijken met een berekening van de lokale toestandsdichtheid voor fotonen kunnen de stralende en niet-stralende bijdragen in het verval van de atomen worden bepaald. Omdat deze geometrie relatief eenvoudig is kan men de resultaten van Hoofdstuk 6 gebruiken als test voor het concept van lokale toestandsdichtheid. Daarnaast is het effect van concentratie-doving in rekening gebracht.

Om de toestandsdichtheid te onderzoeken in bolvormige microcavities kan men erbium ionen implanteren en deze als probe gebruiken. Hoofdstuk 7 behandelt de luminescentie van erbium geïmplanteerde SiO_2 colloïden met een diameter van 340 nm. De luminescentie intensiteit en levensduur van de erbium ionen wordt bepaald als functie van warmtebehandelingstemperatuur en erbium concentratie. De gemeten levensduur is 17 ms, wat suggereert dat de Er ionen een hoog kwantum rendement hebben. Hoofdstuk 8 gaat dieper in op concentratie-doving en een vergelijking wordt gemaakt tussen de vervalssnelheid van Er^{3+} ionen in bollen met een diameter van 175 en 340 nm. Het verschil in vervalsnelheid komt overeen met het verschil berekend uit de lokale toestandsdichtheid voor bolvormige SiO_2 deeltjes.

De ruimtelijke variatie in deze toestandsdichtheid wordt verder uitgewerkt in Hoofdstuk 9. De berekende toestandsdichtheid als functie van de diameter van de SiO_2 bol vertoont een aantal maxima en minima. Zowel de diameter waarbij deze maxima optreden als de radiële positie van de maxima komen overeen met die van Mie resonanties van de bol. Een dunne laag SiO_2 gegroeid volgens de methode van Hoofdstuk 5, en vervolgens geïmplanteerd met Er kan worden gebruikt om de stralende vervalsnelheid van Er in SiO_2 te bepalen: 54 s^{-1}. Deze informatie kan vervolgens worden gebruikt om de toestandsdichtheid te onderzoeken in de met Er gedoteerde SiO_2 bollen. De toestandsdichtheid kan in dit geval worden gevarieerd door de bollen onder te dompelen in een vloeistof te die dezelfde brekingsindex heeft als die van de bollen. Tevens wordt de relatie tussen the toestandsdichtheid en Förster energie-overdracht nader toegelicht in een Appendix.

De deeltjes beschreven in de Hoofdstukken 7, 8 en 9 zijn allen optisch gedoteerd met erbium met behulp van ionen implantatie. Helaas levert dit per implantatie slechts een beperkt aantal deeltjes op. Hoofdstuk 10 introduceert een alternatieve, nat chemische methode om colloïdale SiO_2 deeltjes te maken die zijn gedoteerd met zeldzaam aard ionen. Door gebruik te maken van een zuur gekatalyseerde reactie ontstaan ronde, bulk gedoteerde deeltjes met een relatief brede grootteverdeling. De luminescentieeigenschappen van dergelijke deeltjes gedoteerd met Er, Tb en Eu wordt besproken. Door een groei procedure toe te passen waarbij reeds aanwezige groeikernen verder worden aangegroeid kunnen luminescerende deeltjes worden gemaakt met een scherp gepiekte grootteverdeling. In dit geval wordt een dunne, Er gedoteerde schil van SiO_2 aangegroeid op bestaande SiO_2 bollen. Dergelijke luminescerende bollen kunnen worden gebruikt als probe in colloïdale fotonische kristallen.

Tot slot beschrijft Deel III een reeks experimenten aan driedimensionale fotonische kristallen. Deze kristallen bestaan uit een stapeling van poly-kristallijne silicium staafjes gemaakt door middel van microfabricage technieken. Hoofdstuk 11 bespreekt de golflengte-afhankelijke reflectiviteit van deze fotonische kristallen als functie van de hoek van inval, de polarisatie van het licht en de oriëntatie van het kristal. De gemeten reflectiviteit wordt vergeleken met berekeningen. Voor een kristal met een eindige dikte hangt de reflectiviteit als functie van golflengte af van zowel de polarisatie als de oriëntatie van het oppervlak voor een kristal met een eindige dikte. Een superstructuur die aanwezig is in de kristallen leidt tot een aantal goed gedefinieerde minima in de reflectiviteit. Deze minima komen overeen met berekeningen voor dezelfde superstructuur. Het veranderen van de spontane emissie van atomen in deze structuur wordt beschreven in Hoofdstuk 12. Een brede luminescentie band is zichtbaar in de experimenten en wordt toegeschreven aan intrinsieke defecten van het poly-kristallijne Si. Een sterke afname van de intensiteit wordt waargenomen voor golflengten die in de fotonische bandkloof liggen. De veranderingen in het spectrum worden geanalyseerd aan de hand van een model dat de toestandsdichtheid voor fotonen en de interne Bragg verstrooiing in het kristal meeneemt. Uit het model blijkt dat het kwantum rendement van de lichtbron een belangrijke rol speelt. Uit de analyse blijkt verder dat de lichtintensiteit afneemt met 5 dB per eenheidscel. Dit is consistent met bestaande transmissiemetingen en berekeningen aan vergelijkbare kristallen.

Dankwoord

Een proefschrift schrijven kun je niet alleen. Daarom wil ik iedereen bedanken die de afgelopen jaren een bijdrage heeft geleverd. Een aantal mensen wil ik hier in het bijzonder noemen.

Mijn promotor en begeleider Albert Polman wil ik bedanken voor alle wetenschappelijke ideeën en daarbij behorende discussies die verwerkt zijn in dit proefschrift. Daarnaast heb ik enorm veel geleerd van de opbouwende kritiek van Albert bij het opschrijven en presenteren van de resultaten van onderzoek. Ook de overige groepsleden wil ik bedanken voor hun bijdrage aan dit proefschrift. Met veel plezier heb ik deelgenomen aan de werkbesprekingen, de dagelijkse discussies en andere activiteiten met de groepsleden. Bedankt Jan ter Beek, Johan Derks, Mark Brongersma, Teun van Dillen, Gerlas van den Hoven, Jeroen Kalkman, Pieter Kik, Lenneke Slooff, Christof Strohhöfer, Nick Hamelin, Jose dos Santos, Edwin Snoeks, Anna Tchebotareva, Basjan Berkhout, Michaël Hensen, Joan Penninkhof, Max Siem, Dirk Vossen, Jan van der Elsken, Hideo Isshiki en Sjoerd Roorda. Mijn kamergenoten Jan van der Elsken, Lenneke Slooff en later ook Jeroen Kalkman wil ik in het bijzonder bedanken voor de gezelligheid, de goede sfeer en de vele discussies op onze kamer. Lenneke zorgde ervoor dat er in ieder geval één opgeruimd bureau was en was bovendien de trotse eigenaar van de planten en een pluche hond op de kamer. Jan zorgde voor een leerzame en welkome afwisseling door onderzoek aan PVP/water mengsels te doen. Met veel plezier denk ik terug aan de tijd besteed aan dit onderzoek bij het ESRF in Grenoble samen met met Jan van der Elsken, Jan Michielsen, Christof Strohhöfer en Jeroen Kalkman.

Zonder de ondersteuning van de groepstechnici Johan Derks en Jan ter Beek was dit proefschrift nooit mogelijk geweest. Jan en Johan zorgde niet alleen voor de apparatuur, maar waren daarnaast altijd bereid om uit te leggen hoe iets werkt. Jan wil ik bedanken voor de spoedcursus solderen die ik kreeg toen ik snel een nieuwe voeding voor de RBS nodig had. Johan Derks heeft mij bijvoorbeeld uitgelegd hoe een SF_6 detector werkt, nadat ik zelf had vastgesteld dat batterijen in serie best een hoge spanning kunnen leveren. Ook noem ik hier de mensen van de werkplaats, E&I en de tekenkamer die altijd klaar stonden om me te helpen met de meest uiteenlopende wensen en problemen.

Een aantal mensen leverde een directe bijdrage aan het onderzoek in dit proefschrift. Van de begeleiding en ideeën van Edwin Snoeks in het eerste jaar van mijn promotie heb ik enorm veel geleerd. Ad Lagendijk gaf mij een programma dat lokale toestandsdichtheid uit kan rekenen. Ik wil Ad bedanken voor zijn uitleg en omdat hij mij heeft overtuigd om zelf zo'n programma te (her)schrijven. Zonder de uitleg van Adriaan Tip, Han van der Lem en Alexander Moroz had ik de theorie nodig voor dit proefschrift nooit doorgrond. Bovendien blijkt in de praktijk dat Alexander altijd een computerprogramma bij de hand heeft om de dingen die hij zegt ook echt uit te rekenen. Zonder de prettige samenwerking met Emile van der Drift en Tony Zijlstra waren er nooit Si paaltjes geëtst in de cleanroom van DIMES in Delft. Daarnaast was ook de hulp van Michiel Blauw, Arjan van Zuuk, Maurice van den Boer en Jeroen Kalkman onmisbaar om het etsproces uiteindelijk zelf onder de knie te krijgen. Door de uitstekende samenwerking met Alfons van Blaaderen zijn er colloïden in dit proefschrift gekomen. Bovendien blijkt dat Alfons vaak een logische verklaring heeft voor de verrassingen waar je als fysicus tegen op loopt als je deze colloïden zelf probeert te maken. Lenneke Slooff implanteren van erbium in silica colloïden. Dirk Vossen, Michaël Hensen en Basjan Berkhout deden het onderzoek dat resulteerde in drie hoofdstukken van dit proefschrift. Rene Koper polijste de amorf silicium waveguides en wist bovendien hoe je aan saffier substraten kunt komen die weinig chroom bevatten. I would like to thank Shawn Lin and Jim Fleming from Sandia for all scientific discussions and for the fruitful collaboration that started with sending me some pieces of the woodpile sample. In a very short period of time, Boris Gralak managed to calculate, understand and explain the experimental reflectivity of these samples.

Dankzij de volleyballers van VCW, VV Compaen en VVA was het mogelijk om naast het onderzoek ook te ontspannen. Tot slot wil mijn ouders en mijn zusje Mathilde bedanken voor hun niet aflatende belangstelling in alles wat ik doe.

Curriculum Vitae

Michiel de Dood werd geboren in Landsmeer op 18 januari 1975. Vanaf 1987 bezocht hij de Scholengemeenschap Noord waar hij in 1993 het VWO diploma behaalde. In hetzelfde jaar begon hij aan een studie Natuurkunde aan de Universiteit van Amsterdam. In 1996 verrichte hij een zes maanden durende stage in de groep van Prof. Dr. A. Polman aan het FOM-Instituut voor Atoom- en Molecuulfysica (AMOLF) in Amsterdam, waar hij het optische doteren van silicium met erbium ionen bestudeerde. Zijn afstudeerstage deed hij bij het Shell Research and Technology Centre Amsterdam onder begeleiding van Dr. B.F.M. Pots en Dr. A.J.N. Vreenegoor, waar hij onderzoek deed aan de stroming van olie/water mengsels. Het doctoraal examen Natuurkunde aan de Universiteit van Amsterdam met als specialisatie Technische Natuurkunde werd "cum laude" afgelegd in november 1997. Aansluitend begon hij zijn promotie onderzoek in de groep Opto-elektronische materialen van Prof. Dr. A. Polman aan het FOM Instituut voor Atoom- en Molecuulfysica. De resultaten van dit onderzoek staan beschreven in dit proefschrift.

List of publications

This thesis is based on the following publications:

Chapter 2: *Design and optimization of 2-D photonic crystal waveguides based on silicon*
M. J. A. de Dood, E. Snoeks, A. Moroz and A. Polman
IEE Opt. Quant. Elec. **34**, 145 (2002)

Chapter 3: *Fabrication of two-dimensional photonic crystal waveguides at 1.5 μm in silicon by deep anisotropic dry etching*
T. Zijlstra, E. W. J. M. van der Drift, M. J. A. de Dood, E. Snoeks and A. Polman
J. Vac. Sci. Technol. B **17**, 2734 (1999)

Chapter 4: *Amorphous silicon waveguides for microphotonics*
M. J. A. de Dood, T. Zijlstra, E. W. J. M. van der Drift and A. Polman
submitted to J. Appl. Phys.

Chapter 5: *Novel method for solution growth of thin silica films from tetraethoxysilane*
D. L. J. Vossen, M. J. A. de Dood, T. van Dillen, T. Zijlstra, E. W. J. M. van der Drift, A. van Blaaderen and A. Polman
Adv. Mat. **12**, 1434 (2000)

Chapter 6: *Luminescence quantum efficiency and local optical density of states in thin film ruby made by ion implantation*
T. M. Hensen, M. J. A. de Dood and A. Polman
J. Appl. Phys. **88**, 5142 (2000)

Chapter 7: *Erbium-implanted silica colloids with 80% luminescence quantum efficiency*
L. H. Slooff, M. J. A. de Dood, A. van Blaaderen and A. Polman
Appl. Phys. Lett. **76**, 3682 (2000)

Chapter 8: *Modified spontaneous emission in erbium-doped SiO_2 spherical colloids*
M. J. A. de Dood, L. H. Slooff, A. Moroz and A. van Blaaderen and A. Polman
Appl. Phys. Lett. **79**, 3585 (2001)

Chapter 9: *Local optical density of states in SiO_2 spherical microcavities: Theory and experiment*
M. J. A. de Dood, L. H. Slooff, A. Moroz and A. van Blaaderen and A. Polman
Phys. Rev. A. **64**, 033807 (2001)

Chapter 10: *Acid based synthesis of monodisperse rare earth doped colloidal SiO_2 spheres*
M. J. A. de Dood, B. Berkhout, C. M. van Kats, A. Polman and A. van Blaaderen
submitted to Chem. Mater.

Chapter 11: *Superstructure and finite size effects in a Si photonic woodpile crystal*
M. J. A. de Dood, B. Gralak, A. Polman, J. G. Fleming and Shawn-Yu Lin
submitted to Phys. Rev. B

Chapter 12: *Modified spontaneous emission from erbium doped photonic woodpile crystals*
M. J. A. de Dood, A. Polman, J. G. Fleming and Shawn-Yu Lin
submitted to Phys. Rev. Lett.

Other publications to which the author of this thesis contributed:

Incorporation, excitation and de-excitation of erbium in crystal silicon
M. J. A. de Dood, P. G. Kik, J. H. Shin and A. Polman
MRS Symp. Proc. **422**, 219 (1996)

Excitation and deexcitation of Er^{3+} in crystalline silicon
P. G. Kik, M. J. A. de Dood, K. Kikoin and A. Polman
Appl. Phys. Lett. **70**, 1721 (1997)

1, 2 and 3 dimensional photonic materials made using ion beams: fabrication and optical density-of-states
M. J. A. de Dood, L. H. Slooff, T. M. Hensen, D. L. J. Vossen, A. Moroz, T. Zijlstra, E. W. J. M. van der Drift, A. van Blaaderen and A. Polman
Proceeding of the NATO advanced study institute on photonic crystals and light localization, Crete, Greece, June 18–30, 2000, ed. by C. M. Soukoulis, p. 555 (2001)

Effects of heat treatment and concentration on the luminescence properties of erbium-doped silica sol-gel films
L. H. Slooff, M. J. A. de Dood, A. van Blaaderen and A. Polman
J. Non-Cryst. Sol. **296**, 158 (2001)